JLS, Mgr, MFE Matls. 10-19

DOE/ER-0046/10

Damage Analysis and Fundamental Studies

Quarterly Progress Report
April-June 1982

August 1982

U.S. Department of Energy
Assistant Secretary for Energy Technology
Office of Fusion Energy
Washington, DC 20545

NOTICE

This report was prepared as an account of work sponsored by the United States Government. Neither the United States nor the U.S. Department of Energy (DOE), nor any of its employes, nor any of its contractors, subcontractors or their employes, makes any warranty, expressed or implied, or assumes any legal liability or responsibility for any third party's use or the results of such use of any information, apparatus, product or process disclosed in this report, or represents that its use by such third party would not infringe privately owned rights.

Printed in the United States of America
Available from
National Technical Information Service
U.S. Department of Commerce
5285 Port Royal Road
Springfield, VA 22161

NTIS price codes
Printed copy: A13
Microfiche copy: A01

DOE Richland WA

DOE/ER-0046/10
UC-20,20c

Damage Analysis and Fundamental Studies

Quarterly Progress Report
April-June 1982

August 1982

U.S. Department of Energy
Assistant Secretary for Energy Technology
Office of Fusion Energy
Washington, DC 20545

FOREWORD

This report is the eighteenth in a series of Quarterly Technical Progress Reports on ***Damage Analysis and Fundamental Studies*** (OAFS), which is one element of the Fusion Reactor Materials Program, conducted in support of the Magnetic Fusion Energy Program of the U.S. Department of Energy (DOE). The first eight reports in this series were numbered DOE/ET-0065/1 through 8. Other elements of the Fusion Materials Program are:

- Alloy Development for Irradiation Performance (ADIP)
- Plasma-Materials Interaction (PMI)
- Special Purpose Materials (SPM).

The OAFS program element is a national effort composed of contributions from a number of National Laboratories and other government laboratories, universities, and industrial laboratories. It was organized by the Materials and Radiation Effects Branch, DOE/Office of Fusion Energy, and a Task Group on ***Damage Analysis and Fundamental Studies,*** which operates under the auspices of that branch. The purpose of this series of reports is to provide a working technical record of that effort for the use of the program participants, the fusion energy program in general, and the DOE.

This report is organized along topical lines in parallel to a Program Plan of the same title so that activities and accomplishments may be followed readily, relative to that Program Plan. Thus, the work of a given laboratory may appear throughout the report. The Contents is annotated for the convenience of the reader.

This report has been compiled and edited under the guidance of the Chairman of the Task Group on ***Damage Analysis and Fundamental Studies,*** D. G. Doran, Hanford Engineering Development Laboratory (HEDL). His efforts, those of the supporting staff of HEDL, and the many persons who made technical contributions are gratefully acknowledged. M. M. Cohen, Materials and Radiation Effects Branch, is the DOE counterpart to the Task Group Chairman and has responsibility for the **DAFS** program within DOE.

G. M. Haas, Acting Chief
Materials and Radiation Effects Branch
Office of Fusion Energy

CONTENTS

	Page
Foreword	iii
Figures	xi
Tables	xix

CHAPTER 1: IRRADIATION TEST FACILITIES

1. RTNS-II Irradiations and Operations (LLNL) 3

Irradiations were performed for a total of seventeen different experimenters during this quarter.

After nearly four years of operation, the accelerator tube electron trap failed, causing approximately three weeks of unscheduled outage.

Plans for fabrication of a new accelerator column have begun.

The first U.S.-Japan Steering Committee meeting was held April 19-21 in Tokyo. An initial list of experiments was approved.

CHAPTER 2: DOSIMETRY AND DAMAGE PARAMETERS

1. Dosimetry Results for the TRIO Test in ORR (ANL) 9

Dosimetry was performed for the TRIO tritium recovery experiment in the Oak Ridge Research Reactor (ORR). The tritium production rate from the $^6Li(n,\alpha)$ reaction calculated using the measured flux-spectrum is in excellent agreement with Oak Ridge measurements.

The status of all other dosimetry is summarized in Table I.

2. Experiments at the IPNS Spallation Neutron Source (ANL) 16

Dosimetry results are presented for an irradiation by G. Hurley (LANL) at IPNS (ANL) on February 22-27, 1982 (described elsewhere in this report). The maximum neutron fluence was 1.55×10^{17} n/cm^2 (>0.1 MeV), 2.23×10^{17} n/cm^2 (total).

CONTENTS (Cont'd)

Page

3. Helium Production Cross Sections for 14.8-MeV Neutrons (RIES) 19

Total helium production cross sections for ~14.8-MeV neutrons have been determined for LiF, PbF_2, F, Li, B, the separated isotopes of Li and B, and the three alloys HT-9, 9Cr-1Mo, and Type 316 stainless steel. Some minor alloy constituents are significant contributors. The measured $^7Li(n,n't)\alpha$ cross section is ~30% higher than a recent evaluation.

4. Damage Energy for (n,γ) and Beta-Decay (ANL) 28

Calculation of recoil-atom energy distributions from neutron capture reactions have been revised to take into account the effects of incident neutron energy, gam-ray recoil momentum summing and y-y angular correlations in y-cascades, lifetimes of the intermediate states, and recoil effects resulting from subsequent 8-decay when relevant.

5. Nuclear Data Applications in Radiation Damage Studies (HEDL) 39

The calculated transmutation rate of V-15%Cr-5%Ti is low except in mixed spectrum reactors such as HFIR.
The first module of the NJOY code has been successfully modified to handle data in the >20-MeV ENDF/B formats.

6. A Semi-Empirical Kinetic Model for Quenching of High Energy Displacement Cascades (HEDL) 44

The quenching stage of simulated cascades was accomplished using the stochastic computer code ALSOME with exaggerated values for defect mobilities and critical recombination and clustering reaction distances. Quenching parameter values were chosen to fit experimental defect yields. The number of defect pairs after quenching and after annealing, and the number of freely migrating defects, vary linearly with cascade damage energy from 10 to 100 keV.

CONTENTS (Cont'd)

Page

7. Comparison of Neutron and Gamma Irradiation Damage in Organic Insulators (LANL) 53

Three epoxy- and three polyimide-based materials were neutron irradiated in IPNS-1 to an average fluence of 1.51 x 10^{21} n/cm^2, E_n >0.1 MeV, at 4.2 K. The gamma dose was less than 15% of the neutron dose (Gy). The environmental and thermal conditions during and after irradiation were similar to those employed in a previous study of gama irradiation effects at ORNL. Incomplete measurements of mechanical, electrical, and optical properties have disclosed some differences between neutron and gamma effects.

CHAPTER 3: FUNDAMENTAL MECHANICAL BEHAVIOR

1. Correlation of Hardness and Strength Data for High Energy Neutron Irradiated Annealed 316 Stainless Steel (HEDL) 77

Strength values derived from hardness data are in good agreement with actual tensile data for 14-MeV neutron-irradiated annealed 316 stcinless steel.

2. Hardening of Irradiated Alloys Due to the Simultaneous Formation of Vacancy and Interstitial Loops (UCLA and HEDL) 84

A model based on homogeneous time-dependent rate theory is presented for the simultaneous nucleation and growth of vacancy and interstitial loops in irradiated metals.
A simple hardening model relating the microstructural calculations to changes in tensile strength gives good agreement with hardening data for copper irradiated in RTNS-11 at room temperature.

3. A Model for the Evolution of Network Dislocation Density in Irradiated Metals (HEDL and U. of Wisconsin) 106

A litemture review shows that the network dislocation density in irradiated metals approaches a satumtion level which is relatively

Page

insensitive to starting microstructure, stress, irradiation temperature, displacement rate and helium level. A model, taking into account the correlated nature of dislocation components in a dense array, has been developed to explain this insensitivity.

4. Relationships Between Crack Propagation and Tensile Properties in Type 316 Stainless Steel Foil Microspecimens (U. of Virginia) **130**

It has been demonstrated that some tensile data obtained from 40-μm thick foil microspecimens pulled in-situ in an HVEM are related to bulk tensile data. The in-situ data are related to the manner in which the main crack propagates through the thin (<1-μm) regions of the specimen. Statements about specimen ductility may possibly be made from this relationship.

CHAPTER 4: CORRELATION METHODOLOGY

1. Cavity Formation and Solute Segregation in Dual-Ion Irradiated Fe-20Ni-15Cr Alloy (ANL) 145

Swelling of specimens receiving heliwn deposition rates of 15 or 50 appm He per dpa at 975K tends to achieve a limiting value after ∿70 dpa. Grain boundaries and voids are increasingly enriched in nickel, with a corresponding depletion of the nickel concentration in the matrix, for increasing displacement damage up to 2.70 dpa. For displacement damage >70 dpa, the nickel enrichment appears to diminish. The change in chromiwn concentration at the grain boundaries and voids and in the matrix is opposite to the change in nickel concentration and of smaller magnitude.

CONTENTS (Cont'd)

Page

2. On Radiation-Induced Segregation and the Compositional Dependence of Swelling in Fe-Ni-Cr Alloys (U. of Wisconsin and HEDL) 157

It appears that elemental segregation to void surfaces plays an important role in the development of voids. Previously unconsidered drift terms are shown to arise in the description of the bias as a result of elemental segregation. When compounded with the operation of the inverse Kirkendall segregation mechanism, these terms provide an explanation for the marked variation of void nucleation and swelling with nickel concentration.

3. The Influence of Cold Work Level, Solute and Helium Content on the Swelling of "Pure" AISI 316 (Fe-17Cr-16.7Ni-2.5Mo) (HEDL) 181

Examination of "pure 316" specimens irradiated to 3-5 dpa in ORR shows that both the volume and density of voids are insensitive to cold work.
The preinjection of 30 appm helium appears to suppress visible swelling; however, both density change measurements and postirradiation aging studies indicate that swelling may exist in the form of unresolvable cavities.

4. The Effect of Helium on Swelling in Stainless Steel: Influence of Cavity Density and Morphology (UCSB) 199

Data on irradiated 316 stainless steel suggests that the cavity density scales as $(He/dpa)^p$, where $0<p<1$. A rate theory model, calibrated using data from EBR-11 irradiations of 20% cold worked 316 stainless steel, was used to examine the parametric dependence of cavity swelling on the value of p and the He/dpa ratio. Beyond a critical value of p there is a bifurcation in the cavity evolution path from microstructures dominated by precipitate-associated

Page

voids to microstructure dominated by matrix bubbles. The model predicts peak swelling near the fusion He/dpa ratio suggesting that the use of fission reactor swelling data my lead to non-conservative estimates of swelling for fusion.

5. Microstructural/Microchemical Evolution of AISI 316 Irradiated at Temperatures in the Range 650-750°C (HEDL) 233

Swelling in two specimens irradiated in EBR-II to temperatures of 700-720°C is found to be comparable to that observed at 650°C and below, but the void densities are lower. Voids appear first in grains that have nickel levels below 12-13 wt.%. The matrix content of nickel declines to ~9% as the swelling increases.

6. Lithium Doping of 316 Stainless Steel to Simulate Irradiation Damage in a Fusion Reactor Environment (MIT) 249

Austenitic stainless steel containing a uniform distribution of lithium was prepared using rapid solidification processing and a powder metallurgy salt decomposition technique. The advantage of a lithium dopant is that it produces only helium and hydrogen.

FIGURES

Page

CHAPTER 2

1. Dosimetry Results for the TRIO Test in ORR (ANL)

FIGURE 1. Flux Spectrum Measured for the A2 Position in ORR for the TRIO Experiment. 15

FIGURE 2. Vertical Flux Gradients Measured in Position A2 of ORR. 15

4. Damage Energy for (n,γ) and Beta-Decay (ANL)

FIGURE 1. Typical Neutron Capture Recoil Event. 31

5. Nuclear Data Applications in Radiation Damage Studies (HEDL)

FIGURE 1. Transmutation of V-15%Cr-5%Ti in MFE Facilities: Vanadium Concentration. 42

FIGURE 2. Transmutation of V-15%Cr-5%Ti in MFE Facilities: Chromium Concentration. 42

6. A Semi-Empirical Kinetic Model for Quenching of High Energy Displacement Cascades (HEDL)

FIGURE 1. The Number of Defect Pairs Remaining After Quenching and Short-Term Annealing of Isolated Cascades in Copper as a Function of PKA Damage Energy. 49

7. Comparison of Neutron and Gamma Irradiation Damage in Organic Insulators (LANL)

FIGURE 1. A.C. Electrical Properties of G-10 CR Control Samples at 295K. 58

FIGURE 2. A.C. Electrical Properties of G-10 CR Irradiated Samples at 295K. 59

FIGURE 3. A.C. Electrical Properties of G-10 CR Samples at 80K. 60

FIGURE 4. A.C. Electrical Properties of G-10 CR Irradiated Samples at 80K. 61

FIGURE 5. Three-Point Flexure Strength of Five Materials Before (c) and After (i) Neutron Irradiation at 4.2K. 63

FIGURES (Cont'd)

		Page
FIGURE 6.	"Yield" and Failure Strains for Samples in Figure 5.	63
FIGURE 7.	Flexure Modulus of Samples in Figure 5.	65
FIGURE 8.	Compression Strength of Five Materials Before (c) and After (i) Neutron Irradiation at 4.2K.	65
FIGURE 9.	Failure Strain in Compression for Samples in Figure 8.	66
FIGURE 10.	Compression Modulus for Samples in Figure 8.	66
FIGURE 11.	Photographs Contrasting the Appearance of Failed G-10 CR.	68

CHAPTER 3

1. Correlation of Hardness and Strength Data for High Energy Neutron Irradiated Annealed 316 Stainless Steel (HEDL)

FIGURE 1.	Comparison of $\Delta\sigma_y$, the Measured Increase in the 0.2 Percent Offset Tensile Yield Strength, of Two Heats of Annealed Type 316 Stainless Steel and the Strengthening of Reference Heat 316 Stainless Steel Calculated from Diamond Pyramid Hardness (DPH) Data.	82

2. Hardening of Irradiated Alloys Due to the Simultaneous Formation of Vacancy and Interstitial Loops (UCLA and HEDL)

FIGURE 1.	Small Defect Clusters and Their Associated Hardening Observed in Copper and Simple Copper Alloys Irradiated in RTNS-II with 14-MeV Neutrons at 25°C.	87
FIGURE 2.	Calculated Concentrations of Major Irradiation-Induced Defects Which Contribute to Hardening of Copper Irradiated in RTNS-II at 25°C.	97
FIGURE 3.	Calculated Fluence Dependence of Average Radius for Vacancy and Interstitial Loops in Copper Irradiated in RTNS-II at 25°C.	98
FIGURE 4.	Fluence Dependence of Various Fractions Describing Distribution of Defects.	100
FIGURE 5.	Calculated Major Contributions to the Increase in 0.2% Offset Yield Stress of Copper at 25°C in RTNS-II.	101

FIGURES (Cont'd)

Page

FIGURE 6. Effects of Self-Interstitial Trapping on the Predicted Increase of Yield Stress of Copper Irradiated at 25°C. 102

FIGURE 7. A Comparison Between Theoretical Calculations and Experimental Measurements of Copper Hardening Due to RNTS-II Irradiation at 25°C. 102

3. A Model for the Evolution of Network Dislocation Density in Irradiated Metals (HEDL and U. of Wisconsin)

FIGURE 1. Dependence of Dislocation Loop Density on Starting Condition and Fluence in Aluminum Irradiated in the Siloe Reactor at 55°C. 109

FIGURE 2. Micrographs Showing Dislocation and Loop Microstructures Induced in AISI 316. 110

FIGURE 3. Frank Loop Densities Observed in 20% Cold-Worked AISI 316 Fuel Pin Cladding Irradiated in EBR-II. 111

FIGURE 4. Total Dislocation Density Observed in 20% CW M316 Fuel Pin Cladding Designated V1294. 111

FIGURE 5. Saturation of Network Dislocation Density in Both 20% Cold-Worked and Annealed AISI 316 After Irradiation in EBR-II. 114

FIGURE 6. Network Dislocation Density Measured in Three 20% Cold-Worked AISI 316 Fuel Pin Cladding Doses Ranging From 20 to 50 dpa in EBR-II. 114

FIGURE 7. Independence of Dislocation Density on Temperature and Starting Condition in M316 Fuel Pin Cladding Irradiated in the Dounreay Fast Reactor. 115

FIGURE 8. Independence of Dislocation Density in AISI 316 on Starting Condition, Temperature and Displacement Level After Irradiation in the Rapsodie Fast Reactor. 115

FIGURE 9. Saturation of Dislocation Density at High Displacement Rates in Annealed AISI 316 at 525°C and Annealed 321 at 600°C for Two Deeply Penetrating Ions. 116

FIGURE 10. Saturation of Dislocation Density at 600°C in Shallow Penetration Ion Bombardment Experiments. 116

FIGURES (Cont'd)

Page

FIGURE 11. Dependence of Saturation Dislocation Density on Surface Influence, as Demonstrated by Dependence of Dislocation Density on Temperature and Displacement Rate. 118

FIGURE 12. Dislocation Saturation Level is Independent of Helium Content in Dual Ion Irradiations of Fe-20Ni-15Cr at 700°C. 118

FIGURE 13. Schematic Representation of Dislocation Network Evolution in Metals Without Surface Influence. 119

FIGURE 14. Schematic Representation of Correlated Movement of Dislocation Pairs (dipoles). 121

FIGURE 15. Predictions of the Evolution of Dislocation Density in AISI 316 at 500°C for Starting Densities of 7×10^{11} cm/cm^3 and 4×10^8 cm/cm^3, Chosen to Represent Cold-Worked and Annealed Conditions. 126

FIGURE 16. Calculations of Dislocation Climb Velocity V for Several Values of Bias Difference Between Dislocations in Different Configurations. 126

4. Relationships Between Crack Propagation and Tensile Properties in Type 316 Stainless Steel Foil Microspecimens (U. of Virginia)

FIGURE 1. Graph Illustrating the Relationship Between the Ultimate Tensile Strength (UTS) Determined from HVEM Microtensile Specimens and the UTS of Bulk Specimens. 134

FIGURE 2. Graph Illustrating the Relationship Between Reduction of Area for HVEM Microtensile Specimens and Bulk Specimens. 135

FIGURE 3. Graph of Cumulative Crack Tip Displacement Length, L, Versus Total Elongation (Total Crosshead Displacement) Obtained From Continuous HVEM Video Recordings. 137

FIGURE 4. Graph of Crack Length Versus Total Elongation Illustrating Three Distinct Average Slopes, Each Representative of a Specimen Test Condition. 138

CHAPTER 4

1. Cavity Formation and Solute Segregation in Dual-Ion Irradiated Fe-20Ni-15CR Alloy (ANL)

FIGURE 1. Dependence of Average Cavity Diameter on Displacement Damage in Fe-20Ni-15Cr Alloy. 149

FIGURES (Cont'd)

		Page
FIGURE 2.	Dependence of Cavity Number Density on Displacement Damage in Fe-20Ni-15Cr Alloy.	149
FIGURE 3.	Dependence of Cavity Volume Fraction on Displacement Damage in Fe-20Ni-15Cr Alloy.	150
FIGURE 4.	Microstructures of Dual-Ion Irradiated Fe-20Ni-15Cr Alloy (50 appm He per dpa).	152
FIGURE 5.	Dependence of Ni and Cr Concentration at Grain Boundaries on Displacement Damage in Fe-20Ni-15Cr Alloy (50 appm He per dpa).	153
FIGURE 6.	Dependence of Ni and Cr Concentration at Voids on Displacement Damage in Fe-20Ni-15Cr Alloys (50 appm He per dpa).	153
FIGURE 7.	Dependence of Ni and Cr Concentration in the Matrix on Displacement Damage in Fe-20Ni-15Cr Alloy (50 appm He per dpa).	154

2. On Radiation-Induced Segregation and the Compositional Dependence of Swelling in Fe-Ni-Cr Alloys (U. of Wisconsin and HEDL)

FIGURE 1.	Lattice Parameter in Å for Gamma-Phase Alloys at Room Temperature.	161
FIGURE 2.	Shear Modulus (in 10 MPa) for Fe-Ni-Cr Alloys at Room Temperature.	162
FIGURE 3.	STEM Image of Void and Composition Profiles Obtained in EDX Microanalysis in Neutron-Irradiated Fe-15Cr-25Ni-0.3Si Alloy Irradiated in EBR-II at 510°C.	166
FIGURE 4.	Microanalysis Geometry and Composition Profiles Derived from Fe-15Cr-25Ni Irradiated in EBR-II at 540°C.	167
FIGURE 5.	Activation Free Energy for Self-Diffusion in Binary Fe-Ni Alloys.	174
FIGURE 6.	Thermodynamic Factor for Binary Fe-Ni Alloys.	175
FIGURE 7.	Coefficient of the Kirkendall Force on Vacancies in Binary Fe-Ni Alloys.	176
FIGURE 8.	Possible Variation of the Coefficient for the Kirkendall Force on Interstitials as a Function of the Composition of Binary Fe-Ni Alloys.	176

FIGURES (Cont'd)

Page

3. The Influence of Cold Work Level, Solute and Helium Content on the Swelling of "Pure" AISI 316 (Fe-17Cr-16.7Ni-2.5Mo) (HEDL)

FIGURE 1. Dependence of Swelling on Impurity Level at 625-635°C in Nickel-Ion-Irradiated AISI 316. 185

FIGURE 2. Void Microstructure in Annealed and 20% Cold-Worked Fe-17Cr-16.7Ni-2.5Mo Irradiated in ORR at 550°C to 4 dpa. 187

FIGURE 3. Effect of Foil Thickness on Number Density of Visible Voids. 189

FIGURE 4. Effect of (a) Solution Annealing and (b) Cold-Working 20% on Void Formation in AISI 316 Stainless Steel Irradiated in EBR-II at 560°C to 4.5 dpa. 189

FIGURE 5. Under-Focused (Top) and Over-Focused (Bottom) Images of Cavities in Fe-17Cr-16.7Ni-2.5Mo + 30 appm Helium Irradiated in ORR at 550°C for 4 dpa an then Aged One-Quarter Hour at 900°C. 191

FIGURE 6. Distribution of Visible Cavities Observed in Specimen Described in Figure 5. 192

FIGURE 7. Effect of Cold Work on Swelling of AISI 316 Stainless Steel at High Neutron Fluence. 193

FIGURE 8. Dependence of Neutron-Induced Swelling on Cold Work Level in AISI 316 at 550°C. 193

4. The Effect of Helium on Swelling in Stainless Steel: Influence of Cavity Density and Morphology (UCSB)

FIGURE 1. Influence of Helium/dpa Ratio on Cavity Density and Morphology, EBR-II vs. HFIR. 201

FIGURE 2. Influence of Prior Heat Treatment in HFIR on Cavity Density and Morphology. 202

FIGURE 3. Influence of Helium/dpa Ratio on Cavity Density and Void Swelling in Dual-Ion Irradiation of Ti-Modified 316. 203

FIGURE 4. Temperature Dependence of Dislocation Density (ρ_d) and Cavity Density (N_c) Used in Model. 206

FIGURES (Cont'd)

		Page
FIGURE 5.	Comparison of Predicted and Observed Fluence and Temperature Dependence of Swelling for Fast Reactor Conditions.	212
FIGURE 6.	Comparison of Predicted Fluence Dependence of Swelling Behavior for EBR-II, HFIR, and Fusion at the Indicated Temperatures and Values of p.	215
FIGURE 7.	Predicted Swelling at 75 dpa for HFIR and Fusion as a Function of p.	217
FIGURE 8.	Predicted Temperature Dependence of Incubation Exposure (τ=dose to 1% swelling) and Steady-State Swelling Rate ($\dot{S}$=swelling rate at 75 dpa) for Fusion When Normalized to EBR-II Values.	217
FIGURE 9.	Predicted He/dpa Ratio Dependence of Swelling at 75 dpa and at the Indicated Temperature and Values of p.	219

5. Microstructural/Microchemical Evolution of AISI 316 Irradiated at Temperatures in the Range 650-750°C (HEDL)

FIGURE 1.	High Temperature Swelling of 20% CW AISI 316 Stainless Steel Specimens Showing Comparison Between CN-13 Creep Tube Data with Data at 650°C for CN-13 and Three Closely Related Heats.	235
FIGURE 2.	High Temperature Swelling of CN-13 Creep Tube KE6 at 700-718°C and 6.2 x 10^{22} n/cm^2 (E >0.1 MeV).	236
FIGURE 3.	Local Matrix Composition of Nickel in Two Adjacent Grains of Specimen K65 of 20% Cold-Worked AISI 316 Irradiated at 667-710°C and 7.5 x 10^{22} n/cm^2 (E >0.1 MeV).	239
FIGURE 4.	Typical EDX Spectra of Specimen K65.	240
FIGURE 5.	Line-of-Sight Composition Profile Along a Traverse Across a Void in Specimen K65.	242
FIGURE 6.	Line-of-Sight Composition Profile Along a Traverse Across a Grain Goundary Separating Voided and No-Void Regions in Specimen K65.	242
FIGURE 7.	Line-of-Sight Composition Profile Along a Traverse Across a Grain Boundary Showing Evidence of Nickel Segregation.	243
FIGURE 8.	Line-of-Sight Composition Profile Across Precipitate/Matrix Interface in Specimen K65.	243

FIGURES (Cont'd)

Page

6. Lithium Doping of 316 Stainless Steel to Simulate Irradiation Damage in a Fusion Reactor Environment (MIT)

FIGURE 1. SEM Micrograph Showing the Morphology of Rapidly Solidified Powders of 316 Stainless Steel Alloyed with 1% Al. 254

FIGURE 2. SEM Micrograph Showing the Morphology of Attrited Flakes. 254

FIGURE 3. Neutron Autoradiograph of 316-Type Stainless Steel Without Lithium Addition. 257

FIGURE 4. Neutron Autoradiograph of 316-Type Stainless Steel Doped with 1000-wppm Lithium. 257

TABLES

Page

CHAPTER 2

1. Dosimetry Results for the TRIO Test in DRR (ANL)

TABLE 1. Status of Reactor Experiments. 10

TABLE 2. Activation Rates for TRIO 1. 13

TABLE 3. Neutron Flux Values for TRIO 1. 14

2. Experiments at the IPNS Spallation Neutron Source (ANL)

TABLE 1. Dosimetry Results for IPNS. 17

3. Helium Production Cross Sections for 14.8-MeV Neutrons (RIES)

TABLE 1. Experimental Helium Generation Cross Sections for ∿14.8-MeV Neutrons. 22

TABLE 2. Total Helium Production Cross Sections of Candidate Fusion Reactor Alloys for 14.8-MeV Neutrons. 24

TABLE 3. Contributions of Constituent Elements to Total Helium Production Cross Sections of Selected Alloys for 14.8-MeV Neutrons. 26

4. Damage Energy for (n,γ) and Eeta-Decay (ANL)

TABLE 1. Primary Displacement Energy Cross Sections. 35

TABLE 3. Neutron Capture Damage for HFIR. 37

5. Nuclear Data Applications in Radiation Damage Studies (HEDL)

TABLE 1. Transmutations of V-15%Cr-5%Ti at 50 dpa. 41

7. Comparison of Neutron and Gamma Irradiation Damage in Organic Insulators (LANL)

TABLE 1. Results of Gas Bottle Analyses. 56

TABLE 2. D.C. Resistivity for Four Each Control and Irradiated Specimens for G-10 CR. 62

TABLES (Cont'd)

Page

CHAPTER 3

1. Correlation of Hardness and Strength Data for High Energy Neutron Irradiated Annealed 316 Stainless Steel (HEDL)

TABLE 1. Chemical Composition. 79

TABLE 2. Heat Treatments and Baseline Properties. 80

TABLE 3. Type 316 Stainless Steel Strengthening Data. 81

2. Hardening of Irradiated Alloys Due to the Simultaneous Formation of Vacancy and Interstitial Loops (UCLA and HEDL)

TABLE 1. Definition of Terms. 90

TABLE 2. Material Parameters for Copper. 93

4. Relationships Between Crack Propagation and Tensile Properties in Type 316 Stainless Steel Foil Microspecimens (U. of Virginia)

TABLE 1. Comparison of Some Tensile Properties of HVEM Foil and Bulk Specimens for AISI Type 316 Stainless Steel. 133

CHAPTER 4

2. On Radiation-Induced Segregation and the Compositional Dependence of Swelling in Fe-Ni-Cr Alloys (U. of Wisconsin and HEDL)

TABLE 1. Typical Values for the Potentials of the Drift Forces in Fe-Ni Alloys. 177

3. The Influence of Cold Work Level, Solute and Helium Content on the Swelling of "Pure" AISI 316 (Fe-17Cr-16.7Ni-2.5Mo) (HEDL)

TABLE 1. Void Formation in Fe-17Cr-16.7Ni-2.5Mo Specimens. 187

TABLE 2. Effect of Cold Work on Swelling of Pure Metals. 194

TABLES (Cont'd)

Page

5. Microstructural/Microchemical Evolution of AISI 316 Irradiated at Temperatures in the Range 650-750°C (HEDL)

TABLE 1. Composition Determined by Broad Beam Scan in Specimen K65. 237

TABLE 2. Matrix Spot Analysis of Composition in Specimen K65. 238

TABLE 3. EDX Analysis of Specimen KE6. 245

TABLE 4. EDX Analysis of Voids in Specimen KE6. 246

CHAPTER 1

IRRADIATION TEST FACILITIES

RTNS-II IRRADIATIONS AND OPERATIONS

C. M. Logan and O. W. Heikkinen (Lawrence Livermore National Laboratory)

1.0 Objective

The objectives of this work are operation of RTNS-II (a 14-MeV neutron source facility), machine development, and support of the experimental program that utilizes this facility. Experimenter services include dosimetry handling, scheduling, coordination, and reporting. RTNS-II is dedicated to materials research for the fusion power program. Its primary use is to aid in the development of models of high-energy neutron effects. Such models are needed in interpreting and projecting to the fusion environment engineering data obtained in other neutron spectra.

2.0 Sumnary

Irradiations were performed for a total of seventeen different experimenters during this quarter.

After nearly four years of operation, the accelerator tube electron trap failed. This caused approximately three weeks of unscheduled outage for repair. Plans for fabrication of a new accelerator column have begun.

The first U.S.-Japan Steering Committee meeting was held April 19-21 in Tokyo.

3.0 Program

Title: RTNS-II Operations (WZJ-16)
Principal Investigator: C. M. Logan
Affiliation: Lawrence Livermore National Laboratory

4.0 Relevant OAFS Program Plan Task/Subtask

TASK II.A.2,3,4.
TASK II.B.3,4
TASK II.C.1,2,6,11,18.

5.0 Irradiation - C. M. Logan, D. W. Heikkinen and M. W. Guinan

Irradiations performed during this quarter are listed in the following table. Some of the samples were irradiated simultaneously. Some of the experiments are ongoing.

Principal Contact	Sample Irradiated
T. Iida (Osaka)	Fiber optic cable - Optical transmission measurements Transistor circuits - Performance during irradiation Coaxial cable - Neutron-induced voltage breakdown
M. Terasawa (Toshiba) M. Kawashima (Sumitomo) K Kadotani (Hitashi)	Insulators - Electrical properties
H. Matsui (Nagoya)	Li_2O - X-ray diffraction measurements TiC - Low temperature resistivity measurements
K. Kawamura (Tokyo)	$Pb_{80}Si_{20}$ - X-ray diffraction measurements
Y. Ogawa (Nagoya)	Al alloys - Activation analysis
R. Hartmann (Northrop)	Integrated circuits - Performance after irradiation
J. Fowler (LANL)	Macor, Sapphire - Changes in electrical/mechanical properties
D. Kaletta (Karlsruhe)	Nb,V,Ni - Microstructure and tensile strength

Principal Contact	Sample Irradiated
C. Snead (BNL)	Nb_3Sn - Critical current
G. Woolhouse (Aracor)	$Hg_{81}Cd_{19}Te$ - Activation analysis
R. Mallon (LLNL)	Oil Shale - fluidized oil shale bed transport using ^{28}Al activity
M. Summers (LLNL)	KDP crystal frequency convertor - Index of refraction
R. Borg (LLNL)	Geological samples - Xe diffusion masurements
R. Hopper (LLNL)	^{235}U and Optical Materials - Etched fission fragment tracks in optical materials for surface treatment
M. Guinan (LLNL)	Zr, Pt, Ni - Low temperature resistivity measurements

5.1 RTNS-II Status - C. M. Logan and D. W. Heikkinen

The 50-cm target seal caused no problems during this quarter. Use of the 50-cm targets increased average neutron production by ∿25%. Individual targets showed larger increases in neutron yield. As expected, target lifetime also increased with the present beam levels.

The accelerator column electron trap failed after nearly four years of usage. This necessitated its removal for repair and replacement of components. This was the major source of unscheduled outage.

A design review of the accelerator column has been essentially completed. Efforts have been made to better shield the ceramic insulator sections from uv light and soft x-rays. In addition, o-ring seals will be employed for ease of assembly.

The joint U.S.-Japan Steering Committee meeting in Tokyo on April 19-21, approved an initial list of experiments to be done at RTNS-II. With the

exception of an irradiation for M. Kiritani (Hokkaido), no attempt has been made to firmly schedule these experiments as yet.

A Rigaku x-ray diffractometer from Japan has been temporarily installed in the right target room. This was done pending completion of the modifications to the Van de Graaff room where it will be housed permanently.

6.0 Future Work

Irradiations will be continued for T. Iida (Osaka), R. Borg (LLNL), R. Mallon (LLNL), J. Fowler (LANL), D. Kaletta, G. Woolhouse (Aracor) and K. Kawamura (Tokyo) during the next quarter. An irradiation for M. Kiritani (Hoikkaido) will be completed during this quarter. Irradiations for W. Barmore (LLNL) and M. Guinan (LLNL) are tentatively scheduled.

A transmission electron microscope coming from Japan will be installed and checked out at RTNS-II during the next quarter.

6.1 Publications

"Tritium Target Performance at RTNS-II," D. W. Heikkinen and C. M. Logan to be presented at the Application of Accelerators in Research and Industry, Denton Texas, November 8-10, 1982. UCRL 87770

CHAPTER 2

DOSIMETRY AND DAMAGE PARAMETERS

DOSIMETRY RESULTS FOR THE TRIO TEST IN ORR

L. R. Greenwood (Argonne National Laboratory)

1.0 Objective

To establish the best practicable dosimetry for fission reactors and to provide dosimetry and damage analysis for ORR experiments.

2.0 Summary

Results are presented for a test of the TRIO experiment in position A2 of the Oak Ridge Research Reactor (ORR). The flux-spectrum was adjusted using 17 activation reactions and gradients were determined along and across the assembly. The calculated tritium production rate from the $^{6}Li(n,\alpha)$ reaction is in excellent agreement with measurements made at Oak Ridge National Laboratory. The status of all other dosimetry is summarized in Table I.

3.0 Program

Title: Dosimetry and Damage Analysis

Principal Investigator: L. R. Greenwood

Affiliation: Argonne National Laboratory

4.0 Relevant DAFS Program Plan Task/Subtask

Tasks II.A.1 Fission Reactor Dosimetry

TABLE I

Status of Reactor Experiments

	Facility/Experiment	Status/Comments
ORR	-MFE1	Completed 12/79
	-MFE2	Completed 06/81
	-MFE4A	Completed 12/81
	-MFE4B	Samples expected 07/82
	-MFE4C	Irradiation in Progress
	-TBC07	Completed 07/80
	-TRIO - Test	Completed 07/82
	-TRIO 2	Samples Provided 07/82
HFIR	-CTR32	Completed 04.82
	-CTR30,31, 34, 35	Irradiations in Progress
	-T1, T2, T3	Irradiations in Progress
	-RBI, RB2, RB3	Irradiations in Progress
	-CTR 39-45	Planning in Progress
Omega West	-Spectral Analysis	Completed 10/80
	-HEDL 1	Completed 05/81
EBR II	-X287	Completed 09/81
IPNS	-LASL 1 (Hurley)	Completed 06/82

5.0 Dosimetry Measurements for the ORR-TRIO tests

An irradiation test was conducted in ORR on April 26-27, 1982 for the TRIO experiment to measure and recover tritium from fusion blanket materials ($LiAlO_2$). The flux monitor wires were irradiated in position A2 for 8.93 h for a total exposure of 253.35 MWH. Eight aluminum tubes were positioned around the TRIO assembly to measure flux and spectral gradients. Seven tubes contained TI, Fe, Ni, and Co-Al gradient wires, measuring 6" in length, span ning the maximum flux position. The eighth tube measured 35" in length and contained 17 different materials including gadolinium covers and fission monitors for a spectral analysis. Gradient wires were also included to span the entire A2 assembly.

The samples were gamma counted with Ge(Li) spectrometers and the resultant saturated activities are listed in Table 11. These results were then used to adjust a calculated neutron spectrum using the STAYSL computer code. The resultant flux values are listed in Table II.

The flux spectrum is shown in Figure 1. The dotted and dashed lines represent errors for each flux group; however, the groups are highly correlated. A covariance error matrix thus must be used to calculate errors in integral quantities. Integral flux errors are typically 5-10 %, as listed in Table III.

The measured spectrum was also used to calculate the tritium production rate from the $^6Li(n,\alpha)$ reaction. The result agrees very well with measurements made at Oak Ridge National Laboratory (ORNL).[1] The measured value was then included with our activation rates to adjust the neutron flux spectrum. The measured and calculated values agree within 3.4%. The measured

values have an estimated accuracy of ± 5%. The thermal neutron flux was also found to agree quite well with self-powered neutron detector measurements at ORNL.[2]

Vertical flux gradients are shown in Figure 2. The maximum flux position was about 5" below midplane, as expected at the start of a fuel cycle. Later in the cycle the maximum will be near to the center of the TRIO experiment at about 3" below midplane.

Horizontal flux gradients can be summarized as follows:

1. The thermal flux decreases about 21% across the assembly (4.5 cm) from east to west (away from the core).
2. The thermal flux is about 23% lower inside the TRIO assembly due to absorption in a stainless steel ring (6.4 mm).
3. The fast flux decreases sharply (~60%) from northeast to southwest on a line roughly pointing towards the center of the core.
4. The thermal flux varies less than 10% inside the TRIO assembly, in the region where the tritium measurments will be conducted.

6.0 Reference

1. F. Dyer, Oak Ridge National Laboratory, private communication (1982).
2. I. T. Dudley, Oak Ridge National Laboratory, private communication (1982).

7.0 Future Work

Dosimetry capsules are now being fabricated for the TRIO-1 experiment. The status of other ongoing experiments is summarized in Table I.

TABLE II

Activation Rates for TRIO 1

ORR-A2; April 26,1982; Norm to 30 MW

Maximum Flux Height in Position 8

Reaction	$\sigma\phi$ (atom/atom-s)	Gd Cover
$^{58}Fe(n,\gamma)59Fe$	1.08×10^{-10}	
$^{59}Co(n,\gamma)60Co$	3.70×10^{-9}	
$^{176}Lu(n,\gamma)^{177m}Lu$	3.92×10^{-7}	
$^{45}Sc(n,\gamma)46sc$	2.53×10^{-10}	yes
$^{197}Au(n,\gamma)^{198}Au$	2.15×10^{-8}	yes
$^{237}N_p(n,\gamma)238N_p$	7.22×10^{-9}	yes
$^{238}U(n,\gamma)^{239}Np$	1.02×10^{-9}	yes
$^{237}Np(n,fission)$	1.17×10^{-10}	yes
$^{238}U(n,fission)$	2.26×10^{-11}	yes
$^{54}Fe(n,p)54Mn$	5.38×10^{-12}	
$^{58}Ni(n,p)58Co$	6.86×10^{-12}	
$^{46}Ti(n,p)46Sc$	7.30×10^{-13}	
$^{47}Ti(n,p)47Sc$	1.26×10^{-12}	
$^{48}Ti(n,p)48Sc$	1.99×10^{-14}	
$^{27}Al(n,\alpha)24N_a$	4.59×10^{-14}	
$^{55}Mn(n,2n)54Mn$	1.69×10^{-14}	
$^{93}Nb(n,2n)^{92m}Nb$	3.05×10^{-14}	

TABLE III

Neutron Flux Values for TRIO 1

ORR-A2; April 26,1982; Nom to 30 MW

Spectral Measurement in Position 8

Energy	Elux ($x10^{14}$ n/cm^2-s)	Uncertainty (± %)
Total	3.79	5
Thermal (<.5eV)	1.31	6
(2200 m/s)	1.16	
0.5eV-0.11MeV	1.20	9
>0.11 MeV	1.27	7
>1 MeV	0.58	6

Tritium Production Rate $^6Li(n,\alpha)T$ (30 MW):

Calculated (ANL): 9.22 x 10^{-8} $t/^6Li$-s

Measured (ORNL)[1]: 8.91 x 10^{-8} $t/^6Li$-s

Ratio (M/C) = 0.966

8.0 Publication

1. L. R. Greenwood, "A New Calculation of Thermal Neutron Damage and Helium Production in Nickel," submitted to the Journal of Nuclear Materials (1982).

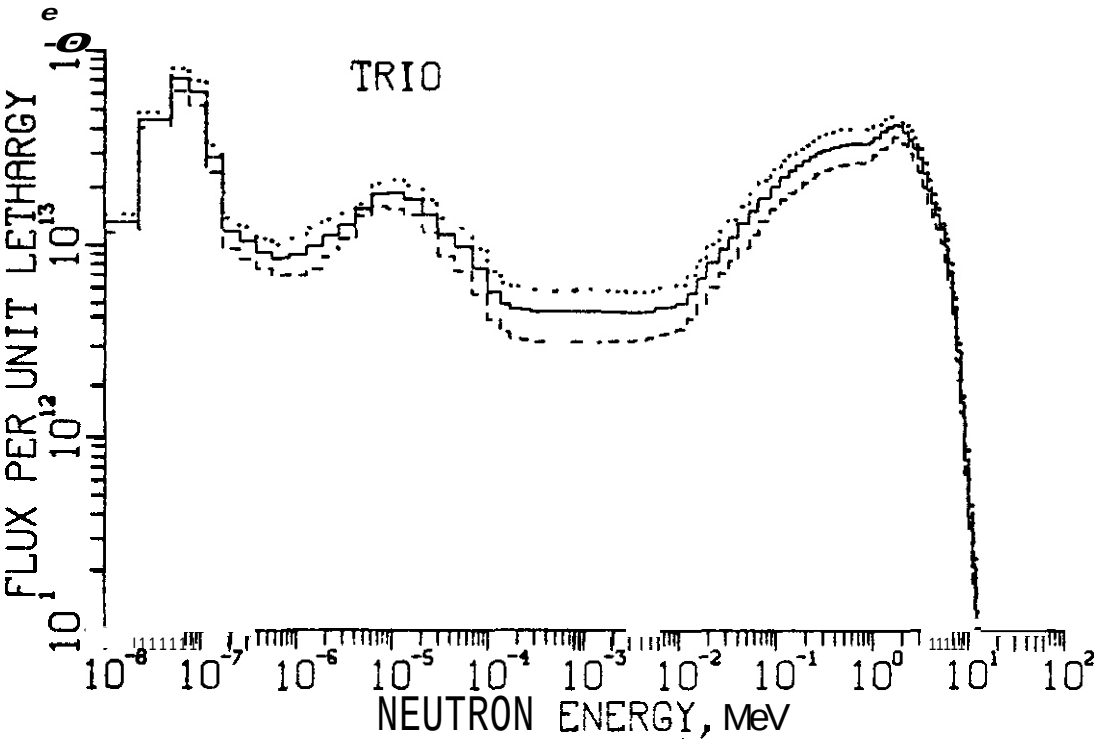

1. Flux spectrum measured for the *A2* position in ORR for the TRIO experiment. Dotted and dashed lines represent one standard deviation; however, the flux groups are highly correlated.

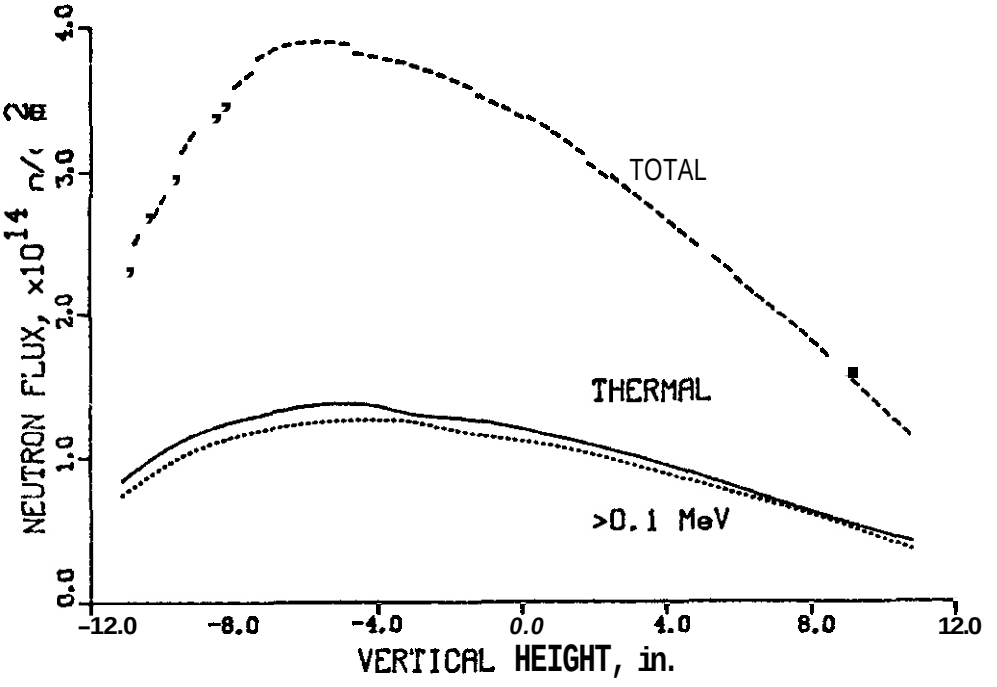

2. Vertical flux gradients measured in position *A2 of* ORR. The maximum flux is *5"* below midplane at the start of the fuel cycle, but will rise to 3" below midplane where TRIO is centered.

EXPERIMENTS AT THE IPNS SPALLATION NEUTRON SOURCE

L. R. Greenwood (Argonne National Laboratory)

1.0 Objective

To characterize the neutron flux and energy spectrum at IPNS and to provide OFE experimenters with dosimetry and damage analysis.

2.0 Summary

Dosimetry results are presented for an irradiation by G. Hurley (LANL) at IPNS (ANL) on February 22-27, 1982. The maximum neutron fluence was 1.55 x 10^{17} n/cm^2 (>0.1 MeV) and 2.23 x 10^{17} n/cm^2 (total).

3.0 Program

Title: Dosimetry and Damage Analysis

Principal Investigator: L. R. Greenwood

Affiliation: Argonne National Laboratory

4.0 Relevant DAFS Program Plan Task/Subtasks

Task II.A.2 - High-Energy Neutron Dosimetry

5.0 Accomplishments and Status

Organic insulator materials were irradiated for G. Hurley (LANL) in the Radiation Effects Facility (REF) of the Intense Pulsed Neutron Source (IPNS) located at Argonne National Laboratory. This spallation source uses a 400-MeV proton

beam with peak intensity of about 8 μA and a depleted uranium target surrounded by a lead reflector. The samples were cooled to liquid helium temperature in a vertical cryostat (VT2) adjacent to the target. The irradiation lasted for 117 hours from February 22-27, 1982. The total protons on target were 1.46 x 10^{19} with a time-averaged current of 5.56 μA.

Nickel dosimeter wires were included with the specimens. The $^{58}Ni(n,p)^{58}Co$ reaction was then used to determine the neutron exposure, relying on previous spectral measurements to characterize the facility. Five nickel wires were located around the assembly holding the specimens. The wires were gamma-counted and the results are listed in Table I.

Table I

Dosimetry Results for IPNS

$^{58}Ni(n,p)^{58}Co$ Activities are Listed

Fluence Values estimated accurate to ± 10%

Sample	Activity (+ 2%)	Neutron Fluence (x 10^{17} n/cm^2)	
	(x10^{-28} atom/atom-P)	Total	>0.1 MeV
1	6.09	2.20	1.53
2	6.09	2.20	1.53
3	6.17	2.23	1.55
4	5.94	2.15	1.49
5	5.88	2.13	1.47

The activity values show only a slight gradient values show only a slight gradient (<5%). Fluences were calculated from the $^{58}Ni(n,p)^{58}Co$ spectral-averaged

cross sections determined previusly at IPNS. The total neutron flux is 218 n/m^2-p with 151 n/m^2-p for neutrons above 0.1 MeV. The present fluences have an estimated accuracy of ± 10%. Dose and damage calulcations are now in progress.

6.0 References

1. M. A. Kirk, R. C. Birtcher, T. H. Blewitt, L. R. Greenwood, R. J. Popek, and R. R. Heinrich, "Measurements of Neutron Spectra and Fluxes at Spallation-Neutron Sources and Their Application to Radiation Effects Research," Jourl. Nucl. Mater. 96, 37 (1981).

7.0 Future Works

Work is now in progress to determine the dose delivered to the insulator materials irradiated at the IPNS and to calculate other damage parameters. More experiments are being planned at IPNS.

8.0 Publications

1. L. R. Greenwood and R. J. Popek, "Methods of Neutron and Proton Dosimetry at Spallation Sources," Proceedings of the ICANS-VI, International Collaboration on Advanced Neutron Sources, Argonne National Laboratory, June 27-July 2 (1982).

2. R. C. Birtcher, M. A. Kirk, T. H. Blewitt and L. R. Greenwood, "Measurement of Neutron Spectra and Fluxes at the IPNS Radiation Effects Facility, Proceedings of the ICANS-VI International Collaboration on Advanced Neutron Sources, Argonne National Laboratory, June 22-July 2 (1982).

HELIUM PRODUCTION CROSS SECTIONS FOR 14.8-MeV NEUTRONS

D. W. Kneff, B. M. Oliver, M. M. Nakata, and H. Farrar IV (Rockwell International, Energy Systems Group)

1.0 Objective

The objectives of this work are to measure helium generation rates of materials for Magnetic Fusion Reactor applications in the ~14.8-MeV T(d,n) neutron environment, to characterize the T(d,n) neutron field of the Rotating Target Neutron Source-I1 (RTNS-11), and to develop helium accumulation neutron dosimeters for this test environment.

2.0 Summary

The neutron fluence map for the high-flux region of the RTNS-II neutron environment has been extended over a larger volume using helium accumulation neutron dosimetry. Total helium production cross sections for ~14.8-MeV neutrons have been determined for LiF, PbF_2, F, Li, B, the separated isotopes of Li and B, and the three alloys HT9, 9Cr-1Mo, and Type 316 stainless steel. Analysis of the alloy results indicates that some of the minor alloy constituents can be significant contributors to helium production in these alloys, and thus affect their helium-related irradiation performance. The measured ^{7}Li(n,n't)α cross section is ~30% higher than a recent evaluation.

3.0 Program

Title: Helium Generation in Fusion Reactor Materials
Principal Investigators: D. W. Kneff and H. Farrar IV
Affiliation: Rockwell International, Energy Systems Group

4.0 Relevant OAFS Program Plan Task/Subtask

Subtask II.A.2.2 Flux-Spectral Definition in RTNS-II
Subtask II.A.4.2 T(d,n) Helium Gas Production Data

5.0 Accomplishments and Status

5.1 RTNS-II Neutron Fluence Mapping

The neutron fluence map generated for the high-flux irradiation volume of the joint Rockwell International-Argonne National Laboratory (ANL)-Lawrence Livermore National Laboratory (LLNL) RTNS-II experiment has been extended to a larger volume. This irradiation experiment was described in detail previously,(') and the neutron fluence map for the primary irradiation volume of the high-flux miniature sample capsule was given in the previous Damage Analysis and Fundamental Studies (DAFS) Quarterly Progress Report.[2] The present mapping effort extended the mapped region to encompass a set of aluminum dosimetry wires and platinum-encapsulated helium generation materials loaded in holes near the outside edge of the stainless steel capsule.

This map extension is based on helium accumulation neutron dosimetry provided by the aluminum wires. The wires were etched (to remove potential helium recoi1 effects), segmented, and analyzed by high-sensitivity gas mass spectrometry for generated helium. The results showed that the map for the primary capsule volume gives fluence values lower than the actual neutron fluences at large radial distances from the neutron source axis (distances beyond the specified limits of validity for that map). These results were then used to construct an empirical expression which, when multiplied by the three-dimensional fluence map for the primary irradiation volume (Ref. 2), gave a neutron fluence value at each aluminum segment location that best reproduced the Al(n,total helium) cross section. This cross section was assumed to be 144 ± 7 mb, based on two previous sets of RTNS-I experimental measurements.[3] Additional aluminum samples incorporated in the primary RTNS-II irradiation volume were also segmented and analyzed for helium. The cross section derived by combining those results (which were independent of the aluminum dosimeters) with the map for the primary irradiation volume[2] is 143 ± 10 mb. This is in excellent agreement with the RTNS-I results, providing confidence in the use of aluminum as a dosimeter for ~14.8-MeV T(d,n) neutrons.

Based on this analysis, the neutron fluence for that part of the capsule irradiation volume bounded by 8 mm $\leq$ R $\lesssim$ 10 mm is given by the following empirical expression:

$$\Phi_{R>8}(R,\Delta Z) = \Phi(R,\Delta Z)\left\{1 + (R-8)\left[0.116-0.0287(\Delta Z)+0.0019(\Delta Z)^2\right]\right\}. \quad (1)$$

Here R is the radial distance from the neutron source axis (in nun), and AZ is the axial distance from the front face of the irradiation capsule (in mm). [The axial distance from the outside face of the rotating target assembly is given by Z = AZ + 0.76 mm.] The term $\Phi(R,\Delta Z)$ is the fluence expression derived for the primary irradiation volume, as given in Ref. 2. Equation (1) was subsequently used to evaluate helium production cross sections for several platinum-encapsulated materials irradiated near the periphery of the experimental capsule.

5.2 Helium Production Cross Sections for Li, B, F, Pt, LiF, and PbF_2

Helium production cross section measurements have been completed for several additional pure elements, separated isotopes, and compounds irradiated in the -14.8-MeV T(d,n) neutron spectrum of RTNS-II. These measurements were part of a program supported by the Office of Basic Energy Sciences of the U.S. Department of Energy, to determine helium generation cross sections of a wide variety of elements and isotopes of interest to the fusion community. The helium measurements were performed using high-sensitivity gas mass spectrometry. The cross section results are presented in Table 1.

Li, ^{6}Li, ^{7}Li, and F were irradiated as the compounds LiF, ^{6}LiF, ^{7}LiF, and PbF_2, respectively. Milligram quantities of each compound were enclosed in miniature (1.3-mm diameter by 6.4-mm long) platinum capsules. Cross sections were first determined for the irradiated compounds. Those results are presented in Table 1 as cross sections per atom of material, and thus represent weighted averages of the individual constituent cross sections. The fluorine cross section was then obtained from PbF_2 by unfolding the previously measured

TABLE 1

EXPERIMENTAL HELIUM GENERATION CROSS SECTIONS FOR ~14.8-MeV NEUTRONS

Material	Cross Section (mb)	Material	Cross Section (mb)
PbF_2	334 ± 24	F	501 ± 36[a]
^{N}LiF	455 ± 33	^{N}Li	409 ± 60[b]
^{6}LiF	569 ± 41		639 ± 75[b]
^{7}LiF	441 ± 32	^{7}Li	381 ± 58[b]
^{N}B	390 ± 28		
^{10}B	691 ± 49	Al	143 ± 10[c]
^{11}B	306 ± 22	Pt	0.71 ± 0.10[d]

[a] Derived from PbF_2
[b] Derived from LiF
[c] Adopted value = 144 ± 7 mb, based on two RTNS-I irradiations
[d] Revised value, based on additional information from fluence map extension

lead cross section (0.62 mb, Ref. 2). The lithium cross sections were unfolded from the measured LiF cross sections using this fluorine result. The cross section uncertainties for lithium and its isotopes are significantly larger than for the other materials. This follows from the comparable cross section uncertainties for F and LiF, and the fact that the fluorine generates a significant fraction of the helium in LiF at 14.8 MeV. Since the quoted uncertainties include a common uncertainty for the absolute map normalization, they are partially correlated. This was taken into account in the uncertainty calculations.

Small corrections were made to the measured isotopic cross sections of both lithium and boron to account for the small impurity concentration of the other isotope of the same element. As a consistency check on the isotopic

measurements, the natural lithium and boron cross sections were also determined from the measured isotopic cross sections using weighted averages. The resultant cross sections, 400 ± 55 mb for lithium and 383 ± 24 mb for boron, are in excellent agreement with the directly measured natural lithium and boron cross sections of 409 ± 60 mb and 390 ± 28 mb, respectively.

The ^{7}Li helium production cross section for fast (up to 15 MeV) neutrons is of particular interest to fusion reactor designers, because of the contribution of the $^{7}Li(n,n't)\alpha$ reaction to tritium breeding in lithium blanket designs. Our measurement is -30% higher than a recent evaluation of this cross section at 14.8 MeV.[4] Additional samples of Li, B, and their separated isotopes have been irradiated in RTNS-I, and analysis of those materials has been initiated.

The platinum cross section listed in Table 1 is a revision of a previously reported value,[5] based on additional helium analysis results from the periphery of the irradiation capsule. This slightly revised value (decreased by 4%) was used to correct the measured helium generation in the platinum-encapsulated materials (LiF and PbF_2) for the small contribution from the capsule itself.

5.3 Helium Production Cross Sections of Candidate Fusion Reactor Alloys

Helium production cross section measurements have also been completed for the austenitic and ferritic alloy steels incorporated in the RTNS-II irradiation experiment. These materials were analyzed as part of a program supported by the U.S. Department of Energy's Office of Fusion Energy. The materials included samples of Type 316 stainless steel, HT9, and 9Cr-1Mo, provided by E. E. Bloom and M. L. Grossbeck of the Oak Ridge National Laboratory (ORNL). Also included was a Type 316 stainless steel alloy manufactured as a fuel element wire wrap for the Fast Flux Test Facility (FFTF). This material was supplied by E. P. Lippincott of the Hanford Engineering Development Laboratory (HEDL).

The alloys are listed in Table 2, and the measured cross section results are given in Column 3 of that table. The irradiated samples were etched, segmented, and analyzed by high-sensitivity gas mass spectrometry for generated helium. The cross sections were determined by combining these helium results with the neutron fluence values for the individual alloy segment locations. The fluence values were obtained from the fluence map derived for this RTNS-II irradiation.[2]

Composite cross sections for these alloys, determined from the individually measured cross sections of the alloys' constituent elements[2,3,5] using weighted averages, are also listed in Table 2. These composite cross sections are in excellent agreement with the directly measured alloy cross sections, demonstrating the self-consistency of the helium measurement technique. Note that all four materials have very similar helium production cross sections for -14.8-MeV neutrons.

TABLE 2

TOTAL HELIUM PRODUCTION CROSS SECTIONS OF CANDIDATE FUSION REACTOR ALLOYS FOR 14.8-MeV NEUTRONS

		Cross Section (mb)	
Material	Identification	Measured	Composite Result from Constituent Elements
316 Stainless Steel	Teledyne Allvac Heat 81598 (FFTF Wire Wrap)	56.5 ± 4*	55.8 ± 4
316 Stainless Steel	ORNL Heat X15893	56 ± 4	53.2 ± 4
HT9	ORNL Heat XAA3587	55 ± 4	55.4 ± 4
9Cr-1Mo	ORNL Heat XA3590	50 ± 4	51.3 ± 4

Table 3 gives the calculated percentage helium contribution of each constituent element to the helium production cross sections for the measured alloys. This table also lists the compositions of the four alloys, and the pure element cross sections used in the calculations. The alloy compositions (based on analyses supplied by ORNL and HEDL for their respective alloys) are listed here as weight percentages, although they were converted to atom percentages for the calculations. Estimated total helium production cross sections were used for those elements whose cross section measurements have not been completed. However, these elements represent only a 0.6-1.8 atom % (and ~1 mb) contribution to each alloy, and uncertainties in the estimates have little effect on the results. Helium analyses have been, or will soon be, initiated for RTNS-11-irradiated samples of N, O, S (in compound form), C (as graphite; diamonds were used in previous analyses), Mn, and W.

Examination of Table 3 shows that the minor alloy constituents carbon and silicon produce a significant percentage (up to 17%) of the helium in these alloys. In particular, the fact that the ferritic steels (HT9 and 9Cr-1Mo) have cross sections nearly equal to that of 316 stainless steel, in spite of their small nickel contents, can be attributed primarily to the helium contribution from carbon. (The large carbon cross section reflects the fact that the 3α breakup reaction predominates for 14.8-MeV neutron bombardment.) The slightly smaller helium production cross section for 9Cr-1Mo appears to be due in part to the lower carbon content of that alloy heat. The difference between the measured and calculated cross sections for ORNL-supplied 316 stainless steel (Table 2) may also be attributable to carbon; the chemical analysis for that alloy, performed by a different analytical laboratory than for the ferritics, does not list C, N, or O.

In general, it appears that some of the minor components of the alloy steels can have an important effect on the helium-related irradiation properties of these steels, and must be considered when designing fusion reactor alloys for optimum irradiation performance.

TABLE 3

CONTRIBUTIONS OF CONSTITUENT ELEMENTS TO TOTAL HELIUM PRODUCTION CROSS SECTIONS OF SELECTED ALLOYS FOR 14.8-MeV NEUTRONS

Element	Cross Section (mb)	316 SS (FFTF)		316 SS (ORNL)		1019 (ORNL)		9Cr-1Mo (ORNL)	
		Composition (wt. %)	% Helium Contribution	Composition (wt. %)	% Helium Contribution	Composition (wt. %)	% Helium Contribution	Composition (wt. %)	% Helium Contribution
B	390	0.0003	0.01	0.0002	0.01	<0.001	<0.01	<0.001	<0.01
C	900	0.0593	4.43	--	--	0.21	15.67	0.090	7.28
N	~500*	0.0059	0.21	--	--	0.020	0.71	0.050	1.93
O	~406**	0.0027	0.07	--	--	0.005	0.13	0.007	0.19
Al	144	0.01	0.05	--	--	0.053	0.28	0.017	0.10
Si	218	0.477	3.69	0.67	5.44	0.18	1.39	0.08	0.67
P	~200*	0.016	0.11	--	--	0.011	0.07	0.008	0.06
S	~200*	0.0047	0.03	0.02	0.13	0.004	0.02	0.004	0.03
Ti	37	<0.0001	<0.001	--	--	0.003	<0.01	0.002	<0.01
V	18.6	0.02	0.01	0.06	0.02	0.27	0.10	0.209	0.08
Cr	34	17.173	11.20	17.3	11.82	11.99	7.81	8.62	6.08
Mn	~40*	1.53	1.11	1.7	1.29	0.50	0.36	0.36	0.28
Fe	48	64.641	55.39	65.364	58.71	84.767	72.54	89.344	82.90
Co	40	0.033	0.02	0.23	0.16	0.017	0.01	0.013	0.01
Ni	100	13.737	23.33	12.4	22.08	0.43	0.73	0.11	0.20
Cu	51	0.013	0.01	0.01	0.01	0.05	0.04	0.03	0.03
Ga	~40*	--	--	0.002	<0.01	--	--	--	--
Ge	~40*	--	--	0.0003	<0.001	--	--	--	--
As	~40*	--	--	0.002	<0.01	<0.001	<0.001	<0.001	<0.001
Zr	10.1	--	--	0.0001	<0.001	<0.001	<0.001	<0.001	<0.001
Nb	14	<0.01	<0.01	0.03	<0.01	0.018	<0.01	0.063	0.01
Mo	14	2.277	0.33	2.1	0.32	0.93	0.14	0.98	0.15
Sn	1.5	--	--	0.01	<0.001	0.002	<0.001	0.003	<0.001
Sb	~1*	--	--	0.0005	<0.001	--	--	--	--
W	~1*	--	--	0.1	<0.001	0.54	<0.01	0.01	<0.001
Pb	0.62	--	--	0.001	<0.001	--	--	--	--

*Estimate, based on systematics of measured pure element cross sections
*Preliminary measured value

6.0 References

1. D. W. Kneff, B. M. Oliver, M. M. Nakata, and H. Farrar IV, "Characterization of the RTNS-II Neutron Field," in Damage Analysis and Fundamental Studies, Quarterly Progress Report July-September 1980, DOE/ER-0046/3, U.S. Department of Energy, 25 (1980).

2. D. W. Kneff, B. M. Oliver, M. M. Nakata, and H. Farrar IV, "RTNS-II Fluence Mapping and Helium Generation Cross Sections," in Damage Analysis and Fundamental Studies, quarterly Progress Report January-March 1982, DOE/ER-0046/9, U.S. Department of Energy (1982).

3. D. W. Kneff, B. M. Oliver, M. M. Nakata, and H. Farrar IV, "Experimental Helium Generation Cross Sections for Fast Neutrons," J. Nucl. Mater., 103 & 104, 1451 (1981).

4. P. G. Young, "Evaluation of $n+^{7}Li$ Reactions Using Variance-Covariance Techniques," Trans. Am. Nucl. Soc., 39, 272 (1981).

5. B. M. Oliver. D. W. Kneff, M. M. Nakata, and H. Farrar IV, "Helium Generation Cross Sections for 14.8-MeV Neutrons," in Damage Analysis and Fundamental Studies, Quarterly Progress Report October-December 1981, DOE/ER-0046/8, U.S. Department of Energy, 31 (1982).

7.0 Future Work

The helium analysis of RTNS-irradiated materials will continue. Primary near-term emphasis will be on the elements N, O, C, and Mn from RTNS-II, and on the B and LiF samples irradiated in RTNS-I.

8.0 Publications

None.

DAMAGE ENERGY FOR (n,γ) AND BETA-DECAY

R. K. Smither and L. R. Greenwood (Argonne National Laboratory)

1.0 Objective

To describe the production of displaced atoms in materials and environments of interest in MFR development. Specifically, to include the (n,γ) and beta-decay effects and the effect of the incident neutron energy for neutron capture events and revise all data according to ENDF/B-V.

2.0 Summary

The theory has been developed and the calculations performed to revise the damage files and calculation procedures to more accurately calculate the displacement damage resulting from the neutron capture reactions. The recoil-atom energy distributions are now computed taking into account the effects of the incident neutron energy, the gamma-.ray recoil momentum summing and y-y angular correlations of the multiple y-cascades, the lifetimes of the intermediate states, and the recoil effects resulting from subsequent β-decay when relevant. Previous calculations only considered the recoil energy associated with the prompt gamma emission following neutron capture. In some cases the incident neutron energy and/or the 8-decay related recoils will dominate the recoil energy calculations.

3.0 Program

Title: Dosimetry and Damage Analysis

Principal Investigator: L. R. Greenwood

Affiliation: Argonne National Laboratory

4.0 Relevant DAFS Program Plan Task/Subtasks

Task II.B.l Calculation of Defect Production Cross Sections

5.0 Accomplishments and Status

A. Modification of Damage and Displacement Production Cross Section Files and Calculation Procedures to Improve the Accuracy of the Neutron Capture Calculations and to Include the Effects of Subsequent 4-Decav When Appropriate

R. K. Smither and L. R. Greenwood (ANL)

Prior to the modification of the computer codes discussed below the (n,γ) reaction was included in the calculations of nuclear displacements by assuming that all neutron capture events resulted in a single average recoil energy which was added to the average displacement energy resulting from the other reactions. This average recoil energy for the (n,γ) process was calculated by assuming that all gammas emitted following neutron capture were independent events regardless of the possible effects of multiple gamma cascades with short lifetime intermediate states and γ-γ angular correlations or the effects of the incoming momentum of the incident neutron. Also, no attempt was made to include the displacement damage caused by the recoil of the beta-particle or the neutrino resulting from the beta-decay processes that often follows neutron capture. In some cases, more displacement damage results from

the E-decay processes or the recoil generated by the incoming neutron momentum than from the gamma-ray recoils.

A typical neutron capture recoil event is shown in Figure 1. The neutron capture process (n+A) is followed by the emission of two energetic gamma rays (γ_1 and γ_2) before the recoiling atom (B) slows down. This is followed by the emission of two low energy gamma-rays (γ_3 and γ_4) each of which is emitted after the atom has come to rest. The (n,γ) process is then followed by the emission of a beta-particle and a neutrino and finally by a gamma ray (γ_5). A number of secondary knockon displacements (S) are generated as the primary recoiling atom (B) slows down. The recoil energy of the displaced atom is given by equation (1) following the emission of the second energetic gamma ray where m_oc^2 = 931 MeV, the energy associated with one atomic mass unit.

$$E_{recoil}(n+\gamma+\gamma) = \frac{1}{2(A+1)}\left[\frac{E_{\gamma_1}^2}{m_oc^2} + 2E_n - 2E_n\sqrt{\frac{2E_n}{m_oc^2}}\cos\theta_1 + \frac{E_{\gamma_2}^2}{m_oc^2} - 2\left(\frac{E_{\gamma 2}^2}{m_oc^2}\right)^{1/2}\left(\frac{E_{\gamma 1}^2}{m_oc^2} + 2E_n - 2E_{\gamma 1}\sqrt{\frac{2E_n}{m_oc^2}}\cos\theta_1\right)^{1/2}\cos\theta_2\right] \quad (1)$$

The average recoil energy assuming an isotopic emission of the two gamma rays is given by equation (2).

$$\bar{E}_{recoil}(n+\gamma+\gamma) = \frac{1}{2(A+1)}\left[2E_n + \frac{E_{\gamma_1}^2}{m_oc^2} + \frac{E_{\gamma_2}^2}{m_oc^2}\right] \quad (2)$$

The average recoil energy per neutron capture for the sequence shown in Figure 1 is given in equation (3).

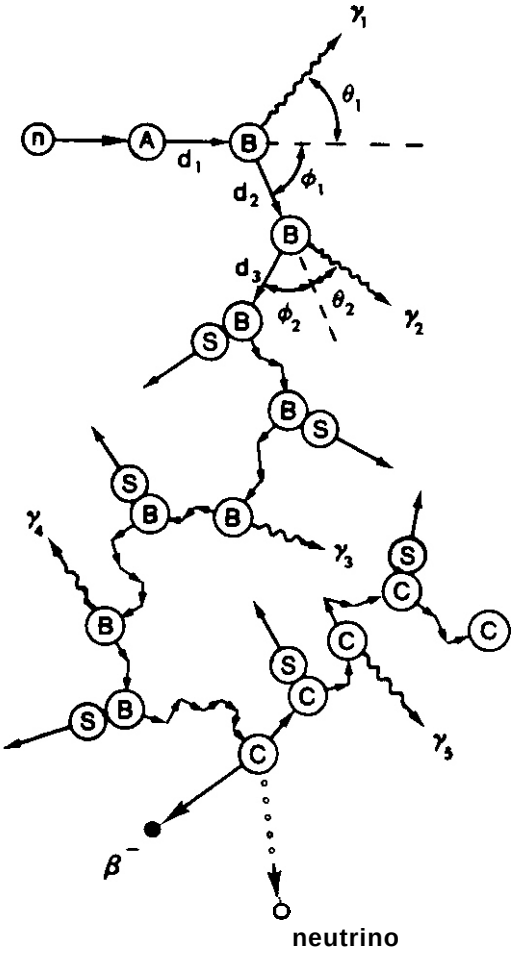

Fig. 1 Typical neutron capture recoil event. The neutron (n) strikes the target nucleus (A) and is captured, producing nucleus (B) which recoils a distance (d_1) before emitting a gamma ray (γ_1). An additional gamma ray is emmited (γ_2) after "B" recoils a distance (d_2) and a number of secondary recoil displacements (S) are produced before the nucleus (B) comes to rest. A third gamma ray (γ_3) is emitted and the recoiling atom (B) produces an additional secondary displacement before coming to rest. A fourth gamma ray is emitted and the recoiling atom (B) produces another secondary displacement (S) before coming ro rest. A β^- and a neutrino are then emitted as nucleus "B" 8-decays to form nucleus "C". The recoiling "C" produces a secondary displacement before coming to rest. A gamma ray (γ_5) is then emitted and the recoiling atom (C) produces a secondary displacement before coming to rest.

$$E_{recoil}(n+4\gamma+\gamma+\beta) = \frac{1}{2(A+1)}\left[2E_n + \frac{E_{\gamma_1}^2}{m_oc^2} + \frac{E_{\gamma_2}^2}{m_oc^2} + \frac{E_{\gamma_3}^2}{m_oc^2} + \frac{E_{\gamma_4}^2}{m_oc^2} + \frac{E_{\gamma_5}^2}{m_oc^2} + \bar{E}_r(\beta)\right] \quad (3)$$

where $\bar{E}_r(\beta)$ is the average recoil energy following β-decay. Because of the angular correlation between the E-particle and the neutrino this value must be calculated separately for each case. A typical value for $\overline{E_r(\beta)}$ is about 60% to 80%of the maximum recoil energy, $E_{recoil}(\beta$ max.), which is given by equation (4),

$$E_{recoil}(\beta\ max) = \frac{E_\beta^2(max)}{2(A+1)m_oc^2} \cdot \left[1 + \frac{2m_ec^2}{E_\beta(max)}\right] \quad (4)$$

where m_ec^2 is the energy associated with the rest mass of an electron. Details of these calculations and the calculation of some PKA spectra are given in the previous DAFS Report No. DOE/ER-0046/9.

For pure thermal neutron capture the incident neutron energy E_n can be neglected, leaving only the gamma and β-decay contribution in equation (3). If the (n,γ) event produces a stable nucleus there will *not* be *any* contribution from the β-decay terms and equation (3) becomes equation (5).

$$\bar{E}_{recoil}(\gamma+\gamma+\gamma+\gamma) = \frac{1}{2(A+1)m_oc^2}\left[E_{\gamma_1}^2 + E_{\gamma_2}^2 + E_{\gamma_3}^2 + E_{\gamma_4}^2\right] \quad (5)$$

which identical to the result if one considers each gamma ray as a separate recoil event and sums the recoil energies. Prior to the modification discussed here the average recoil energy for the (n,γ) process that was added to the recoil damage energy generated by the other neutron reactions was just

equation (5) averaged over all the gamma cascades. This averaged sum simplifies to give equation (6).

$$\bar{E}_{recoil}(n,\gamma) = \frac{1}{2(A+1)m_o c^2} \sum_i a_i E_{\gamma i}^2 \qquad (6)$$

where "ai" is the fractional intensity, gammas per neutron capture, for the i th gamma ray in the (n,γ) spectrum.

The computer program was modified to include the additional recoil energy produced by the β-decay process and by the incident neutron energy. This was done in three steps. First the average recoil energy generated by the 8-decay process was calculated as a function of element and isotope for the fusion related materials. Before this value was added to the (n,γ) related recoil energy both the (n,γ) and the β-decay recoil energies were multiplied by the appropriate Lindhard factor to remove the fraction of the recoil energy that goes into electronic damage. The two displacement related energies were then added together and tabulated by element and/or isotope. This combined displacement energy is then added to the incident neutron energy (calculation is done in 100 energy subgroups) to obtain the appropriate displacement energy for the neutron capture reaction for the neutron energy subgroup being calculated. This displacement energy is then multiplied by the appropriate cross section and flux for the incident energy subgroup and summed over subgroups to obtain the total contribution to the displacement damage from the neutron capture reaction.

These calculations are summarized in Table I. Column 1 gives the element or isotope, columns 2, 3, and 4 give the maximum recoil energy, the average recoil energy per neutron capture and the part of the average recoil energy associated with displacement damage (average times Lindhard factor), respectively, for the gamma rays emitted following neutron capture. Columns 5, 6, and 7 give the maximum recoil energy, average recoil energy per neutron capture and the fraction associated with displacement damage (average times Lindhard factor), respectively for the 0-decay process and any gamma rays emitted following the β-decay, when appropriate. Column 8 is the sum of columns 4 and 7 and is the new value that is used in the calculation of displacement damage. Column 9 is the ratio of the new displacement damage energy, column 8, to the old value, column 3. It should be remembered that column 8 is added to the recoil energy of the incident neutron (also corrected for the Lindhard factor) to obtain the total displacement damage energy. For the neutron capture reaction, the ratio in column 9 is essentially the comparison of the new displacement energy with the old displacement energy for a pure thermal source.

Table II lists the new values for neutron capture displacement damage cross sections with the Lindhard correction for a position in the core of the HFIR reactor at ORNL. The total displacement damage cross sections for the different materials are also given for comparison. In most cases the neutron capture reaction contributes only a few percent or less of the total displacement damage cross section but in a few cases like Cl, Co, Ag, and Au, the contribution is the order of 10%-40%. Of course, caution must be used in these cases to properly account for neutron self-shielding and burnup.

TABLE I

PRIMARY DISPLACEMENT ENERGY CROSS SECTIONS

Element or Isotope	(n,γ) MAX (eV)	(n,γ) AVE (eV)	(n,γ) AVE x L.F. (eV)	β-Decay MAX (eV)	β-Decay AVE (eV)	β-Decay AVE x L.F (eV)	Sum (n,γ)+ β-decay (eV)	Ratio New/old
^{1}H	1329	1329	528	--	--	--	528	.397
^{2}H	7013	7013	1035	3.5[a]	2.5[a]	2.2[a]	1035[a]	.147
^{3}He	56849	56849	3988	--	--	--	3988	.070
^{4}He	--	--	--	--	--	--	--	
^{6}Li	4043	3200	1824	--	--	--	1824	.57
7Li	277	250	195	3.0 x 10^{6}[b]	3.0 x 10^{6}[b]	7360[b]	7555[b]	30.2
^{9}Be	2494	1912	1M7	47c	42C	35[c]	1307[c]	.684
^{10}B	6408	933	711	--	--	--	711	.762
^{11}B	544	472	367	8611	5955	3646	4013	8.50
^{12}C	939	891	671	--	--	--	671	.753
N	3945	2309	1657	4011	2	2	1659	.718
O	546	365	291	742	1	1	292	.800
19P	1148	822	642	1517	722	565	1207	1.468
^{23}Na	1086	566	453	795	200	165	618	1.092
Mg	2544	745	570	186	5	4	574	.770
^{27}Al	1148	640	514	499	190	158	674	1.053
si	1950	730	564	65	1	1	565	.774
P	1057	550	446	78	63	54	500	.909
Cl	1098	639	518	413	16	14	532	.833
K	1335	413	341	205	9	8	349	.845
Ca	1514	468	385	412	4	3	388	.829
Ti	1508	481	400	72	.1	.1	400	.832
V	1259	426	356	203	105	91	447	1.049

TABLE I (Cont'd)

Element or Isotope	(n,γ) MAX (eV)	(n,γ) AVE (eV)	(n,γ) AVE x L.F. (eV)	β-Decay MAX (eV)	β-Decay AVE (eV)	β-Decay AVE x L.F (eV)	Sum (n,γ)+ β-decay (eV)	Ratio New/old
Cr	906	670	553	92	1	1	554	.827
Mn	507	385	324	167	82	71	395	1.026
Pe	917	473	395	42	.2	.2	395	.835
Co	264	362	305	89[d]	63[d]1	55[d]	360[d]	.994
Ni	973	592	491	56		.1	491	.829
cu	526	413	348	79	20	18	366	896
Zr	436	162	141	36	.5	.5	142	.877
Nb	297	126	111	36	.1	.1	111	.881
Mo	469	119	105	76	.2	.2	205	.882
^{107}Ag	262	146	129	22	15	14	143	.985
^{109}Ag	226	126	111	55	38	36	166	1.132
Ta	108	16	14	14	5	5.	19	1.188
^{180}W	136	18	17	1	1	1	18	1.0
^{182}W	112	15	14	--	--	--	14	.933
^{183}W	160	21	20	--	--	--	20	.952
^{184}W	97	13	12	2	1	1	13	1.0
^{186}W	86	12	11	9	4	4	15	1.250
^{197}Au	114	68	62	6	4	4	66	.971
Pb	140	140	126	3	--	--	126	.900

[a] 12 yr half-life so the β-decay component is not in the sum.

[b] ^{8}Be breaks up into 2 α's so the value is for the 2 α's, and is included in the sum.

[c] 1.6 x 10^{6} yr half-life so the β-decay component is not in the sum.

[d] 5.5 yr half-life so the β-decay component is not in sum.

TABLE II

NEUTRON CAPTURE DAMAGE FOR HFIR

Element or Isotope	(n,γ) (keV-b)	Total (keV-b)	Fraction (%)
^{1}H	.066	1.69	3.9
^{3}He	.027	5553	--
^{4}He	--	3.06	--
^{6}Li	(.024)	2905	--
^{7}Li	(.093)	4.00	0.2
^{9}Be	.0075	10.91	0.01
^{10}B	.121	3.26×10^{6}	--
^{11}B	.0069	12.07	0.01
C	.0012	14.43	--
N	.043	14.36	0.3
^{16}O	1.8×10^{-5}	20.46	--
^{23}Na	.115	23.73	0.5
Mg	.019	23.96	0.1
^{27}Al	.056	22.84	0.3
Si	.041	22.31	.02
Cl	5.95	23.54	25.4
K	.256	18.84	1.4
Ca	.060	19.83	0.3
Ti	.839	21.51	3.9
V	.781	24.08	3.2
Cr	.621	21.21	2.9
Mn	1.882	23.44	8.0

Table II cont.

Element Isotope	(n,γ) (keV-b)	Total (keV-b)	Fraction (%)
Fe	.358	18.76	1.9
Co	5.151	23.83	21.6
Ni	.781	20.20	3.9
cu	.532	18.30	2.9
Zr	.038	19.70	0.2
Nb	.126	18.13	0.7
Mo	.304	20.24	1.5
^{107}Ag	2.36	18.28	13.0
^{108}Ag	11.30	27.77	42.2
Ta	.591	12.ll	4.9
^{182}W	.386	11.55	3.3
^{183}W	.296	11.11	2.9
^{184}W	.065	11.24	0.6
^{186}W	.452	11.45	3.9
^{197}Ai	4.70	15.57	30.1
Pb	.010	12.74	0.1

NUCLEAR DATA APPLICATIONS IN RADIATION DAMAGE STUDIES

F. M. Mann (Hanford Engineering Development Laboratory)

1.0 Objective

The objective of this work is to develop and maintain a computer code system to calculate the amounts of solid and gas transmutants at various facilities used by OFE experimentalists and to supply processed nuclear data.

2.0 Summary

The transmutation of V-15%Cr-5%Ti in various MFE facilities has been calculated. Except for HFIR, where large compositional changes occur, little transmutation is evident in this material.

The first module of the NJOY code has been successfully modified to handle data in the >20-MeV ENDF/B formats.

3.0 Program

Title: Irradiation Effects Analysis (AKJ)
Principal Investigator: D. G. Doran
Affiliation: Hanford Engineering Development Laboratory

4.0 Relevant DAFS Program Plan Task/Subtask

II.A.4.5 Gas Generation Rates
II.B.1 Calculation of Defect Production Cross Sections
II.C.4.1 Effects of Solid Transmutation Products on Microstructure

5.0 Accomplishments and Status

5.1 Solid and Gas Transmutation Product Calculation

The REAC code system was used to calculate the transmutation of V-15%Cr-5%Ti as a function of dpa in various MFE irradiation facilities. The results for 50 dpa are displayed in Table 1, with Figures 1 and 2 showing the fraction of V and Cr present in the alloy as a function of time.

The nonthermal facilities show relatively little change in composition. Hydrogen production is about a factor of 10 lower than in steels,[**]) and helium production is about a factor of 5 lower.

HFIR shows significant compositional changes, however. At 60 dpa there are about equal amounts of V and Cr. The C concentration also increases appreciably. Although hydrogen production (due to nitrogen) is only slightly lower than found for fusion first wall positions, HFIR produces over an order of magnitude less helium.

A HEDL-TME, "Transmutation of Alloys in MFE Facilities as Calculated by REAC," is being prepared. This report will document transmutations in PCA, HT-9 and V-15%Cr-5%Ti in various facilities.

5.2 Calculation of Damage Parameters

The first module of the NJOY nuclear data processing code [2] was modified to handle the ENDF/B formats for neutron data with energies greater than 20 MeV and for charged particle data. The modification of succeeding modules will continue.

TABLE 1

TRANSMUTATIONS OF V-15%Cr-5%Ti AT 50 dpa

Element*	Original Number Density (%)	Relative Change of Original Elements (%)						
		HFIR	FFTF	INTOR	STARFIRE	UWMAK-1	TASKA	FMIT
V	80.0	-32.0	-0.2	-0.8	-0.67	-0.2	-0.15	-0.2
Cr	14.6	175.0	0.9	2.8	2.45	-0.2	-0.18	-0.5
Ti	5.3	-0.1	0.0	3.5	3.2	3.9	2.8	4.6
N	0.19	-13.0	-0.3	-0.[illegible]	-0.75	-0.6	-0.51	-0.7
O	0.073	cross sections not in library						
C	0.072	34.0	0.4	[illegible].0	0.91	0.5	0.53	0.3
Fe	0.050	4.9	0.0	-0.6	-0.33	-0.5	-0.32	-0.4
Mo	0.030	-1.5	-0.5	-0.7	-0.66	-0.5	-0.35	-0.3
Cu	0.005	cross sections not in library						

*Listed in order of original abundance.

Element*	Original Number Density (%)	New Elements (ppm) [≥10 ppm in at least 1 facility]						
		HFIR	FFTF	INTOR	STARFIRE	UWMAK-1	TASKA	FMIT
H		286.0	[illegible]	416.0	3[illegible]7.0	466.0	[illegible]20.0	547.0
He		7.8	3.[illegible]	152.0	1[illegible]9.0	166.0	16.0	182.0
B		6.0	3.[illegible]	4.2	4.5	4.8	3.3	6.[illegible]
Ca		+	+	7.7	9.8	9.6	7.1	19.0
Sc		+	+	16.0	18.0	17.0	13.0	42.0
Mn		71.0	+	4.0	2.7	2.4	1.6	1.[illegible]
Tc		3.[illegible]	1.0	1.4	1.2	+	0.6	+
Ru		1.[illegible]	+	+	0.3	+	0.1	+

*Listed in order of mass

+<10 ppm

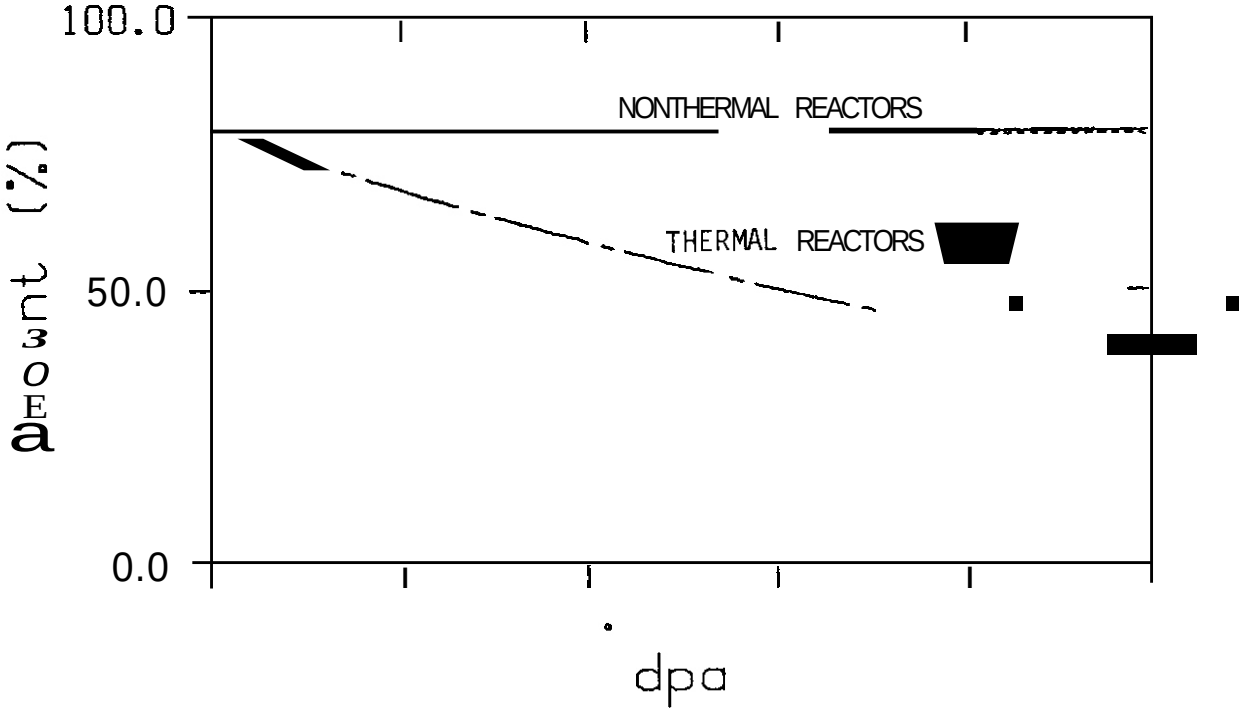

FIGURE 1. Transmutation of V-15%Cr-5%Ti in MFE Facilities: Vanadium Concentration.

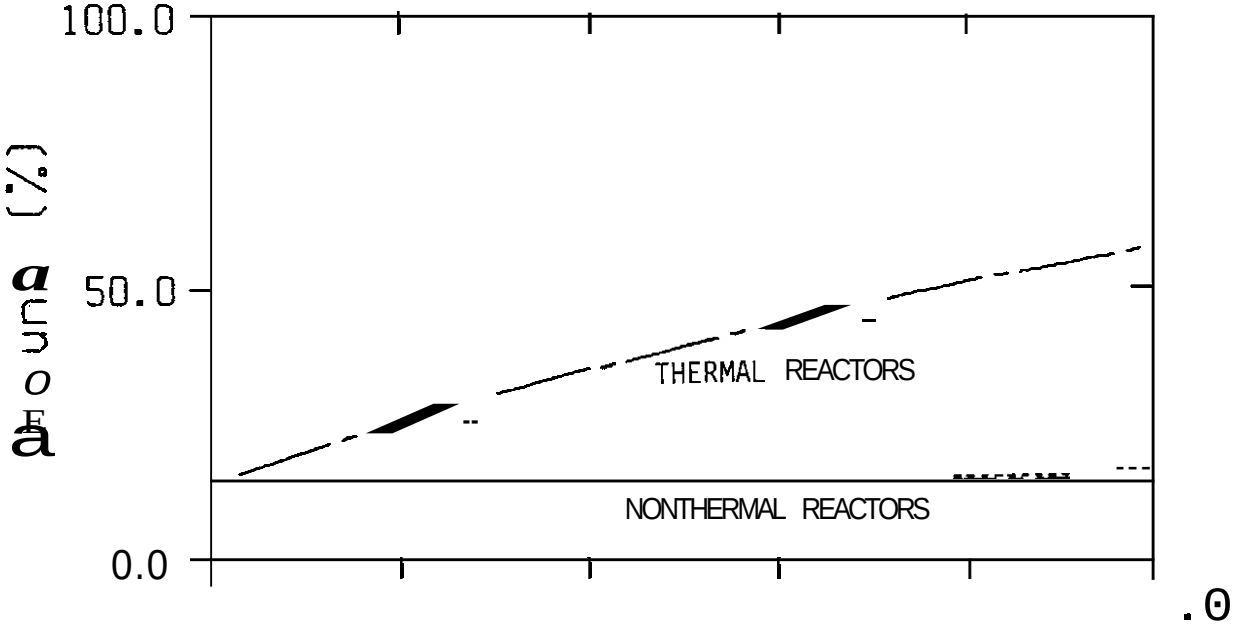

6.0 References

1. J. F. Bates, F. A. Garner and F. M. Mann, "The Effect of Solid Transmutation Products on Swelling in 316 Stainless Steel," Damage Analysis and Fundamental Studies Quarterly Progress Report, DOE/ER-0046/6, April-June 1981, p. 190.

2. R. E. MacFarlane, R. J. Barrett, D. W. Muir and R. M. Barcourt, "The NJOY Nuclear Data Processing System: User's Manual," LA-7584-M (ENDF-272), Los Alamos National Laboratory, Los Alamos, NM, 1978.

A SEMI-EMPIRICAL KINETIC MODEL FOR QUENCHING OF HIGH ENERGY DISPLACEMENT CASCADES

H. L. Heinisch (Hanford Engineering Development Laboratory)

1.0 Objective

The objective of this work is to develop computer models for the simulation of high energy cascades which will be used to generate defect production functions for correlation analysis of radiation effects.

2.0 Summary

Defect production in high energy displacement cascades has been modeled using the computer code MARLOWE to generate the cascades and the stochastic computer code ALSOME to simulate the cascade quenching and short-term annealing of isolated cascades. The quenching is accomplished by using ALSOME with exaggerated values for defect mobilities and critical reaction distances for recombination and clustering only during the quenching stage. Then normal mobilities and reaction distances are used during short-term annealing. The quenching parameter values were chosen such that the best fit to experimental defect yields was obtained. The number of defect pairs after quenching and after annealing, and the number of freely migrating defects, vary linearly with the cascade damage energy from 10 to 100 keV. Cascades generated in a crystal having thermal displacements were found to be in better agreement with experiments after quenching and annealing than cascades generated in a non-thermal crystal.

3.0 Program

Title: Irradiation Effects Analysis (AKJ)
Principal Investigator: D. G. Doran
Affiliation: Hanford Engineering Development Laboratory

4.0 Relevant DAFS Program Plan Task/Subtask

Subtask II.B.2.3 Cascade Production Methodology

5.0 Accomplishments and Status

5.1 Introduction

In a previous DAFS Quarterly Progress Report [1] a scheme was introduced for modeling the quenching stage of high energy displacement cascades. This quenching model has now been applied to cascades generated by the MARLOWE computer code for copper having thermal displacements representative of a temperature of 300K. The quenching parameters were adjusted so as to provide the best agreement with information extracted from experiments. The energy dependence of the numbers of defects remaining after quenching and subsequent short-term annealing was investigated for isolated cascades from primary knock-on atoms (PKAs) of 10 to 100 keV.

5.2 The Quenching Model

MARLOWE models only the collisional phase of cascade development, which occurs in about 10^{-13} sec, so it does not deal with the recombination and clustering which occurs as the energetic cascade region quickly comes *to* thermal equilibrium with the remainder of the crystal (cascade quenching). Cascade quenching can only be properly simulated by fully dynamical cascade models. However, for cascade energies high enough to be of interest, such an approach may not presently be computationally feasible. And, even if feasible, the dynamical simulations are not practical for generating statistically significant numbers of high energy cascades. Therefore, some simplified parametric model of cascade quenching must be developed to bridge the gap in a physically reasonable way between MARLOWE and short-term annealing that occurs through normal, thermally activated diffusion.

So far, this parametric model has consisted of the simple recombination of pairs in a static, MARLOWE-generated cascade.[2] As a first step toward a more realistic quench model, a kinetic recombination model using the short-term annealing code ALSOME has been devised. The annealing code has been modified to pre-process the cascades with quenching values for the parameters, and then to anneal them with normal parameter values.

There are essentially four adjustable parameters in this quenching scheme: the critical reaction distances for recombination, interstitial clustering, vacancy clustering, and the time duration of the quench. The quench time was fixed at 100 interstitial jumps. The other parameter values were chosen so the results produced the best match to available experimental data.[3-5] More details about ALSOME and the quenching model are in the earlier report.[1]

The fact that thermal displacements are included in the model is much more significant than the value of the temperature chosen for the cascade simulations. Cascades generated at a temperature of only a few degrees are more similar to those generated at 300K than to non-thermal cascades. The value of the "temperature" at which the cascade is generated also has little meaning in the context of the short-term annealing model. The short-term annealing of an isolated cascade is modeled as a sequence of events within the cascade region which depends on the relative mobilities of the defects. It is roughly characterized as the motion of the interstitials followed by the motion of the vacancies. This is especially true for low temperatures, where the interstitials are orders of magnitude more mobile than the vacancies. In fact, the simulation results are not very sensitive to the relative mobilities, depending much more on the positions of the defects. Thus, throughout the short-term annealing simulations relative mobilities representative of low temperatures are used. The concept of temperature enters into short-term annealing, therefore, when the sequence of events is interrupted. For example, if the simulation is terminated when few mobile interstitials remain, but before vacancies have started moving, the result represents the short-term annealing at a lattice temperature such that interstitials are relatively mobile and vacancies are relatively immobile.

The earlier quenching study was done for 30 keV cascades generated in a non-thermal lattice. The quenching parameters were re-evaluated for the present cascades, which were generated at 300K for energies from 10 to 100 keV. Quenching parameter values were chosen so as to give the best fit to defect yields extracted from resistivity data on low temperature irradiated Cu. The recombination occurring during the quenching phase should be only slightly affected by the lattice temperature, hence the resistivity measurements for cascades produced at low temperatures where defects (at equilibrium) are immobile should give a reasonable value for the number of pairs remaining after the quench.

The cascades are treated as isolated cascades, and a volume is prescribed about each cascade such that once a defect exits this volume it does not return. Short-term annealing simulations terminate when no mobile defects remain within this volume. The annealing occurs in two distinct phases: first the migration of interstitial defects which are orders of magnitude more mobile than vacancies, then the migration of the mobile vacancy defects which remain. Throughout the annealing, ALSOME reports on the total number of Frenkel pairs and the numbers and types of mobile and stationary defect clusters. In particular, the state of the system is noted at the end of the quench, after interstitial migration, and at the termination of short-term annealing.

The numbers of freely migrating interstitial and vacancy defects, i.e., those not clustering or recombining within their own cascade, have been inferred from experiments.[3-5] In the simulation these are the defects which escape the cascade region during short-term annealing.

Cascades at 30 keV were used to screen the quenching parameter values. Several sets of parameters were found which could produce the correct defect yields after quenching, as well as resulting in appropriate numbers of free defects after short-term annealing of the quenched cascades. The final parameter values were chosen by selecting the set which gave the best fit to post-quenching defect yields throughout the energy range.

5.3 Results

Sets of ten cascades were used at each energy. With respect to this relatively small sample size, the results are fairly sensitive to the value of the recombination distance, but relatively insensitive to the critical reaction distances for clustering. Variations of half a lattice parameter in one of the clustering distances make little difference in the defect yields. Since the vacancy and interstitial populations are interdependent, the numbers of free defects are more sensitive to the relative values of recombination and clustering distances than to their magnitudes. For example, changing the interstitial clustering affects the number of free vacancies. The number of free vacancies after short-term annealing is strongly affected by how many small, but immobile, vacancy clusters are reduced to mobile size by recombinations during annealing.

The quenching parameter values which are deemed best at present have single point defect critical reaction distances for recombination of 2.8 a (lattice parameters), for interstitial clustering of 2.3 a, and for vacancy clustering of 2.3 a. In addition, in the process of determining critical reaction distances, vacancy clusters are given radii representative of loops rather than spherical clusters, making large clusters more effective.

The results of quenching with this model and the subsequent short-term annealing are presented in Figure 1. The average values for ten cascades at each energy are plotted, including error bars indicating plus or minus one standard deviation. The line drawn through the "quenched" points has been extracted from resistivity measurements on low-temperature-irradiated copper. Lines through the "annealed," "free interstitial," and "free vacancy" points are 0.78, 0.15 and 0.04 times the "quenched" line respectively.

Interpretation of experiments by Theis and Wollenberger [3] indicates that for fission neutron irradiated copper about 15% of the initial interstitials (i.e., after quenching) escape the cascade at ~170K. Experiments by Blewitt, et al.[4] in Cu_3Au indicate that about 4% of vacancies remain mobile at ~470K. These

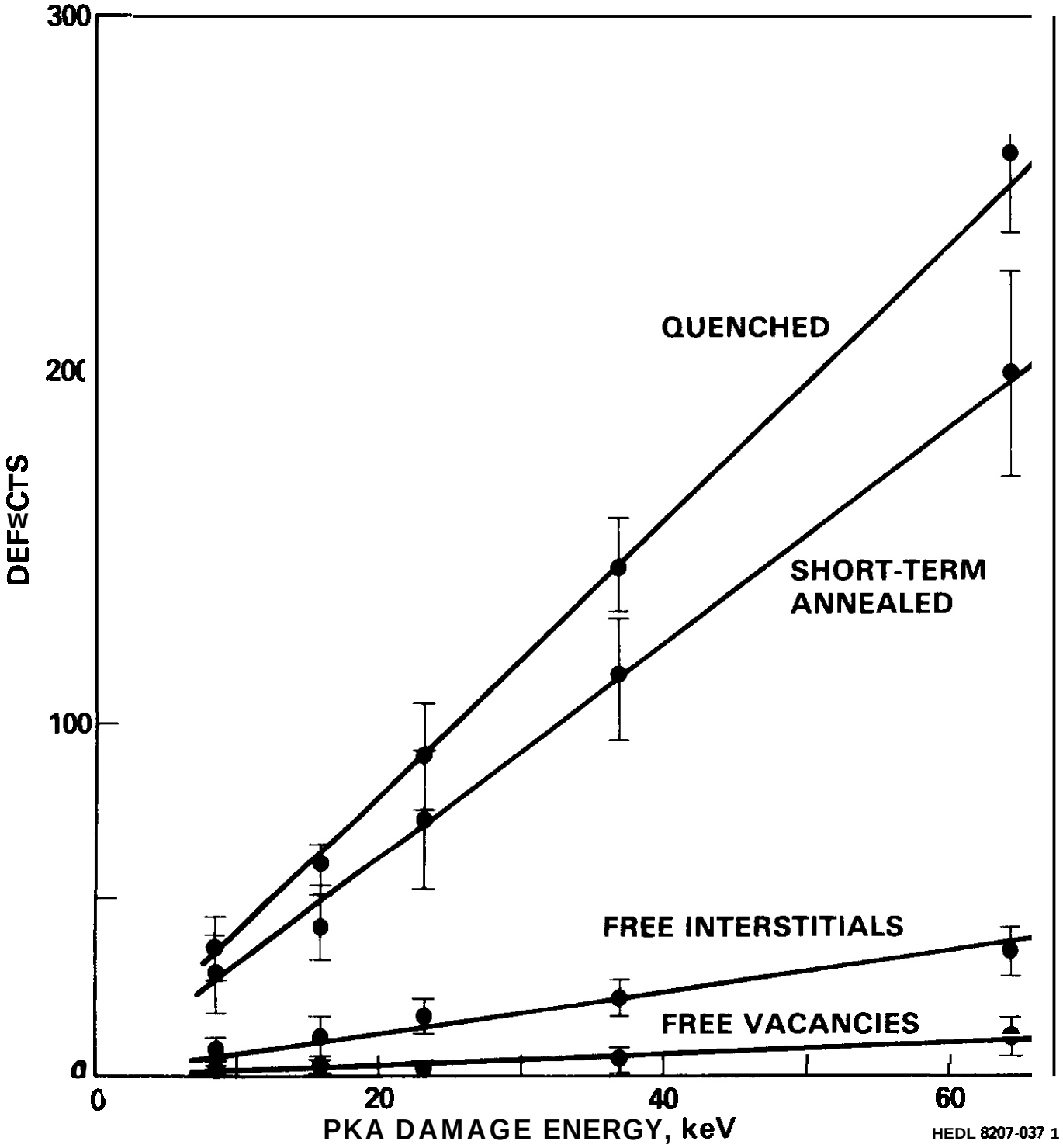

FIGURE 1. The Number of Defect Pairs Remaining After Quenching and Short-Term Annealing of Isolated Cascades in Copper as a Function of PKA Damage Energy. Free vacancies and interstitials are the defects which do not recombine or cluster within the cascade during annealing.

results, which are also consistent with experiments by Goldstone, et al.,[5] were used as a guideline for the optimization of the quenching parameters at 30 keV. The fractions of free defects in the simulations appear to be independent of damage energy, although this was not used as a criterion for the selection of quenching parameter values. This is not an unexpected result, however, given the nature of cascade configurations as a function of energy.[6]

In the earlier study, done on non-thermal cascades, a lower limit for the fraction of free interstitials of about 20% was found, even at extreme values of the quenching parameters. In the present study on cascades at 300K the "experimental" value of the fraction of free interstitials of ∿15% is easily achieved. At the periphery of the cascade some fraction of the interstitials is almost certain to escape the cascade region regardless of what happens within the rest of the cascade. The 300K cascades exhibit a smaller average pair separation than the non-thermal cascades.[7] Hence, a smaller fraction of the interstitials in the 300K cascades are independent of the action within the central part of the cascade. This result may be interpreted as a further illustration of the necessity to include thermal displacements in cascade simulations.

There are no direct experimental values for the number of defect pairs remaining after short-term annealing of isolated cascades. However, annealing experiments on low fluence, low temperature irradiated copper, with primarily cascade-producing irradiation such as ions or high energy neutrons should provide this information for interacting cascades. After Stage I recovery, there should be few mobile interstitials. Those which have escaped their own cascade will have interacted with another, assuming the density of intrinsic sinks is low. The total number of pairs remaining when mobile interstitials are no longer in the cascade volume (approximately Stage I) is about 82% of that after quenching, independent of the cascade energy. If one assumes that the interstitials which escape a cascade recombine in equal portions with vacancy and interstitial clusters of other cascades, then the simulation predicts a Stage I recovery of about 26%. Recovery measurements[8] for Cu irradiated with 400-keV Ar ions and d-Be neutrons at 6K

indicate a Stage I recovery of 32-36%. Better agreement with experiment is obtained if one assumes all the free interstitials eventually result in recombinations. The disposition of the free defects, within this model, will be established when ALSOME is used to simulate interacting cascades.

The simple model employed here for quenching and annealing is incapable of simulating realistic clustering or loop formation (indeed, not even the most sophisticated models can do this), nevertheless, it is interesting to discuss the cluster size distributions produced in these simulations. In particular, the cluster size distributions reveal something about the nature of the distribution of defects in a cascade as a function of energy. The distribution of vacancy cluster sizes, after annealing, for 30-and 100-keV cascades are quite similar, and they have the same average cluster size. Cascades at these two energies also have the same number of clusters per unit damage energy. This implies that, even after quenching and short-term annealing (at least with respect to the model used here), a high energy cascade can be considered as a collection of closely-spaced, lower energy subcascades or lobes.

5.4 Conclusions

When only static recombination was used to simulate cascade quenching,[2] far too many freely migrating defects remained after short-term annealing. The kinetic quenching model, which is a very-short-term exaggerated version of short-term annealing, is capable of producing results for both total defect yields and free defects which agree with experiments. The linear dependence of defect yields on damage energy and the independence of relative cluster size distributions from damage energy indicate that, even after quenching and annealing, the high energy cascades behave as a collection of lower energy subcascades and lobes. The cascades generated in a crystal having thermal displacements were found to be in better agreement with experiments after quenching and annealing than cascades generated in a non-thermal crystal.

6.0 References

1. H. L. Heinisch, DAFS Quarterly Progress Report, January- March 1982, DOE/ER-0046/9 (1982) 86.

2. H. L. Heinisch, D. G. Doran and D. M. Schwartz, Effects of Radiation on Materials, ASTM Special Technical Publication 725 (1981) 191.

3. U. Theis and H. Wollenberger, J. Nucl. Mater., 88 (1980) 121.

4. T. H. Blewitt, A. C. Klank, T. Scott and W. Weber, Proceedings of International Conference on Radiation-Induced Voids in Metals, Albany, NY, 1971, J. W. Corbett, L. C. Ianniello, Eds., NTIS, CONF-710601 (1972) 757.

5. J. A. Goldstone, D. M. Parkin and H. M. Simpson, J. Appl. Phys., 51 (1980) 3690.

6. H. L. Heinisch, J. Nucl. Mater., 103 (1981) 1325.

7. H. L. Heinisch, Proceedings of International Conference on Neutron Irradiation Effects, Argonne National Laboratory (1981), in press.

8. R. S. Averback, R. Benedek and K. L. Merkle, J. Nucl. Mater., 75 (1978) 162.

7.0 Future Work

Quenching and short-term annealing of interacting cascades will be modeled.

COMPARISON OF NEUTRON AND GAMMA IRRADIATION DAMAGE IN ORGANIC INSULATORS

G. F. Hurley, J. D. Fowler, Jr., R. Liepins, B. Jorgensen, and J. Hamond
(Los Alamos National Laboratory)

1.0 Objective

This study is being carried out to determine the effects of neutron irradiation at 4.2 K on epoxy and polyimide insulators, and to compare these effects with those from gamma irradiations at the same temperature, and in the same materials.

2.0 Sumnary

Three epoxy- and three polyimide-based materials have been neutron-irradiated in IPNS-I to a dose of 1.51 x 10^{21} n/m^2, E_n>0.1 MeV at 4.2 K. The environmental and thermal conditions during and after irradiation were similar to those employed in a previous study of gama-irradiation effects at ORNL, to facilitate comparison of the irradiation effects. In the present study, we have determined the flexural and compressive mechanical properties parallel to the fabric warp direction, at 75 K. DC and AC conductivities and loss tangent have been measured for one of the materials. Infrared spectra and differential scanning calorimetry (DSC) have been recorded for several of the materials. These studies, which are not yet complete, have disclosed selected differences when compared to results for gamma-irradiations.

3.0 Program

Title: Radiation Damage Analysis and Computer Simulation (Radiation Effects in Organic Insulators)

Principal Investigator: G. F. Hurley

Affiliation: Los Alamos National Laboratory

4.0 Relevant DAFS Program Plan Task/Subtask

Task II.B.4: Damage Production in Insulators
Subtask II.B.4.3: Experimental Validation/Calibration of Theory

5.0 Accomplistunents and Status

5.1 Introduction

In a previous report on this study, [1] we presented the requirements for organic insulation in magnetic confinement fusion reactors, and showed that neutron radiation damage studies are needed to evaluate materials to meet these requirements. Since information on behavior of several candidate materials after gamma-irradiation is already available, our initial approach is to compare changes after neutron and after gama irradiation in these materials. This will permit determination of the validity of the gamma damage effects studies relative to the end application, and will also permit assessment of the behavior in the different radiation environments of various future reactors.

This report presents the initial results of mechanical and electrical tests on a series of materials irradiated in the IPNS-I. In addition, we have examined the IR spectra and carried out differential scanning calorimetry for several of the materials. All of these evaluations are continuing.

5.2 Irradiation Experiment in IPNS-I

Samples for irradiation were G-10 CR, G-11 CR, Norplex NP-530, Spaulradm, and SiO_2-filled Epon 828 epoxy with an aromatic cure. These materials were described in a previous report.[1]

Samples were weighed, measured, photographed and then stacked in an aluminum foil pouch inside a copper cylinder. Nickel dosimetry wires were attached axially around the edge of the pouch at 90° intervals, with an additional wire

approximately in the center. The copper cylinder was then electron-beam welded to a cap with a copper tube extending outward, and sent to IPNS for irradiation.

At IPNS a 10 foot length of stainless steel tube was mated to the copper tube extending from the experimental assembly. Swagelok fittings were used throughout. A 1.2 liter gas collection bottle and valve was placed at the far end of the tubing. The volume of the bottle was about 3 times the total enclosed volume of the rest of the system. The assembly was helium leak-tested and evacuated with a diffusion pump.

After insertion in the IPNS target area, the system was cooled to liquid helium temperature. Helium gas was introduced into the assembly, allowed to condense at one atmosphere, and then valved off. After 3-1/2 days of irradiation, the helium was pumped from the system, which was then valved off and warmed to room temperature. Midway during the irradiation time, the assembly was rotated 180° about the vertical axis to insure uniform irradiance in the sample volume.

One day after warmup, the gas bottle valve was opened to allow a gas sample collection. The valve was then closed, the bottle removed, and a new bottle attached. After 28 days, the second bottle was valved off and removed. The copper subassembly, containing the samples, was then removed and returned to Los Alamos along with the gas bottles. Samples were removed, reweighed, photographed, and stored in a desiccator.

Dosimetry from the five nickel foils was analyzed by Larry Greenwood, ANL.* Results indicate a fairly uniform fluence of $1.51 \pm 0.03 \times 10^{21}$ n/cm^2, $E_n >$ 0.1 MeV. Gamma dose is not accurately known but is estimated to be no more than 15% of the neutron dose.

Quantitative analysis of the content of the two gas bottles was done as Los Alamos. Results are shown in Table 1. Interpretation of these results is incomplete. Most of the helium which was found may well be a remnant of the

*See report in Chapter 2.

atmosphere during irradiation. After removal from the irradiation capsule, samples were again weighed and measured. No significant sample weight changes or dimension changes were recorded. All of the samples were found to have changed color. The most interesting change occurred for Kapton. Neutron-irradiated Kapton (-2×10^6 Gy) was found strongly discolored, equivalent to material gama-irradiated to 1×10^8 Gy. In contrast, gama-irradiated material, after a dose of 1×10^7 Gy, was visibly indistinguishable from the starting material. Both neutron- and gamma-irradiated material were examined in IR spectroscopy (Section 5.3.3).

5.3 Results

5.3.1 Electrical Tests

The material G-10 CR was chosen as the first candidate for post-irradiation electrical measurements. Since it is an epoxy, any radiation-induced alterations should show up in this material relatively early. Measurements of D.C.

TABLE 1

RESULTS OF GAS BOTTLE ANALYSES

Pressure (Bomb + 20 cc gauge @ 26°C)	1-Day spl 20.0 torr	1-Mo. spl 26.6 torr
H_2	71 mol%	23 mol%
He	8	1.7
N_2 + CO	13	60
O_2	1.5	12
Ar	3	0.4
CO_2	0.8	1.6
Hydrocarbons*	2.3	0.8

*Hydrocarbon mixture, saturated and unsaturated, mostly $< C_4$. CH_4 is not more than half the total. There is evidence of Oxygen-containing or possibly Nitrogen-containing materials. These may be fragments of alcohols or light amines. There is a trace of acetone and of light aromatics.

conductivity and A. C. dielectric properties were conducted according to ASTM Standards D 257-78 and D 150-78.

Standard three-terminal electrodes were painted onto the 19 mm diameter disks using a commercially available silver paint. Guarded electrode diameters were about 8 mm, giving area-to-thickness ratios of 10 to 12. The electrodes were applied to the irradiated samples subsequent to irradiation. Control samples were immersed in liquid helium after the electrodes had been applied.

To measure D.C. resistivity, a battery power supply of 300 V was used, and current in the guarded circuit after 1 minute was measured with a Keithley 642 electrometer. Results for four controls and four irradiated samples are shown in Table 2. A very small radiation-induced decrease was seen at room temperature. Any change at 80 K was masked by measurement fluctuations. Measurements with no sample in the apparatus indicate that the ultimate measurable resistivity for samples with this geometry is about 2×10^{15} ohm-m.

Dielectric constant and loss tangent measurements were made on the same samples with a Gen Rad model 1616 capacitance bridge driven with an input signal of 4 to 10 V rms. Results of these measurements are shown in Figs. 1-4. There was a moderate increase in dielectric constant after irradiation, but loss tangents remained essentially unchanged.

In summary, all measured electrical properties of G-10 CR at this dose showed at most only small changes.

5.3.2 Mechanical Testing

Irradiated flexure and compression samples were aged in vacuum for 4 weeks for gas collection, and then removed to ambient conditions for shipment to Los Alamos. All samples were stored in a desiccator at room temperature for at

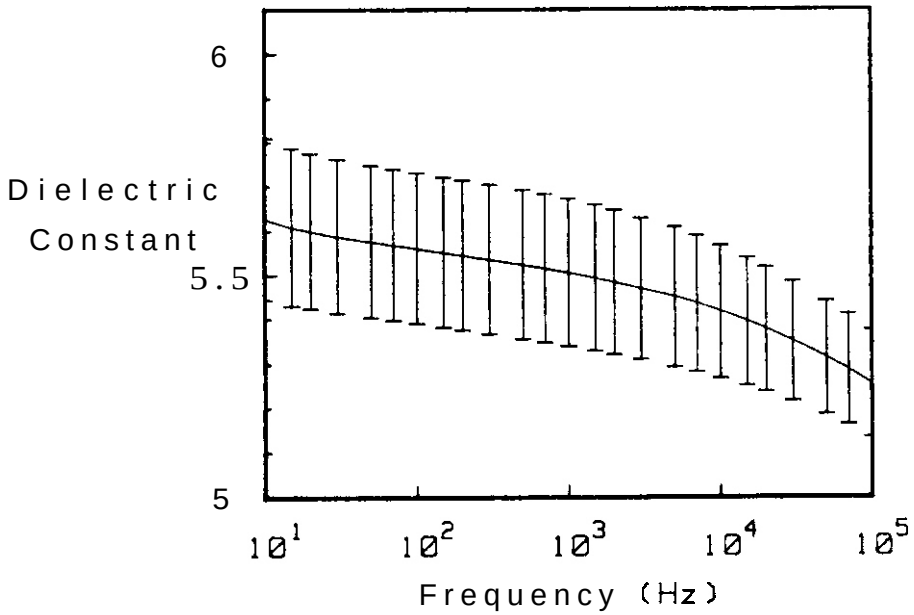

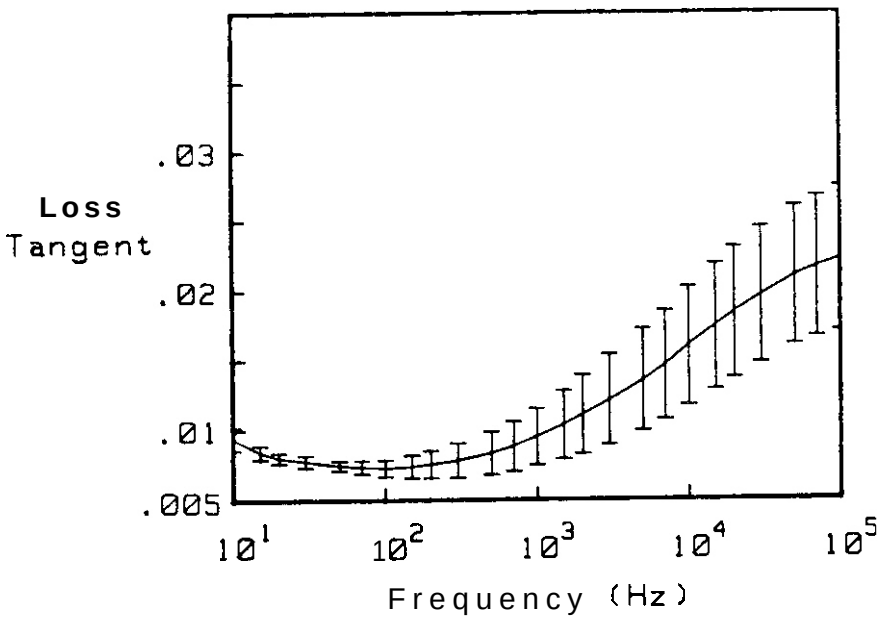

FIGURE 1. A.C. **Electrical Properties** of **G-10 CR Control Samples at 295 K. Error Bars are One Sample Standard Deviation.**

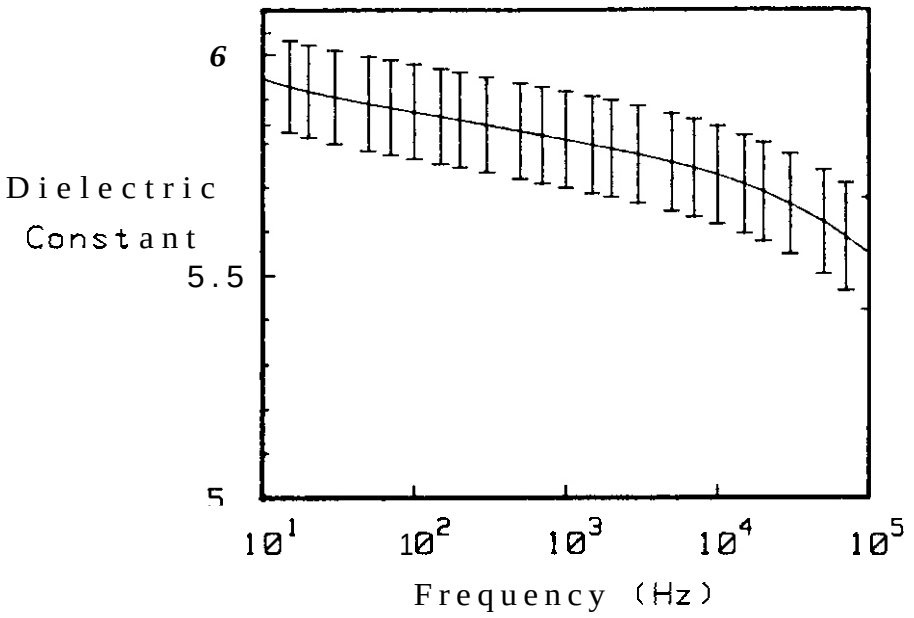

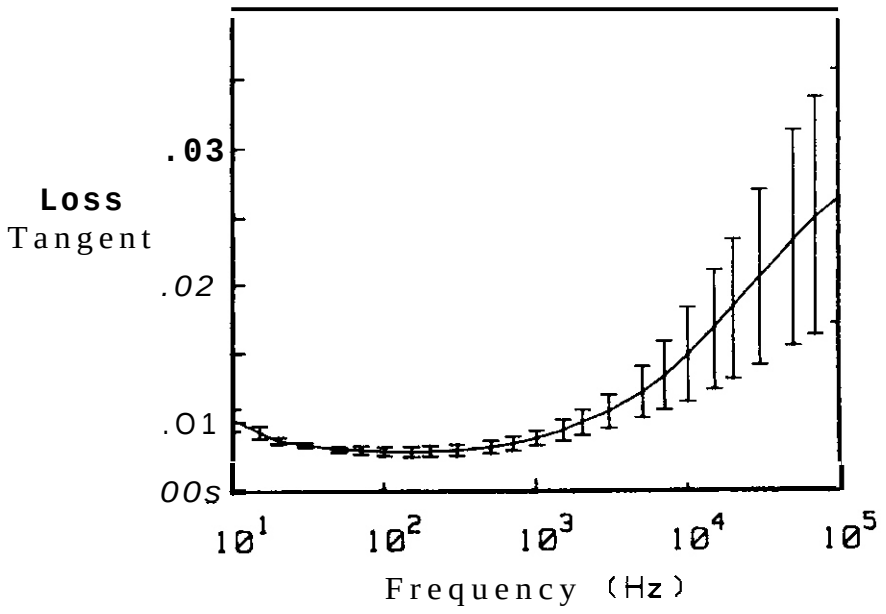

FIGURE 2. A.C. Electric1 Properties of G-10 CR Irradiated Samples at 295 K. Error Bars are One Sample Standard Deviation.

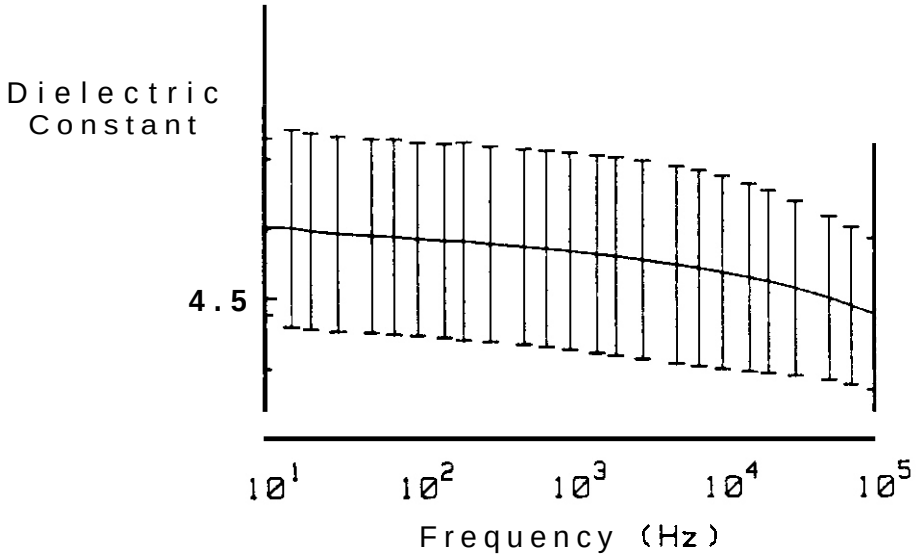

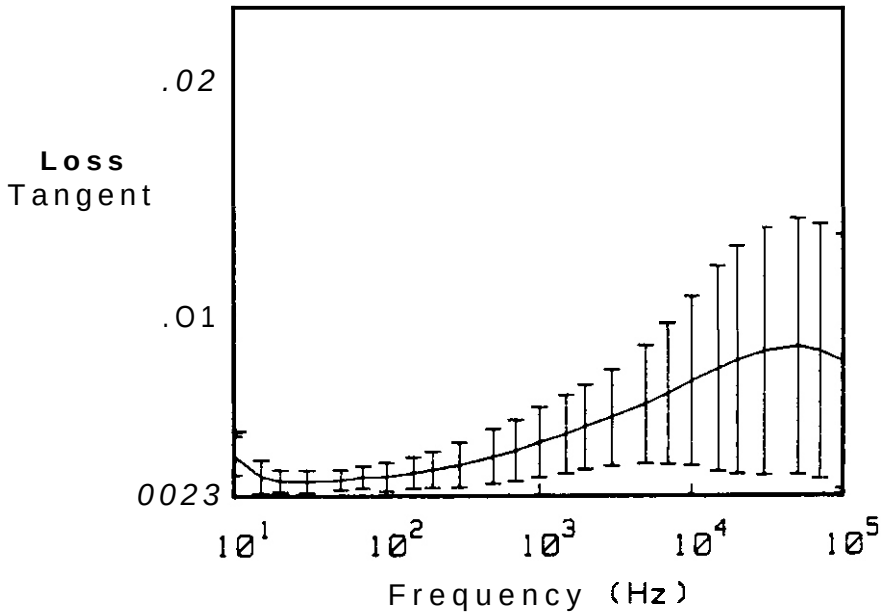

FIGURE 3. A.C. **Electrical Properties** of **G-10 CR Samples at 80 K. Error Bars are One Sample Standard Deviation.**

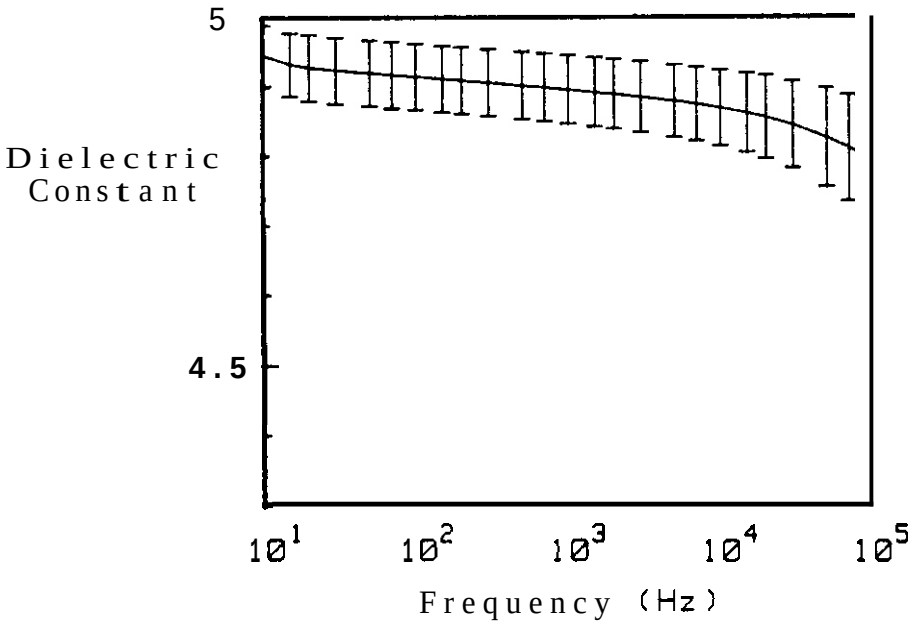

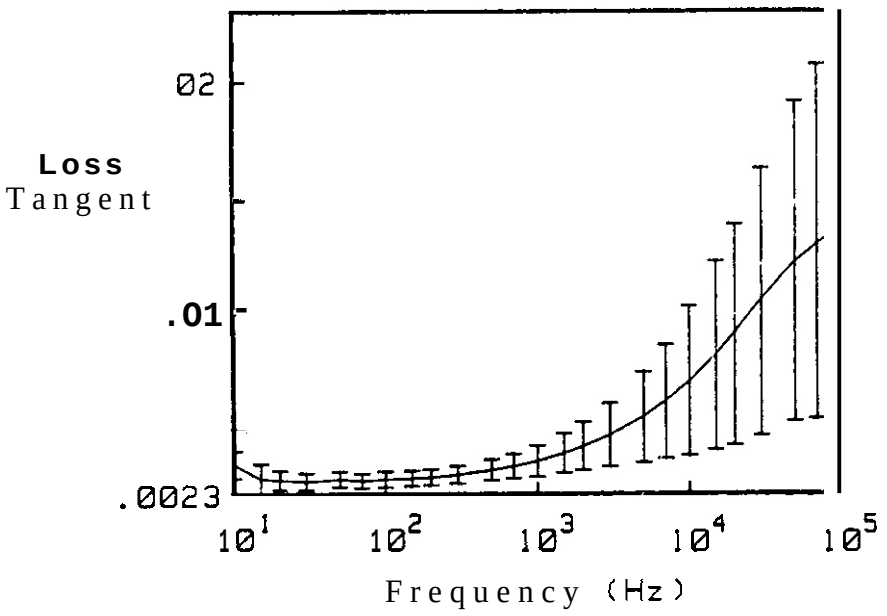

FIGURE 4. A.C. Electrical Properties of G-10 CR Irradiated Samples at 80 K. Error Bars are One Sample Standard Deviation.

TABLE 2

D.C. RESISTIVITY FOR FOUR EACH CONTROL AND IRRADIATED SPECIMENS FOR G-10 CR. UNITS ARE OHM-METERS. LISTED UNCERTAINTIES ARE ONE SAMPLE STANDARD DEVIATION.

Type/Temperature	295 K	80 K
Control	$5.45 \times 10^{13} \pm 7.41 \times 10^{12}$	$5.57 \times 10^{14} \pm 2.30 \times 10^{14}$
Irradiated	$3.26 \times 10^{13} \pm 5.27 \times 10^{12}$	$6.39 \times 10^{14} \pm 2.92 \times 10^{14}$

least 2 weeks prior to testing. Control samples were cooled to liquid helium temperature, rewarmed, and then stored in a desiccator.

Flexure tests were carried out at 75 K using a three point bend test fixture actuated by the cryogenic compression test apparatus described previously.(1) Deflections were measured by means of an LVDT which detected relative movement of the plattens of the compression fixture. Length between outer spans was 2.54 cm, and pin diameter was 6.4 mm. Samples were 3.2 x 1.6 mm in cross section and were tested with the major stress parallel to the warp direction. Deflection rate was 1.3 mm/min. This test procedure follows the requirements of ASTM D 790-80.

Test results were analyzed to determine modulus of rupture (MOR), flexural modulus, and flexural strain. MOR was calculated using the simple beam formula which is valid for maximum fiber strains of 5% or less. These parameters are plotted in Figs. 5 to 7.

MOR results, Fig. 5, show that only one of the materials, G-10 CR, showed a small reduction in strength. The apparent average reduction for G-11 CR of 2% is not considered significant. The reduction for G-10 CR was 16%.

The flexure strain results, Fig. 6, give both the strain at initial failure (yield), as well as the nominal strain at fracture. The former refers to the value of strain at which a distinct break in the stress-strain curve occurred, accompanied by an audible ping. In the unreinforced Epon 828 samples, initial

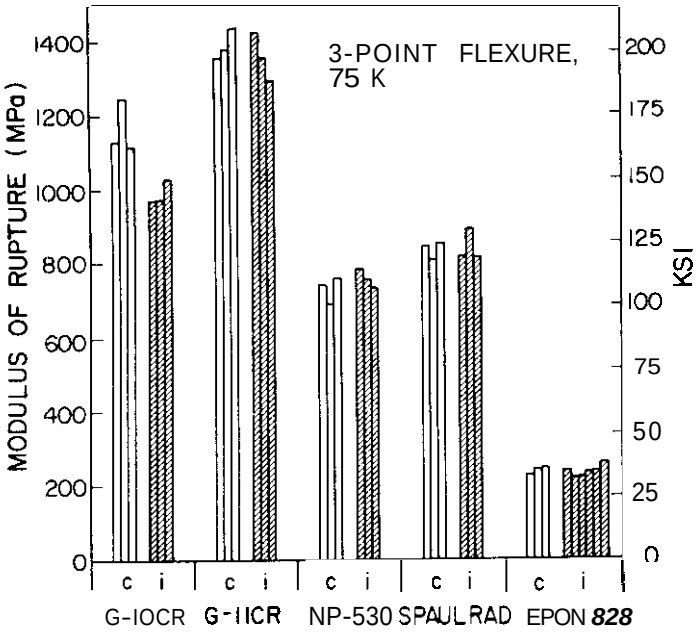

FIGURE 5 Three-Point Flexure Strength of Five Materials Before (c) and After (i) Neutron Irradiation at 4.2 K.

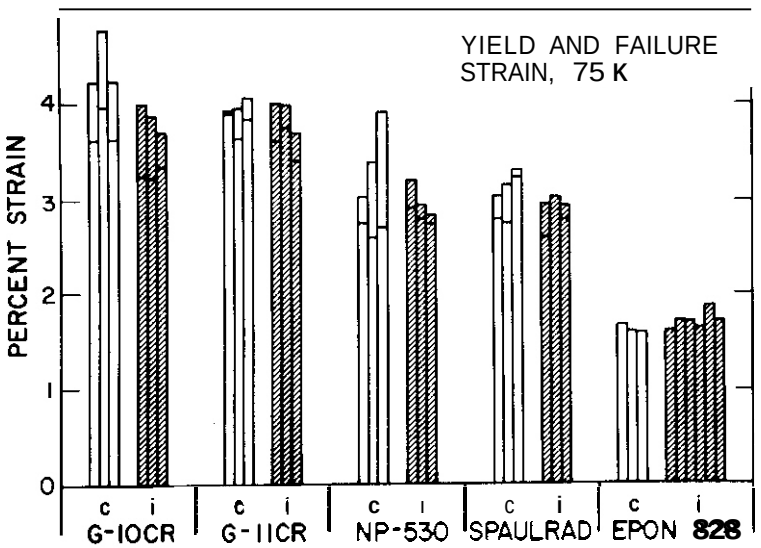

FIGURE 6. "Yield" and Failure Strains for Samples in Fig. 5. Terms are Explained in Text.

and ultimate values were the same. Changes are noted in the strain results for two materials, G-10 CR and NP-530. In the case of the G-10 CR, both yield and failure strains were reduced by 10-12%, somewhat less than the strength reduction. Interestingly, in the case of the NP-530, the effect of irradiation was to move the failure strain down, and yield strain up. In addition, a possible slight reduction of both yield and failure strain is noted for G-11 CR, but not large enough to be concluded significant. Results for flexural modulus, Fig. 7, show small increases for G-11 CR and Spaulrad™, a small decrease for G-10 CR, and no change in the other two materials.

Compression tests were carried out at 75 K on samples 6.4 mm diameter and 12.7 mm long. In the case of the fiberglass reinforced materials, samples were oriented with the fabric warp direction parallel to the compression axis. Crosshead velocity was 0.25 mm/min, and strain was detected by means of an LVDT.

Ultimate compression strength, failure strain and compression modulus are presented in Fig. 8 to 10. Average strength of G-10 CR decreased, as did the NP-530. G-11 CR and Spaulradm both appeared to show a gain. Epon 828 samples exhibited yielding and flow, with substantial plastic strain. The entries for Epon 828 in Fig. 8 give the 0.2% offset yield stress at the lower mark, and the true stress at failure at the top of each column. Results show a small increase in yield stress and a small decrease in true stress.

Trends in the strains to failure shown in Fig. 9, and in the compression moduli shown in Fig. 10 are consistent with the strength results. G-10 CR and NP-530 both showed decreases in failure strain with no change in modulus. In the entries for Epon 828, in Fig. 9, the full bars show overall percentage shortening, while the lower marks give the true, plastic strain. The plastic stress-strain curves showed a clear trend toward decreased ductility in the irradiated samples. In Fig. 10, the G-11 CR samples, alone, appeared to show a change, with the modulus increased about 14%.

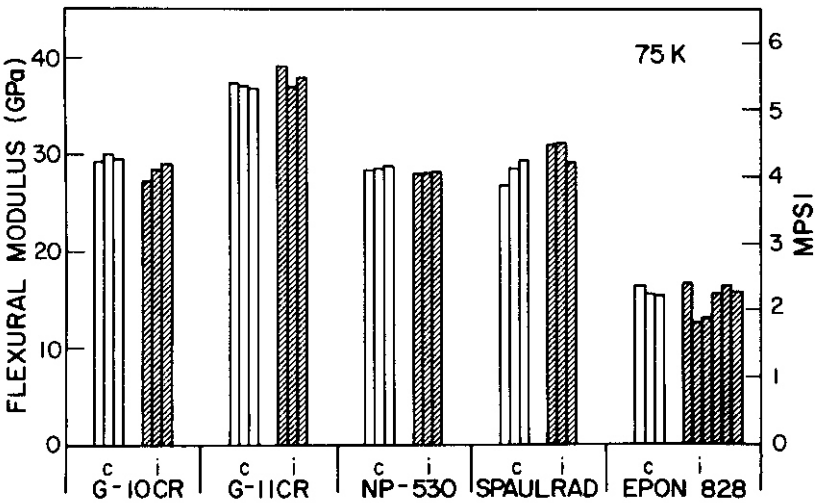

FIGURE 7. Flexural Modulus of Samples in Fig. 5.

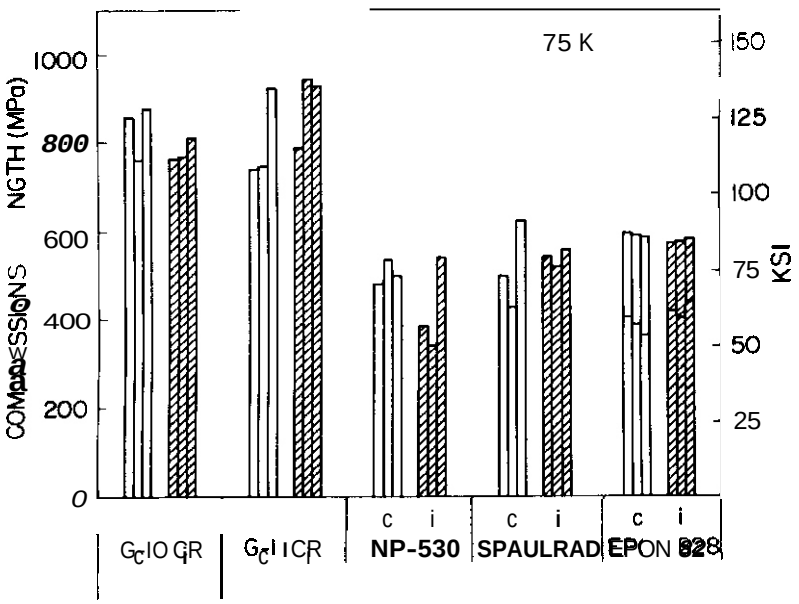

FIGURE 8. Compression Strength of Five Materials Before (c) and After (i) Neutron Irradiation at 4.2 K. Entries for Epon 828 Give the 0.2% Offset Yield Stress (Lower Bar), and Ultimate True Fracture Stress.

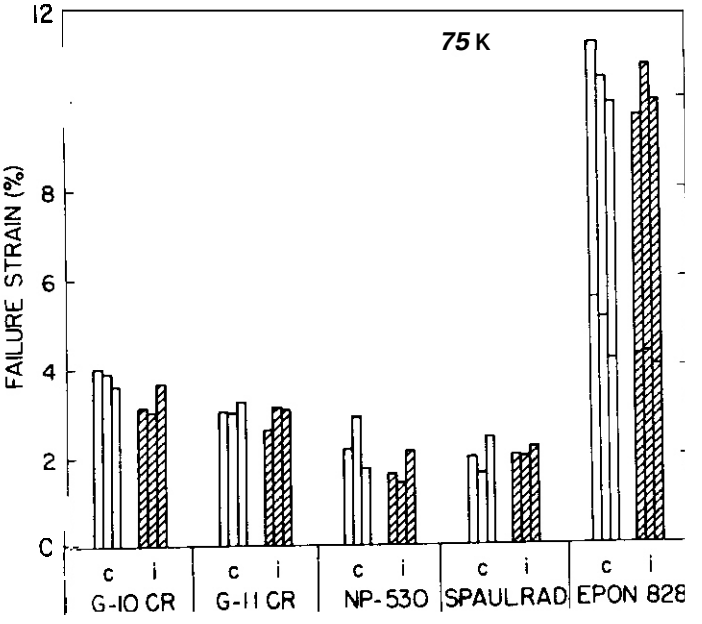

FIGURE 9. Failure Strain in Compression for Samples in Fig. 8. Entries for Epon 828 Give True Plastic Strain (Lower Bar) as Well as Total Strain.

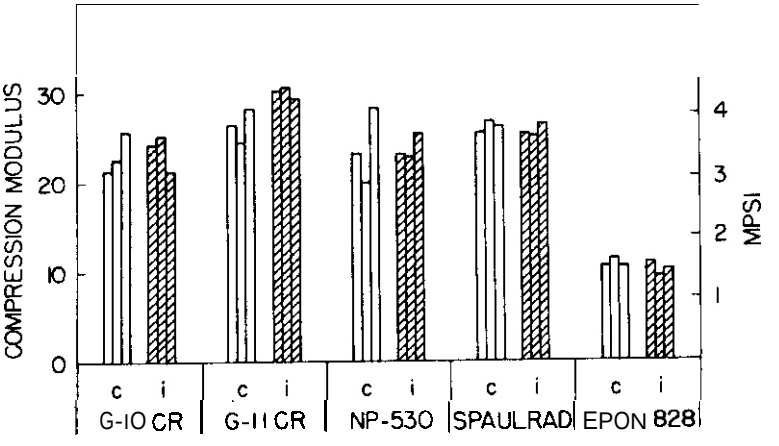

FIGURE 10. Compression Modulus for Samples in Fig. 8.

The appearance of all of the samples fractured in flexure was characterized and disclosed differences between materials to be more prominent than differences between irrradiated and control samples of the same material. In all cases, the glass cloth reinforced materials tended to buckle on the compression side, under the loading pin, with tearing, "brooming" of the broken yarns, and delamination occurring on the tensile side. Figure 11 contrasts failure in an irradiated sample of 6-10 CR, with that in a control sample of NP-530. The features of note are the more extensive damage zones in the polyimide compared to the epoxy, with both delamination and buckling being more prominent in the former. We have not yet detected any specific effects of radiation damage in the fracture appearances.

The silica filled epoxy material failed by cleavage with no noteworthy alterations in the irradiated material. A preliminary examination of this material has been carried out by SEM to look for evidence of change in fracture path or for evidence for gas generation at particle-matrix interfaces. No such evidence has been found. Examination of the other materials by SEM will continue.

In comparing the results of the flexure and compression tests, the most consistent findings appear to be a decrease in strength and corresponding decrease in failure strain for the G-10 CR, increase in modulus for G-11 CR, decrease in failure strain of NP-530, and combined reduction of ultimate stress and strain of glass-filled Epon 828, measured in compression. All of these changes were small and, by themselves, represent no limitation to their use in a magnet environment.

5.3.3 Chemical Radiation Effects

The structure of a polymer is commonly characterized by its macro- and microstructural parameters. The former deals with such parameters as molecular weight, molecular weight distribution, and branching. The latter deals with the manner in which the monomer units are assembled to form the

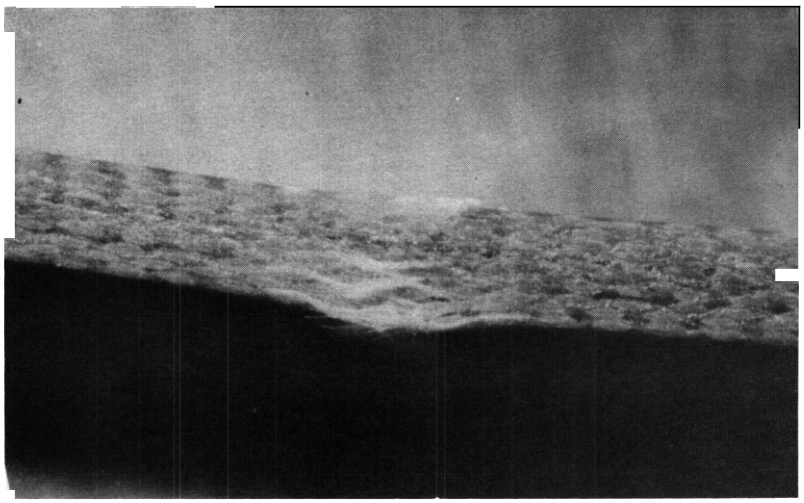

(a)

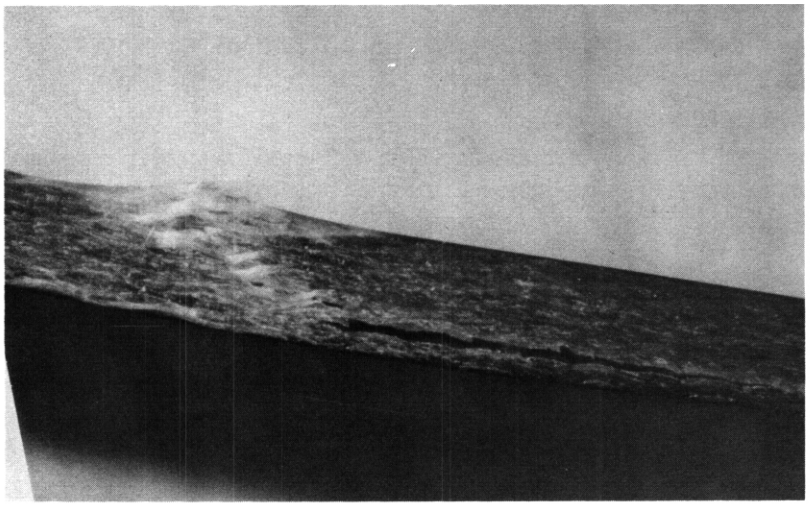

(b)

FIGURE 11. Photographs Contrasting the Appearance of Failed G-10 CR (Irradiated) in (a) With NP-530 (Control) in (b) Flexure Samples. Tensile Surfaces are Lower Edges. Note the Prominent Delamination in (b).

polymer chain. Both characteristics strongly affect the physical properties of the polymer and its performance under different conditions and both characteristics are affected by high energy radiation, especially, at high total doses.

In this initial effort we have solved the problem of preparing samples for spectroscopic analysis from intractable materials (G-10 CR, Norplex NP-530); have developed a sample preparation technique for examining radiation induced surface effects vs bulk effects; have performed a cursory infrared spectroscopic analysis on G-10 CR, Norplex NP-530, and Kapton; have performed a cursory differential scanning calorimetry analysis on G-10 CR, G-11 CR, Spaulradm, Norplex NP-530, and Kapton from 39°C to 410°C; have proposed three model compounds for a typical epoxy (Epon 828) resin cured with an aromatic primary amine, aliphatic primary amine, and an aromatic acid, and have ordered the required materials for their synthesis.

Samples were prepared for spectroscopic examination by microtoming, using either a glass or diamond knife. Development of such a technique is necessary for insoluble, cured materials and permits sampling the material in such a way as to sample both surface and bulk effects. Using this technique we have also prepared 1 μm thick surface layer samples for examination of the surface vs bulk radiation induced effects.

While results and analysis of these samples are not yet complete, the following observations have been made:

G-10 CR — No drastic changes were observed in any of the major absorption bands; however, detectable specific minor surface and bulk absorption changes, indicative of chemical transformations, were observed.

Norplex NP-530 — No drastic changes were observed in any of the major absorption bands. However, there were detectable minor

changes in the bulk but not the surface samples. This is different from the G-10 CR samples which showed also surface specific changes.

Kapton — This material showed small but distinct spectral changes after irradiation. In this case, too, a sample was examined after gamma irradiation under environmental conditions similar to those in the neutron-irradiated sample. Infrared spectra were distinctly different from either the control or the neutron-irradiated sample.

Differential scanning calorimetery (DSC) was also carried out on G-10 CR, Norplex NP-530, and G-11 CR, Kapton, and Spaulradm. In the 39° to 410°C temperature range at the heating rate of 10°/min., none of the samples (sample weight from 3.8 to 6.1 mg) showed a glass transition temperature, melting point or a decomposition point. Three of the samples did show a weight loss:

	% wt. loss
G-10 CR, unirradiated	13
irradiated	15
Norplex NP-530, unirradiated	6
irradiated	6
G-11 CR, unirradiated	< 6
irradiated	< 6

Two of the samples, G-10 CR and Norplex NP-530, in the non-irradiated state underwent a significant curing reaction at the DSC analysis conditions.

Kapton was the most thermally stable in the non-irradiated as well as the gamma-irradiated state as it showed no apparent effects upon the sample as perceived by the DSC analysis. The neutron-irradiated material has not yet

been tested. This was followed by the Spaulrad™ samples which showed only a slight exothermic effect in the irradiated sample at temperatures above 298°C.

We have proposed the following model compounds for a typical epoxy (Epon 828) resin cured with:

aranatic primary amine -

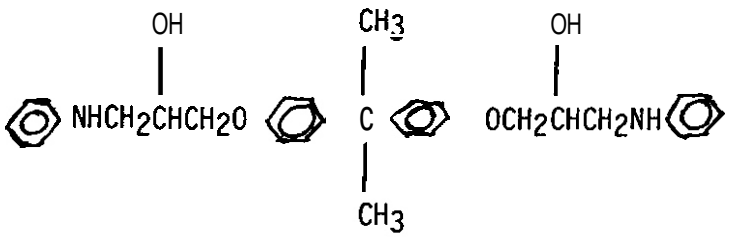

aliphatic primary amine -

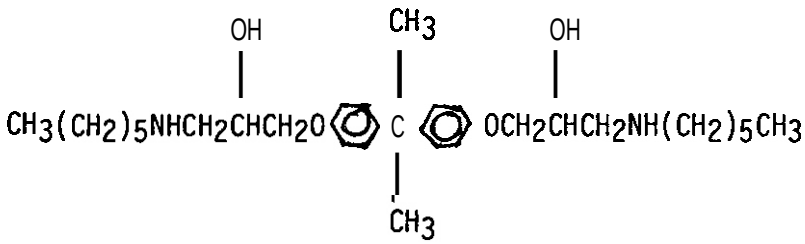

aromatic acid -

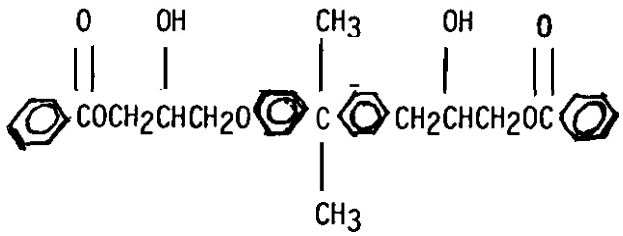

Materials are on order to prepare these compounds.

5.4 Comparison with Gamma-Irradiation

No detailed comparison with previous results from the work of Coltman and coworkers or others on the changes in properties of the same or similar materials after gamma-irradiation has as yet been attempted. Results of electrical tests so far are consistent with those of Coltman *et al.*[2] in that radiation-induced changes in D.C. conductivity are small at this dose. The reduction in strength of G-10 CR, while that of G-11 CR is maintained, is consistent with the aromatic cure used with the latter, and with the extrapolation of the Oak Ridge data.3 However, this reduction, for G-10 CR, appears to have occurred at a dose lower than we would have anticipated.[3,4]

6. References

1. G. F. Hurley, J. D. Fowler, Jr., and D. M. Parkin, "Neutron-Irradiation Plan for Calibration of Gamma and Neutron Damage Effects in Organic Insulators" in Damage and Fundamental Studies Quarterly Progress Report for October-December, 1981, in press.

2. R. R. Coltman, Jr., C. E. Klabunde, R. H. Kernohan, and C. J. Long, "Radiation Effects on Organic Insulators for Superconducting Magnets," ORNL/TM 7077, Nov. 1979.

3. R. R. Coltman, Jr., Oak Ridge National Laboratory, Personal Communication, May 1981.

4. R. H. Kernohan, R. R. Coltman, Jr., and C. J. Long, "Radiation Effects on Organic Insulators for Superconducting Magnets," ORNL/TM 6708, March 1979.

7. Future Work

Work continues on this project in four areas: continuation of experimental measurements on samples from the first IPNS irradiation, correlation of these results with literature results for gamma irradiations, preparation of model compounds for comparative determination of structural changes in neutron and gama irradiations, and preparation of further irradiation experiments for

the IPNS-I, and for RTNS-II. We will seek higher dose in IPNS-I, and we will be looking at spectral effects in the RTNS-II work.

Acknowledgements. The authors are pleased to acknowledge the help of Mark Kirk, ANL, in carrying out the irradiation in IPNS, and of Larry Greenwood, ANL, who is performing the dosimetry. The G-10 CR, G-11 CR, and Spaulrad™ were supplied by the Spaulding Fibre Co., Tonawanda, N.Y., and the NP-530 by Norplex Div., VOP Inc., Lacrosse, WI. The authors also thank R. R. Coltman, Jr., ORNL, for irradiating Kapton samples in the BSR.

CHAPTER 3

FUNDAMENTAL MECHANICAL BEHAVIOR

CORRELATION OF HARDNESS AND STRENGTH DATA FOR HIGH ENERGY NEUTRON IRRADIATED ANNEALED 316 STAINLESS STEEL

N. F. Panayotou (Westinghouse Hanford Company)

1.0 Objective

The objective of this work is to determine the effects of high energy neutrons on damage production and evolution, and the relationships of these effects to effects produced by fission reactor neutrons. Specific objectives of the current work are the development of techniques to extract from miniature specimen geometries information on the change in mechanical properties of neutron irradiated metals.

2.0 Summary

A major goal of the DAFS program involves obtaining accurate measurements of the changes in the flow behavior of neutron irradiated metals from miniature specimen geometries. Indenter type hardness techniques have been applied to transmission electron microscopy (TEM) disk-type specimens in an effort to extract relative hardening data. Since microhardness tests are localized, they do not preclude either the continued irradiation or the further study of TEM disk specimens by other post-irradiation analytical techniques.

In a previous report[1] strength values derived from hardness data were shown to be in good agreement with actual tensile data for neutron irradiated copper. In this report a similar result is reported for annealed 316 stainless steel.

3.0 Program

Title: Irradiation Effects Analysis (AKJ)
Principal Investigator: D. G. Doran
Affiliaton: Westinghouse Hanford Company

4.0 Relevant DAFS Program Plan Task/Subtask

Subtask II.B.3.2 Experimental Characterization of Primary Damage State; Studies of Metals

II.C.6.3 Effects of Damage Rate and Cascade Structure on Microstructure; Low-Energy/High-Energy Neutron Correlations

II.C.11.4 Effects of Cascades and Flux on Flow; High-Energy Neutron Irradiations

II.C.18.1 Relating Low-Exposure and High-Exposure Microstructures; Nucleation Experiments

5.0 Accomplishments and Status

5.1 Introduction

The optimum use of the available irradiation volume of high energy neutron sources is requisite for an aggressive fusion materials development program. Tensile testing of miniature specimens compatible with high energy neutron sources has been shown to be feasible.[2,3] However there is still a very definite need for a technology which can extract mechanical property and microstructural data without destroying the test article. The use of transmission electron microscopy (TEM) disk specimens and standard diamond pyramid microhardness (DPH) test techniques is one of the technologies being developed to meet this challenge. Each DPH test, or indent, damages only a small fraction of the specimen, allowing a single specimen to be repeatedly re-irradiated and tested, or to be analyzed by several post-irradiation techniques.

Originally conceived mainly as a scoping tool to measure radiation induced hardening it has been determined that, at least for copper and annealed type 316 stainless steel, the DPH measured hardening is directly proportional to the measured increase in the 0.2 percent offset yield strength. The results for copper have been reported previously.[1] The results for annealed type 316 stainless steel are reported here.

5.2 Experimental Procedure

Three millimeter diameter TEM disk specimens of Reference Heat 316 stainless steel, heat number X15893, were fabricated by punching from as-rolled 20 percent cold worked, 0.3 mm thick sheet stock. The composition of the stock material is listed in Table 1. Each specimen was permanently engraved using a laser engraving system. In preparation for heat treatment the specimens were cleaned and then sealed along with a tantalum getter in a quartz ampul which had been evacuated and then back-filled with argon gas to a pressure of one quarter atmosphere. The specimen heat treatment, grain size and baseline hardness value are listed in Table 2.

The TEM disk specimens together with niobium dosimetry foils were then loaded into specimen holders and irradiated at 25°C at the Rotating Target Neutron Source (RTNS)-II at Lawrence Livermore National Laboratory (LLNL). RTNS-II is an accelerator based neutron source which employs a 400-keV deuteron beam incident upon a tritium loaded, water cooled, rotating target to produce 14-MeV neutrons by a T(d,n) reaction.

TABLE 1

CHEMICAL COMPOSITION (WEIGHT PERCENT)

Element	Reference Heat 316 SS Heat #X15893	HEDL 316 SS Heat #V87210[3]	LLNL 316 SS[4]
Si	0.69	0.5	0.60
Al		0.01	
S	0.015	0.009	
Cr	16.81	16.6	17.3
Fe	Balance	Balance	Balance
Ni	12.10	13.5	12.4
C	0.056	0.05	0.059
cu		0.08	
Mo	2.39	2.4	2.1
Mn	1.63	1.5	1.83
Ti	<0.01	0.002	
P	0.035	0.01	
Nb		0.03	
N		0.006	0.021
B		0.001	

TABLE 2

HEAT TREATMENTS AND BASELINE PROPERTIES

Metal	Heat Treatment	Average Grain Diameter (μm)	Hardness (kg/mm^2)	0.2% Offset Yield Strength, MPa
Reference Heat 316 Heat #X15893	950°C/10m/AC	16	177±6 @ 100g	-
HEDL 316 Heat #V87210[3]	975°C/15m/AC	32	-	284±21
LLNL 316[4]	1050°C/1h/WQ	27	-	269

AC: Air Cool
WQ: Water Quench

Prior to microhardness testing the TEM disk specimens are secured to a standard plastic metallographic mount using a cyanocrylate adhesive. Except for a light cleaning of the surface of the TEM disk no other surface preparation was employed. Tests were performed at 25°C using a Tukon-type hardness testing machine fitted with a standard 136" diamond pyramid indenter. For each metal a load was selected which would produce an indent whose depth of penetration did not exceed one-twentieth of the thickness of the test specimen. Once determined, the same load was always used to follow the hardening of a given metal. This procedure minimized the influence of the specimen support on the measured DPH value while producing indents whose diagonals could be accurately measured. Using a Filar type eyepiece each DPH indent was imaged at a magnification which permitted the diagonals of the indent to be measured to 0.1 μm. The baseline hardness value listed in Table 2 is the average of at least fifteen DPH indents performed on a single TEM disk specimen. Also listed is the 1σ spread in the DPH data.

Included in Tables 1 and 2 are the compositions, heat treatments, average grain diameters and baseline offset yield strengths of two heats of type 316 stainless steel. Sheet type tensile specimens of an LCNL 316 stainless steel were irradiated at RTNS-I. The details of this experiment were reported elsewhere.[4] Wire type tensile specimens of a HEDL 316 stainless steel, heat number V87210, were irradiated at RTNS-II. The details of this experiment were also reported elsewhere.[3] All tensile specimens were irradiated and tested at 25°C.

5.3 Experimental Results

The strengthening data for type 316 stainless steel are listed in Table 3. The hardness value reported for irradiated specimens is the average of at least five indents performed on a single TEM disk specimen. The change in the 0.2 percent offset yield strength, $\Delta\sigma_y$, was deduced from hardness data using the following relationship

$$\Delta\sigma_Y \text{ (MPa)} = K \text{ ADPH (kg/mm}^2\text{)} \quad (1)$$

where K *is* a numerical constant equal to approximately 3.27 and ADPH is the change in the diamond pyramid hardness value with increasing neutron exposure. These data are plotted as $\Delta\sigma_Y$ versus neutron fluence in Figure 1.

TABLE 3

TYPE 316 STAINLESS STEEL STRENGTHENING DATA

TENSILE DATA				HARDNESS DATA		
HEOL 316 SS[3]		LLNL 316 SS[4]		Reference Heat 316 SS		
Fluence 10^{17} n/cm²	$\Delta\sigma_Y$ MPa	Fluence 10^{17} n/cm²	$\Delta\sigma_Y$ MPa	Fluence 10^{17} n/cm²	ADPH kg/mm²	$\Delta\sigma_Y$ MPa
0.55	12±21			0.29	-5±7	16±23
0.56	4±29			0.56	6f7	20±23
0.59	15±21					
0.64	6±29	0.65	29	0.67	0.5±7	2±23
		0.75	42			
		0.80	39			
		0.90	47			
		0.95	49			
		1.3	52			
1.5	36±30	1.5	63			
1.7	21±21	1.7	60	1.7	8+9	26±29
1.7	40±31	2.0	71			
1.8	34±30	2.5	70			
				3.4	22±7	72±23
6.5	122±35			5.8	33±8	108526
6.6	95±34			8.1	36±7	118±23
7.5	98±34			8.3	29±9	95±29
9.4	82±33			11.0	40±8	131±26
11.5	128±36					

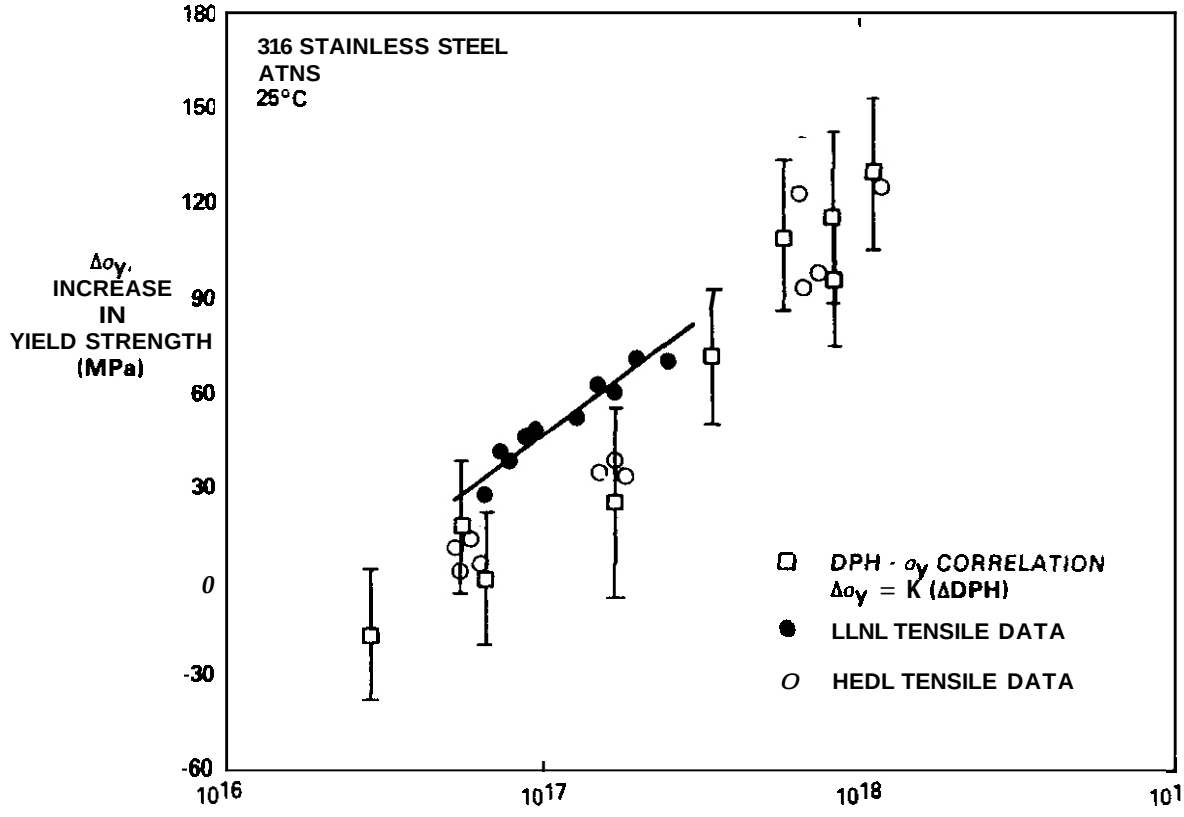

The measured $\Delta\sigma_Y$[2] are plotted for wire tensile specimens of HEDL 316 stainless steel over a fluence range of $5.5 \cdot 10^{16}$ to $1.15 \cdot 10^{18}$ n/cm^2 in Figure 1. Over this fluence range the measured $\Delta\sigma_Y$ approached 130 MPa. The measured $\Delta\sigma_Y$ of sheet type tensile specimens of LLNL type 316 stainless steel over a fluence range of $6.5 \cdot 10^{16}$ to $2.5 \cdot 10^{17}$ n/cm^2 are also plotted.[4] Over this fluence range the measured $\Delta\sigma_Y$ was 70 MPa. Hardness data for Reference Heat 316 stainless steel was obtained over a fluence range of $2.9 \cdot 10^{16}$ to $1.1 \cdot 10^{18}$ n/cm^2. The increase in hardness of this stainless steel over this fluence range is 40 kg/mm^2. The 1σ spread in the DPH values ranges from 2 to 4 percent. Using Equation (1) the hardness data was converted to a measure of the increase in the 0.2 percent offset yield strength and plotted in Figure 1. The error bars shown in Figure 1 represent the 1σ spread in $\Delta\sigma_Y$, calculated from DPH data.

The average calculated strengthening values based on DPH data are in excellent agreement with the HEDL tensile data and, within 1σ error limits, are in good agreement with LLNL tensile data. In a previous report it was argued that a correlation 1ike Equation (1) between increased hardness and increased strength is reasonable for annealed fcc metals whose yield strength has increased by less than a factor of four.[1] In this study the maximum strengthening for annealed 316 stainless steel was less than a factor of 1.5.

5.4 Conclusions

Standard DPH testing of TEM disk specimens is an effective method of studying high energy neutron radiation induced damage. For some fcc metals, in addition to providing a measure of hardening, the increase in diamond pyramid hardness with fluence varies directly with the measured increase in 0.2 percent offset tensile yield strength. Accordingly, the strengthening of such metals in the fluence range studied can be determined easily and inexpensively from miniature specimens.

6.0 References

1. N. F. Panayotou, "Prediction of the Change in the Offset Yield Strength of Copper Due to High Energy Neutron Irradiation Using Vickers Microhardness Data," DAFS Quarterly Progress Report, DOE/ER-0046/5, (January-March 1981), p. 65.

2. R. H. Jones, D. L. Styris, E. R. Bradley, L. R. Greenwood and R. R. Heinrich, J. Nucl. Mat., 85 & 86, 889 (1979).

3. N. F. Panayotou, R. J. Puigh and E. K. Opperman, "Miniature Specimen Tensile Data for High Energy Neutron Source Experiments," J. Nucl. Mat., 103 & 104, 1523 (1981).

4. R. R. Vandervoort, E. L. Raymond and C. J. Echer, Rad. Eff., 45, 191 (1980).

7.0 Future Work

The strength-hardness correlation reported here will be extended to other metals in the DAFS program.

HARDENING OF IRRADIATED ALLOYS DUE TO THE SIMULTANEOUS FORMATION OF VACANCY AND INTERSTITIAL LOOPS

N. M. Ghoniem, J. Alhajji (University of California, Los Angeles) and
F. A. Garner (Hanford Engineering Development Laboratory)

1.0 Objective

The object of this effort is to provide a mechanistic framework on which to model the effect of irradiation on mechanical properties and dimensional stability under irradiation.

2.0 Summary

Clustering of irradiation produced point defects is recognized to impede dislocation motion and hence influence mechanical deformation characteristics. In this paper, a model is presented for the simultaneous nucleation and growth of vacancy and interstitial loops in irradiated metals. The model is based on homogeneous time-dependent rate theory. Conservation equations are developed for single defects as well as defect clusters. Defect conservation equations include production by irradiation and thermal sources and destruction by mutual recombination, migration to sinks, and clustering into loops. Interstitial clustering is assumed to occur by diffusion of interstitial atoms. Vacancy loops, on the other hand, are assumed to form by an athermal cascade collapse process. The density of such loops is determined as a result of the production of cascades and the finite loop lifetime. Cascade overlap and coalescence are also included in the model.

The calculations are extended to the analysis of the radiation-induced changes in tensile properties due to formation of interstitial and vacancy loops. A simple hardening model relates the microstructural calculations to predictions of changes in tensile strength. The results of this study show good agreement

with hardening data for copper irradiated in RTNS-II at room temperature. The results also provide insight on differences in microstructural results observed in various experimental studies on copper.

3.0 Program

Title: Helium Effects on Swelling
Principal Investigator: N. M. Ghoniem
Affiliation: University of California, Los Angeles

4.0 Relevant DAFS Program Plan Task/Subtask

II.C.14 Models of Flow and Fracture Under Irradiation

5.0 Accomplishments and Status

5.1 Introduction

Experimental investigations over the last two decades have established that exposure of metals at relatively low temperatures to neutron irradiation results in an increase in the yield strength. However, this strengthening is not necessarily beneficial. Radiation-induced strengthening has been directly linked to a loss of ductility in austenitic steels, and to a shift in the ductile-to-brittle transition temperature (DBTT) in ferritic steels.

The confident design of structural components that must withstand the rigors of an irradiation environment requires that irradiation-induced changes in properties be included in the design process. For example, the anticipated low temperature failure of the first wall in conceptual designs of Tandem Mirror Fusion Reactors has been predicted to arise from the irradiation shift of the DBTT.[1] It is technologically important, therefore, to study the response of alloys to irradiation hardening. Recent experimental work using the Rotating Target Neutron Source (RTNS-II) has been directed toward the study of this phenomenon in a fusion-relevant spectrum.[2]

Neutron irradiation leads to the production of single vacancies, interstitials and impurity atoms. Vacancy aggregates formed in collision cascades may also collapse athermally to form depleted zones or vacancy loops. The subsequent interactions and agglomeration of these defects are now recognized to be the primary cause of irradiation hardening. Figure 1 shows typical irradiation-induced microstructures and the associated hardening that is observed in copper irradiated in RTNS-II at 25°C.

In this paper, we develop a model for the simultaneous formation of vacancy and interstitial aggregates at low temperatures. The model is not a comprehensive microstructural description applicable under all irradiation conditions. The formation of precipitates, cavities and dislocation networks at higher temperatures are excluded.

The microstructural evolution at higher temperatures is much more complex and microstructurally-based mechanical property correlations are largely phenomenological in nature.[3-4] The phenomenological approach is useful for interpolation or extrapolation beyond the range of existing data. However, for low temperature irradiation where the goal is to study the connection of fundamental studies to practical questions, a different approach can be employed. Therefore, the first objective of this work is to investigate the simultaneous nucleation and growth of both vacancy and interstitial loops in irradiated materials at low temperature ($T < T_{m/3}$), where T_m is the melting point. The second objective will be to apply the microstructural insight gained in this study to the description of the irradiation-induced hardening phenomenon.

5.2 Simultaneous Clustering of Vacancies and Interstitials

The model presented here is essentially a time-dependent nucleation and growth model for both vacancy and interstitial loops. Conservation equations are developed for single defects as well as defect clusters. Point defect conservation equations include production by irradiation and thermal sources, and destruction by mutual recombination, migration to sinks and clustering into loops. Interstitial clustering is assumed to result from diffusional migration

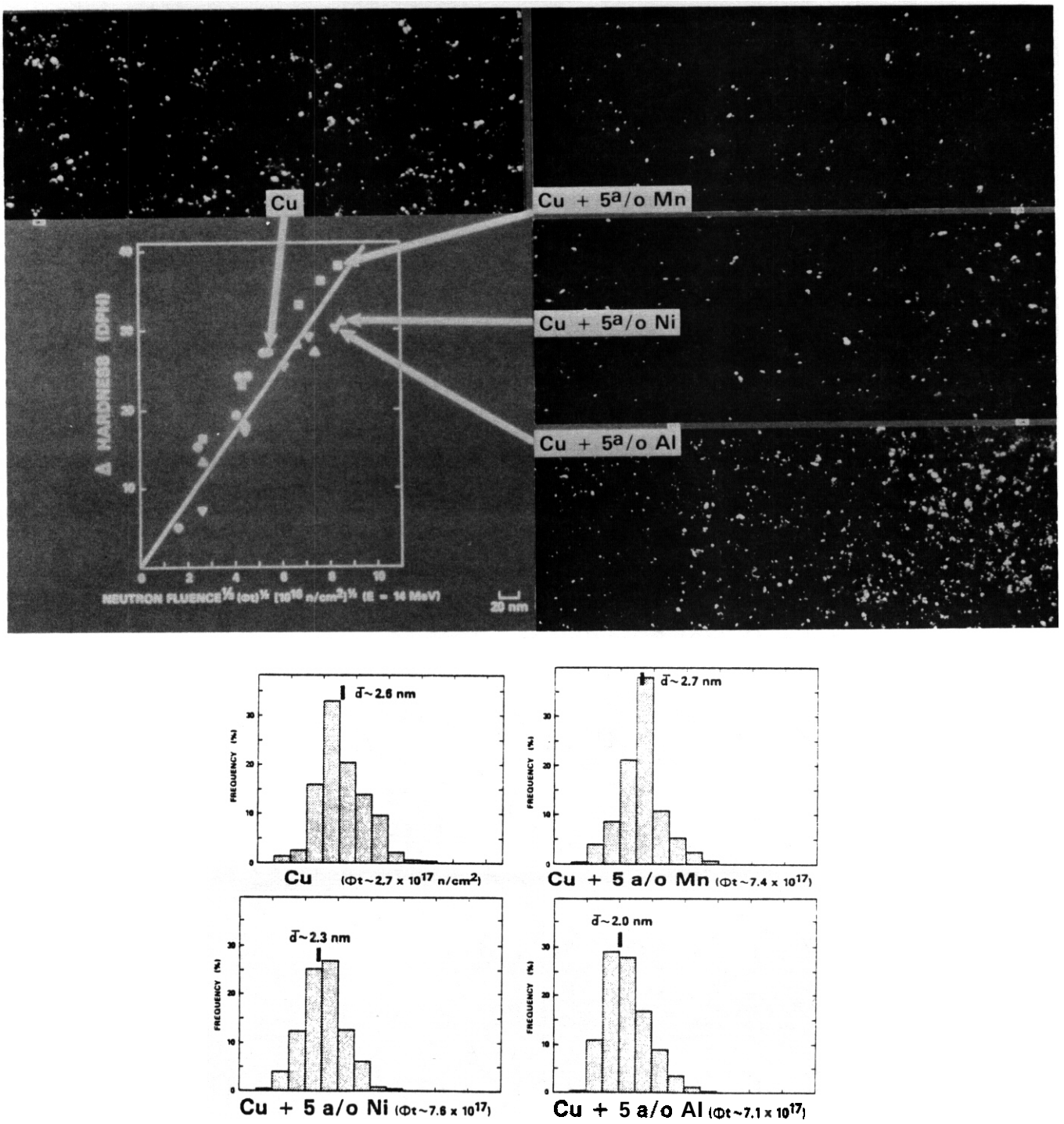

FIGURE 1. Small Defect Clusters and Their Associated Hardening Observed in Copper and Simple Copper Alloys Irradiated in RTNS-II with 14-MeV Neutrons at 25°C.(2) The size distributions of the clusters are also shown, but it is important to note that these studies provided evidence that a substantial fraction of the defect clusters lie below the resolution or visibility limit of the microscopy techniques employed.

of interstitial atoms. Vacancy loop formation, on the other hand, is assumed to result from the athermal collapse of collision cascades. In other words, the nucleation of vacancy loops is characterized by collisional rather than diffusional atomistic events. The average sizes of both interstitial and vacancy loops are determined by the competition between defect absorption and vacancy emission. It is also assumed that recently produced vacancy loops may coalesce with existing loops. This mechanism leads to growth of both types of loops (vacancy and interstitial), as will be shown later.

The following rate equations describe the evolution of defect populations and must be solved simultaneously. The notation employed in these equations is defined in Table 1, with the exceptions of concentrations C, diffusivities D and rate constants K. P_d is the damage production rate in dpa/sec, $Q_{v\ell}$ is the fraction of vacancies in loops, and $F_{e\ell}$ is the loop line tension in eV/cm^2.

$$\frac{dC_v}{dt} = (1 - \varepsilon)\, P_d - Z_v^n \rho_d^n D_v (C_v - C_v^e)$$

$$- Z_v^{\ell} \rho_d^{il} D_v \left\{ C_v - C_v^e \exp\left(- \frac{[\gamma_{sf} + F_{el}(\bar{R}_{il})]b^2}{kT} \right) \right\}$$

$$- Z_v^{l} \rho_d^{vl} D_v \left\{ C_v - C_v^e \exp\left(\frac{[\gamma_{sf} + F_{e\ell}(\bar{R}_{i\ell})]b^2}{kT} \right) \right\}$$

$$- \alpha C_v C_i - K_v^{2i} C_v C_{2i} - K_v^{3i} C_v C_{3i} \qquad (1)$$

$$\frac{dC_i}{dt} = P_d + K_v^{2i} C_v C_{2i} + 2\gamma_{2i} C_{2i} - K_i^i C_i^2 - \alpha C_v C_i$$

$$-K_i^{2i} C_i C_{2i} - K_i^{3i} C_i C_{3i} - Z_i^{\ell} D_i C_i (\rho_d^{\ell} + \rho_d^{il}) - Z_i^n D_i C_i \rho_d^n \qquad (2)$$

$$\frac{dC_{2i}}{dt} = \frac{1}{2} K_i^i C_i^2 + K_v^{3i} C_v C_{3i} - K_i^{2i} C_i C_{2i}$$

$$- K_v^{2i} C_v C_{2i} - \gamma_{2i} C_{2i} \tag{3}$$

$$\frac{dC_{3i}}{dt} = K_i^{2i} C_i C_{2i} + K_v^{4i} C_v C_{4i} - K_i^{3i} C_i C_{3i}$$

$$- K_v^{3i} C_v C_{3i} \tag{4}$$

$$\frac{dN_{il}}{dt} = K_i^{2i} C_i C_{2i} \tag{5}$$

$$\frac{d\bar{R}_{il}}{dt} = \frac{1}{b} \left\{ Z_i^{\ell} D_i C_i - Z_v^{\ell} D_v C_v + D_v C_v^e \exp\left(- \frac{[\gamma_{sf} + F_{el}(\bar{R}_{il})]}{kT} b^2 \right) \right\} \tag{6}$$

$$\frac{dN_{vl}}{dt} = \frac{\varepsilon P_d \Omega}{\pi \bar{R}_{vl}^2(0)\, b} \left\{ 1 - \left(\frac{V}{\Omega}\right) N_{vl} \right\} - \frac{N_{vl}}{\tau} \tag{7}$$

$$\frac{dQ_{vl}}{dt} = \varepsilon P_d + Z_v^{\ell} \rho_d^{vl} D_v C_v - Z_i^{\ell} \rho_d^{vl} D_i C_i$$

$$- \rho_d^{vl} D_v C_v^e \exp\left(\frac{[\gamma_{sf} + F_{el}(\bar{R}_{vl})]}{kT} b^2 \right) \tag{8}$$

$$\tau = \frac{-\bar{R}_{vl}(0)}{\left[\frac{d\bar{R}_{vl}}{dt}\right]_{\bar{R}_{v\ell}(0)}} \tag{9}$$

$$\frac{d\bar{R}_{vl}}{dt} = \frac{1}{b}\left\{ Z_v^{\ell} D_v C_v - Z_i^{\ell} D_i C_i - D_v C_v^{e} \exp\left(\frac{[\gamma_{sf} + F_{el}(\bar{R}_{vl})]}{kT}\right) b^2 \right\} \quad (10)$$

$$\bar{R}_{v\ell} = \left[\frac{Q_{v\ell}\Omega}{\pi b N_{v\ell}}\right]^{\frac{1}{2}} \quad (11)$$

TABLE 1

DEFINITION OF TERMS

Symbol	Definition	Units
V	Capture volume of a vacancy loop	cm^3
Z_v^{ℓ}	Interstitial/vacancy loop bias factor for vacancies	-
Z_i^{ℓ}	Interstitial/vacancy loop bias factor for interstitials	-
γ_{sf}	Stacking fault energy	eV/cm^2
ν	Poisson's ratio	-
$\nu_{i,v}$	Interstitial/vacancy vibrational frequency	s^{-1}
Ω	Atomic volume	cm^3
ρ_d^n	Network dislocation density	cm/cm^3
ρ_d^{il}	Line dislocation density, interstitial loop	cm/cm^3
ρ_d^{vl}	Line dislocation density, vacancy loop	cm/cm^3
α	Point defect recombination coefficient	s^{-1}
γ_{2i}	Di-interstitial dissociation rate	s^{-1}
ϵ	Fraction of vacancies produced directly in vacancy loops	-
τ^{vl}	Lifetime of an individual vacancy loop	s^{-1}
$\Delta\tau_{SR}$	Increase in the shear stress due to short range interaction	ksi
$\Delta\tau_{LR}$	Increase in the shear stress due to long range interaction	ksi
$\Delta\tau$	Total increase in shear stress	ksi
$\Delta\sigma$	Total increase in yield stress	ksi

Equations (1-11) were numerically solved using standard numerical methods for stiff ordinary differential equations.[5] These equations are obtained by simply describing the balance between processes for production and destruction using homogeneous rate theory, as described in References 6 and 7.

Self-interstitial atoms are considered to migrate betwnen trapping sites. Their diffusion coefficient is determined by an effective migration energy such that $E^m_{eff} = E^m_i + E^t_i$, where E^m_i is the migration energy and E^t_i is the trap binding energy. This was shown by Mansur [8] to be a reasonable approximation to describe trapping, providing the trapping is not particularly strong. The trap-hindered motion of self-interstitial results in agglomeration due to the increased formation of di-interstitials, as described in equation (2). Since di-interstitials can be destroyed by thermal dissociation or vacancy impingement,[7] the critical nucleus size for interstitial loops is therefore taken as three atoms. A time-dependent rate equation is therefore developed for the total number of interstitial loops by integrating the nucleation current for clusters that grow past the critical nucleus size. This current is described in equation (5). The size distribution of interstitial loops is approximated by an average radius $\overline{R}_{il}$ given in equation (6). The interstitial loop of average size grows by interstitial absorption and vacancy emission, and shrinks by vacancy absorption.

The description of formation and growth of vacancy loops is treated differently. Since vacancies diffuse too slowly at low temperature to allow agglomeration, the formation of vacancy loops must arise from collisional events and cascade collapse. The rate equation for vacancy loop concentration therefore represents a balance between direct production by irradiation and evaporation of loops both thermally or by irradiation. Moreover, as the density of cascades increases, an increasing fraction of crystal space will not be available for further production $\{1 - (V/\Omega)N_{v\ell}\}$ without overlap of cascades occurring. V is an effective loop volume for coalescence, R is the atomic volume and $N_{v\ell}$ is the fractional loop concentration. This is a mechanism by which loops can grow, not by diffusional processes, but due to collisional events. The vacancy loops are essentially unstable, however. Their lifetime, τ, is determined by the net flux of interstitials to them and their rate of vacancy emission. These processes tend to

reduce the lifetime of the loop, in complete contrast to the behavior of loops of interstitial character. When a vacancy loop is formed, it immediately acts as a net interstitial sink because of the dislocation character of its perimeter. Si-ahmed and Wolfer [9] proposed that both vacancy and interstitial loops can grow in coexistence if the non-linear elasticity effects on the strain field are factored into the bias calculations. In the present model, this is not a necessary condition, and simultaneous loop growth can proceed by cascade overlap for vacancy loops. For cascade collapse modeling, the coalescence volume is chosen to be a sphere with a radius that is three times the vacancy loop radius. Input parameters chosen to represent relatively pure copper are listed in Table 2.

5.3 Irradiation Hardening at Low Temperature

It is traditional to describe the effects of irradiation hardening with models that acount for the interactions of various defects which act as barriers resisting the motion of dislocations. The resistance forces have been classified as either long-range (LR) or short-range (SR). The long-range forces are due to the repulsive interaction between moving dislocations and the dislocation network. The long-range interaction of the stress fields of dislocation loops is significant when the loops are large. In this study, loops were considered large when their average radius exceeds ~ 25 Å.

Short-range forces arise from the interaction between moving dislocations and small defects lying in the slip plane. Such defects impose pinning forces on the moving dislocations at points of contact. Solution hardening by solute atoms functions in this manner. Since the temperature of interest for this study is low, the small defects which contribute to solution hardening are only those abundant in this temperature range. We therefore include single vacancies, single interstitials, di- and tri-interstitials and small vacancy and interstitial disks.

The total increase in the shear stress, $\Delta\tau$, due to irradiation is given by:

$$\Delta\tau = \Delta\tau_{SR} + \Delta\tau_{LR} \, . \tag{12}$$

TABLE 2

MATERIAL PARAMETERS FOR COPPER

Parameter	Definition	Numerical Value	Reference
	FIXED PARAMETERS		
E_i^m	Migration energy of single interstitial	0.12 eV	(28)
E_v^m	Migration energy of single vacancy	0.72 eV	(29)
E_{2i}^B	Binding energy of di-interstitials	1.19 eV	(30)
$R_{v1}(0)$	Radius of the newly born vacancy loop	15 Å	(6)
	ASSUMED PARAMETERS		
ε	Fraction of vacancies produced directly in vacancy loops	10%	
E_i^t	Trap binding energy	0.28	
Z_i^ℓ	Loop bias factor for interstitials	1.02	
Z_i^n	Network bias factor for interstitials	1.02	

Solution hardening by tetragonal distortions was first investigated by Fleischer.[10] He classified the hardening process as being either gradual or rapid. Gradual hardening was attributed to substitutional impurities, and is caused by an elastic mismatch between solute atoms and the alloy matrix. On the other hand, small atomic disks or single defects tend to cause a highly asymmetrical lattice distortion, which is deemed responsible for the rapid hardening observed under irradiation.

The maximum force per unit length on the moving dislocation is F^{max}/ℓ, where F^{max} is the maximum force exerted by the defect and ℓ is the inter-defect spacing. Hence, the increase in shear stress, τ, to move the pinned dislocation is

$$\tau = \frac{F^{max}}{b} , \tag{13}$$

where b is the slip vector of the dislocation, and I. is defined by

$$I. = (dN)^{-1/2} , \tag{14}$$

where d is the defect diameter and N is its volumetric concentration.

In the case of a tetragonal distortion, the maximum force is calculated using a method suggested by Cochardt, et al.[11] By calculating the interaction energy and maximuzing its derivative, the maximum force was shown to be

$$F^{max} = G\Delta\varepsilon b^4/\alpha y_{min}^2 , \tag{15}$$

where y_{min} is the distance of the closest defect to the slip plane, and α is a numerical factor for the different slip planes in a face-centered cubic lattice. $\Delta\varepsilon$ is a measure of the strain due to tetragonality distortion, and has been assigned a value of 0.55 for an interstitial atom, 0.08 for a divacancy and 1.00 for a vacancy or interstitial loop. It was also concluded by Westbrook[12] in an experimental study of the NiAl intermetallic compound, that single vacancies are more potent hardeners than are single self-interstitial atoms.

Assuming additive contributions to the increase in the shear stress, the total contribution for short-range interaction is

$$\Delta\tau_j = \frac{Gb}{\beta} \{\Sigma N_i d_i\}^{1/2} , \tag{16}$$

where the subscript j describes a particular defect, i refers to the size class of the same defect, and β is a numerical factor ranging from 1.0 to 4.0.[13-17] In this study, we adopt Fleischer's value for small loops of 6 = 3.7.[10]

Network dislocations contribute to long-range hardening[18] according to the expression

$$\Delta\tau = \alpha Gb \sqrt{\rho_d^n} , \tag{17}$$

where ρ_d^n is the network dislocation density. The coefficient α has been measured at values of 0.15 to 0.3.[18] This effort employs Johnson's value $\alpha = 0.2$,[19] which was confirmed recently.[4]

The elastic interaction between prismatic dislocation loops and network dislocations is only significant when the loops are large. Loops were considered large at an arbitrary radius of 25 Å. The interaction of the stress fields between dislocation loops and network dislocations has been investigated by Kroupa and Hirsch.[20] Using Friedel's estimate[21] of the average distance between interacting loops, Kroupa and Hirsch[20] show that

$$\Delta\tau_{LR} = \frac{GbdN^{2/3}}{\eta} \tag{18}$$

where η is a numerical factor ranging from 1.45 to 16.[20-23] Experimental results by Holmes[23] suggest a value of 1.45 for 316 stainless steel. Since the incremental increase in the shear stress caused by short-range barriers is proportional to $\langle\ell\rangle^{-1}$, where $\langle\ell\rangle$ is the average distance between obstacles, $\Delta\tau_{SR}$ can be described by

$$\Delta\tau_{SR} \sim \{\Sigma(n_j d_n)\}^{1/2} \tag{19}$$

where the sum is over defect type **j**. The total short-range hardening must therefore be expressed as

$$\Delta\tau_{SR} = \{\Delta\tau_V^2 + \Delta\tau_I^2 + \Delta\tau_{2I}^2 + \Delta\tau_{3I}^2 + \Delta\tau_{VI}^2 + \Delta\tau_{IL}^2\}^{1/2} . \tag{20}$$

According to the Von Mises criterion, the relation between the incremental changes in shear and yields stresses is

$$\Delta\tau_Y = \sqrt{3}\,\Delta\tau . \tag{21}$$

Hence, the irradiated tensile strength, σ_i, is expressed by

$$\sigma_i = \sigma_0 + \Delta\sigma_Y \tag{22}$$

where σ_0 is the unirradiated yield strength.

During the early stages of irradiation, both vacancy and interstitial loops are known to be small and function as short-range barriers. The yield strength at low fluence for well-annealed material is therefore

$$\sigma_i = \sigma_o + \frac{1}{2} Gb \{(Nd)_{vl} + (Nd)_{IL} + (Nd)_v\}^{1/2} \tag{23}$$

At higher fluences, the interstitial loop density tends to saturate while the loops continue to grow. Therefore,

$$\sigma_{\cdot} = \sigma \quad + 1.2\ Gb\ (N$$

$$\frac{1}{2} Gb \{(Nd)_{vl} + (Nd)_v\}^{1/2} \quad \text{for } d_{IL} > 50\ \text{Å} \ . \tag{24}$$

5.4 Results and Discussion

Recent room temperature irradiations of copper and other metals in RTNS-II are aimed at identifying the nature of displacement damage produced by 14-MeV neutrons.[2,24] In such experiments, the accumulated displacement dose is correlated with changes in mechanical properties. Both microhardness [2] and tensile tests [24] have been employed in these studies. In this section, the model developed in the previous section is applied to copper irradiated in RTNS-II at room temperature. Values chosen for relevant model parameters are listed in Table 2. The aim of the analysis in this section is to

(1) identify the major components of damage as well as the fuence dependence of their size and density;

(2) account for the observed hardening by each individual damage component; and

(3) extrapolation of existing data to higher fluences.

The calculated concentrations of single vacancies, single interstitials, vacancy loops and interstitial loops are shown as functions of the accumulated neutron fluence in Figure 2. Concentrations of di- and tri-interstitial clusters are not shown in this figure because of their low values. Single defect concentrations are seen to reach quasi-steady-state by about 10^{16} n/cm^2. Beyond

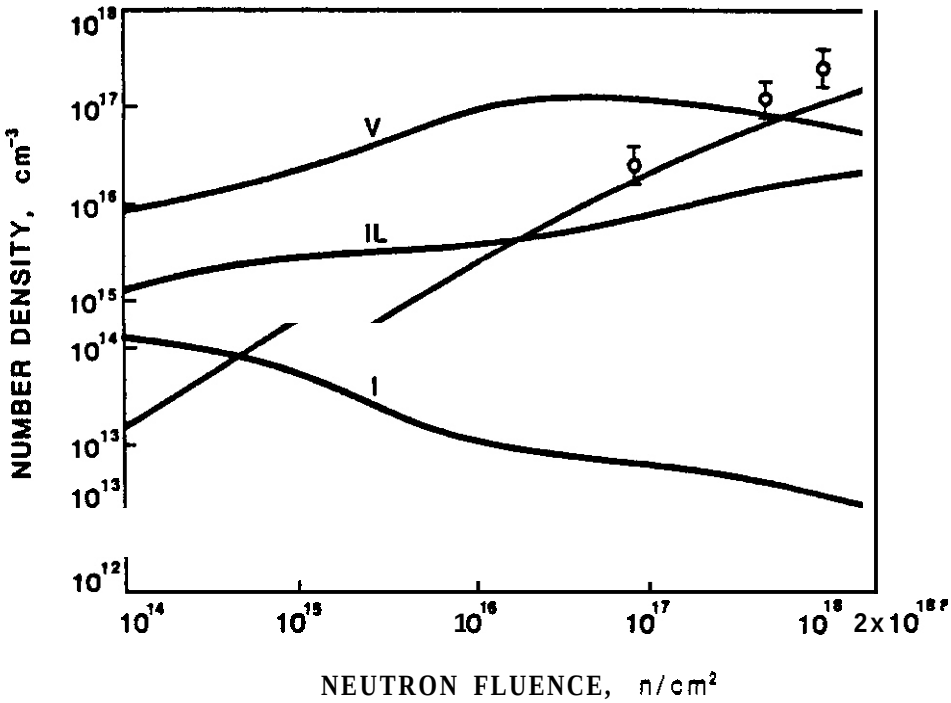

FIGURE 2. Calculated Concentrations of Major Irradiation-Induced Defects Which Contribute to Hardening of Copper Irradiated in RTNS-II at 25°C. Data shown are from Reference 2.

this fluence, their concentrations slowly decline due to the concomitant increase in density of larger sinks for these defects. It is interesting to note that there are essentially two time scales for the buildup of defect concentrations. The first one is associated with single defects until they reach quasi-steady-state values ($\sim 10^{16}$ n/cm^2), and the second is for the development of loop microstructure ($\sim 10^{18}$-10^{19} n/cm^2).

The average radius of a vacancy loop that forms during a cascade collapse event stays roughly constant up to $\sim 5 \times 10^{17}$ n/cm^2, and then starts to decrease due to absorption of interstitial atoms. All vacancy loops are assumed to be produced at an average radius of 15 Å. At a given time, there is a mixture of freshly produced loops and older ones. Due to the absorption of excess interstitials, the average size is reduced as irradiation proceeds. At higher fluences ($>10^{19}$ n/cm^2) significant cascade overlap commences, and vacancy loops start growing again.

On the other hand, interstitial loops grow continuously by diffusion of point defects and their average radius is a monotonically increasing function of neutron fluence. This behavior is shown in Figure 3.

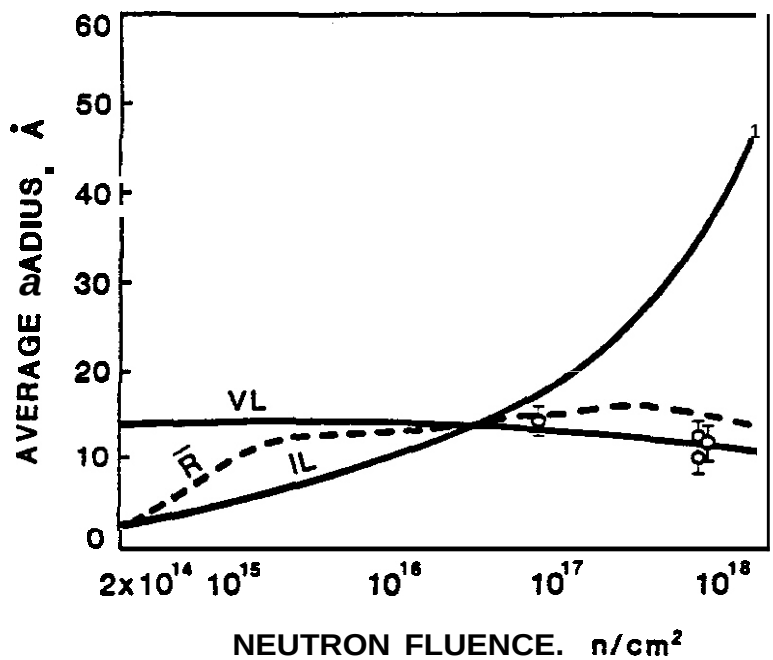

FIGURE 3. Calculated Fluence Dependence of Average Radius for Vacancy and Interstitial Loops in Copper Irradiated in RTNS-II at 25°C. The radius for the combined population is also shown in comparison with measurements. (2)

Various experimental observations have been made regarding the distribution of irradiation-produced clusters of vacancies and interstitials in copper.[2,25-27] Roughly equal numbers of vacancies and interstitials in their respective clusters were reported by Brager, et al.,[2] and by Larson and coworkers.[25] However, other investigators reported a range of twice as many vacancies as interstitials to less than half as many vacancies as interstitials in loops.[26-27] While the differences may arise from resolution problems in the microscope, the present model predicts a partitioning of point defects into loops that is fluence and

temperature dependent. Therefore, these experimental observations may not be inconsistent. In order to study the distribution of produced point defects, we define the following:

$$f_1 = \text{fraction of defects in clusters}$$

$$= \frac{\text{number of clustered defects}}{\text{irradiation dose}}$$

$$= \frac{N_{v\ell}\pi R_{v\ell}^2\ b + N_{i\ell}\pi R_{i\ell}^2\ b}{\text{dpa}} \tag{25}$$

$$f_2 = \text{interstitial fraction of defects in clusters}$$

$$= \frac{\text{number of interstitial atoms in clusters}}{\text{total number of defects in clusters}}$$

$$= \frac{N_{i\ell}.R_{i\ell}^2}{(N_{v\ell}.R_{v\ell}^2 + N_{i\ell}.R_{i\ell}^2)} \tag{26}$$

$$f_3 = \text{fraction of loops of vacancy character}$$

$$= \frac{N_{v\ell}}{N_{i\ell} + N_{v\ell}} \tag{27}$$

Figure 4 shows the behavior of the fractions f_1, f_2 and f_3 as a function of irradiation fluence. It is seen that the fraction of defects in clusters decreases from 28% at 10^{15} n/cm^2 down to only 10% by a fluence of 10^{18} n/cm^2. This is reasonably consistent with the observation of Brager and coworkers [2] that at least 9.4% of the defects survive at fluence in the mid-10^{17} n/cm^2 range. Within the clustered point defects, there are more interstititals in clusters than vacancies, however. The fraction f_2 is around 60% in the same fluence range. At low fluence, the sink for interstitial atoms has not been completely created, and therefore interstititals continue to form new clusters rather than only annihilate at sinks or with other vacancies. Equilibrium

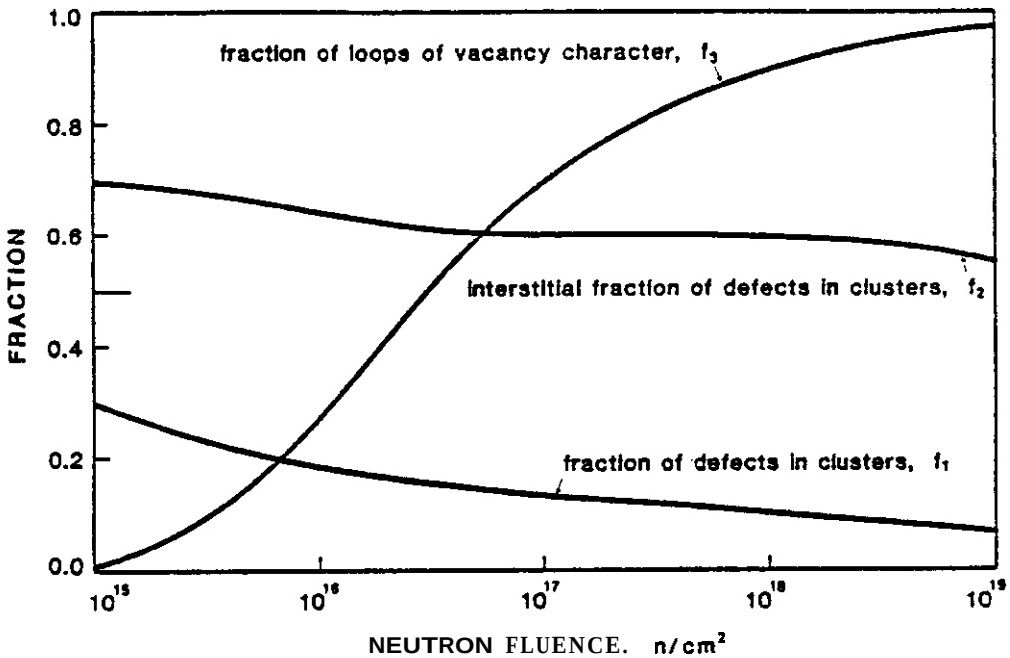

FIGURE 4. Fluence Dependence of Various Fractions Describing Distribution of Defects.

sink conditions are established beyond a fluence of 10^{19} n/cm^2, and the fraction of interstitials in clusters approaches 50%. The relative number of vacancy loops to total loops, f_3, is also shown in Figure 4. The fraction of loops of vacancy character increases throughout the irradiation. At higher fluences, the majority of the loops are composed of vacancies. Since these loops are smaller on the average than interstitial loops, a larger fraction of them will be invisible in the microscope.

The predicted contributions to the increase in the 0.2% offset yield stress are shown as a function of fluence in Figure 5. The contribution of single vacancies has been omitted from the figure because the hardness measurements were made almost a year after irradiation.[2] With a vacancy mean lifetime of only a few thousand seconds, it is unlikely that vacancies in supersaturation will contribute to hardening.

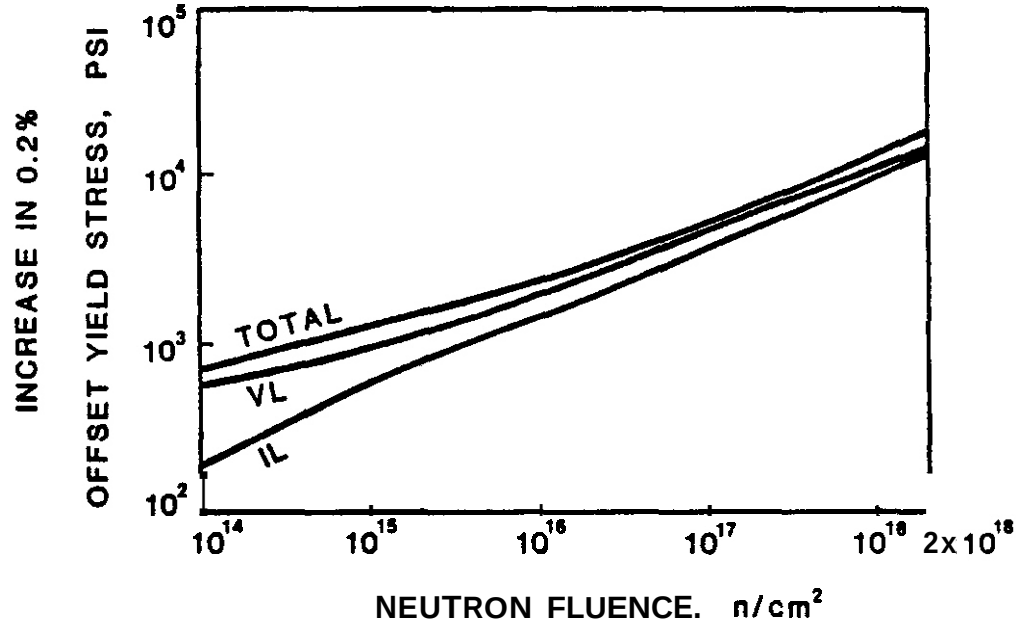

FIGURE 5. Calculated Major Contributions to the Increase in 0.2% Offset Yield Stress of Copper at 25°C in RTNS-II.

Since interstitial atoms cluster by diffusion, atomic-size traps are expected to influence their ability to cluster. Figure 6 shows the effects of various levels of self-interstitial trapping on the increase in the yield stress. A trapping energy of 0.28 eV produces results that are consistent with the experimental observations of Brager and coworkers.[2] Figure 7 shows a comparison between the hardening calculations and Brager's experimental results for relatively pure copper at 25°C after RTNS-II irradiation.

At low fluence ($\lesssim 10^{16}$ n/cm^2), irradiation hardening is primarily due to very small interstitial loops. The increase in the yield stress is small and increases at a very slow rate up to $\sim 2 \times 10^{16}$ n/cm^2. Hardening at this early stage is due to the rapid formation of interstitial loops with a slow growth rate. Beyond $\sim 2 \times 10^{16}$ n/cm^2, vacancy loops accumulate to a significant level, and begin to account for the majority of hardening by short-range interactions.

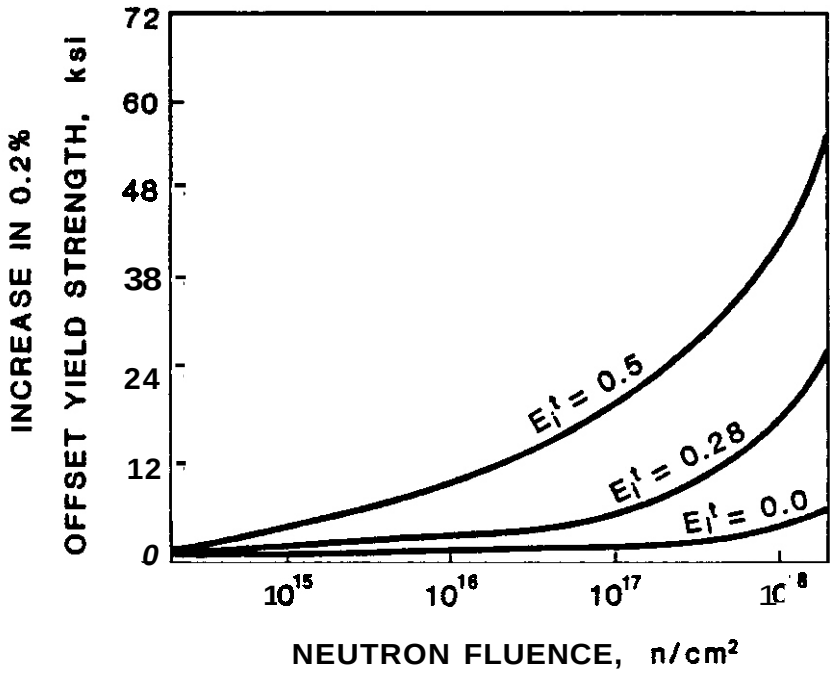

FIGURE 6. Effects of Self-Interstitial Trapping on the Predicted Increase of Yield Stress of Copper Irradiated at 25°C. E_i^m = 0.117 eV.

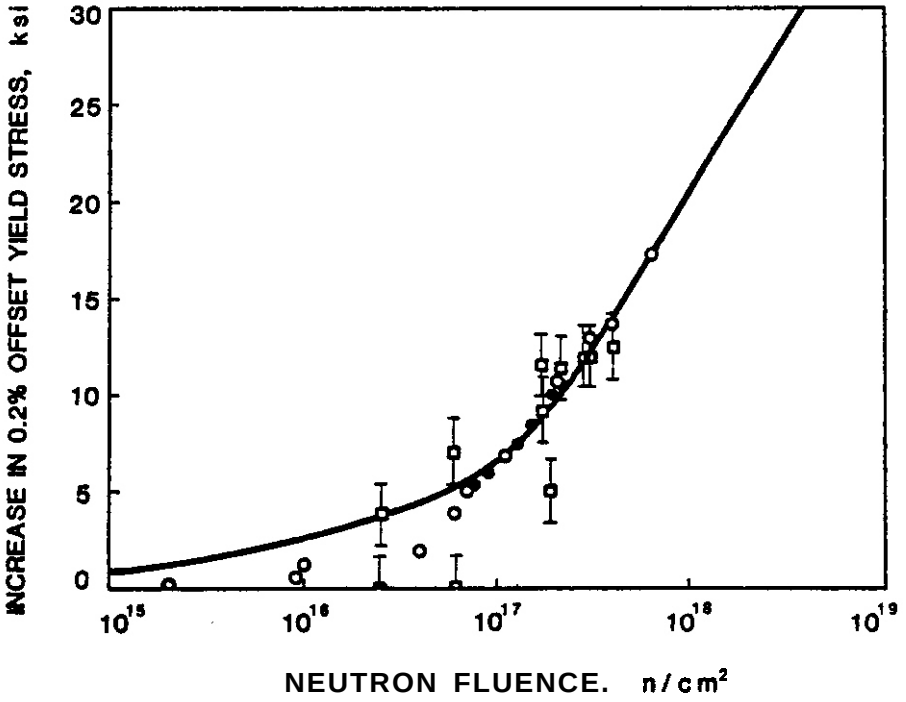

FIGURE 7. A Comparison Between Theoretical Calculations and Experimental Measurements of Copper Hardening Due to RTNS-II Irradiation at 25°C. Solid circles = LLL Cu.(24) Open circles = Cominco Cu.(24) Squares = OAFS copper.(2)

Since the average vacancy loop diameter does not drastically change with fluence, the change in yield strength or hardening will increase as $\sim N^{\frac{1}{2}}$, or $\Delta\sigma_Y \sim (\phi t)^{\frac{1}{2}}$. This is in agreement with the results shown in Figure 1. However, for high fluences ($\gtrsim 10^{21}$ n/cm^2) saturation will begin to set in due to overlap of cascades.

5.5 Conclusions

The following conclusions can be drawn from this study on irradiation of copper at 25°C in RTNS-II.

(1) Nucleation and growth of loops occur simultaneously throughout irradiation.

(2) Below a fluence of approximately 2 x 10^{16} n/cm^2, the density of vacancy loops is lower than the density of interstitial loops, while the average radii show the opposite trend.

(3) During irradiation, the interstitial fraction of total defects in clusters is always larger than the vacancy fraction. The remainder of vacancies exist as single vacancies.

(4) The fraction of total defects produced that survive in clusters decreases with fluence. Calculations of this fraction agree with measured values in the range where data are available.

(5) Increased interstitial atom trapping leads to an earlier acceleration of irradiation hardening.

(6) The measured hardening of copper can be related to the radiation-induced microstructural alterations observed by microscopy. Model-based predictions of those microstructural alterations can be employed in extrapolation of the data and to understanding of the fundamental processes involved.

6.0 References

1. N. M. Ghoniem and R. W. Conn, "Assessment of Ferritic Steels for Steady-State Fusion Reactors," Proceedings of International Atomic Energy Agency Technical Meeting on Fusion Reactor Design, Tokyo, Japan, October 1981.

2. H. R. Brager, F. A. Garner and N. F. Panayotou, J. Nucl. Mater., 103 and 104 (1981) 995.

3. G. R. Odette and D. Frey, J. Nucl. Mater., 85 and 86 (1979) 817.

4. F. A. Garner, M. L. Hamilton, N. F. Panayotou and G. O. Johnson, J. Nucl. Mater., 103 and 104 (1981) 803.

5. A. C. Hindmarch, Lawrence Livermore National Laboratory Report, UCID-3001, Revision 3 (1974).

6. R. Bullough, B. Eyre and R. Krishan, Proc. R. Soc., London, A-346 (1975) 81.

7. N. M. Ghoniem and O. D. Cho, Phys. Stat. Sol., (a), 54 (1979) 171.

8. L. K. Mansur, Acta. Met., 29 (1981) 375.

9. A. Si-Ahmed and W. G. Wolfer, "Of the Simultaneous Formation of Interstitial and Vacancy-Type Loops During Irradiation," Proc. International Conference on Dislocation Modeling of Physical Systems, Pergamon Press, 1981, p. 142.

10. R. L. Fleischer, Acta. Met., 10 (1962) 835.

11. A. W. Cochardt, G. Schoeck and H. Wiedersich, Acta. Met., 3 (1955) 533.

12. J. H. Westbrook, Editor, "Properties of Intermetallic Compounds," Symposium Proceedings for the 15th Meeting of the Electrochemical Society, Philadelphia, PA, May 3-7, 1959, p. 28.

13. K. H. Westmacott, Phil. Mag., 11 (1966) 239.

14. A. J. E. Forman, Phil. Mag., 17 (1968) 353.

15. A. L. Bement, Jr., Proceedings 2nd International Conference on the Strength of Metals and Alloys, ASM (1970) 693-728.

16. P. Coulomb, Acta. Met., 10 (1962) 835.

17. E. Orowan, "Internal Stresses in Metals and Alloys," Institution of Metallurgists, London, (1948) 451.

18. J. D. Embury, Strengthening Methods in Crystals, A. Kelly and R. B. Nicholson, Eds., J. Wiley and Sons, New York (1971), Chapter 6.

19. G. D. Johnson, F. A. Garner, H. R. Brager and R. L. Fish, "A Microstructural Interpretation of the Fluence and Temperature Dependence of the Mechanical Properties of Irradiated AISI 316," Effects of Radiation on Materials: Tenth Conference, ASTM STP 725, D. Kramer, H. R. Brager and J. S. Perrin, Eds., American Society for Testing and Materials, 1981, pp. 393-412.

20. F. Kroupa and P. B. Hirsch, "Dislocations in Solids," Faraday Society, p. 49.

21. J. Friedel, "Dislocations," Addision-Wesley (1964) 219-273.

22. H. Shiotani, H. Kimura, R. Hasiguti and R. Maddin, Acta. Met., 15 (1967) 287.

23. J. J. Holmes, R. E. Robbins, J. L. Brimhall and B. Mastel, Acta. Met., 16 (1968) 955.

24. J. B. Mitchell, "Exploratory Experiments Comparing Damage Effects of High-Energy Neutrons and Fission-Reactor Neutrons in Metals," Lawrence Livermore National Laboratory Report, UCRL-52388, January 1976.

25. B. C. Larson, J. F. Barhorst and T. S. Noggle, "Low-Temperature Damage in Metals," Oak Ridge National Laboratory Report, ORNL-5640, Septebmer 1980.

26. M. Ruhle, F. Häussermann and M. Rapp, Phys. Stat. Sol., 39 (1970) 609.

27. J. Narayan and S. M. Ohr, J. Nucl. Mater., 85 and 86 (1979) 515.

28. J. W. Corbett, R. B. Smith and R. M. Walker, Phys. Rev., 114 (1959) 1452.

29. R. W. Balluffi, J. Nucl. Mater., 69 and 70, (1978) 240.

30. R. Johnson, Phys. Rev., 152 (1966) 629.

7.0 Future Work

This effort will continue, concentrating first on a revision of hardening coefficients based on the results of this study and then proceeding into the modeling of irradiation creep.

8.0 Publications

This report will be published in the proceedings of the Eleventh ASTM International Symposium on Effects of Radiation on Materials, Scottsdale, AZ, June 27-29, 1982.

9.0 Acknowledgements

The authors would like to thank Sandia Laboratories and the United States Department of Energy, Division of Inertial Confinement Fusion for their support of this work through Contract DOE28-0270 with UCLA and Contract DOE-AC06-FF02170 with Westinghouse Hanford Company.

A MODEL FOR THE EVOLUTION OF NETWORK DISLOCATION DENSITY IN IRRADIATED METALS

F. A. Garner (Hanford Engineering Development Laboratory) and W. G. Wolfer (University of Wisconsin)

1.0 Objective

The object of this effort is to provide models for the radiation-induced microstructural evolution of metals and thus provide framework on which to develop fission-fusion correlations.

2.0 Summary

It is well known that the total dislocation density that evolves in irradiated metals is a strong function of irradiation temperature. The dislocation density comprises two components, however, and only one of these (Frank loops) retains its temperature dependence at high fluence. The network dislocation density approaches a saturation level which is relatively insensitive to starting microstructure, stress, irradiation temperature, displacement rate and helium level. The latter statement is supported in this paper by a review of published microstructural data. It is shown that the influence of surface proximity can obscure the independence of temperature and displacement rate however.

A model has been developed to explain the insensitivity to many variables of the saturation network dislocation density. This model does not assume random motion of dislocations by climb and glide but takes into account the correlated nature of dislocation components in a dense array. The model also explains how the rate of approach to saturation can be sensitive to displacement rate and temperature while the saturation level itself is not very dependent on these variables. It is predicted that the insensitivity of the saturation level to temperature will persist until thermal emission of vacancies from network dislocations becomes important. At higher displacement rates typical of charged particle simulation

experiments, the temperature at which thermally-induced climb of dislocations becomes important is increased as both the point defect and microstructural densities undergo an upward shift with displacement rate.

3.0 Program

Title: Irradiation Effects Analysis (AKJ)
Principal Investigator: D. G. Doran
Affiliation: Hanford Engineering Development Laboratory

4.0 Relevant DAFS Program Plan Task/Subtask

II.C.17 Microstructural Characterization

5.0 Accomplishments and Status

5.1 Introduction

When metals are irradiated at elevated temperatures with fast neutrons or charged particles to large damage levels, a substantial restructuring of their microstructure occurs. One facet of this evolution is the development of a dislocation microstructure composed of network dislocations and various types of dislocation loops. Although it is well known that the total dislocation line length is often a strong function of temperature, it now appears that in bulk material only the Frank loop component retains its temperature dependence at high fluence. It also appears that the network component of the dislocation microstructure approaches a saturation level which is remarkably insensitive to the starting microstructure and to many material and environmental variables.

The temperature independence of the saturation level can be obscured in charged particle irradiations where the influence of the surface is large. This report examines the available data to assess the validity of the concept of saturation density. A model is then developed to explain this behavior.

It was shown earlier that in AISI 316 all microstructural components (voids, loops, network dislocations, precipitates) approach saturation levels during irradiation.[1-3] With the exception of network dislocations, all are known to be sensitive to temperature, stress and displacement rate. Helium and other gases are known to affect the density of voids and sometimes the early evolution of Frank loops. The orientation of the latter is also quite sensitive to the magnitude and spatial orientation of the stress state.[4-8]

Since the radiation-induced dislocation loops are the major source of radiation-induced network line length, it may appear surprising at first that the parametric sensitivities of dislocation loops are not expressed in their progeny. Examination of loop behavior during irradiation will provide the insight needed to explain this apparent anomaly.

5.2 Evolution of Dislocation Loop Microstructure

To this point we have addressed dislocation loops in general terms only. There is a variety of loops which may form, but the major contributors are Frank loops composed of platelets of interstitial atoms lying parallel to the close-packed planes of the crystalline matrix. Frank loops composed of vacancies have been observed to form simultaneously with interstitial loops but usually occur only in well-annealed materials at low fluence and prior to the extensive formation of network dislocations.[1] Si-Ahmed and Wolfer have explained this observation in terms of the relative point defect capture efficiencies of both types of Frank loops and that of network dislocations.[9]

Although Frank interstitial loops can unfault and the resultant loops rotate to other orientations, it is the sessile nature of the Frank loop that limits the rate of evolution of the dislocation microstructure. While other dislocation components can glide as well as climb, the Frank loop can only extend its boundaries and increase its line length by net absorption of interstitial atoms.

It is also important to note that while the loops are the primary source of new line length, the size distribution and density of Frank loops is controlled just

as strongly by the density and mobility of the network dislocations. This has been demonstrated in several studies that show that the size distribution of loops is controlled not only by their growth rate but also by the probability that the loops will unfault upon intersection with other dislocation components.[5,8]

When loops grow in the relatively open spaces of annealed material, they tend to overshoot the saturation level characteristic of the temperature and displacement rate as shown in Figure 1. Once the loops start to intersect, however, the "oversized" loop distribution is rapidly reduced in both mean size and density, approaching the same level imposed on loops which evolve in dense networks of dislocations.[10] This overshoot and saturation process can be observed directly in high voltage electron irradiations. A typical example of such experiments is that of Fisher and coworkers on pure copper.[11]

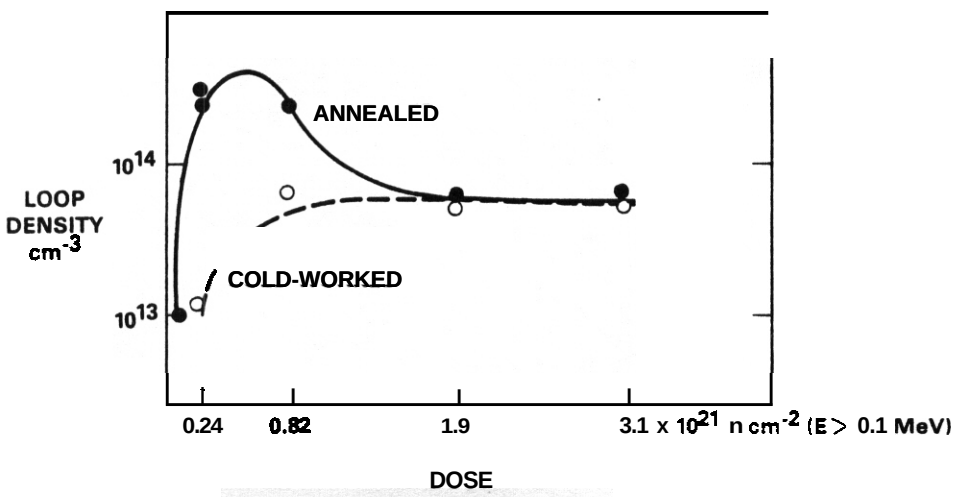

FIGURE 1. Dependence of Dislocation Loop Density on Starting Condition and Fluence in Aluminum Irradiated in the Siloe Reactor at 55°C, as Reported by Risbet and Levy.[10]

The eventual independence of loop number density and mean size on starting cold-work level and fluence have also been demonstrated in AISI 316 by Brager and coworkers[1,5] and is shown in Figures 2 and 3. The strong temperature dependence of the loop density is primarily responsible for the strong temperature dependence of total dislocation density shown in Figure 4.

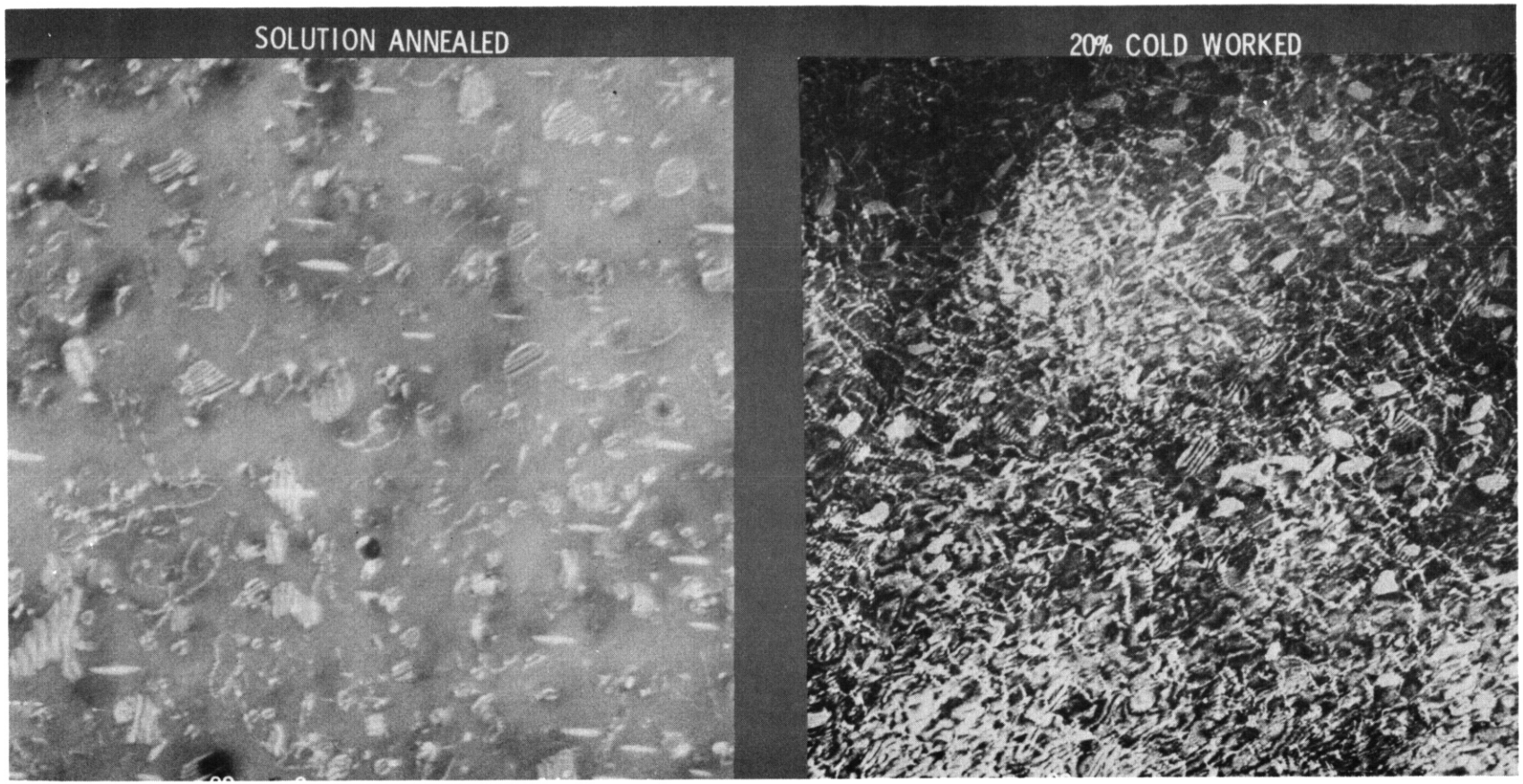

FIGURE 7 Micrographs Showing Dislocation and Loop Microstructures Induced in AISI 316.[5] The annealed specimen contains many Frank loops at 2.0×10^{22} n/cm^2 (E >0.1 MeV), with mean size of 372 Å and density 10.2×10^{14} cm^3. The 20% cold-worked specimen at 3.0×10^{22} n/cm^2 contains a similar density of loops, 11.4×10^{14} cm^{-3} with mean size of 424 Å.

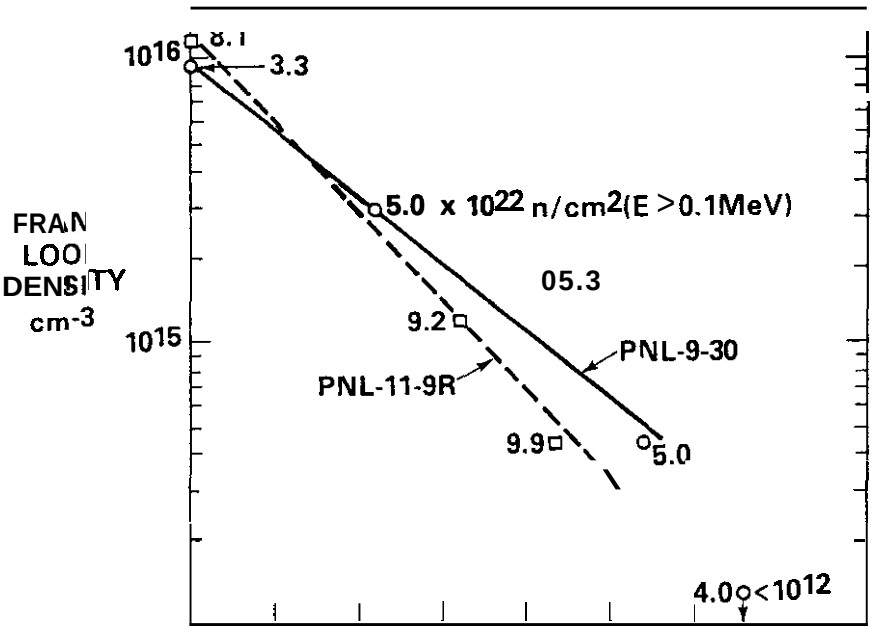

FIGURE 3. Frank Loop Densities Observed in 20% Cold-Worked AISI 316 Fuel Pin Cladding Irradiated in EBR-II. (5) Note that the loop density does not change appreciably with increasing fluence.

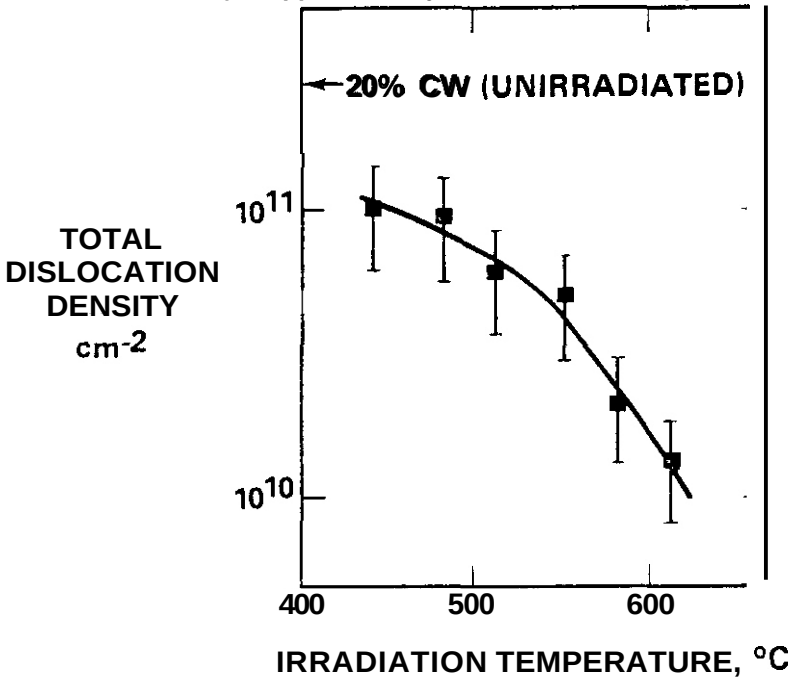

FIGURE 4. Total Dislocation Density Observed in 20% CW M316 Fuel Pin Cladding Designated V1294, as Reported by Bramman and Coworkers. (28) The preirradiation density is also shown.

In effect, the existence of a saturation density of network dislocations leads to a constant intersection probability of Frank loops and a constant rate of production of new line length. Before proceeding then it is necessary to convince ourselves that the network saturation density is indeed relatively insensitive to the pertinent variables in both bulk and surface-affected volumes.

5.3 Influence of Surface Proximity

It is important to recognize that the saturation dislocation density that evolves will be the result of competing processes of production and loss of line length. In bulk material this process will be unaffected by the loss to specimen surfaces that is characteristic of charged particle irradiations, particularly in relatively soft materials and for ions of shallow penetration. Igata and coworkers [12] have provided a simple depth-independent expression which describes the contribution of surface losses to reduction of the saturation density. They state that the change of dislocation density, ρ, as a function of irradiation time, t, can be expressed as

$$\frac{d\rho}{dt} = S_o - \alpha\rho - \beta\rho^2 \qquad (1)$$

where

ρ = dislocation density,

S_o = dislocation production rate due to radiation,

α = coefficient. for rate of dislocation density change due to slip to surface or cross slip due to local internal stress, and

β = coefficient for rate of decrease of dislocation density due to mutual interaction, arising mainly from cross slip or climb motion under irradiation.

At the steady state, the saturation dislocatio density ρ_s can be expressed as

$$\rho_s = \frac{-\alpha + \sqrt{\alpha^2 + 4\beta S_o}}{2\beta} \qquad (2)$$

This expression shows that surface losses will reduce ρ_s whenever $\beta S_o > 0$. These losses will be slightly dependent on temperature since the friction stresses experienced by network dislocations are temperature-dependent, thereby increasing the influence of surface image forces. The Frank loops also increase in size with temperature, increasing their probability of intersecting the surface. The proximity of the surface will also tend to reduce S_o in a strongly temperature-dependent manner as point defects are lost to the surface. These three factors will tend to cause the saturation density at high temperatures to fall below the level generated in bulk material.

Despite these losses the dislocation density that evolves in structural metals during ion or electron irradiation experiments is frequently in the same limited range of densities observed in neutron irradiation (10^{10} - 10^{11} cm^3).

5.4 Review of Network Dislocation Density Data

Figure 5 shows that the dislocation density of both 20% cold-worked and solution annealed AISI 316 converged at a density of 6 ±3 x 10^{10} cm^{-2} at 500°C when irradiated in EBR-II in the absence of stress.[1,5] Figure 6 shows that stressed fuel pin cladding saturated in this density range for temperatures between 375 and 555°C.[1] A similar insensitivity of network dislocation density to starting condition, stress and temperature has been observed in United Kingdom irradiations[13] of M316 (Figure 7) and AISI 316L in the French reactor program[14] (Figure 8).

Hudson has shown (Figure 9) that during irradiation at high displacement rates and far from specimen surfaces the dislocation density saturated at a level just below 10^{11} cm^2 which was relatively insensitive to irradiation temperature and ion identity.[15] Azam and coworkers (Figure 10) demonstrated that even in low energy ion experiments conducted very near foil surfaces that the saturation dislocation density in AISI 316L was approximately 3 x 10^{10} cm^{-2} at 600°C, independent of starting condition and helium content.[14] Similar results have been obtained in low energy ion irradiation of titanium-modified 316 SS.[16]

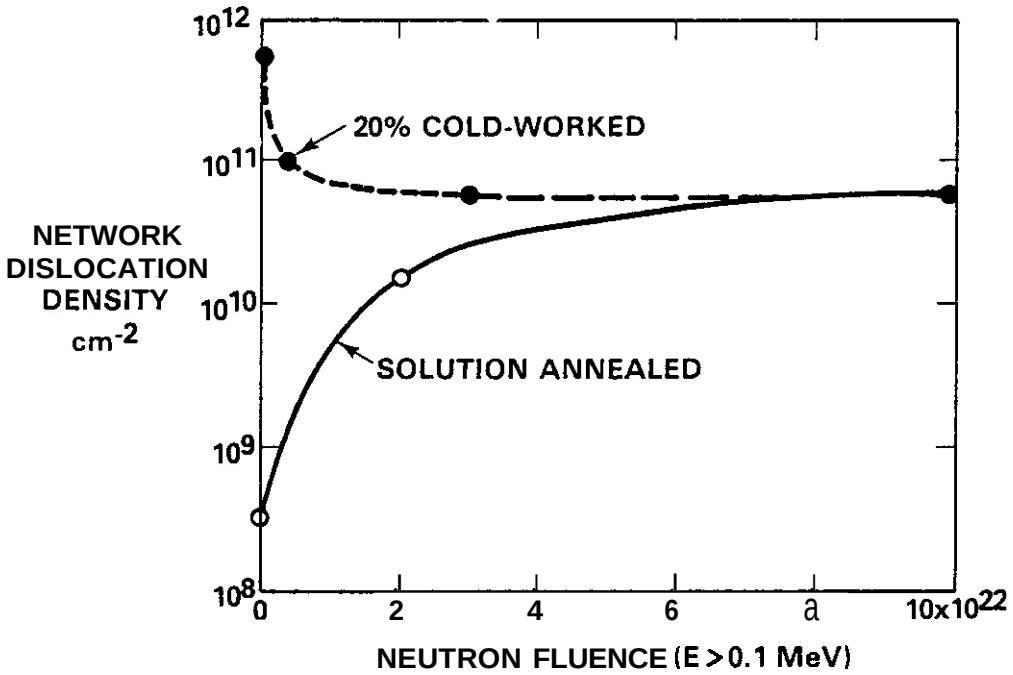

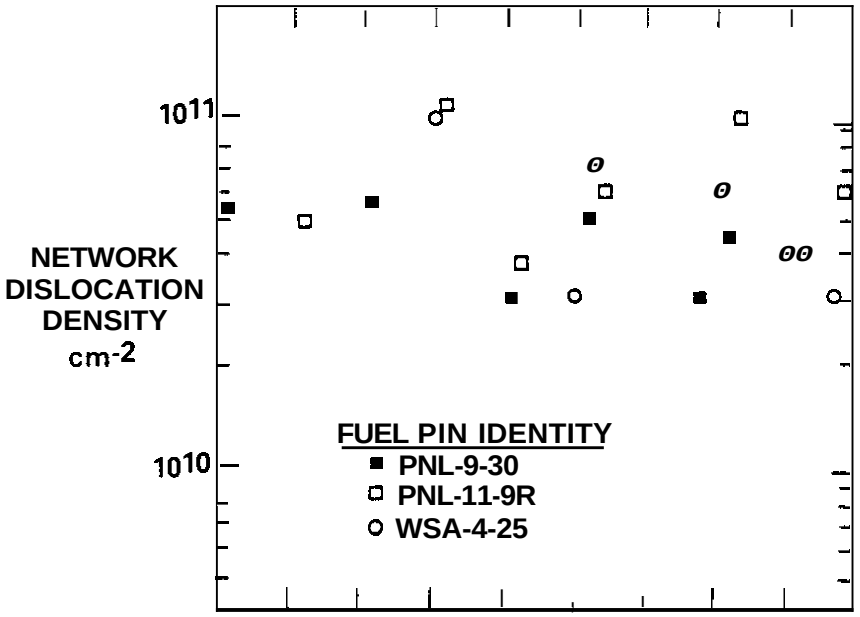

FIGURE 6. Network Dislocation Density Measured in Three 20% CW AISI 316 Fuel Pin Cladding at Doses Ranging from 20 to 50 dpa in EBR-II. (1)

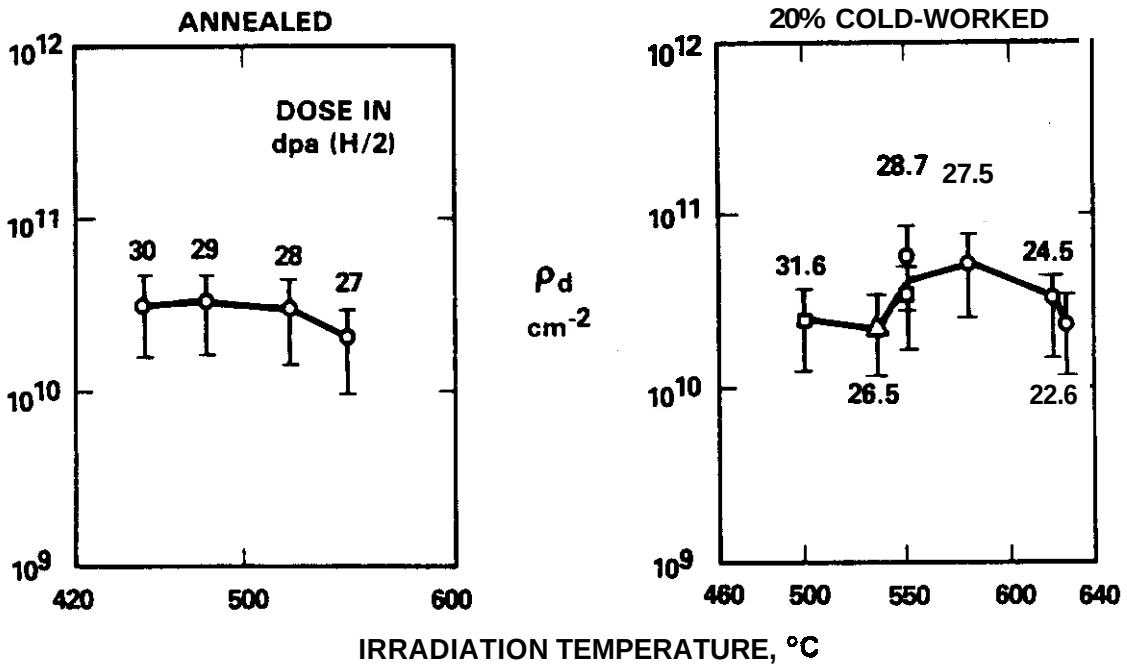

FIGURE 7. Independence of Dislocation Density on Temperature and Starting Condition in M316 Fuel Pin Cladding Irradiated in the Dounreay Fast Reactor as Reported by Brown and Linekar.(13) The numbers beside each data point are the exposure levels in Half-Nelson dpa.

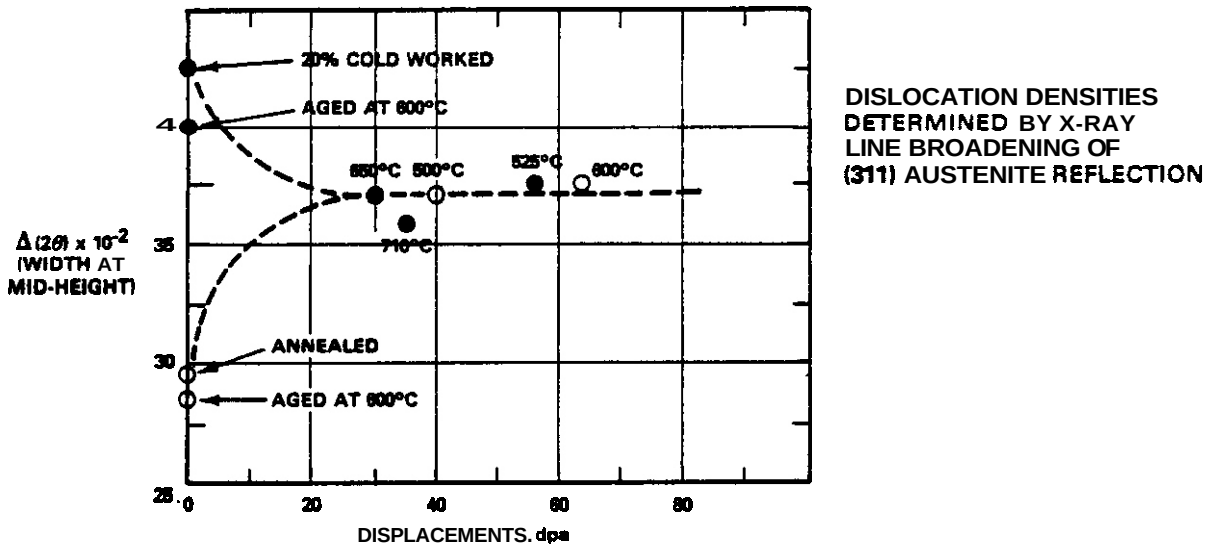

FIGURE 8. Independence of Dislocation Density in AISI 316 on Starting Condition, Temperature and Displacement Level After Irradiation in the Rapsodie Fast Reactor as Reported by Azam, Delaplace and Le Naour.(14) The Δ(2θ) measurement arises from X-ray line broadening measurments on bulk material.

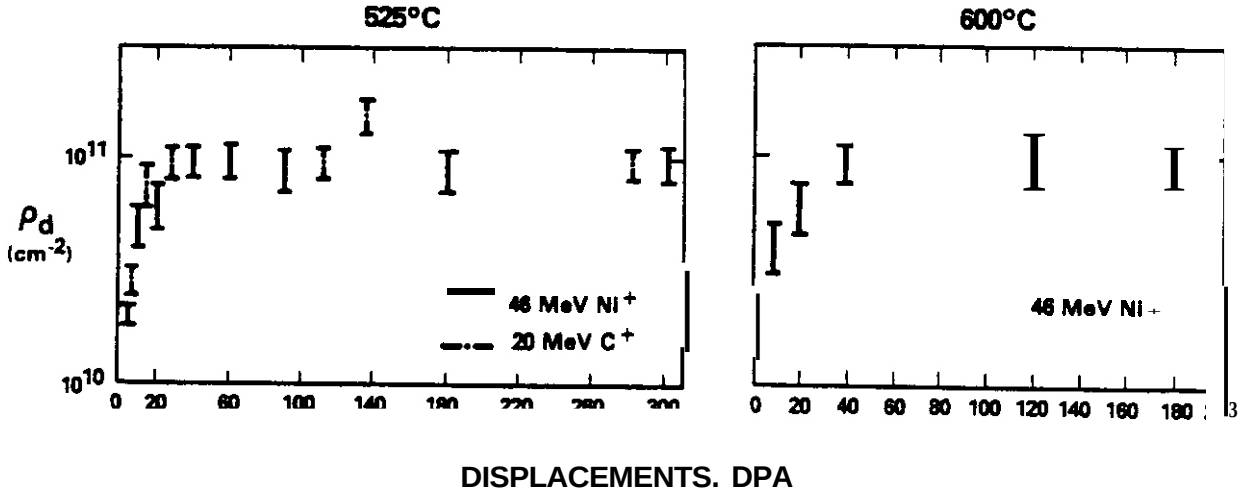

FIGURE 9. Saturation of Dislocation Density at High Displacement Rates in Annealed AISI 315 at 525°C and Annealed 321 at 600°C for Two Deeply Penetrating Ions as Reported by Hudson.(15)

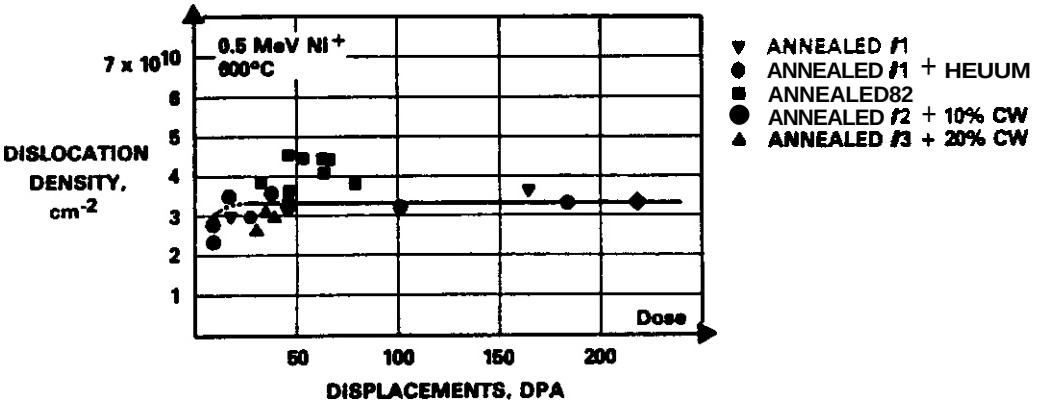

FIGURE 10. Saturation of Dislocation Density at 600°C in Shallow Penetration Ion Bombardment Experiments, Showing Independence of Starting Condition, Heat Identity and Helium Content. Reproduced from Azam, La Naour and Delaplace.(14)

Azam and coworkers also showed that the saturation dislocation density in their surface-affected experiments increased weakly with incrasing displacement rate at 600°C. This represents a reduction in the surface influence as S_0 in Equation 1 increases and the size of Frank loops decreases. They also demonstrated a weak dependence of saturation density on irradiation temperature in these shallow penetration experiments, reflecting the temperature sensitivity of the coefficient *a* in Equation 1. The sensitivity of the saturation level to both temperature and displacement rate is shown in Figure 11.

Several groups of researchers have also shown that during dual ion irradiation various alloys develop saturation densities which are relatively insensitive to the helium/dpa ratio and to the mode and schedule of helium injection.[17-20] An example of this behavior for a soft alloy without solute is shown in Figure 12. The low saturation level of $\sim 2 \times 10^{10}$ cm^{-2} reflects the soft nature of the alloy and the proximity of the surface.

5.5 A Model for the Evolution of Network Dislocation Density in Irradiated Metals

It has been shown that the saturation network dislocation density that evolves at high fluence in irradiated bulk metals is remarkably insensitive to temperature, displacement rate, stress, helium content or starting microstructure. The major features of this evolution are shown in Figure 13 and can be described as being the result of the competitive action of two primary mechanisms in a material where there are no additional losses of dislocation line length to surfaces or substantial losses to grain boundaries. These two primary mechanisms are (a) generation of line length by loop growth and interaction with other components of the network and (b) recovery processes involving annihilation of line length.

5.6 Description of Recovery Processes

Both thermally activated and radiation-induced climb of edge dislocation leads to encounters of dislocations, some of which result in annihilation of line

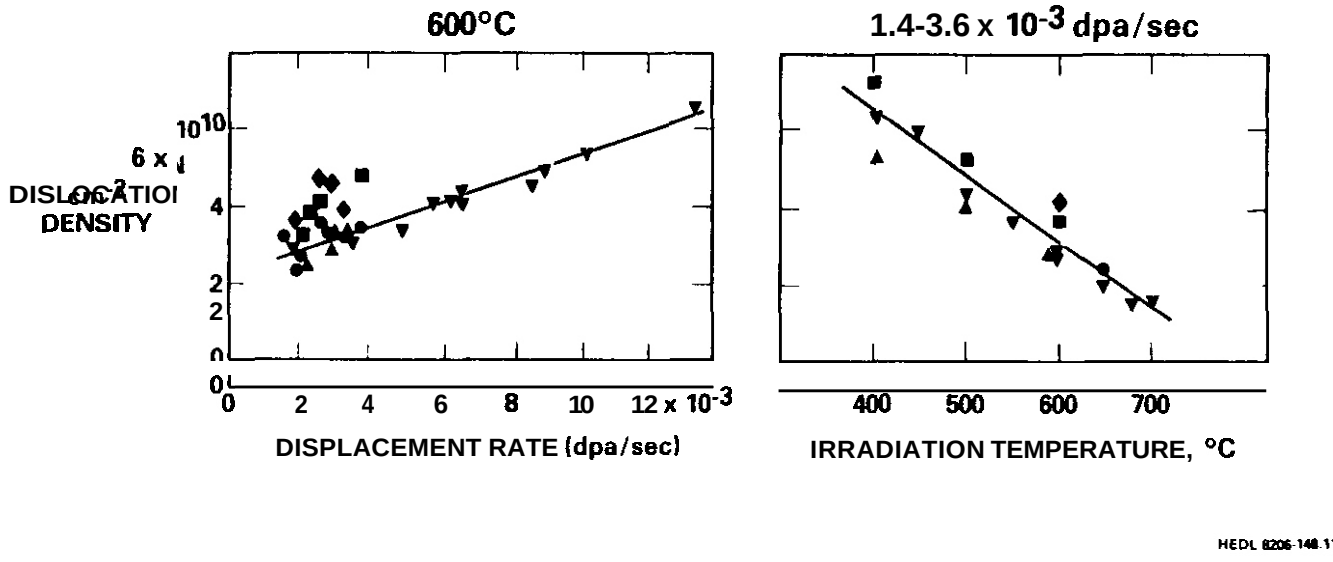

FIGURE 11. Dependence of Saturation Dislocation Density on Surface Influence, as Demonstrated by Dependence of Dislocation Density on Temperature and Displacement Rate.(14) All symbols are defined in Figure 10.

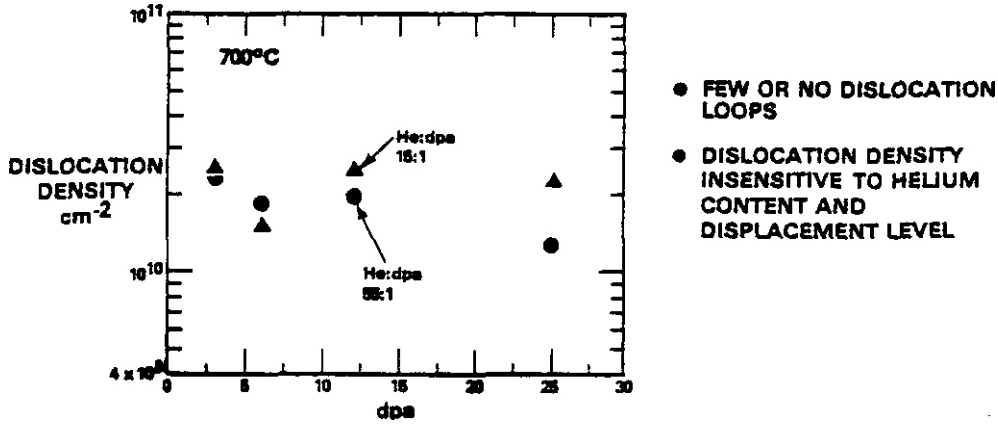

FIGURE 12. Dislocation Saturation Level is Independent of Helium Content in Dual Ion Irradiations of Fe-20Ni-15Cr at 700°C as Reported by Agarwal and Coworkers.(19) According to Agarwal, preinjected specimens (15 appm, not shown) attained the same dislocation density.

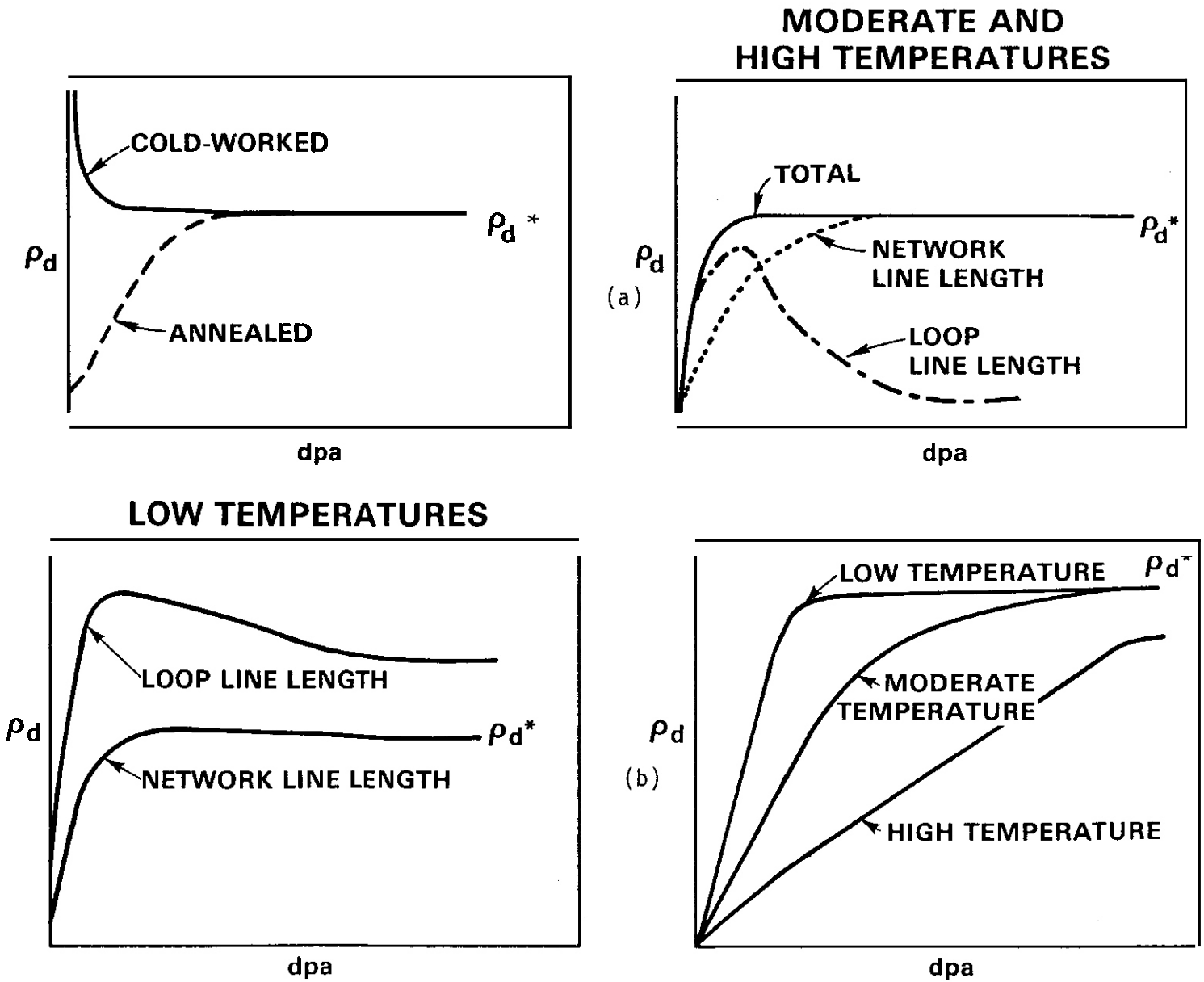

FIGURE 13. Schematic Representation of Dislocation Network Evolution in Metals Without Surface Influence.

length and recovery. The rate of annihilation of the network dislocation density ρ is commonly assumed to be proportional to ρ^2 in recovery models for thermal creep. The same assumption is expressed in Equation 1. The ρ^2 dependence is based on the simple argument that the chance encounter of two edge dislocations with opposite Burgers vectors on the same glide plane is proportional to ρ^2. This assumption is only appropriate when the motion of edge dislocations by climb and glide is completely random.

On the other hand, in the absence of large creep deformations, the motions of adjacent edge dislocations are actually correlated during radiation-induced recovery. Consider, for example, the simple model of an edge dislocation structure shown in Figure 14a. Numerous edge dislocations can be paired up into dislocation dipoles, **i.e.,** closest pairs of parallel edge dislocations with opposite Burgers vectors on parallel glide planes. As a result of radiation-induced climb, a pair may either increase or decrease the distance $h(t)$ between the parallel glide planes. When $h(t)$ increases, the members of the pair become partners in other dipole configurations until eventually they pair up in such a way that the corresponding values of the glide plane separation $h(t)$ decrease with time. As a result, the members of approaching pairs eventually interact primarily with each other, and the orientation of the dipole tends to remain at an angle of 45" (the minimum energy configuration) to the glide plane as $h(t)$ decreases further. Subsequent motion by climb and glide is then completely correlated.

This argument can be made more general by stating that the configuration of continuously climbing dislocations is determined by their mutual interaction, and that the network will always adjust by glide to minimize the total elastic interaction energy of the network. Again, glide and climb motions are correlated.

In order to arrive at the rate of annihilation of network dislocations consider the dislocation array shown in Figure 14a. The number of adjacent dislocations able to form dipoles is obviously $\rho/2$. On the average the time required for the two dislocations to climb to a common glide plane is equal to $\tau = h_0/2V$,

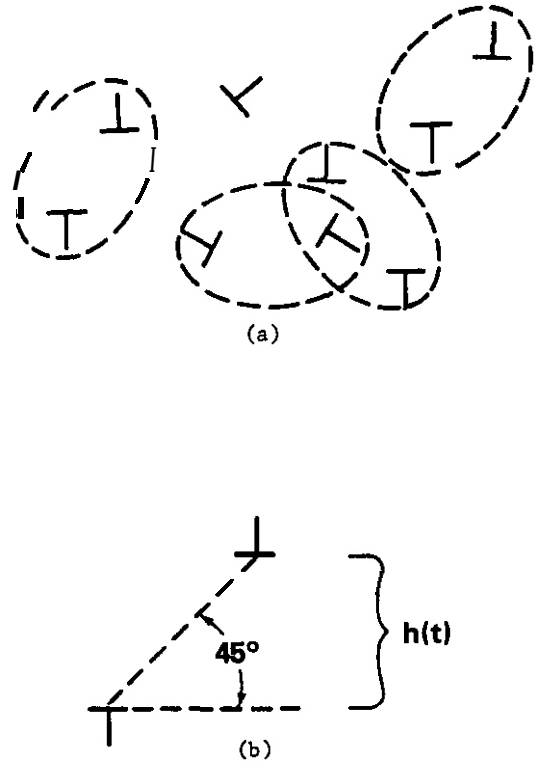

FIGURE 14. Schematic Representation of Correlated Movement of Dislocation Pairs (dipoles).

where h_0 is the initial dipole separation distance and V the dislocations climb velocity. Consequently, the rate of annihilation is $(\rho/2)/\tau$ or $\rho V/h_0$. On the average, we may assume that $\pi h_0^2 = 1/\rho$, so that the annihilation rate is equal to $\sqrt{\pi}\, V \rho^{3/2}$.

5.7 Description of Generation Processes

The generation of network dislocations by the formation, growth, coalescence and unfaulting of Frank loops is a complicated process. However, several facts can be utilized to simplify matters for this derivation.

First, detailed computer solutions by many authors,[21-25] have shown that formation of an interstitial loop occurs very quickly, requiring only a few seconds of irradiation. Furthermore, both coalescence and unfaulting of loops are relatively fast processes in comparison to that of loop growth. As a result, the generation of network dislocations occurs at a rate dictated by the lifetime τ_ℓ of an interstitial loop, defined as the period from its formation to its coalescence with other components of the network. If R(t) is the radius of a loop, its growth rate can be calculated by differentiating the expression describing the growth rate of loop area and is given by

$$dR/dt = b^2[Z_i^\ell D_i C_i - Z_v^\ell D_v C_v + Z_v^\ell D_v C_{vo}^\ell] \quad , \tag{3}$$

where b is the Burgers vector, Z_i^ℓ and Z_v^ℓ the loop bias factors, D_i and D_v the diffusion coefficients, and C_i and C_v the concentrations for interstitials and vacancies, respectively. C_{vo}^ℓ is the vacancy concentration in thermodynamic equilibrium with the loop.

If Equation 3 is written in the abbreviated fashion

$$\frac{dR}{dt} = b^2 \Phi \quad , \tag{4}$$

then Φ is a function which depends on displacement rate, stress, temperature and the total sink density according to conventional rate theory. After the first generation of loops has been formed, it is no longer dependent on the individual loop radii. Hence Equation 4 can be integrated to obtain the loop lifetime as

$$\tau_\ell = \overline{R_{max}}/b^2 \Phi \quad , \tag{5}$$

where $\overline{R_{max}}$ is the average maximum loop radius in a quasi-stationary population.

Brager, Garner and Guthrie [5] have shown that $\overline{R_{max}}$ is proportional to $\rho^{-\frac{1}{2}}$ in well-developed microstructures at high fluence. Therefore, the generation rate of dislocations is proportional to $1/\tau_\ell$ or $b^2\Phi\rho^{\frac{1}{2}}$.

5.8 The Evolution of Network Dislocation Density

Assuming no other losses the rate of change of dislocation density is

$$\frac{d\rho}{dt} = B\rho^{\frac{1}{2}} - A\,\rho^{3/2}\ , \tag{6}$$

where

$$B \sim b^2\Phi$$

and

$$A \sim V = b^2[Z_i^d\, D_i\, C_i - Z_v^d\, D_v\, C_v + Z_c^d\, D_v\, C_{vo}^d] + V_{th}\ . \tag{7}$$

Apart from the different bias factors for edge dislocations, Z_i^d and Z_v^d, and the different thermal vacancy concentration C_{vo}^d in equilibrium with the edge dislocation, the radiation-induced contribution to the climb velocity V is very similar to the average loop growth rate $b^2\Phi$.

In fact, the loop bias factors as well as C_v^ℓ differ from the corresponding values for edge dislocations only for small loop radii (less than 50 Å).[7] Therefore, B is essentially proportional to the loop growth rate in Equation 4. Note that in a saturation network the size distribution of loops is invariant,[7-8] and thus the ratios Z_i^ℓ/Z_i^d and Z_v^ℓ/Z_v^d are also invariant.

The second term in this equation, V_{th}, represents the thermally induced climb rate which determines the rate of recovery in the absence of radiation. Since thermal recovery is significant only at temperatures above 650°C for typical fast reactor irradiation, it can be neglected at lower irradiation temperatures.

At higher displacement rates the temperature at which V_{th} becomes important tends to increase as the microstructural densities undergo an upward shift in temperature.

Therefore, there is some relatively high temperature (dependent on displacement rate) below which the ratio B/A becomes a constant independent of the various sink densities. The strong temperature dependence of both A and B cancels, yielding a temperature-independent value of B/A. The saturation dislocation density, defined by $d\rho/dt = 0$ is

$$\rho_S = B/A \ . \tag{8}$$

This means that below the temperature where V_{th} is important the saturation density is not only independent of temperature and the details of the temperature-dependent microstructure but also independent of the starting microstructure. Since stress also makes no substantial changes in terms of Equations 3 and 7 at temperatures where V_{th} is unimportant, this means that the saturation density should also be essentially independent of stress. This independence also explains why ion bombardment experiments reach the same saturation range as do unstressed neutron irradiation experiments. The differential swelling inherent in ion irradiations leads to large levels of stress in the irradiated region of the foil.[26-27] It has been shown however that the application of stress to irradiated metals speeds up the early evolution toward the saturation state.[1,5,7]

The solution to Equation 6 is given by

$$\rho(t)/\rho_s = \frac{1 - e^{-x} + \sqrt{\rho_o/\rho_s}\,(1 + e^{-x})}{1 + e^{-x} + \sqrt{\rho_o/\rho_s}\,(1 - e^{-x})} \ , \tag{9}$$

where ρ_o is the initial dislocation density and

$$x = A\sqrt{\rho_s}\ t$$

$$= \sqrt{\pi\rho_s}\ V t \tag{10}$$

Since A and V are dependent on temperature, the approach to the saturation level ρ_s is also dependent on temperature.

Using a saturation dislocation density of 6×10^{10} cm^{-2},[1] an initial dislocation density of 4×10^{8} cm^{-2} for annealed 316 and 7×10^{11} cm^{-2} for 20% CW 316, the fluence-dependent dislocation densities according to Equation 9 are shown in Figure 15. The relationship between fluence and the variable x was chosen such that the dislocation density for annealed 316 reaches the value of 2×10^{10} cm^{-2} at 2×10^{22} n/cm^2, as reported for AISI 316 irradiated in EBR-II at 500°C.[7] This fluence value corresponds to x = 1.2, so that

$$x = \frac{0.6\ \phi t}{10^{22}} \tag{11}$$

where the fluence is given in units of n/cm^2 (E >0.1 MeV).

The dislocation climb velocity V was also computed according to rate theory for a displacement rate of 1.0×10^{-6} dpa/s. The results are shown in Figure 16. At low temperature, recombination of point defects results in a reduced climb velocity. Since the dislocation bias decreases slightly with temperature, the climb velocity also decreases at high temperatures.

It is seen from Figure 16 that the climb velocity is proportional to the bias difference between dislocations in different configurations. Dislocation climb occurs even in the absence of voids as a result of these bias differences. Assuming that 1% difference in bias is a typical value, it is possible to compute independently according to Equation 10 the relationship between the fluence and the variable x. At 500°C, the climb velocity is computed to be V = 1.0 Å/dpa, or for a displacement rate of 1.0×10^{-6} dpa/s, V = 10^{-12} cm/s. Hence

$$x = \sqrt{\pi \rho_s}\ Vt = \sqrt{\pi \rho_s}\ \frac{V}{\phi}\ \phi t$$

$$= 1.74 \times 10^{-22}\ \phi t \tag{12}$$

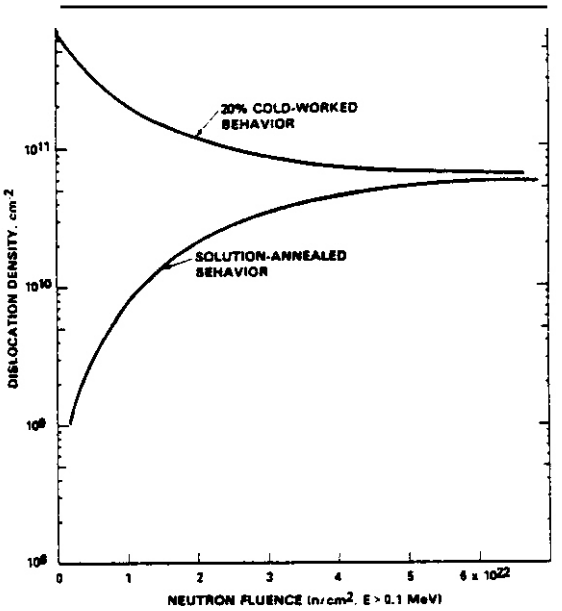

FIGURE 15. Predictions of the Evolution of Dislocation Density in AISI 316 at 500°C for Starting Densities of 7 x 10^{11} cm/cm^3 and 4 x 10^8 cm/cm^3, Chosen to Represent Cold-Worked and Annealed Conditions.

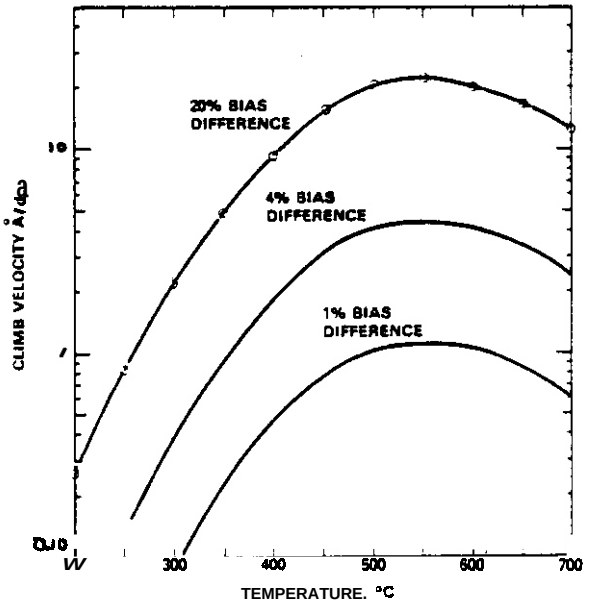

FIGURE 16. Calculation of Dislocation Climb Velocity V for Several Values of Bias Difference Between Dislocations in Different Configurations. The displacement rate was assumed to be 10^{-6} dpa/sec.

assuming a neutron flux of 2.5 x 10^{15} n/cm^{2}s. The numerical factors in Equations 11 and 12 are equal within 10%.

5.9 Conclusions

It appears that it is possible to explain how the rate of approach to the saturation density of network dislocations is dependent on temperature but the eventual saturation level is not. The model developed to explain this apparent contradiction also predicts an independence of saturation level on starting microstructure, stress and displacement rate below temperatures where thermal emission of vacancies from dislocations becomes an important factor in their climb rate.

6.0 References

1. H. R. Brager, F. A. Garner, E. R. Gilbert, J. E. Flinn and W. G. Wolfer, "Stress Affected Microstructural Development and the Creep-Swelling Relationship," in Radiation Effects in Breeder Reactor Structural Materials, M. L. Bleiberg and J. W. Bennett, Eds., The Metallurgical Society of AIME, 1977, p. 727.

2. G. D. Johnson, F. A. Garner, H. R. Brager and R. L. Fish, "A Microstructural Interpretation of the Fluence and Temperature Dependence of the Mechanical Properties of Irradiated AISI 316," Effects of Irradiation on Materials: Tenth Conference, ASTM STP 725, D. Kramer, H. R. Brager and J. S. Perrin, Eds., 1981, pp. 393-412.

3. F. A. Garner, M. L. Hamilton, N. F. Panayotou and G. D. Johnson, J. Nucl. Mater., 103 and 104 (1981) 803-808.

4. P. R. Okamoto and S. D. Harkness, J. Nucl. Mater., 48 (1973) 49.

5. H. R. Brager, F. A. Garner and G. L. Guthrie, J. Nucl. Mater., 66 (1977) 301.

6. F. A. Garner and W. G. Wolfer, Trans. Am. Nucl. Soc., (1978) 144.

7. F. A. Garner. W. G. Wolfer and H. R. Braqer, "A Reassessment of the Role of Stress in Development of Radiation Induced Microstructure," in Effects of Radiation on Structural Materials, ASTM STP 683, J. A. Sprague and D. Kramer, Eds., ASTM, 1979, pp. 160-183.

8. D. S. Gelles, F. A. Garner and H. R. Brager, "Frank Loop Formation in Irradiated Metals in Response to Applied and Internal Stresses," Effects of Radiation on Materials: Tenth Conference, ASTM STP 725, K. Kramer, H. R. Brager and J. S. Perrin, Eds., ASTM, 1981, pp. 735-753.

9. A. Si-Ahmed and W. G. Wolfer, "On the Simultaneous Formation of Interstitial and Vacancy Loops During Irradiation," in Dislocation Modeling of Physical Systems, M. F. Ashby, R. Bullough, C. S. Hartley and J. P. Hirth, Eds., Pergamon Press, 1980, p. 142.

10. A. Risbet and V. Levy, J. Nucl. Mater., 46 (1973) 341.

11. S. B. Fisher, R. J. White and K. M. Miller, Phil. Mag. A, 40 (1979) No. 2, p. 239.

12. N. Igata, A. Kohyama and S. Nomura, "Void Swelling in Molybdenum Alloys In-Situ Observed by a High Voltage Electron Microscope," in Ref. 2, p. 627.

13. C. Brown and G. Linekar, "Dislocation Densities in ST and 20% Cold-Worked Type 316 Pin Cladding Irradiated to 30 dpa in PFR," UKAEA TRG-Memo-6571, June 1974.

14. N. Azam, L. Le Naour and J. Delaplace, J. Nucl. Mater., 49 (1973/74) 197.

15. J. A. Hudson, J. Nucl. Mater., 60 (1976) 89.

16. H. Kawanishi, M. Yamada, K. Fukuya and S. Ishino, J. Nucl. Mater., 103 and 104 (1981) 1097.

17. N. H. Packan and K. Farrell, J. Nucl. Mater., 85 and 86 (1979) 677.

18. K. Farrell and N. H. Packan, ibid, p. 683.

19. S. C. Agarwal, G. Ayrault, D. I. Potter, A. Taylor and F. V. Nolfi, Jr., ibid, p. 653.

20. J. A. Spitznagel and A. P. L Turner, Proceedings of Damage Analysis and Fundamental Studies Information Meeting, October 2-3, 1981, p. 298.

21. M. R. Hayns, J. Nucl. Mater., 56 (1975) 267.

22. R. A. Johnson, J. Nucl. Mater., 75 (1978) 77.

23. N. M. Ghoniem and D. D. Cho, Phys. Stat. Sol. (A), 54 (1979) 171.

24. B. O. Hall, J. Nucl. Mater., 91 (1980) 63.

25. N. M. Ghoniem and S. Sharafat, J. Nucl. Mater., 92 (1980) 121.

26. F. A. Garner, G. L. Wire and E. R. Gilbert, in Proceedings of International Conference on Radiation Effects and Tritium Technology for Fusion Reactors, Gatlinburg, TN, 1975, CONF-750989, p. 474.

27. W. G. Wolfer and F. A. Garner, J. Nucl. Mater., 85 and 86 (1979) 583.

28. J. I. Bramman, C. Brown, J. S. Watkin, C. Cawthorne, E. J. Fulton, P. J. Barton and E. A. Little, "Void Swelling and Microstructural Changes in Fuel Pin Cladding and Unstressed Specimens Irradiated in DFR," in Ref. 1, pp. 479-507.

7.0 Future Work

This effort will continue, concentrating on the effect of stress on nucleating and unfaulting loops and the resulting anisotropy in the distribution of network Burgers vectors.

8.0 Publications

An abbreviated version of this report will be published in the Proceedings of the Eleventh ASTM International Symposium on Effects of Radiation on Materials, Scottsdale, AZ, June 27-29, 1982.

RELATIONSHIPS BETWEEN CRACK PROPAGATION AND TENSILE PROPERTIES IN TYPE 316 STAINLESS STEEL FOIL MICROSPECIMENS

R. D. Gerke and W. A. Jesser (University of Virginia)

1.0 Objective

The objective of this report is to relate tensile data to the manner in which the main crack propagates through microspecimens as tested in-situ in a high voltaqe electron microscope (HVEH).

2.0 Summary

It has been demonstrated that some tensile data obtained from 40-μm thick foil microspecimens are related to bulk tensile data. These tensile data are found to be related to the manner in which the main crack propagates through the thin (< 1-μm) regions of the specimen as determined by HVEM video recordings. Possible statements about specimen ductility may be made from this relationship.

3.0 Program

Title: Simulating the CTR Environment in the HVEM
Principal Investigators: W. A. Jesser and R. A. Johnson
Affiliation: University of Viroinia

4.0 Relevant DAFS Program Plan Task/Subtask

Task II.C.13 Effects of Helium and Displacements on Crack Initiation and Propagation

5.0 Accomplishments and Status

5.1 Introduction

Neutron irradiation is known to harden and embrittle structural materials in nuclear fission reactors. Its effect on the mechanical properties of first wall candidate materials for fusion reactors is also of much concern. To study this effect, there is currently much work being done on miniaturized tensile specimens, especially in reactor materials research[1]. This is primarily due to reduced cost of irradiation of the test materials and reduced radiation safety hazard in handling the smaller irradiated microspecimens. Problems arise during the testing of microspecimens in addition to the obvious difficulty in handling and mounting of the specimens prior to testing. Tensile property values in microtensile specimens have been shown to deviate from bulk tensile data. For example, the ultimate tensile strength (UTS) determined from wire type microtensile specimens has been found to be lower than UTS bulk data[2] while yield strength (YS) values of very thin stainless steel foils (down to 3.76 μm thick) have been shown to be greater than bulk YS values.[3] However, microhardness tests appear to be a useful technique for extracting mechanical properties from small specimens in high energy neutron irradiation experiments[4].

In-situ tensile testing of specimens inside a transmission electron microscope (TEM) requires miniature samples of materials. However, due to limited availability of load-elongation TEM straining devices, microstructural phenomena correlated with tensile properties of microspecimens is not widely pursued. It is the aim of this work to use a quantitative load-elongation heating tensile stage [previously described[5]] to perform in-situ tensile tests inside an HVEM in order to link measured tensile properties such as ultimate tensile strength (UTS), elongation (%) and reduction of area (ROA) of the microtensile foil specimens to accepted bulk values and then relate these properties to the manner in which the main crack propagates through the specimen. Possible quantitative measures of relative ductility between specimens may be established through this method.

5.2 Experimental Results and Discussion

5.2.1 Experimental Procedure

In this study all specimens, type 316 stainless steel, were punched from a 1.5-mil (∿ 40-μm) sheet producing rectangularly shaped ribbon specimens, 12.5 x 2.5 mm in dimensions. The specimens were annealed at 1000" C for one hour and then electro-thinned in the center, approximately 2 mm in diameter, leaving a "thick" (∿ 40-μm) portion on each side of the electropolished region. Details of the specimen geometry have been explained in a previous DAFS report(5). The microspecimens were tensile tested in an HVEM under three conditions: 1) unirradiated, tested at room temperature (4 specimens tested), 2) unirradiated, tested at 400" C (3 specimens tested), and 3) neutron irradiated at the LLL RTNS II facility (total fluence ∿ 1 x 10^{22} n/m^2) and tested at room temperature (1 specimen). "Macroscopic" (tensile data) and microscopic (HVEH observations of the main crack) information was obtained from each microspecimen. Tensile data from cold worked (as received) material are also included.

5.2.2 Comparison of Tensile Data From Microspecimens and Bulk Specimens

Quantitative load and elongation measurements have been taken from each specimen and the corresponding load-elongation curves have been previously published in a OAFS report(5). The data from the unirradiated specimens were found to be reproducible which suggests that the data from the one irradiated specimen (condition 3) is meaningful. Original cross-sectional area measurements, determined by edge-on SEM observations of post tensile tested specimens, have also been shown to be consistent between specimens, allowing calculation of tensile properties such as UTS and YS for the micro-tensile specimens. Final cross-sectional areas were also determined from the same SEM micrographs, which when combined with the original cross-sectional areas facilitated the calculation of reduction of area (ROA) of the microspecimen. An additional tensile parameter, elongation (total) to failure (%), was also calculated. To determine elongation, crosshead separation (corrected for machine deformation)

and a gage length for each specimen was needed. The gage lengths for several specimens were determined by optically observing the grain reorientations and slip lines present in the "thick" regions (located on each side of the electro-polish) of post tensile tested specimens. This reqion tended to be nearly constant from specimen to specimen and a value of 1.05 ± 0.07 mm was chosen as the effective gage length for all microspecimens tensile tested.

Comparisons made between tensile properties of the microspecimens and bulk specimens can characterize the effect of specimen geometry in the miniaturized specimens. Some pertinent tensile properties are shown in the Table 1 for bulk values found in the literature and for the HVEM foil microspecimens.

TABLE 1

Comparison of Some Tensile Properties of HVEM Foil and Bulk Specimens for AISI Type 316 Stainless Steel

Specimen Test Condition	# tested	UTS (MPa) Foil	UTS (MPa) Bulk[6]	YS (MPa) Foil	YS (MPa) Bulk'	Reduction of Area (%) Foil	Reduction of Area (%) Bulk[8]	Elongation (%) Foil	Elongation (%) Bulk[8]
R.T. Unirradiated†	4	220 ±20	580	97	260	49	72	23 ±1	52-60
400" C Unirradiated†	3	190 ±10	520	120	170	38	65	13 ±1	40-50
R.T. neutron Irradiated†	1	280	700**[9]	190	370[10]	34	55-65[10]	19	40-48[10]
R.T. cold worked	2	430	760-1030[9]	330	670-930[9]	--	--	28	8-22[9]
R.T. cold worked*	10	450 f40	760-1030[9]	360	670-930[9]	--	--	30 ±3	a-229

Note: Bulk values quoted for cold worked material are for 20-50%cold worked.
* Tensile tested on an Instron Tensile Machine ** estimated 'annealed

one dimension in contrast to bulk specimens where necking can occur in the second ROA dimension. A comparison of the ROA measurements for the HVEM specimens to bulk measurements is shown in Figure 2, which yields a linear relationship. This indicates that ROA for the foils can indeed be determined in the same manner as ROA for bulk specimens.

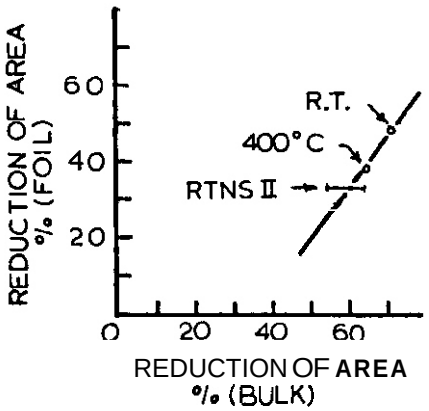

Figure 2: Graph Illustrating the Relationship between Reduction of Area for HVEM Micro-Tensile Specimens and Bulk Specimens.

Elonqation (%), an additional method useful in classifying specimen ductility, has been shown to differ between bulk specimens and the 40-μm thick microspecimens (see Table). The elongation of the HVEM foil specimens were found to be ∿ 40% less than the bulk specimens (13-23% compared to 40-60% for the three major specimen conditions). This difference possibly can be explained by: a) specimen thickness effect constraining necking to approximately one direction and b) flow localization effects accentuated by the thinness of the foil. The elongation for the room temperature unirradiated and RTNS II irradiated microspecimens agree with the trend of the bulk data; however, the 400" C unirradiated case shows an elongation lower than expected. This result may be due to a flow localization mechanism which is most likely more active at higher temperatures. The cold rolled specimens show elongations larger in the foils than in the bulk case. Consideration of the specimen test condition leads to the conclusion that the gage length chosen for the annealed specimens does not apply to the cold worked specimens or possibly that cold working of thin foils has little effect on the elongation that the foil experiences.

5.2.3 Correlations Between Crack Length and Total Elongation

Perhaps the most important microscopic-macroscopic relationship found to date using the quantitative tensile state is the cumulative crack tip displacement length, L, versus total elongation (total crosshead displacement) as plotted in Figure 3. Here a typical example of each specimen condition tensile tested is included. It should be noted that the electropolishing procedure removes approximately 50% of the original cross-sectional area, leaving a new cross-section comprised of 70-80% "thick area (≈ 40 μm) and the remainder a thinner electropolished area. All macroscopic tensile data (i.e. load and/or elongation) are obtained primarily from the 40 μm thick regions while the HVEM microscopic observations come from the small electropolished regions. The graphs in Figure 3 show that both parameters, L and elongation, always increase until the specimen fails (note: Figures 3a-c do not contain data to the point of specimen failure due to the unstable nature of the crack propagation immediately before failure). Also, the manner by which L varies with elongation is not smooth but contains regions where little or no crack propagation takes place even though elongation continues to increase. This step-like relationship to elongation has been observed before[12,13] without a quantitative in-situ tensile stage, but has more recently been shown graphically by using the quantitative load-elongation tensile stage.[11,14] Generally, cracks grow to a certain length and then stop for some time before continuing to propagate, even though the specimen is under a continuously increasing stress. The step-like behavior has been shown to be related to the crack tip behavior. Flat (little crack growth) regions of the graph correspond to slow crack growth with extensive crack tip blunting, while steeper regions correspond to more rapid growth with frequent direction changes and less blunting.[11,14]

The data shown in the L versus elongation plots in Figure 3, although all step-like in behavior, tend to exhibit different average slopes between the different specimen classes. By means of a linear regression on the data, quantitative comparisons of the slopes were made, as shown in Figure 4. The data from the four room temperature and three 400°C unirradiated specimens were

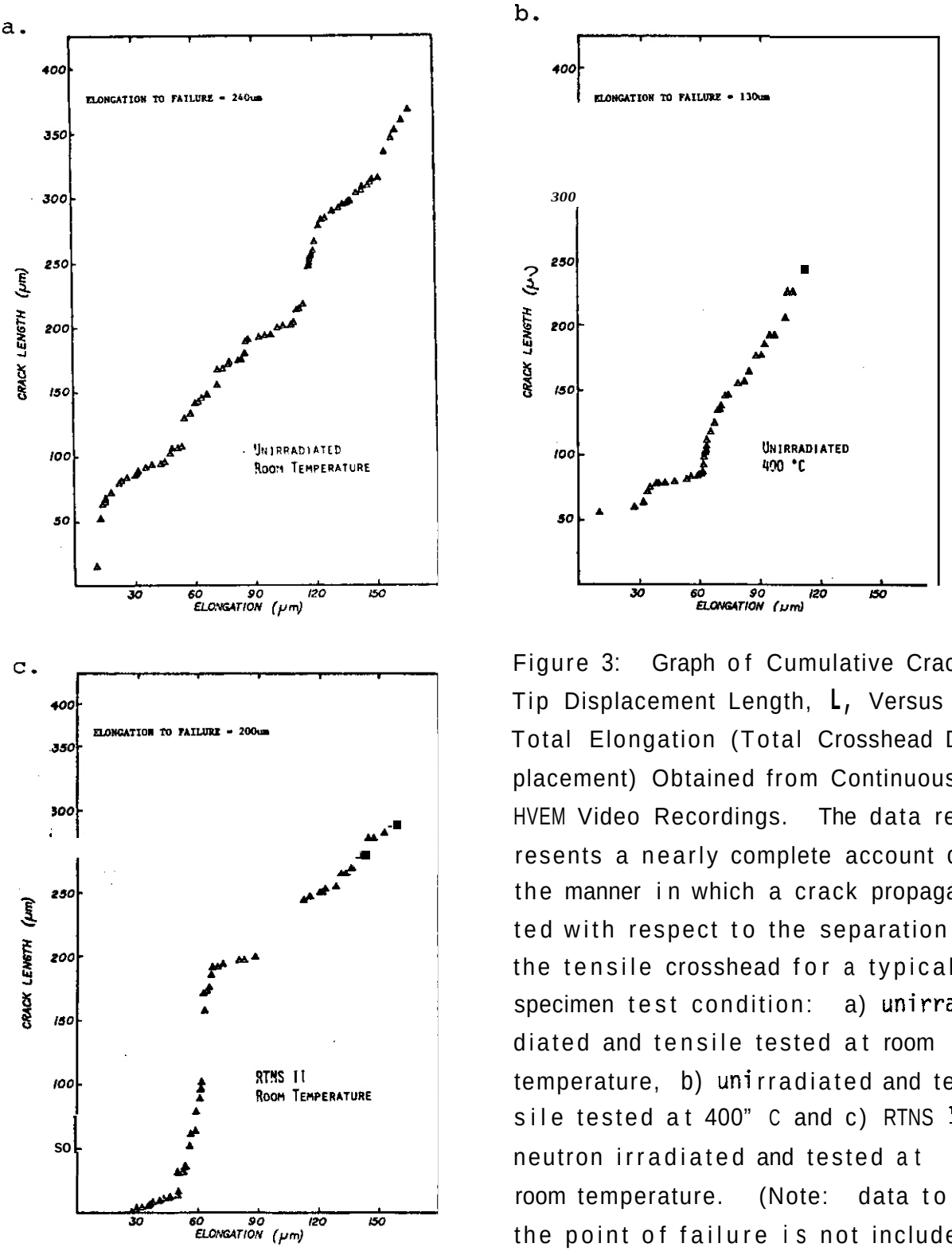

Figure 3: Graph of Cumulative Crack Tip Displacement Length, L, Versus Total Elongation (Total Crosshead Displacement) Obtained from Continuous HVEM Video Recordings. The data represents a nearly complete account of the manner in which a crack propagated with respect to the separation of the tensile crosshead for a typical specimen test condition: a) unirradiated and tensile tested at room temperature, b) unirradiated and tensile tested at 400" C and c) RTNS II neutron irradiated and tested at room temperature. (Note: data to the point of failure is not included).

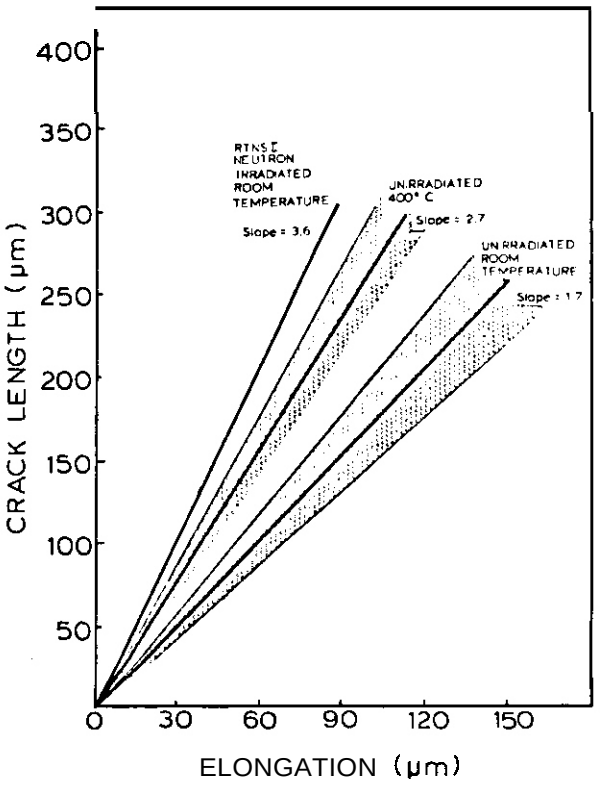

Figure 4: Graph of Crack Length Versus Total Elongation Illustrating Three Distinct Average Slopes, Each Representative of a Specimen Test Condition. Shaded regions represent two standard deviations of the data. Notice that decreasing slope represents and increase in specimen ductility.

fit to straight lines and qrouped to show the spread in the data. The data from the RTNS II specimen are also included for comparison to the other specimens. The fitted lines are shown starting from the origin so that the respective slopes can be best compared. It is evident that there are three distinct slopes in the graph, each representing a specimen class. By considering a steep slope as representing a mostly brittle specimen (much crack growth for little elongation) and a shallow slope representing a mostly ductile specimen (little crack growth for a corresponding amount of elongation) the three specimen classes can be ranked according to their ductility relative to each other. In order of increasing ductility the specimens are ranked: RTNS II, 400"

unirradiated and room temperature unirradiated. Intuition would first tell one that the 400" C specimen should be the most ductile specimen, but examination of bulk tensile properties such as reduction of area and elongation (listed in the table) shows that the 400" C specimen is less ductile than the room temperature specimen. So it seems that decreasing slope of the crack length versus elongation graph does represent an increase in specimen ductility.

5.2.4 Relationship of the Average Slope of Crack Length versus Elongation to Reduction of Area

Since ROA is used to classify specimen ductility, as is the average slope, S, of the L versus elongation curve (as proposed in Section 5.2.3), it is suspected that the two parameters must be related. From a comparison of S with ROA (in the table) it was found that $(ROA)^2 \times S$ is a constant for the three specimen classes tested. This result gives support to the idea that a loss of ductility (as determined by ROA measurements) is associated with a steep increase in slope of crack length versus elongation.

5.3 Conclusions

By use of a quantitative load-elongation tensile stage in-situ in an HVEM, mechanical properties such as ultimate tensile strength and yield strength can be determined for microtensile specimens 40-μm thick by 2.5 mm x 12.5 mm (electropolished for microscopic observation). UTS and YS values were not found to be representative of equivalent parameters for bulk material. However, the UTS of the foils was found to be consistently smaller than UTS of bulk material and related by an empirical equation: UTS (foil) = [UTS (bulk)/2] - 70 MPa.

Reduction of Area measurements for HVEM foil specimens were found to be lower than those for bulk specimens by ∿ 20%. However, ROA measurements for the foil specimens seem to be related to those for bulk specimens in a linear relationship as shown in Figure 2.

Elongation of the HVEM specimens did not agree with elongation for bulk specimens. For instance, elongation for the microspecimens tensile tested at 400°C was much lower than expected from bulk data. This result is thought to be due to a flow localization mechanism which may be more active at higher temperatures in the thin microspecimens.

The quantitative load-elongation HVEM tensile stage used in the in-situ experiments permits determination of additional macroscopic-microscopic relationships. A graph of cumulative crack length (L) plotted against total elongation exhibits a step-like relationship for all specimens. The average slope, S, of the L versus elongation graph, as determined by least squares fit, has been shown to decrease with increasing specimen ductility (Figure 4).

When the average slope, S, is combined with reduction of area (ROA) measurements, $(ROA)^2 \times S$ is a constant, suggesting an additional relationship of S to specimen ductility. .

6.0 References

1. H. E. Chandler, D. F. Baxter, and L. G. Kruger, "Technology Forecast '82 -- Trends in Testing and Inspection Technology," Metal Progress, Vol. 12 No. 1 (January 1982).

2. N. F. Panayotou, R. J. Puigh and E. K. Opperman, "Microtensile Specimen Test Results for High Energy Neutron Source Experiments," 2nd Topical Meeting on Fusion Reactor Materials (August 9-12, 1981), Seattle, Washington; Journal of Nuclear Materials, 103 and 104 (1981), 1523.

3. R. W. Bauer and H. G. F. Wilsdorf, "The Mechanical Behavior in Tension and Fracture Characteristics of Stainless Steel Thin Rolled Foils." in Proceedings of an International Conference on Dynamic Crack Propagation, Lehigh University, Bethlehem, PA (July 10-12, 1972), ed. George C. Sih (Noordhoff International Publishing, Leyden, The Netherlands, 1973), 197.

4. G. E. Lucas and N. F. Panayotou, "Microhardness Tests for High Energy Neutron Source Experiments." 2nd Topical Meeting on Fusion Reactor Materials (August' 9-12, 1981), Seattle, Washington; Journal of Nuclear Materials, 103 and 104 (1981), 1527.

5. R. D. Gerke and W. A. Jesser, "Quantitative Load-Elongation Capabilities of an In-situ Hot Tensile Stage for HVEM Use," DAFS Quarterly Progress Report, DOE/ER-0046/8 (February, 1982), 71.

6. "Mechanical and Physical Properties of Austenitic Chromium-Nickel Stainless Steels at Elevated Temperatures," Section 1 Bulletin B, The International Nickel Company (1963).

7. F. A. Garner, M L. Hamilton, N. F. Panayotou and G. D. Johnson, "The Microstructural Origins of Yield Strength Changes in AISI 316 During Fission or Fusion Irradiation." 2nd Topical Meeting on Fusion Reactor Materials (August 9-12, 1981); Seattle', Washington: Journal of Nuclear Materials, 103 and 104 (1981), 803.

8. Mechanical Properties Data Center, Structural Alloys Handbook, Vol. 2 (Battelle's Columbus Laboratories, Columbus, Ohio), 1980.

9. "Mechanical and Physical Properties of Austenitic Chromium-Nickel Stainless Steels at Ambient Temperatures," Section 1 Bulletin A, The International Nickel Company (1963).

10. R. R. Vandervoort, E. L. Raymond and C. J. Echer, "High Energy Neutron Irradiation Effects on the Tensile Properties and Microstructure of 316 Stainless Steel," Radiation Effects, 45 (1980), 191.

11. R. D. Gerke, "Crack Propagation in Type 316 Stainless Steel Microspecimens," Master's Thesis, University of Virginia (May, 1982).

12. J. I. Bennetch, "Microstructural Aspects of Helium Embrittlement in Stainless Steel," Ph.D. Dissertation, University of Virginia, (May, 1981).

13. T. Hanamura and W. A. Jesser, "In-Situ HVEM Observations of High Temperature Fracture Mechanisms in Neutron-Damaged 304 Stainless Steel," Virginia Journal of Science, 32, No. 3 (1981), 131.

14. R. D. Gerke, T. Hanamura, and W. A. Jesser, "Crack Propagation Characteristics in Helium Irradiated Type 316 Stainless Steel," DAFS Quarterly Progress Report, DOE/ER-0046/6 (August, 1981), 97.

7.0 Future Work

In-situ HVEM tensile tests on austenitic stainless steel which has been neutron irradiated and which contains a variety of microstructural features will be conducted in order to investigate the role of grain boundary sliding in causing intergranular failure in irradiated materials stressed at elevated temperatures.

CHAPTER 4

CORRELATION METHODOLOGY

CAVITY FORMATION AND SOLUTE SEGREGATION IN DUAL-ION IRRADIATED Fe-20 Ni-15 Cr ALLOY

B. A. Loomis, G. Ayrault, S. Gerber, and Z. Wang (Argonne National Laboratory)

1.0 Objective

The objective of this research program is to determine the mechanisms for the microstructural chanqes that occur in fusion reactor materials during neutron or charged-particle irradiation. Special emphasis is placed on the elucidation of the role of helium production rate, displacement damage level, irradiation temperature, and alloying elements in the evolution of the irradiation-damaged microstructure.

2.0 Summary

The swelling due to cavity formation in specimens of an Fe-20 Ni-15 Cr alloy was determined from transmission electron microscopy observations following dual-ion irradiation at 975 K with 3.0-MeV $^{58}Ni^{+}$ and degraded 0.8-MeV $^{3}He^{+}$ ions. An increase of the helium deposition rate from 5 to 50 appm He per dpa resulted in a delay of 5 to 15 dpa, respectively, for the onset of a steady, high swelling rate. The experimental results for the swelling of specimens receiving helium deposition rates of 15 or 50 appm He per dpa suggest that the swelling of the alloy tends to achieve a limiting value after ~70 dpa. The senregation of the nickel and chromium solutes to grain boundaries and voids in the irradiated specimens was determined from analyses using the energy-dispersive x-ray spectroscopy technique. These analyses have shown that the grain houndaries and voids are increasingly enriched in nickel concentration with a corresponding depletion of the nickel concentration in the matrix for increasinq displacement damage up to ~70 dpa. For displacement damage > 70 dpa, the analyses suggest that the nickel enrichment at grain boundaries and voids is diminished from the peak nickel concentration attained at ~70 dpa. The chromium concentration change at the grain boundaries and voids and in the matrix is opposite to the change in nickel concentration and is of smaller magnitude. These experimental results suggest that a correlation exists

between the cavity volume fraction in dual-ion irradiated Fe-20 Ni-15 Cr alloy and the redistribution of nickel and chromium solute.

3.0 Program

Title: Effects of Irradiation on Fusion Reactor Materials
Principle Investigator: B. A. Loomis
Affiliation: Argonne National Laboratory

4.0 Relevant DAFS Program Plan Task/Subtask

Subtask II.C.2.1 Mobility, Distribution and Bubble Nucleation

5.0 Accomplishments and Status

5.1 Introduction

The concurrent production of displacement damage and deposition of helium in materials can he expected to have a significant influence on the evolution of the microstructure in an otherwise displacement-damaged material. Therefore, the dimensional stahility and mechanical properties of materials that are utilized in the environment of a magnetic fusion reactor will depend in large measure on the interaction of the helium with the displacement damage.

In this report, results are presented from a study on the dimensional instability (swelling) that arises in an Fe-20 Ni-15 Cr alloy during the simultaneous production of displacement damage and deposition of helium by dual-ion irradiation. In addition, results are presented on determinations of the redistribution of Ni and Cr solutes from the alloy matrix to grain boundaries and cavities that occurs during irradiation of this alloy.

5.2 Materials and Procedures

The Fe-20 a/o Ni-15 a/o Cr alloy was prepared from high-purity materials by an

initial arc-melting of the constituents in a purified Ar atmosphere and by re-melting during levitation in vacuum for further homogenization. Specimens of the alloy were annealed at 1325 K in an Ar atmosphere for 1 hour and quenched to 300 K.

The annealed alloy specimens were simultaneously irradiated with 3.0-MeV $^{58}Ni^{+}$ and degraded 0.8-MeV $^{3}He^{+}$ ions in the ANL dual-ion irradiation facility (1). The energy of the $^{3}He^{+}$ ions was degraded to give a distribution of helium deposition in the alloy that was similar to the damage-depth distribution for the $^{58}Ni^{+}$ ions. The displacement damage levels (dpa) were calculated by use of the Brice computer codes RASE 3 and DAMG 2 using a displacement energy of 40 eV (2). The displacement damage rate was 3×10^{-3} $dpa \cdot s^{-1}$ at the nominal sectioned depth of 450 nm in the specimens. Three different helium injection rates were utilized in this study. These rates corresponded to He per dpa ratios of 5, 15, and 50 appm He per dpa. Specimens were also pre-injected at 300 K with 15 appm He. The specimens were irradiated at 975 ± 10 K in a vacuum of 10^{-8} torr. The irradiation temperature of 975 K was approximately 50 K above the peak swelling temperature (3).

The irradiated specimens were prepared for TEM observations by jet-thinning to perforation in a 6% $HCLO_4$ - 35% Butyl Cellosolve - 59% MeOH solution at 300 K. Photomicrographs of cavities in the specimen section extending from the 450 nm depth to the ~650 nm depth were obtained with either the Philips EM-400 or the ANL 1-MeV HVEM electron microscopes. The average diameter, number density, and volume fraction of cavities were evaluated from the photomicrographs.

The Ni and Cr concentration in the vicinity of grain boundaries and voids and in the matrix of one series of irradiated specimens (50 appm He per dpa) was determined from analyses using the energy-dispersive x-ray spectroscopy technique in combination with operation of the Philips EM-400 electron microscope. The specimen was tilted at an angle of 30° to the electron beam and viewed by a Si(Li) x-ray detector. The x-ray spectrum was acquired by an ORTEC EEDS-II multi-channel analyzer. The analysis of the x-ray emission data

to obtain elemental compositions was accomplished by use of procedures that have been described by Zaluzec (4). The minimal spot size for analysis of the elemental composition was 30-nm diameter. In this initial study, the minimal spot size was centered on a grain boundary and an interior void and in a matrix region free of voids. The x-ray spectrum was acquired from three widely separated grain boundary, void, and matrix regions for each specimen. The variation of the elemental composition that was determined for the three regions, i.e., three voids, etc., in a specimen was typically 2 a/o.

5.3 Experimental Results

5.3.1 Swelling

The dependence of the average cavity diameter, cavity number density, and cavity volume fraction on displacement damage in the Fe-20 Ni-15 Cr alloy that was dual- or single-ion irradiated at 975 K is shown in Figures 1, 2, and 3, respectively. These parameters are presented in Figures 1, 2, and 3 for specimens either with He injection rates of 5, 15, and 50 appm He per dpa or preinjected with 15 appm He. The data for specimens with less than 20 dpa displacement damage are re-evaluations of data previously presented in Ref. 3.

The average cavity diameter in the dual-ion irradiated specimens decreases with an increase of the He per dpa ratio. The experimental results suggest that the average cavity diameter approaches a limiting value for damage levels > 70 dpa (Figure 1). The pre-injection of He (15 appm) in the alloy specimens causes cavities to he formed with an average diameter that is intermediate to the diameter in specimens with 15:1 and 50:1 (appm He per dpa) He injection rates.

The cavity number density in specimens that received either a 5:1 He injection rate or He preinjection is initally $\sim 10^{20}$ m^{-3} but increases with increasing damage to a limiting value of $\sim 4 \times 10^{20}$ m^{-3} at ~90 dpa (Figure 2). In contrast, the cavity number density in specimens that received 15:1 and 50:1 He injection rates was initially high ($\sim 10^{22}$ m^{-3} at 5 dpa) and then decreased and approached a limiting value with increasing displacement damage.

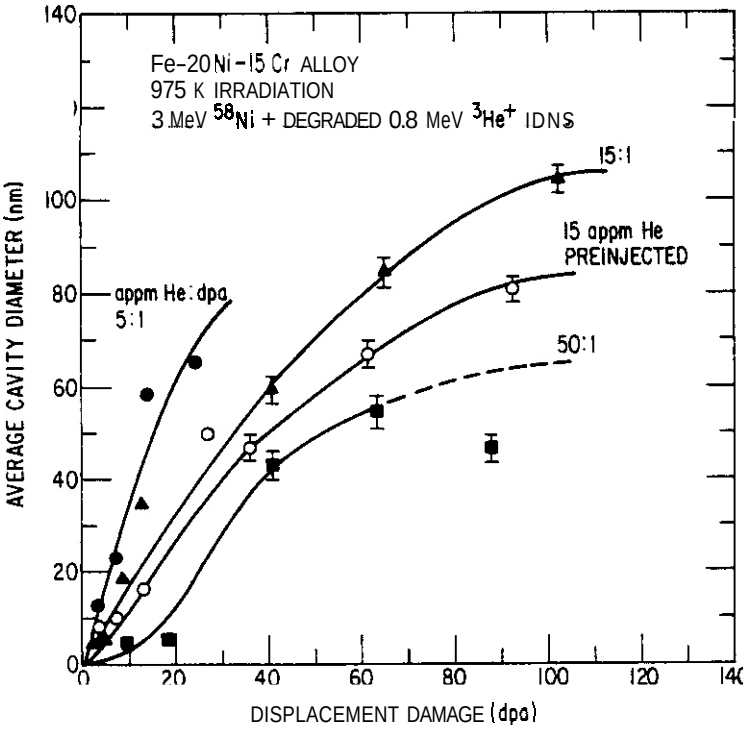

FIGURE 1. Dependence of Average Cavity Diameter on Displacement Damage in Fe-20 Ni-15 Cr Alloy.

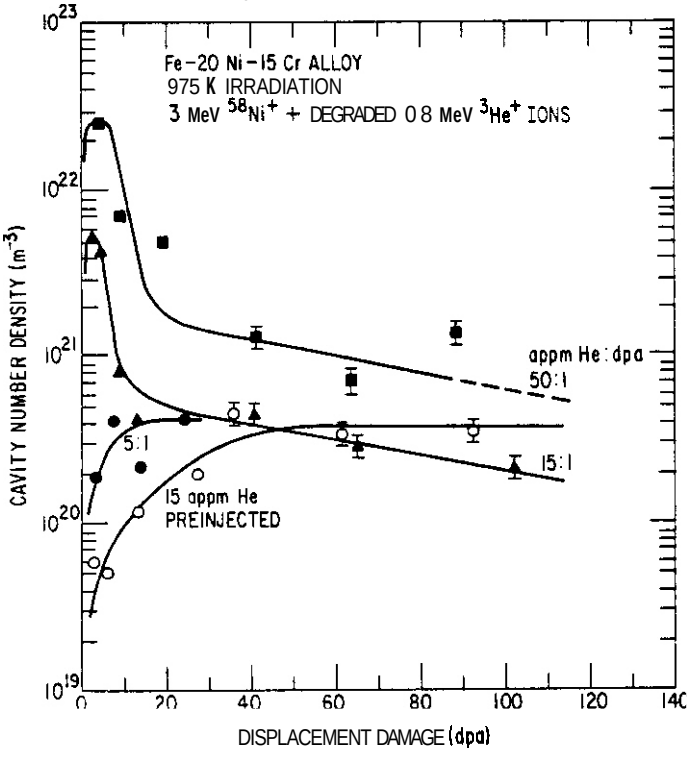

FIGURE 2. Dependence of Cavity Number Density on Displacement Damage in Fe-20 Ni-15 Cr Alloy.

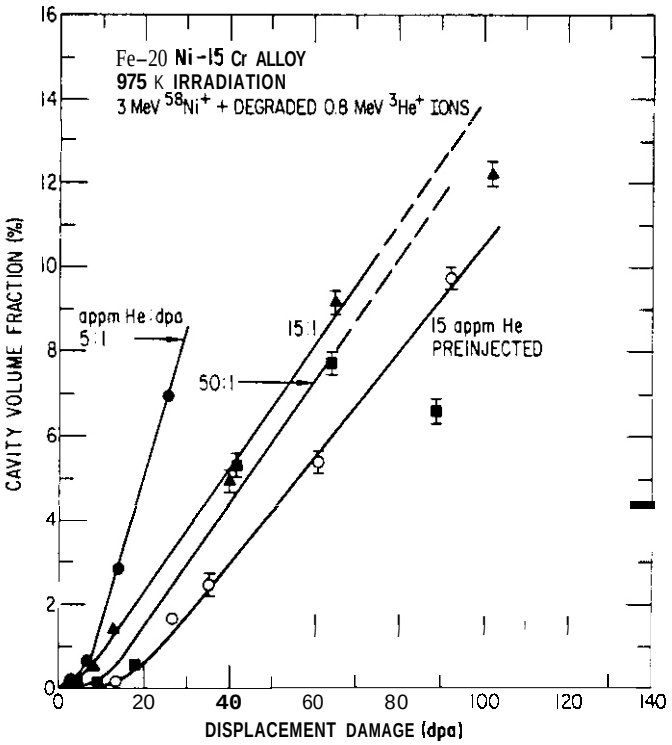

FIGURE 3. Dependence of Cavity Volume Fraction on Displacement Damage in Fe-20 Ni-15 Cr Alloy.

The alloy specimens, regardless of He injection rate or He preinjection, undergo a transitory regime of displacement damage that produces only small cavity volume fraction (<0.5%) before the onset of a constant, high swelling rate. An increase of the He deposition rate from 5:1 to 50:1 appm He per dpa results in a delay of 5 to 15 dpa, respectively, for the commencement of a constant swelling rate; the preinjection of 15 appm He causes a delay of ~20 dpa (Figure 3).

The cavity volume fraction in the dual-ion irradiated specimens for a given displacement damage concentration up to ~100 dpa decreases with an increase of the He:dpa ratio. The preinjection of He results in the lowest cavity volume fraction at each damage level. An increase of the He injection rate from 5:1 to 15:1, 50:1 appm He/dpa results in a significant decrease of the constant high swelling rate, viz. 0.35%/dpa to 0.15%/dpa.

We have shown in Figure 3 for the specimens that received 15:1 or 50:1 He injection rates, a constant rate of swelling, i.e., ~0.15%/dpa, between 15 and 100 dpa. It can be observed that the data points for the highest damage in these specimens show significant deviations from the line for constant swelling rate. We have been unable to attribute these deviations to experimental variations. Therefore, these data suggest that the cavity volume fraction approaches either a limiting value or decreases for displacement damage levels above ~70 dpa for 15:1 and 50:1 He per dpa injection rates. The data to be presented in the following section on the redistribution of Ni and Cr solutes show a similar trend with increasing damage level. Nevertheless, this trend in the dependence of the cavity volume fraction must be regarded as tentative until specimens are dual-ion irradiated to higher damage levels.

The microstructure of the alloy specimens that were dual-ion irradiated at 975 K with a 50:1 He injection rate to 64 and 89 dpa are shown in Figures 4a and 4b, respectively. the microstructures of these irradiated specimens are notahly devoid of precipitates.

5.3.2 Ni and Cr Redistribution

The dependence on displacement damage of the Ni and Cr concentration in the vicinity of grain boundaries and voids and in the matrix for the alloy specimens receiving a He injection rate of 50:1 is shown in Figures 5, 6, and 7, respectively. These experimental results show that the material in the vicinity of grain boundaries (Figure 5) and voids (Figure 6) is significantly enriched in Ni concentration for displacement damage levels between 40 and 100 dpa; the matrix (Figure 7) undergoes a corresponding depletion in Ni concentration. The Cr concentration change at the grain boundaries and voids and in the matrix is opposite to the change in Ni concentration and is of smaller magnitude. The Fe concentration in the matrix during dual-ion irradiation to 90 dpa is essentially unchanged from the as-prepared concentration.

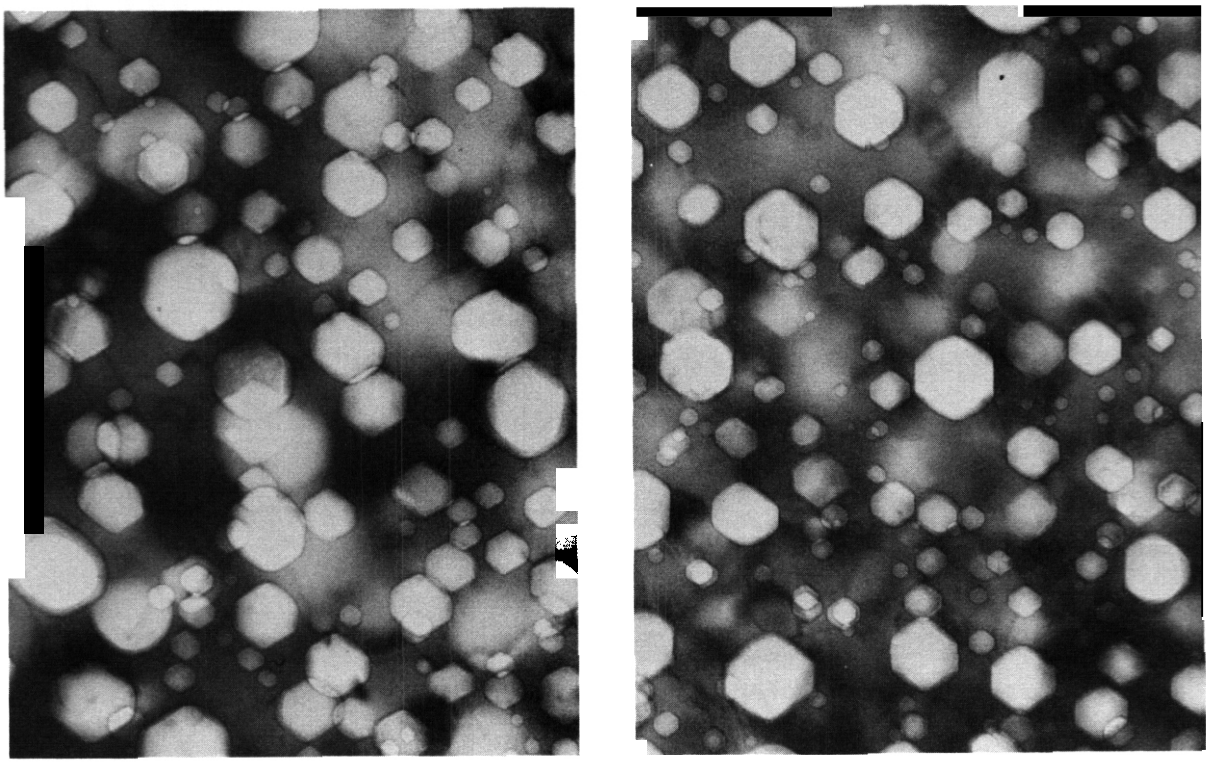

(a) (b)

FIGURE 4. Microstructures of Dual-Ion Irradiated Fe-20 Ni-15 Cr Alloy (50 appm He per dpa): (a) 64 dpa (b) 89 dpa. 120,000X.

These analyses suggest that the grain boundaries and voids are increasingly enriched in Ni concentration for increasing displacement damage levels up to ~70 dpa. For displacement damage levels > 70 dpa, the analyses suggest that the Ni enrichment at grain boundaries and voids is diminished from the peak Ni concentration attained at ~70 dpa. It may be recalled that a similar trend with respect to displacement damage level was suggested by the cavity volume fraction data (Section 5.3.1 and Figure 3).

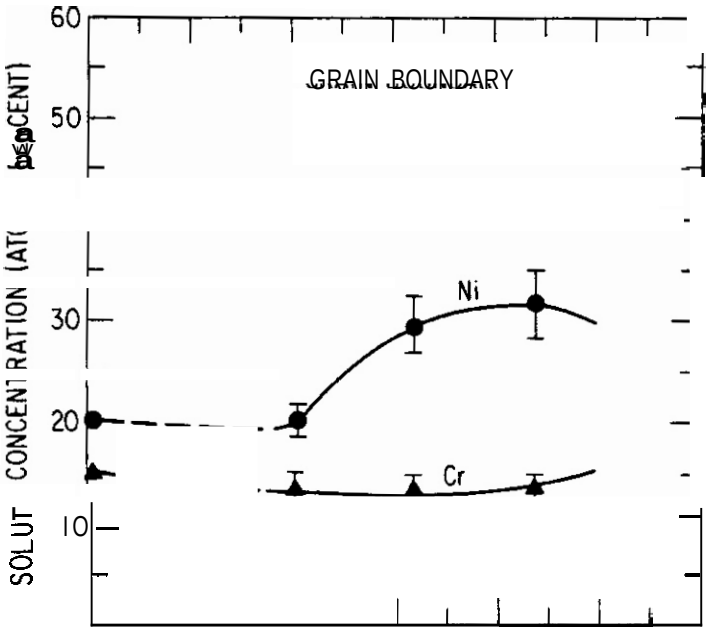

FIGURE 5. Dependence of Ni and Cr Concentration at Grain Boundaries on Displacement Damage in Fe-20 Ni-15 Cr Alloy (50 appm He per dpa).

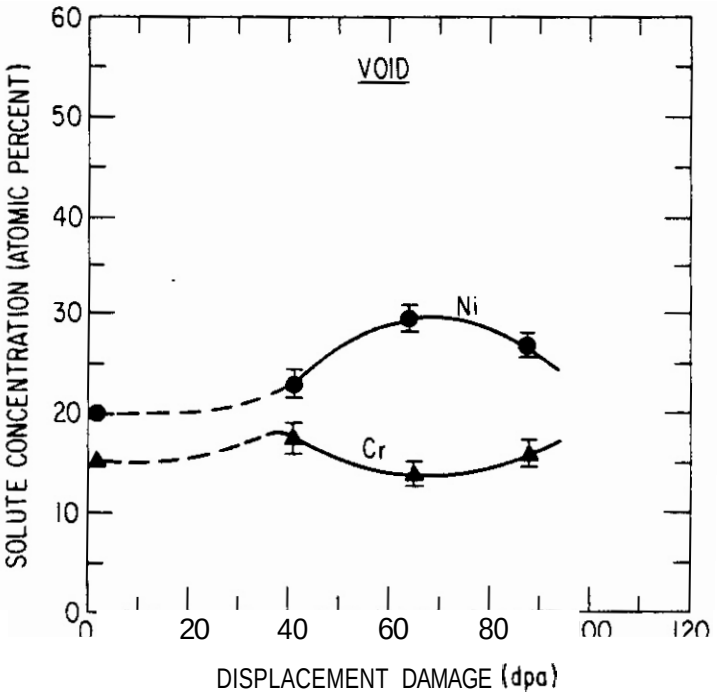

FIGURE 6. Dependence of Ni and Cr Concentration at Voids on Displacement Damage in Fe-20 Ni-15 Cr Alloy (50 appm He per dpa).

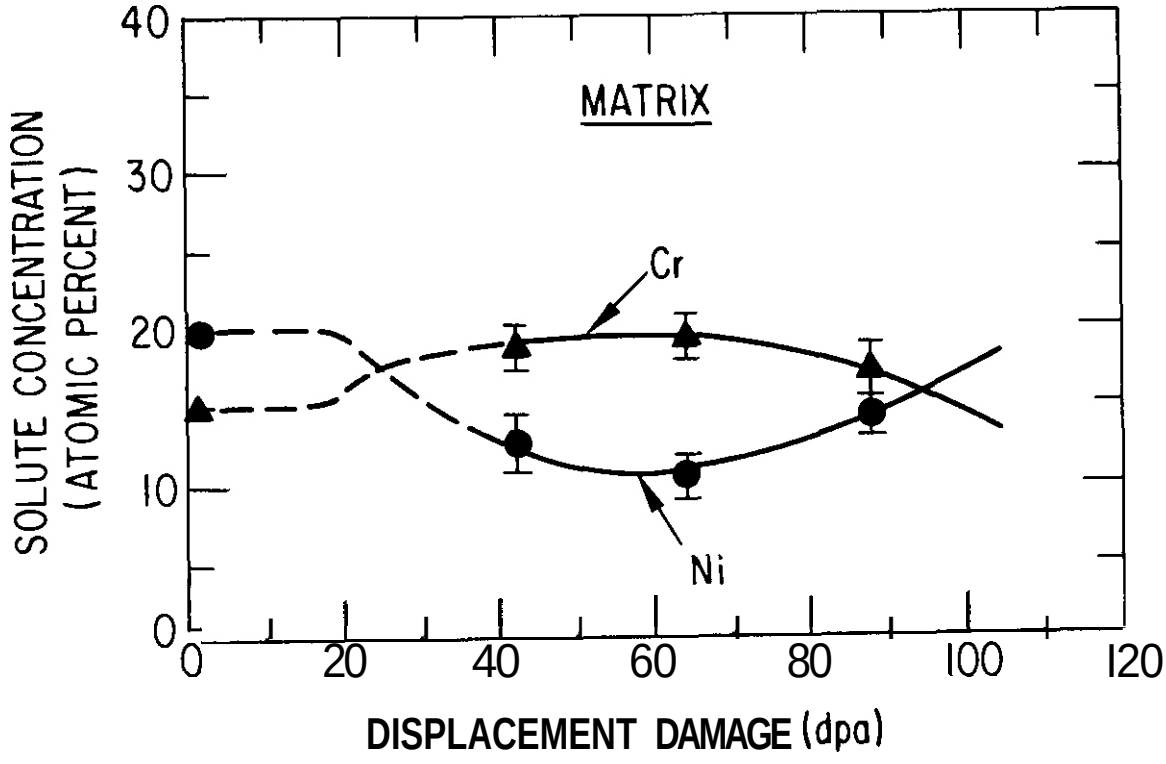

FIGURE 7. Dependence of Ni and Cr Concentration in the Matrix on Displacement Damage in Fe-20 Ni-15 Cr Alloy (50 appm He per dpa).

5.4 Conclusion and Discussion

The experimental results obtained in this study on a dual-ion irradiated Fe-20 Ni-15 Cr alloy show that:

(1) The cavity volume fraction for a given displacement damage concentration decreases with an increase of the He: dpa ratio.

(2) An increase of the He injection rate from 5:1 to 15:1 or 50:1 appm He per dpa results in a decrease of the swelling rate from 0.35%/dpa to 0.15%/dpa.

(3) The alloy, regardless of He injection rate or He preinjection, undergoes during $^{58}Ni^{+}$ ion irradiation a transitory regime of displacement damage that produces only small cavity volume fraction (< 0.5%) before the onset of a constant, high swelling rate.

(4) The material in the vicinity of grain boundaries and voids is significantly enriched in Ni concentration for displacement damage levels between 40 and 100 dpa.

The experimental data suggest that a correlation exists between the cavity volume fraction in the dual-ion irradiated Fe-20 Ni-15 Cr alloy and the redistribution of Ni and Cr solute. Changes in the base composition of steels and Fe-Ni-Cr alloys in the neighborhood of point defect sinks, i.e., voids, grain boundaries, and surfaces, after ion or neutron irradiation have been determined by several experimenters (5,6). These changes in the base composition are attributed to the effects of the flux of point defects to sinks during irradiation. The experimental results obtained up to the present time in Fe-Ni-Cr alloys show that Ni is enriched at the sinks. The enrichment of Ni at sinks is believed to be the consequence of the negative volume size factor (6) or the relatively low diffusion coefficient of Ni (7). The segregation of Ni reduces the vacancy flux to a void and the void growth is inhibited. Therefore, the cavity volume fraction is expected to saturate. The experimental data obtained in this study are essentially in agreement with this thesis. We cannot at the present time account for a decrese of the Ni concentration from the peak value at ~ 70 dpa.

6.0 References

1. A Taylor, J. Wallace, D. I. Potter, D. G. Ryding and B. O. Hall, in: Proc. 1975 Intern. Conf. on Radiation Effects and Tritium Technology for Fusion Reactors, Eds. J. S. Watson and F. W. Wiffen, CONF-750989 (1976) p. I-158.
2. D. K. Price, Sandia Laboratory Report SLA-73-0410 (1973).
3. S. C. Agarwal, G. Ayrault, D. I. Potter, A. Taylor and F. V. Nolfi, Jr., J. Nucl. Mater. 85 & 86 (1979) 653.

4. N. J. Zaluzec, in Introduction to Analytical Electron Microscopy, eds. J. J. Hren, J. I. Goldstein and D. C. Joy, Plenum Press, New York, 1979, pp. 121-167.

5. P. R. Okamoto and H. Idiedersich, J. Nucl. Mater. 53 (1974) 336.

6. A. D. Marwick, W. A. D. Kennedy, D. J. Mazey and J. A Hudson, Scripta Met. 12 (1978) 1015.

7. S. J. Rothman, L. J. Nowicki and G. E. Murch, J. Phys. F: Metal Phys. 10 (1980) 383.

7.0 Future Work

The spatial distribution of Fe, Ni, and Cr concentration will be determined in Fe-20 Ni-15 Cr alloy specimens that received 5:1 or 15:1 He injection rates or He preinjection. The alloy will be irradiated to 125 dpa for an unambiguous determination of saturation effects.

8.0 Publications

1. G. Ayrault, H. A. Hoff, F. V. Nolfi, Jr. and A. P. L. Turner, "Influence of Helium Injection Rate on the Microstructure of Dual-Ion Irradiated Type 316 Stainless Steel", J. of Nucl. Mater. 103 (1981) Part B, 1035.

2. B. A. Loomis and S. B. Gerher, "Swelling of $^{58}Ni^{+}$ and $^{3}He^{+}$ Ion-Irradiated Nh and Nb Alloys", J. Nucl. Mater. 103 (1981) Part B, 1193.

3. J. Nagakawa, V. K. Sethi and A. P. L. Turner," Irradiation Creep in Simple Binary Alloys", J. Nucl. Mater. 103 (1981) Part B, 1275.

ON RADIATION-INDUCED SEGREGATION AND THE COMPOSITIONAL DEPENDENCE OF SWELLING IN FE-NI-CR ALLOYS

W. G. Wolfer (University of Wisconsin), F. A. Garner and L. E. Thomas (Hanford Engineering Development Laboratory)

1.0 Objective

The object of this effort is to provide a model describing the compositional dependence of swelling in Fe-Ni-Cr alloys and its relationship to radiation-induced segregation.

2.0 Summary

When alloys based on the Fe-Ni-Cr system are subjected to irradiation at high temperatures a substantial amcunt of elemental segregation occurs. Two categories of segregation have been observed, one involving radiation-induced precipitation or changes in precipitate composition, and another involving the establishment of compositional gradients near microstructural sinks. While segregation into precipitate phases is known to strongly influence the development of void swelling, it now appears that segregation to void surfaces plays an equally important role in the development of voids. A general feature of both types of segregation is the major role of nickel as a primary segregant.

An investigation of the basic flux equations for diffusion of interstititals and vacancies in superimposed strain and composition gradients shows that several previously unconsidered drift terms arise in the description of the bias as a result of elemental segregation. These terms originate from the compositional dependence of point defect formation and migration energies and the compositional dependence of elastic properties and lattice parameter. When compounded with the operation of the inverse Kirkendall segregation mechanism, these terms strongly alter the bias for void nucleation and growth and provide an explanation for the marked variation of void nucleation and swelling with nickel

concentration. The segregation-induced drift terms are comparable in magnitude to the strain-induced drift terms and are strongly dependent on nickel concentration. This is demonstrated for binary Fe-Ni alloys using published tracer diffusion and thermodynamic data.

3.0 Program

Title: Irradiation Effects Analysis (AKJ)
Principal Investigator: D. G. Doran
Affiliation: Hanford Engineering Development Laboratory

4.0 Relevant DAFS Program Plan Task/Subtask

II.C.l Effects of Material Parameters on Microstructure
II.C. 17 Microstructural Characterization

5.0 Accomplishments and Status

5.1 Introduction

Radiation-induced segregation (RIS) has been found to occur in many alloys during neutron or charged-particle irradiation. A survey of the progress in our understanding of this phenomenon can be found in the proceedings [1-2] of two recent conferences. Although many elements have been observed to participate, silicon and nickel are particularly effective segregants in austenitic alloys. The significance of RIS to void formation and swelling has been recognized by many researchers, although the precise role of the various processes involved is still a matter of active research.

Okamoto, et al.[3] have shown that RIS may be associated with point defect trapping by impurity or alloying elements, and that this trapping modifies the recombination of interstitials and vacancies. As a result, void swelling can be reduced by either vacancy or interstitial trapping, although the latter would require a very large binding energy between the interstitial and the solute atom.

The vacancy-solute binding can also lead to a change of the vacancy diffusivity and thereby affect the void nucleation rate, as shown recently by Garner and Wolfer.[4] While the role of silicon in suppressing swelling can be ascribed at least partially to vacancy-solute binding, the role of nickel cannot, however.

When radiation-induced segregation results in precipitation, void formation and swelling can be strongly affected. Mansur, et al.[5-6] have proposed that voids associated with incoherent precipitates possess a larger collecting surface for point defect absorption. As a result, radiation-induced precipitation may enhance void growth. Another consequence of radiation-induced precipitation is connected with the associated change in the matrix composition of the alloy. Garner [7] has pointed out that radiation-induced precipitation reactions in the austenitic steels generally involve the removal of nickel and silicon from the matrix and that the sensitivity of swelling to many variables is mirrored in the nickel and silicon removal processes.[8] The reduction in the matrix concentrations of these elements then leads to an increase in void swelling as demonstrated in the experimental findings of Johnston, et al.[9]

Finally, RIS can affect both void nucleation and growth by modifying the bias factors of sinks. Wolfer and Mansur [10] have investigated this possibility in detail for voids surrounded by a discrete segregation shell whose elastic properties and lattice parameter differ from those of the matrix. In another paper, Si-Ahmed and Wolfer [11] show that very small differences in these parameters can change void nucleation rates by orders of magnitude.

In this paper, we report on recent investigations on nickel segregation to void surfaces. The associated compositional gradients can extend thousands of Angstroms, and the segregation results in a continuous radial change in the concentration of various elements. Although the discrete shell model of Wolfer and Mansur does not provide an adequate description for this case, the effect of compositional gradients on the void bias is similar to that of the discrete shell.

It is well known that many physical properties, such as thermal expansion, elastic moduli, lattice parameter, and excess free energy, exhibit a marked variation with composition in the Fe-Ni-Cr austenitic alloys. In particular, so-called anomalous variations occur in these properties in the composition range of the Invar alloys, which happens to coincide with the composition range of low-swelling alloys. Accordingly, we suggest in this paper that a possible connection exists between these anomalous variations, the segregation of nickel to microstructural sinks, and the associated modifications of the sink bias factors. An unambiguous correlation cannot yet be made because critical information is lacking on the basic physical properties in this class of alloys. It will become evident, however, that nickel segregation combined with known changes of basic lattice properties will result in a strong modification of the bias, and therefore strongly affect void swelling. In view of this connection, the proposed explanation for the dependence of swelling on the alloy composition has a mechanistic basis that can be incorporated in rate and nucleation theories for void formation, and therefore can be subject to a quantitative examination. In contrast, previous explanations of the compositional variation of swelling are not considered satisfactory when examined in quantitative terms.

Watkins, et al.[12] have proposed that in fcc Fe-Ni-Cr alloys, the iron atoms may exist in two states, an anti-ferromagnetic and a ferromagnetic one. These are postulated to differ in their atomic volumes and in their contributions to the elastic moduli of the alloy. With increasing nickel content, the ratio of anti-ferromagnetic to ferromagnetic iron atoms decreases with a corresponding increase in the lattice parameter and a decrease in the elastic shear modulus. They speculate that the increase of the average atomic volume may imply a greater recombination of interstitials and vacancies.

According to recent results by Wolfer and Si-Ahmed[13] the recombination rate at reactor irradiation temperatures is simply proportional to the lattice parameter. Figure 1 shows the lattice parameter of Fe-Ni-Cr-phase alloys at room temperature.[14] It is seen that the maximum variation with composition is no

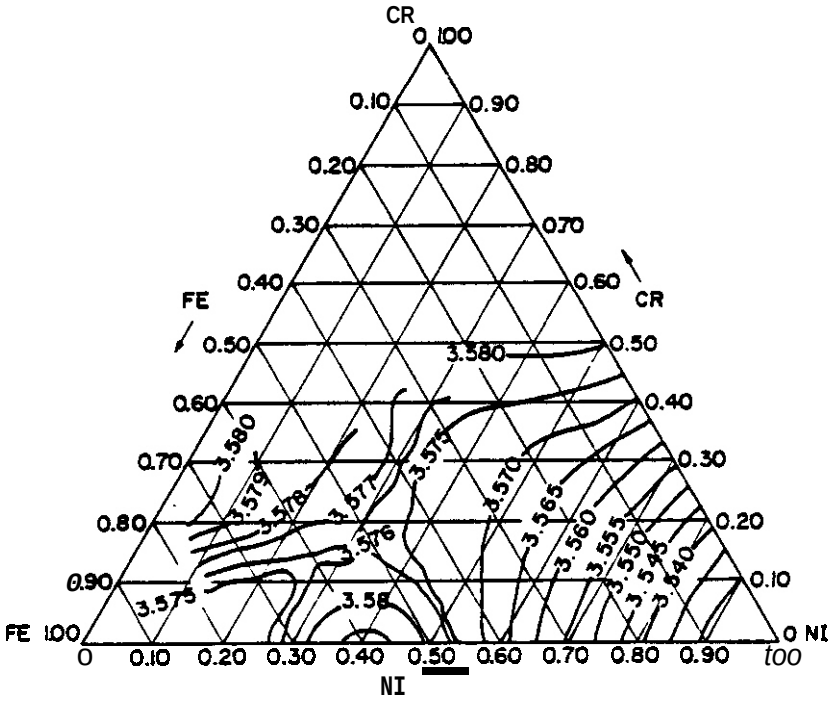

FIGURE 1. Lattice Parameter in Å for Gamma-Phase Alloys at Room Temperature.(14)

more than about 2%. Such a small variation in the recombination rate would not be sufficient to account for the much larger variation observed in the swelling as a function of nickel content.

Another explanation was advanced by Bates [15] based on the variation of the shear modulus with nickel composition. Figure 2 shows the results of Masumoto, et al. [16] for the shear modulus of Fe-Ni-Cr alloys at room temperature. Bates suggested that the arrival ratio of interstitials and vancancies at void embryos decreases with increasing shear modulus. Therefore, in this treatment the void nucleation rate would increase with the shear modulus.

This suggestion was based on a model proposed by Wolfer and Ashkin [17] for the capture efficiency of interstitials at a bare void. In this latter derivation, the image interaction of an interstitial with the void surfaces was not included. When this important interaction was included later by Wolfer and Yoo, [18] it was

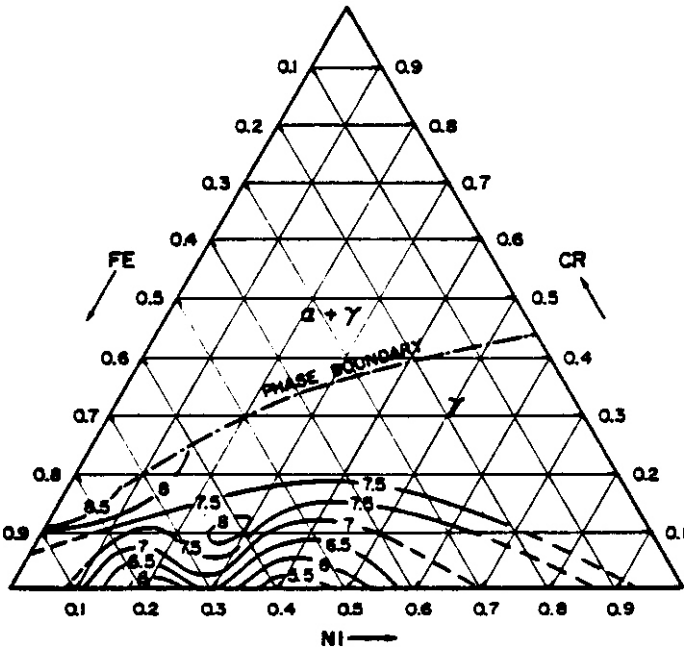

FIGURE 2. Shear Modulus (in 10 MPa) for Fe-Ni-Cr Alloy at Room Temperature.(16)

found that the arrival ratio increases with increasing shear modulus. This would imply that the void nucleation rate increases sharply as the shear modulus drops to its minimum value for a binary Fe-Ni alloy with 40% nickel. In contrast, the data show that both void density and swelling exhibit minimums for this alloy composition.[9]

It should be further noted that Bates did not consider the fact that the'bias factor of dislocations also increases with the shear modulus, and that it is the net bias or bias difference between dislocations and void which is the driving force for both void nucleation and growth.

In any case, homogeneous nucleation of voids without segregant shells was shown to occur with such low probability [11,18] that they cannot be invoked in any explanation of the composition dependence of swelling. In order for void nucleation to proceed at a rate commensurate with experimental findings, segregation

to void embryos must precede their growth. As shown by Si-Ahmed, Wolfer and Mansur [10-11] this requires that segregation must result in a slight compositional change around the void embryo such that the shear modulus increases locally by a few percent and/or that the lattice parameter increases by a few tenths of a percent. Such minor segregation-induced changes are well within the range of the compositional variation of the shear modulus, Figure 2, and that of the lattice parameter, Figure 1. Other segregation-induced changes, to be discussed below, arise from the composition dependence of point defect diffusivities and the inverse Kirkendall effect. Prior to the discussion of these changes, however, it is useful to review the available data for clues to the nature of the influence of segregation on void nucleation and growth.

5.2 Published Experimental Evidence for Nickel Segregation to Voids

Evidence has been accumulating which demonstrates radiation-induced segregation to void surfaces. Nickel segregation to voids in neutron-irradiated AISI 316 (with 12-13.5% nickel and varying silicon levels) has been observed by Brager and Garner.[19-20] Porter and Wood [21] have found that in neutron-irradiated 304 stainless steel (9.3% nickel) voids are surrounded by an austenitic shell embedded in a ferritic matrix. While nickel was shown to segregate into precipitates it was inferred that nickel also segregated to voids. The combined segregation is thought to deplete the matrix to a nickel level below the limit for austenite stability, but the higher nickel content near the void surface resisted the austenite-to-ferrite transformation. Segregation of nickel to void surfaces was also found in titanium-modified AISI 316 by Brun, et al.[22]

Whereas the above observations were made on neutron-irradiated steels, Terasawa, et al.[23] found nickel, silicon and molybdenum segregation to void surfaces in carbon ion irradiations of AISI 316. Marwick, et al.[24] discovered an enrichment of 54% nickel at voids in an alloy with an average nickel content of 34%. Hishinuma, et al.[25-26] irradiated with 1.0 MeV electrons a series of alloys including both commercial steels and an experimental series Fe-17Cr-XNi, where X=12, 35 and 50%. The researchers also observed that the void density obtained at 30 dpa for temperatures above 400°C decreased strongly with increasing nickel content.

Hishinuma, et al.[25,26] further observed that voids in an Fe-17Cr-12Ni alloy exhibited a strain-field contrast in transmission electron microscopy, whereas those in Fe-17Cr-50Ni did not. The incubation times for void nucleation were very short for the low nickel alloy, and long for the high nickel alloy. Since the lattice parameter decreases with increasing nickel content particularly for high nickel alloys (see Figure 1), the lack of a strain-field contrast around voids in the high nickel alloy was interpreted by Hishinuma, et al. to indicate the absence of nickel segregation. Conversely, the strong strain-field contrast in the low nickel alloy was believed to be associated with substantial nickel segregation. It was therefore concluded by Hishinuma that the marked difference in swelling behavior was due to the difference in nickel segregation behavior at void embryos.

5.3 Recent Experimental Studies on Nickel Segregation

In order to obtain further insight on the nature of the segregation process, a series of microanalytical studies are being conducted at Hanford Engineering Development Laboratory using TEM/STEM methods, primarily energy dispersive X-ray microanalysis. The scanning transmission electron microscope with a field emission electron source operated at 100 kV allows X-ray microanalysis using probes as small as 1 to 2 nm. Beam broadening within the specimen controls the ultimate resolution, however. Measurements in a Vacuum Generators HB-501 STEM leads to an estimate of 5 nm spatial resolution in materials with low-to-medium atomic number.[27]

While it is relatively easy to measure compositions by EDX microanalysis at different points on a thin specimen and to construct an apparent composition profile, it is not so easy to extract the actual composition profile around the void. This requires exact knowledge of the specimen thickness and void location in the foil as well as a sophisticated deconvolution of the data using the initial electron distribution in the probe. A discussion of the complexities involved is given in Reference 27.

The degree of nickel segregation to voids has been found to be quite large even for relatively small voids. As shown in Figure 3 the apparent nickel concentration at a precipitate-free void surface is on the order of 40%. (After deconvolution of the profile it is anticipated that the actual surface concentration will be much higher.) This void was found in neutron-irradiated Fe-15Cr-25Ni-0.3Si and was 35 nm in diameter and located at the center of a 55 nm thick foil. The probe diameter was less than 2 nm. Some silicon segregation at the void surface was also observed.

It is not necessary for silicon or other solutes to be present for nickel segregation to occur, however. Figure 4 shows the development of nickel segregation at void surfaces in neutron irradiated Fe-15Cr-25Ni. The apparently lesser level of nickel segregation is primarily a reflection of the larger probe size (8 nm) employed.

A number of important observations relevant to the subject of this paper have been derived from these experimental studies.

a. The primary influence of matrix nickel content on swelling at low fluence is expressed in the void density rather than the size. The void density decreases strongly with increasing nickel content in Fe-15Cr-XNi alloys in the range of 15 to 35% nickel. However, with increasing fluence, differences in void number densities diminish.
b. When the matrix nickel content of a solute-bearing alloy is decreasing due to precipitation of nickel-rich phases, it is found that the matrix nickel content drops below a "critical" level prior to the nucleation of voids.[28]
c. The segregation of nickel occurs in all nickel-bearing Fe-Cr-Ni alloys studied to date. This spans the range of 15-75% nickel and therefore covers the anomalous behavior range at about 35% nickel. Nickel segregation is not confined to voids alone, but also occurs to grain boundaries and dislocation loops. When other solutes are present in the alloy, many of these also segregate to microstructural sinks. A summary of the segregation behavior observed in these studies is presented elsewhere.[28]

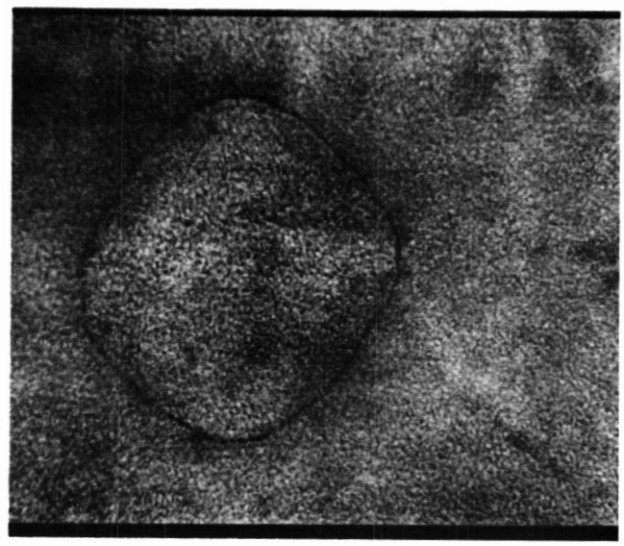

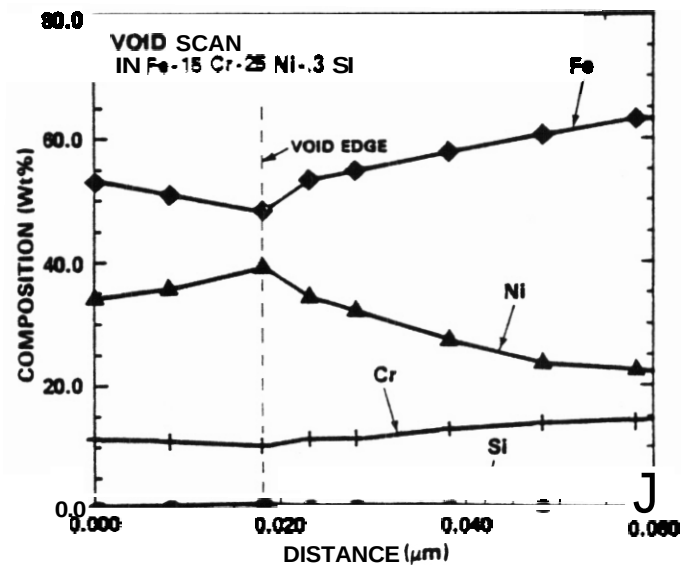

FIGURE 3. STEM Image of Void and Composition Profiles Obtained by EDX Microanalysis in Neutron-Irradiated Fe-15Cr-25Ni-0.3Si Alloy Irradiated in EBR-II at 510°C. Analysis was performed with a 2 nm diameter electron probe in a field ion gun/scanning transmission electron microscope.

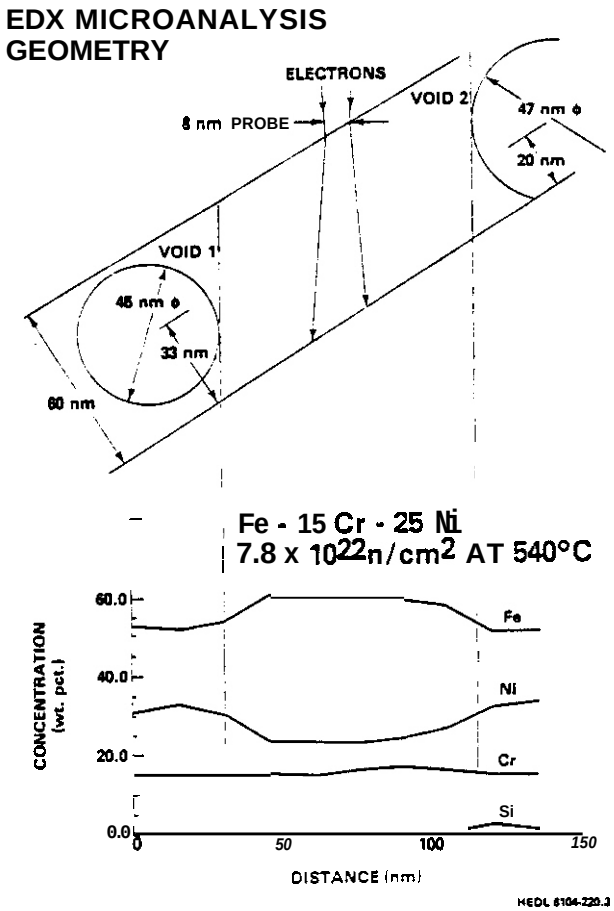

FIGURE 4. Microanalysis Geometry and Composition Profiles Derived from Fe-15Cr-25Ni Irradiated in EBR-II at 540°C. Analysis was performed in a 100 keV TEM/STEM.

5.4 Origin of Segregation-Induced Bias Modifications

The physical basis for the effect of segregation on the bias is to be found in the drift terms contained in the equations for the flux of vacancies and interstititals. In alloys with uniform alloy composition and uniform properties, the flux of point defects to any sink is given by

$$J_o = -\nabla(DC) - \frac{DC}{kT}\nabla U^{\sigma} \qquad (1)$$

where D is the diffusion coefficient for migration, C the concentration of point defects, and U^{σ} is the mechanical interaction with the stress field of the sink to which the point defects are diffusing. As usual, k is the Boltzmann constant, and T is the absolute temperature.

The second term is the only drift term that must be considered when bias factors are computed for uniform materials. During the initial stages of high-temperature irradiations, when RIS has not yet occurred, it may be assumed that Equation 1 is valid.

Due to the different mobilities of alloying elements and impurities, radiation-induced segregation will occur in the vicinity of sinks. Thus, as composition gradients develop, the point defect fluxes will change, and new drift terms are required in Equation 1.

For the case of a substitutional binary alloy consisting of A and B atoms, Wolfer [29] has recently shown that the Equation 1 must be replaced by the following two equations. For the vacancy flux, it is found that

$$J_V = -\nabla(D_V C_V) - \frac{D_V C_V}{kT} \nabla G_V^s + (D_{AV} - D_{BV})\, \alpha C_V \nabla x_A \qquad (2)$$

and the interstitial flux is given by

$$J_I = -\nabla(D_I C_I) - \frac{D_I C_I}{kT} \nabla G_I^s - (D_{AI} - D_{BI})\, \alpha C_I \nabla x_A \qquad (3)$$

Here, the subscripts "V" and "I" indicate quantities for vacancies and interstitials, respectively, $x_A = 1 - x_B$ is the local atomic fraction of A atoms, and

$$a = 1 + d \ln \gamma_A / d \ln x_A \qquad (4)$$

is the thermodynamic factor which differs from one when the solid solution alloy is not ideal, i.e., when the activity coefficient γ_A deviates from unity.

The diffusivities for the A atoms are denoted by D_{AV} and D_{AI} for migration via vacancies and interstitials, respectively, and analogous definitions are employed for the B atoms. The diffusion coefficients for vacancy and interstitial migration are then given by

$$D_V = x_A D_{AV} + x_B D_{BV} \tag{5}$$

and

$$D_I = x_A D_{AI} + x_B D_{BI} \ . \tag{6}$$

A determination of the diffusivities D_{AV} and D_{BV} is possible when tracer diffusion coefficients are known as a function of the alloy composition. If, for example, D_A^* is the tracer diffusion coefficient in the alloy with the composition x_A and a vacancy fraction of $x_V = C_V/N$ (N is the number of atoms per unit volume), then

$$D_{AV} = D_A^*/(x_V f_V) = D_A^{o*}/(x_V^{eq} f_V) \tag{7}$$

where f_V is the correlation factor for diffusion by the vacancy mechanism. For fcc crystals, $f_V = 0.78145$. In general, only the tracer diffusion coefficient D_A^{o*} for thermal equilibrium condition is known when the vacancy fraction is equal to x_V^{eq}. ALthough a relationship similar to Equation 7 can in principle be written down for the diffusivity D_{AI}, it is of no practical significance as $x_I^{eq} \cong 0$. Furthermore, the measurement of a tracer diffusion coefficient for the interstitialcy mechanism is possible only under radiation conditions, and would be obscured by the additional diffusion arising from the vacancy mechanism.

In order to cast the last term in Equations 2 and 3 into a form similar to the other drift terms, we define the Kirkendall forces as

$$F_{KV} = - \frac{(D_{AV} - D_{BV})}{(x_A D_{AV} + x_B D_{BV})} \alpha kT \nabla x_A = -K_V kT \nabla x_A \tag{8}$$

and

$$F_{KI} = \frac{(D_{AI} - D_{BI})}{(x_A D_{AI} + x_B D_{BI})} \alpha kT \nabla x_A = +K_I kT \nabla x_A \tag{9}$$

which can now be compared with the other drift forces ∇G_V^s and ∇G_I^s.

These other drift forces arise from the spatial and compositional dependence of the point defect energy in its saddle point, and they will henceforth be called intrinsic drift forces. The Gibbs free energy G_V^s is composed of the following terms:

$$G_V^s = G_V^f + G_V^m + U_V^s \tag{10}$$

Here, G_V^f and G_V^m are the Gibbs free energies for vacancy formation and migration, respectively, and U_V^s is a mechanical interaction energy to be discussed below.

Both G_V^f and G_V^m are functions of the local alloy composition, and their dependence on x_A can be deduced from measurements of the self-diffusion coefficient as a function of alloy composition. If D_{SD} denotes this coefficient, then the intrinsic drift force on vacancies in the absence of U_V^s is given by

$$\nabla(G_V^f + G_V^m) = -kT\nabla[\ln D_{SD}] \ . \tag{11}$$

As stated earlier, the measurement of a tracer diffusion coefficient for interstitials is impossible. Therefore the definition of the intrinsic drift force on interstititals requires a different approach. In this case, we must utilize the fact that the formation energy of an interstitial is mainly determined by its strain or bulk relaxation energy.[10,29]

$$U_I^{BR} = \frac{2\kappa\mu}{3\kappa + 4\mu} \frac{v_I^2}{\Omega} \tag{12}$$

where μ and κ are the shear and bulk modulus, respectively, and v_I is the interstitial relaxation volume. The energy U_I^{BR} *is* for an interstitial in

the bulk, i.e., far from a free surface, and is henceforth referred to as the bulk relaxation energy. If one uses the value of the relaxation volume v_I for the saddle-point configuration, then $U_I^{BR} \cong G_I^f + G_I^m$.

In a composition gradient, the elastic moduli κ and μ become functions of the point defect's position and Equation 12 is no longer valid in a strict sence. However, since most of the strain energy of a point defect is contributed from the lattice distortions in its immediate surrounding, Equation 12 remains an excellent approximation when the elastic moduli vary little over distances on the order of a few lattice parameters. In fact, it has been shown [29] that when position-dependent elastic moduli $\kappa(\vec{r})$ and $\mu(\vec{r})$ are used in Equation 12, then ∇U_I^{BR} represents an exact upper bound to the actual force $\nabla(G_I^f + G_I^m)$; here $\vec{r}$ denotes the position of the interstitial.

For both vacancies and interstitials, the mechanical interaction U^s is composed of three contributions. First, it contains the interaction U^σ with the stress field of the sink. This contribution remains independent of the radiation-induced segregation unless precipitates form. The second contribution is the image interaction U^{Im} in the case of voids, and it simply represents a correction to the bulk relaxation energy U^{BR} when the point defect approaches the free void surface. Again, this interaction U^{Im} is affected very little by the segregation provided the latter does not result in the formation of a precipitate shell. The final contribution arises from coherency strains, when segregation leads to a spatially varying lattice parameter $a_o(\vec{r})$. If $\bar{a}_o$ is the average latttice parameter, and

$$\eta(\vec{r}) = [a_o(\vec{r}) - \bar{a}_o] / \bar{a}_o \tag{13}$$

the relative variation, then the coherency strain interaction can be shown to be given by [29]

$$U^c = \frac{3\kappa 4\mu}{3\kappa + 4\mu} v\eta(\vec{r}) \ . \tag{14}$$

The physical origin of the segregation-induced bias changes can now be summarized as follows.

Whereas the bias factors of sinks in materials without segregation is due to the action of the interaction force ∇U^{σ} in the case of dislocations, and due to the force $\nabla(U^{\sigma} + U^{Im})$ in the case of voids, additional forces emerge as a result of segregation. These are:

a. the intrinsic force due to the composition dependence of both the point defect formation and migration energy, both can be expressed as a strain energy U^{BR} in the case of interstititals; this force is a function of the local elastic moduli;
b. the lattice-mismatch force ∇U^{C} arising from the coherency strain field when the lattice parameter changes with composition;
c. the Kirkendall force $\vec{F}_K = \pm KkT\nabla\chi_A$, arising from the differences in atomic diffusivities.

5.6 Comparison of the Various Drift Terms

The various drift forces require for their evaluation basic material parameters such as elastic moduli, lattice parameter, atomic diffusivities, and the activity coefficients. These are required both as a function of composition and temperature. Unfortunately, such detailed information is presently not available, and an accurate determination of the drift forces cannot be made. However, it is possible to assess the order of magnitude of these forces with the available data.

For an estimate of the intrinsic and the Kirkendall forces on vacancies we consider the measurements of Million, et al.[30] on tracer diffusion coefficients and the activity coefficient γ_{Ni} in binary austenitic Fe-Ni alloys. For the temperature range between 985 and 1305°C, they found the following relationships for the tracer diffusion coefficients:

$$\log_{10} D_{Ni}^{0*} = 0.537 - \frac{15152}{T} - \chi_{Fe}\left(0.488 - \frac{340}{T}\right) \qquad (15)$$

$$\log_{10} D_{Fe}^{o*} = -0.142 - \frac{14561}{T} + \chi_{Ni} \left(1.106 - \frac{993}{T}\right) \tag{16}$$

Here, T is the absolute temperature, and the diffusion coefficients are given in units of cm^2/s. Using the definition

$$D_{SD} = \frac{1}{f_V} [\chi_{Ni} D_{Ni}^{o*} + \chi_{Fe} D_{Fe}^{o*}] \tag{17}$$

for the self-diffusion coefficient we can compute the intrinsic force or the effective activation energy $-kT \ln D_{SD}$ for self diffusion. Figure 5 shows the results as a function of the nickel composition and temperature. These results were normalized to give the same value of the activation energy at $\chi_{Ni} = 1$. Note that the intrinsic force is equal to the slope of these curves multiplied by the nickel gradient. For a segregation gradient spanning a 20% difference in nickel composition, we find that the potential of the intrinsic force on the vacancies is of the order of 0.01 eV or less, and it can be positive or negative depending on temperature and nickel composition. Note that a decrease in the force potential with increasing nickel means that the vacancy is attracted towards higher nickel concentration.

Equations 15 and 17 can also be used to evaluate the Kirkendall force coefficient K_V defined by the relationship (8). For the thermodynamic factor we use extrapolations of values measured in the temperature range from 950 to 1250°C.[30] Figure 6 shows the measured results as solid lines and our extrapolation to lower temperatures as dashed lines. The Kirkendall force coefficient K_V for vacancies is shown in Figure 7. It is seen that K_V is negative for alloy composition with less than 35% nickel, and positive for high nickel compositions. A negative coefficient K_V implies that the vacancies are attracted to regions of higher nickel concentration whereas positive values imply the reverse. In order to compare the Kirkendall force with other drift forces we integrate the force over a nickel variation of 20%. The resulting potential difference is then found to be on the order of 0.4 kT or less, depending on temperature and alloy composition. Therefore, the Kirkendall force corresponds to an interaction potential on the order of 0.02 eV or less.

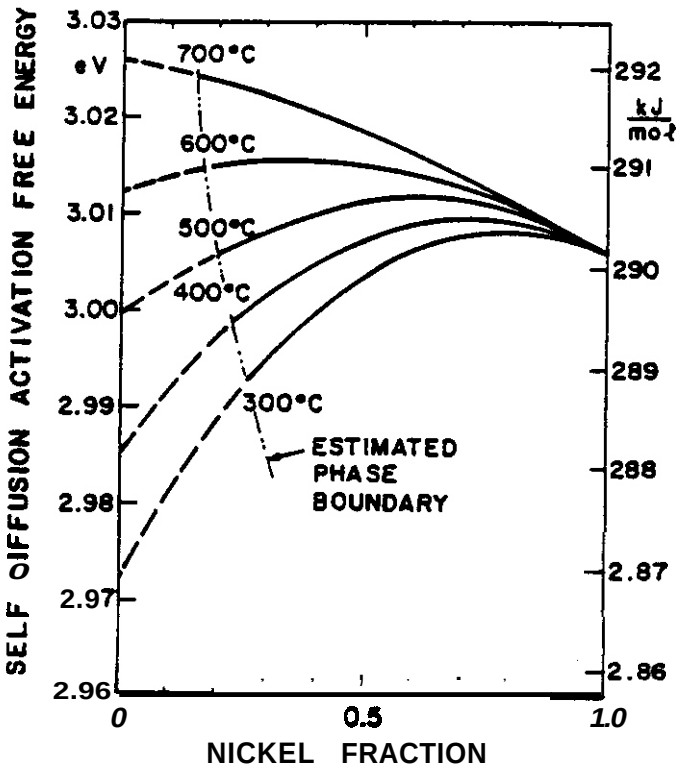

FIGURE 5. Activation Free Energy for Self-Diffusion in Binary Fe-Ni Alloys.

In order to obtain an estimate for the Kirkendall force K_I on interstitials, we suppose that the interstitial formation energy in nickel and in fcc iron differs by

$$G^s_{Ni,I} - G^s_{Fe,I} = \pm 0.05 \text{ eV}$$

and that the energies $G^s_{Ni,I}$ and $G^s_{Fe,I}$ are the activation energies for the tracer diffusion coefficients of nickel and iron migrating as part of a dumbbell interstitial. It turns out that as long as these energies are larger than about 1 eV, only their difference affects the Kirkendall force K_I. The computed values of K_I are shown in Figure 8 for the case that the difference between $G^s_{Ni,I}$ and $G^s_{Fe,I}$ is negative. In this case, the Kirkendall force makes the interstititals migrate preferentially towards higher nickel concentrations. On the other hand, if the difference in the activation energies is positive, then the interstitials are attracted toward regions of lower nickel concentration.

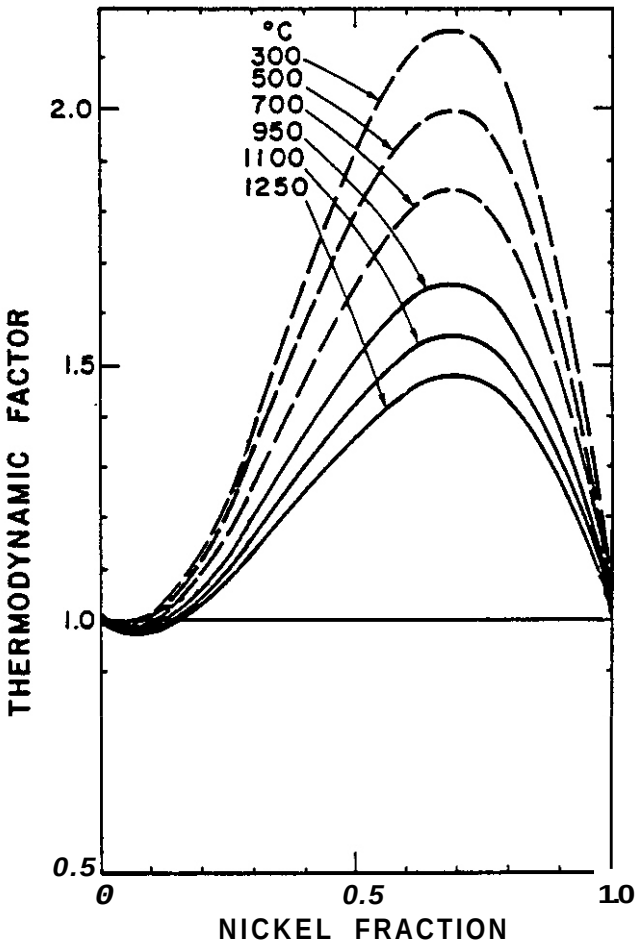

FIGURE 6. Thermodynamic Factor for Binary Fe-Ni Alloys. Solid lines are based on measurements and dashed lines are based on extrapolations.

The magnitude of the Kirkendall force on interstitials is of the same order as the Kirkendall force on vacancies.

The remaining interaction energies U^{σ}, U^{I}, U^{BR} and U^{C} have been evaluated in previous publications,[10,17-18] and typical values are listed in Table 1 together with the above estimates for the potentials of the intrinsic and Kirkendall forces.

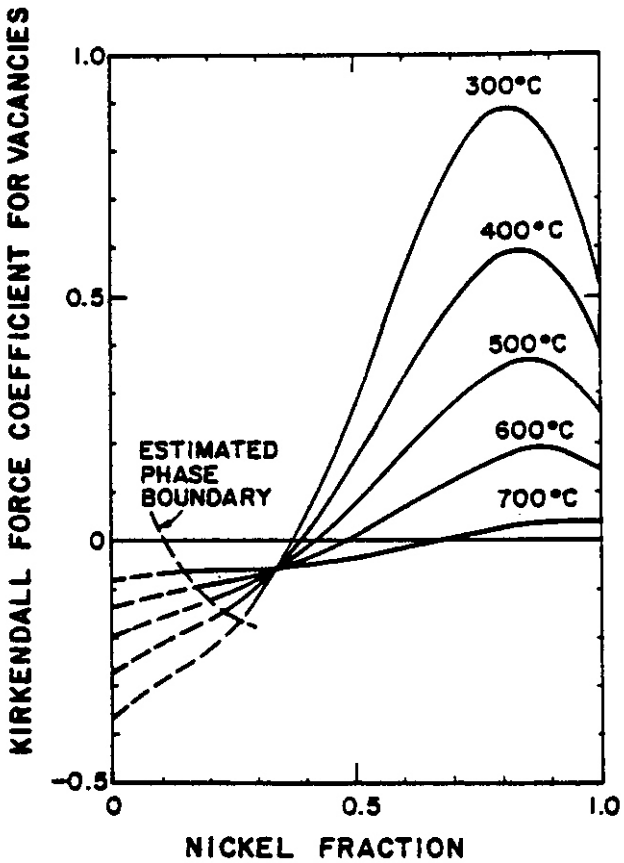

FIGURE 7. Coefficient of the Kirkendall Force on Vacancies in Binary Fe-Ni Alloys

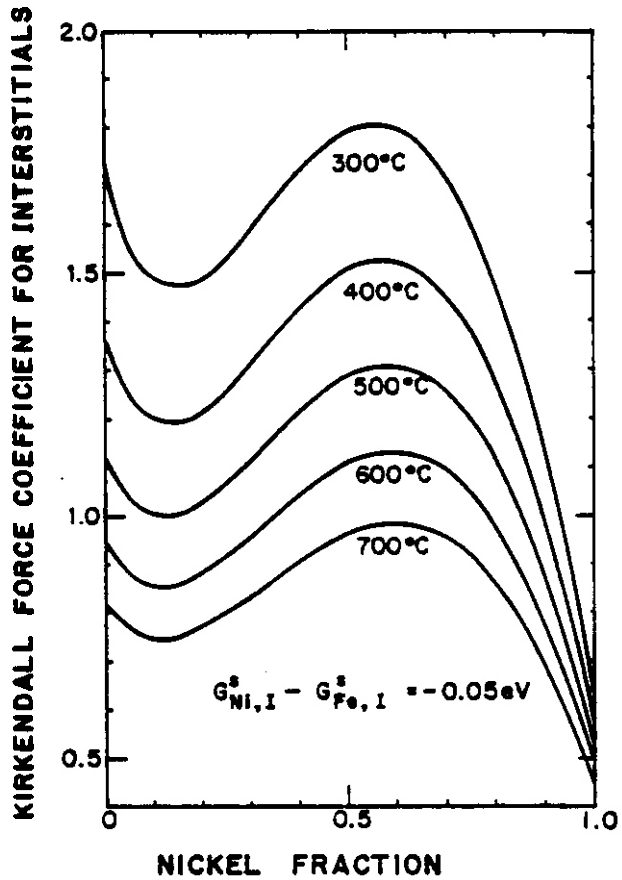

FIGURE 8 Possible Variation of the Coefficient for the Kirkendall Force on Intersititials as a Function of the Composition of Binary Fe-Ni Alloys.

TABLE 1

TYPICAL VALUES FOR THE POTENTIALS OF THE DRIFT FORCES IN FE-NI ALLOYS

Potential Energy in eV (and 10^{-21} J)	Interstitial	Vacancy
U^{σ} at a distance of 10 b* from an edge dislocation and above (upper sign) or below (lower sign) the glide plane	±0.25(±40)	±0.05(±8)
U^{Im} at a distance from the void surface of 2b*	-0.25(-40)	-0.025(-4)
and 5b	-0.005(-0.8)	-0.0005(-0.08)
Change in bulk relaxation energy, ΔU^{BR} for ±3% shear modulus change	±0.24(±39)	±0.006(±1)
U^{c} for a lattice parameter change of ±0.4%	±0.24(±39)	±0.03(±5)
Change of potential for the intrinsic force over a 20% nickel variation	----	$\lesssim$0.01(1.6)
Change of potential for the Kirkendall force over a 20% nickel variation	$\lesssim$0.02(3.2)	$\lesssim$0.02(3.2)

*b = Burgers vector

5.7 Conclusions

When the various potentials are compared in relationship to U^{σ} we arrive at the following conclusions.

a. Radiation-induced segregation introduces new drift forces which are of comparable magnitude to the strain-induced drift force present without segregation. As a result, segregation can profoundly change the bias of sinks for preferential absorption of interstitials or vacancies.

b. The Kirkendall force on interstitials is small in comparison to the other forces. However, the forces on the interstitial introduced by variations in elastic moduli and lattice parameter are significant.

c. On the other hand, the Kirkendall and the intrinsic force on the vacancy are comparable to both the stress-induced force and the force arising from coherency strains, whereas the force originating from the gradient of the elastic moduli is of secondary importance.

d. In general, RIS affects the total force on interstitials to a much larger degree than the total force on vacancies. Therefore, the sink bias factors for interstitials are expected to be changed more than those for vacancies. Nevertheless, since it is the net bias, i.e., the relative difference of bias factors, which determines void nucleation and growth, the effect of RIS on the vacancy bias factors may not be negligible.

e. The reversal of sign for the Kirkendall force at 35% nickel may provide an explanation for the strong dependence of swelling on nickel content below 35% Ni in Fe-Ni-Cr alloys.

f. Since void nucleation is quite sensitive to the void bias, it is anticipated that the primary effect of nickel segregation will be experted on void nucleation rather than growth.

Segregation, and in particular substantial nickel enrichment near sinks, appears to be a general phenomenon in nickel-containing austenitic alloys. Significant bias modifications must accompany this segregation, and the degree and nature of the bias change is expected to be a strong function of the alloy composition and the temperature. However, fundamental properties such as elastic moduli, lattice parameter, atomic diffusivities, and thermodynamic properties as a function of alloy composition and temperature are not sufficiently well known to establish a completely quantitative relationship between alloy composition and void swelling resistance.

6.0 References

1. Workshop on Solute Segregation and Phase Stability During Irradiation, J. L. Stiegler, Editor, J. Nucl. Mater., 83 (1979) 1-237.

2. Proceedings of Symposium on Phase Stability During Irradiation, Pittsburgh, PA, October 1980, J. R. Holland, L. K. Mansur and D. I. Potter, Eds., The Metallurgical Society of AIME, New York, 1981.

3. P. R. Okamoto, N. Q. Lam and H. Wiedersich, Proceedings of the Workshop on Correlation of Neutron and Charged Particle Damage, June 1976, Oak Ridge, TN, J. O. Stiegler, Ed., p. 111.

4. F. A. Garner and W. G. Wolfer, J. Nucl. Mater., 102 (1981) 143-150.

5. L. K. Mansur, M. R. Hayns and E. H. Lee, in Reference 2, pp. 359-382.

6. L. K. Mansur, Phil. Mag. A, 44 (1981) 867-877.

7. F. A. Garner, in Reference 2, pp. 165-189.

8. F. A. Garner and D. L. Porter, "History Dependence and Consequences of the Microchemical Evolution of AISI 315," Effects of Radiation on Materials: Eleventh Conference, ASTM STP 782, H. R. Brager and J. S. Perrin, Eds., American Society for Testing and Materials, 1982, in press.

9. W. G. Johnston, T. Lauritzen, J. H. Rosolowski and A. M. Turkalo, "The Effect of Metallurgical Variables on Void Swelling," in Radiation Damage in Metals, N. L. Peterson and S. D. Harkness, Eds., American Society of Metals, 1976, pp. 227-266.

10. W. G. Wolfer and L. K. Mansur, J. Nucl. Mater., 91 (1980) 265.

11. A. Si-Ahmed and W.G. Wolfer, "Effect of Radiation-Induced Segregation on Void Nucleation," Effects of Radiation on Materials: Eleventh Conference, ASTM STP 782, H. R. Brager and J. S. Perrin, Eds., American Society for Testing and Materials, 1982, in press.

12. J. S. Watkins, J. Standring, A. D. Miodownik and J. H. Gittus, Proceedings of International Conference on Radiation Behavior of Cladding and Structural Materials for Fast Breeder Reactors, Ajaccio Corsica, 1979.

13. W. G. Wolfer and A. Si-Ahmed, J. Nucl. Mater., 99 (1981) 117.

14. W. R. Rees, B. D. Burns and A. T. Cook, J. of the Iron and Steel Inst., 162 (1949) 325.

15. J. F. Bates, J. Nucl. Mater., 87 (1979) 409.

16. H. Masumoto, H. Saito, T. Kona and Y. Sugai, Science Report of the Research Institute, Tohoku University, Series A, 8 (1956) 471.

17. W. G. Wolfer and M. Ashkin, J. Appl. Phys., 47 (1976) 791.

18. W. G. Wolfer and M. Yoo, Proceedings of International Conference on Radiation Effects and Tritium Technology for Fusion Reactors, Gatlinburg, TN, 1975, CONF-750989, Volume 4, 1976, p. 458.

19. H. R. Brager and F. A. Garner, Proceedings of TMS-AIME Symposium on Advanced Techniques for the Characterization of Irradiated Metals, Las Vegas, NV, February 1980, in press. Also in Damage Analysis and Fundamental Studies Quarterly Progress Report, DOE/ER-0046/1, May 1980, p. 157.

20. H. R. Brager and F. A. Garner, in Reference 2, pp. 219-235.

21. D. L. Porter and E. L. Wood, J. Nucl. Mater., 83 (1979) 90.

22. G. Brun, J. Le Naour and M. Vouillon, J. Nucl. Mater., 101 (1981) 109.

23. M. Terasawa, S. Nakahigashi, H. Kamai, T. Takeyama, S. Ohonuki and H. Takahashi, J. Nucl. Mater., 103 and 104 (1981) 1017.

24. A. D. Marwick, W. A. D. Kennedy, D. J. Mazey and J. A. Hudson, Scripta Met., 12 (1978) 1015.

25. A. Hishinuma, Y. Katano and K. Shiraishi, J. Nucl. Mater., 103 and 104 (1981) 1063.

26. A. Hishinuma, Y. Katano and K. Shiraishi, J. Nucl. Sci. Tech., 15 (1978) 690.

27. L. E. Thomas, to be published in Ultramicroscopy.

28. L. E. Thomas, to be published in the Proceedings of the 38th Annual Meeting of the EMSA Society of America, 1982, Washington, DC, Claitors, 1981.

29. W. G. Wolfer, to be published in Journal of Nuclear Materials.

30. B. Million, J. Rozickova, J. Velisek and J. Vrestal, Mat. Sci. Eng., 50 (1981) 43.

7.0 Future Work

This effort will continue as additional data become available.

8.0 Publications

This paper will be published in the Proceedings of the Eleventh ASTM Conference on Effects of Radiation on Materials, Scottsdale, AZ, June 27-29, 1982.

THE INFLUENCE OF COLD WORK LEVEL, SOLUTE AND HELIUM CONTENT ON THE SWELLING OF "PURE" AISI 316 (Fe-17Cr-16.7Ni-2.5Mo)

H. R. Brager and F. A. Garner (Hanford Engineering Development Laboratory)

1.0 Objective

The object of this effort is to determine the relative contribution of cold-work, solute and helium to the microstructural/microchemical evolution of irradiated stainless steel.

2.0 Summary

As part of a larger effort to study the influence and possible synergisms involving solutes, helium and cold working, a simple quaternary alloy representing AISI 316 without solutes was irradiated in the Oak Ridge Research Reactor (ORR). This alloy's composition is Fe-17Cr-16.7Ni-2.5Mo and is designated P-7 or "pure 316." It was irradiated at 350, 550, and 650°C in each of the following conditions: annealed, 20 percent cold worked, annealed plus helium implanted, 20 percent cold worked plus helium implanted and various annealed or cold work plus implanted and aged conditions. The implanted specimens contained a range of helium concentrations injected at ambient temperatures. All specimens chosen for examination by electron microscopy and immersion density were irradiated to 3 to 5 dpa.

In agreement with an earlier microchemically-based prediction it was found that both the volume and density of voids were insensitive to cold work in an alloy lacking minor solutes such as silicon and carbon. This finding is inconsistent with most theoretical treatments of the effect of cold work on swelling in commercial alloys. The high density of dislocations after cold working has been thought to be responsible for the reduction of point defect concentrations and subsequent void nucleation. While the preinjection of 30 appm heliun appeared to suppress visible swelling, this may be an illusion related to resolution problems in imaging very

small voids. Both density change measurements and postirradiation aging studies indicate that swelling may exist in the preinjected specimens in the form of unresolvable cavities.

3.0 Program

Title: Irradiation Effects Analysis (AKJ)
Principal Investigator: D. G. Doran
Affiliation: Hanford Engineering Development Laboratory

4.0 Relevant DAFS Program Plan Task/Subtask

II.C.1 Effects of Material Parameters on Microstructure
II.C.2 Effects of Helium on Microstructure

5.0 Accomplishments and Status

5.1 Introduction

The high temperature irradiation of various 300 series stainless steels in both thermal and fast breeder reactors has recently been shown to lead to two concurrent and interactive evolutions. One involves the microstructural components associated with swelling and irradiation creep[1] and another "microchemical" evolution arises from extensive repartitioning of elements between the matrix and various precipitate phases.[2-11] This latter evolution has been proposed as playing a dominant role in determining much of the radiation response of AISI 316 stainless steel.[2]

It now appears that the microchemical evolution can be divided into two sub-categories. The first involves the segregation of elements (particularly nickel) to microstructural sinks such as voids and dislocations. It has been proposed that much of the dependence of void swelling of Fe-Ni-Cr alloys on nickel content can be explained in terms of the segregation of nickel to void surfaces.[12] This segregation mechanism is not in

itself sufficient to change appreciably the composition of the alloy matrix.

The second category involves the segregation of elements, particularly nickel and silicon, into a variety of precipitate phases, some of which form only under irradiation and redissolve in its absence.[13] This mechanism has the potential for providing a larger reservoir for segregated elements, thereby altering significantly the composition of the alloy matrix. The capacity of this reservoir is largely determined by the level of solutes such as silicon and carbon.[2,3] When in solution, silicon (and carbon at temperatures below approximately 525°C) extends the time required in fast breeder reactors for voids to nucleate.[2] It has been proposed that this occurs due to silicon's influence on the effective vacancy diffusion coefficient.[14]

The rate of removal into precipitates of important elements such as nickel, silicon and carbon has been shown to be directly affected by cold working prior to irradiation.[7,11] It also has been definitively shown that in AISI 316 the temporary suppression of swelling by cold work cannot be correlated to the details of the dislocation density but only to the effect of cold work on the evolution of precipitate phases.[7] It has also been proposed that there is a strong interaction between the dislocation density and the carbon level and that cold work might exert no influence on swelling in the absence of carbon or other interstitial solutes.[2]

These findings are inconsistent with most theoretical treatments of the effect of cold work on swelling. The high density of dislocations after cold working has been thought to be responsible for the reduction of point defect concentrations and subsequent void nucleation.

As part of a larger effort to unravel the intricacies of the swelling/microchemical correlation it was decided to test the validity of the concept of linked behavior between the solute level and the dislocation

density. Since there is also some current controversy over the relative contributions of microchemistry and helium to void growth[9,10], a simple "model" alloy of AISI 316 was examined in which the effects of cold work and heliun could be studied without introducing the complexities of changes in matrix composition or cavity-precipitate interactions. The helium was also introduced by two mechanisms, both preinjection at ambient temperature and by irradiation in a reactor with a thermalized neutron spectrun to produce helium from the "double-nickel" reactions[15,16] $^{58}Ni(n,\gamma)^{59}Ni(n,\alpha)^{56}Fe$.

5.2 Experimental Details

The reactor employed was the Oak Ridge Research Reactor (ORR), using the MFE2 experiment in core position E7. The details of this experiment[17] as well as the displacement and heliun levels attained[18] are reported elsewhere.

The alloy used in the study was the quaternary Fe-17Cr-16.7Ni-2.5Mo, designated variously as P-7 or "pure 316" and supplied by Oak Ridge National Laboratory. This alloy lies near the high nickel end of the composition range typical of AISI 316 and contains less than 0.005 weight percent carbon, low residual elements (less than 0.1 weight percent each) and 0.03 weight percent oxygen. It has been extensively irradiated in other experiments[19-21] and as shown in Figure 1 is known to swell without the hesitation normally exhibited by AISI 316 containing the usual complement of solutes.

This alloy (and four others not discussed in this report) were irradiated side-by-side in the solution annealed, 20 percent cold worked (CW), and cold worked and various aged conditions. The specimens were in the form of 3 mm microscopy disks and heliun preimplantation was uniformly introduced to nominal levels of 0, 10, and 30 appm. The specimens were contained in capsules filled with liquid metal and irradiated to doses of 3 to 5 dpa at nominal temperatures of 350, 550 and 650°C. The volume changes

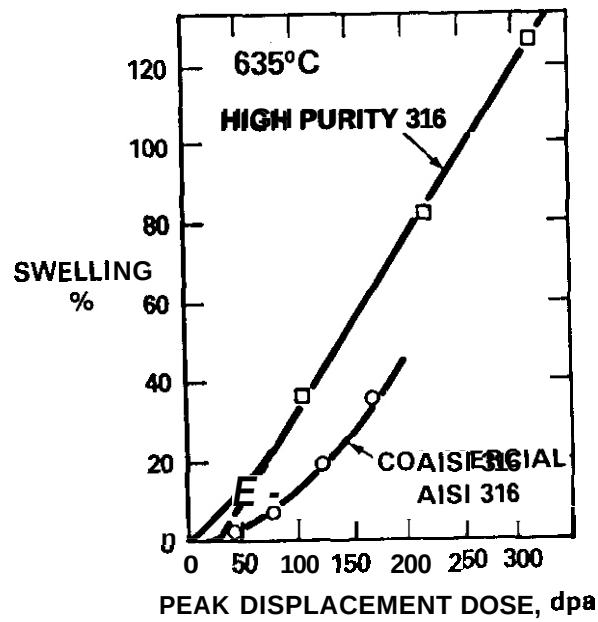

FIGURE 1. Dependence of Swelling on Impurity Level at 625-635°C in Nickel Ion Irradiated AISI 316. (19) "High Purity" (HP316) is the P-7 alloy described in this report.

of the specimens were measured by an immersion density technique with an accuracy of ±0.16 percent. At this time only the specimens at 350 and 550°C have been examined by microscopy.

5.3 Examination of Specimens Without Preinjected Helium

At 350°C and 3 dpa, no identifiable voids or precipitates were observed in either the annealed or 20 percent cold worked specimens. In addition to radiation-induced Frank loops, there were small clusters in both the annealed and cold worked specimens, some of which, however, might be small voids ($\lesssim$3 nm). Attention was particularly concentrated on the specimens iradiated to 4 dpa at 550°C, containing 33 appm of helim introduced by the irradiation in ORR.

The immersion density measurements showed neither significant swelling nor discernible influence from any preirradiation treatment. The mean density for the (1) 20 percent CW, (2) annealed, (3) annealed plus 40 appm He and (4) annealed plus 40 appm He plus 750°C aged were -0.22 percent, -0.15 percent, -0.12 percent and -0.25 percent respectively with a total deviation of approximately ±0.10 percent. Note that these measurements are just on the boundary of the accuracy of the measurement technique.

As shown in Table 1, the void development at this fluence appears to be somewhat variable. Micrographs of the examined material, however, illustrate a surprising consistency and homogeneity in any one void micrograph, Figure 2. In addition, the void densities are shown to decrease with major increases in the foil thickness, Figure 3, for both annealed and cold worked specimens. The increase in threshold size of voids which are resolvable in thick foils appears to dominate over any nonuniformity in the void formation. Note that the range of swelling in each of the annealed and cold worked specimens overlaps, supporting the conclusion that, while apparently nonuniform on a microscopic level, the macroscopic swelling is essentially unaffected by cold working. This result contrasts with the very large effect that cold work has on swelling in austenitic steels such as AISI 316. Figure 4 illustrates the effect that cold work has on suppressing void formation in AISI 316 irradiated at 560°C to 4.5 dpa.

The dislocation density in the annealed specimens is still relatively low, averaging about 1×10^{10} cm^{-2}. A low density ($\sim 4 \times 10^{12}$ cm^{-3}) of large Frank interstitial loops was found, having a mean diameter of approximately 100 nm. The dislocation density in the cold worked specimen was higher at about 4×10^{10} cm^{-2} but with no Frank loops observed. This difference in dislocation density can be seen in Figure 2. No precipitates were observed in either specimen.

TABLE 1

VOID FORMATION IN Fe-17Cr-16.7Ni-2.5Mo SPECIMENS
(550°C IRRADIATION TEMPERATURE; 4 dpa)

Specimen Identification	(*)	Foil Thickness, Å	Void Density, cm^{-3}	Mean Diameter, Å	Swelling, %	Dislocation Density (cm/cm^3)
Annealed	(a)	2000	0.7×10^{15}	114	0.08	3.7 x 109
	(b)	600	5.2×10^{15}	66	0.10	2.1×10^{10}
	(c)	350	3.1×10^{15}	109	0.31	1.7×10^{10}
20% Cold-Worked	(d)	1600	0.9×10^{15}	90	0.04	2.0×10^{10}
	(e)	1600	1.3×10^{15}	70	0.02	4.1×10^{10}
	(f)	1320	0.8×10^{15}	59	0.01	4.0×10^{10}
	(g)	590	3.3×10^{15}	79	0.10	5.0×10^{10}
	(h)	510	4.3×10^{15}	62	0.11	6.3×10^{10}

(*) Letter identified micrograph in Figure 2 corresponding to a portion of the area used to obtain void data.

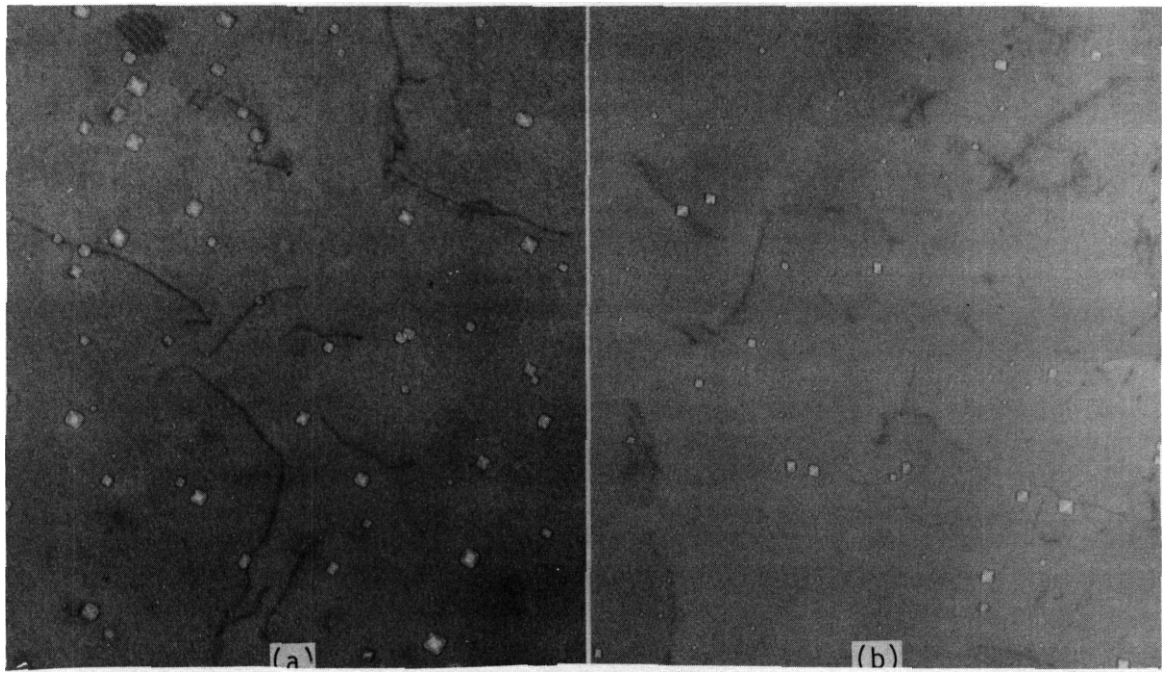

FIGURE 2. Void Microstructure in Annealed and 20% Cold-Worked Fe-17Cr-16.7Ni-2.5Mo Irradiated in ORR at 550°C to 4 dpa. (Micrographs shown in the same order as indicated in Table 1.)

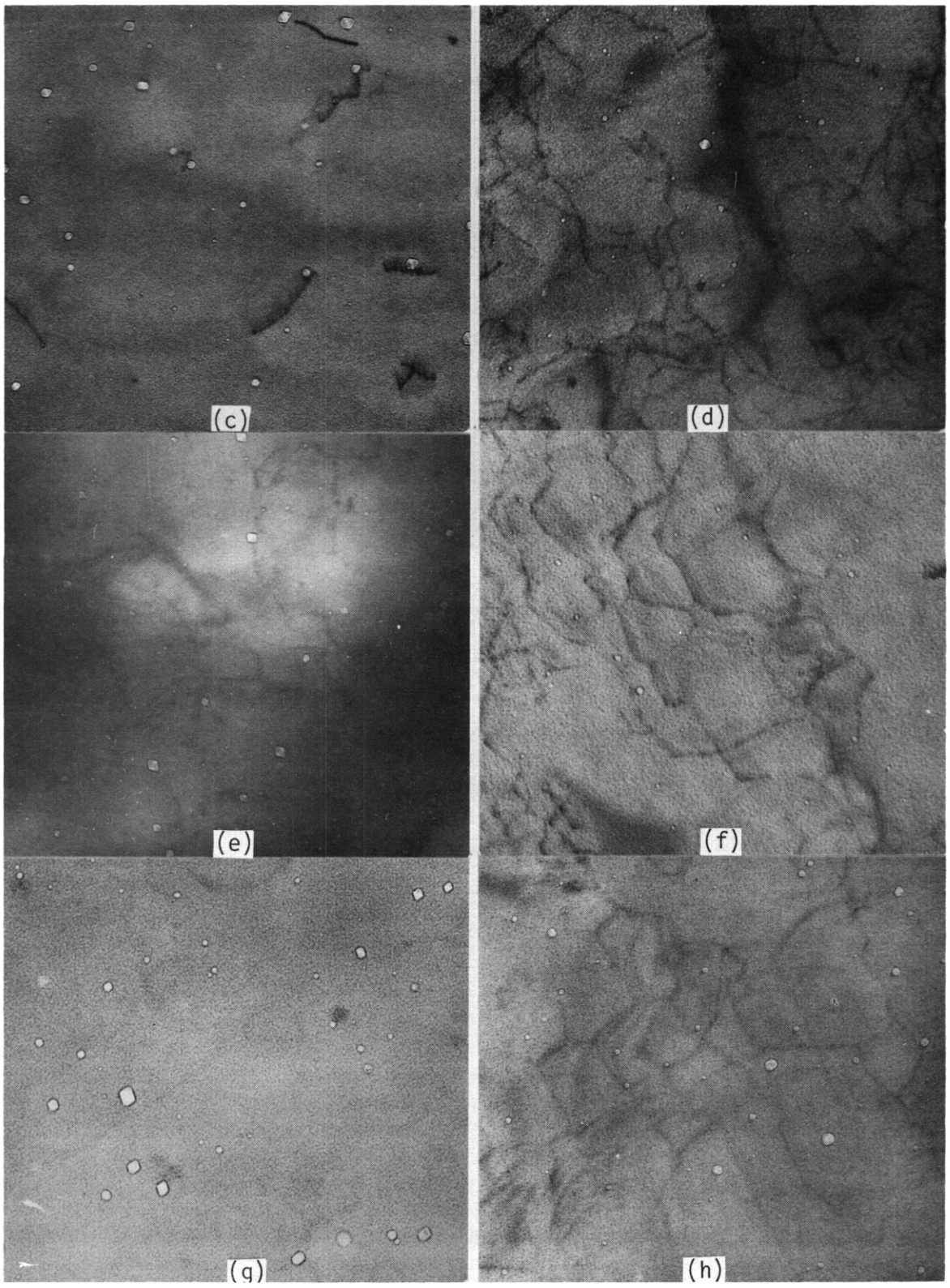

FIGURE 2. (Cont'd)

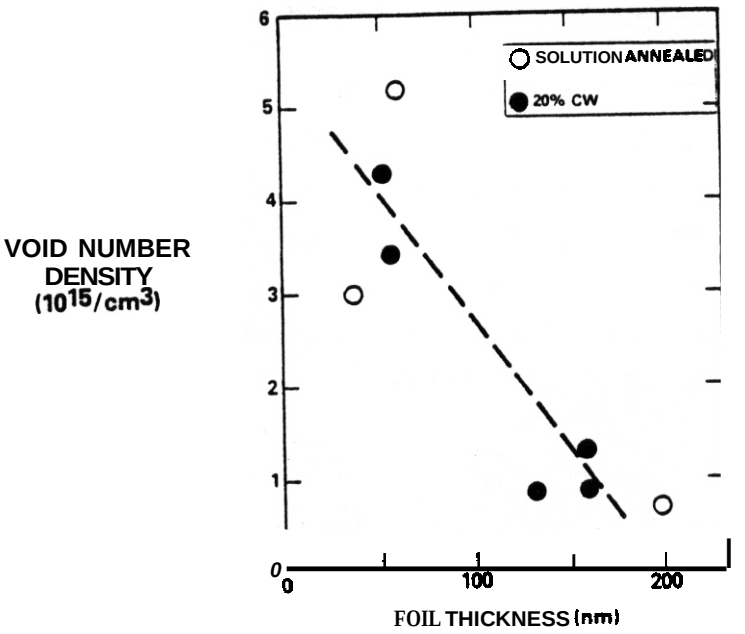

FIGURE 3. Effect of Foil Thickness on Number Density of Visible Voids.

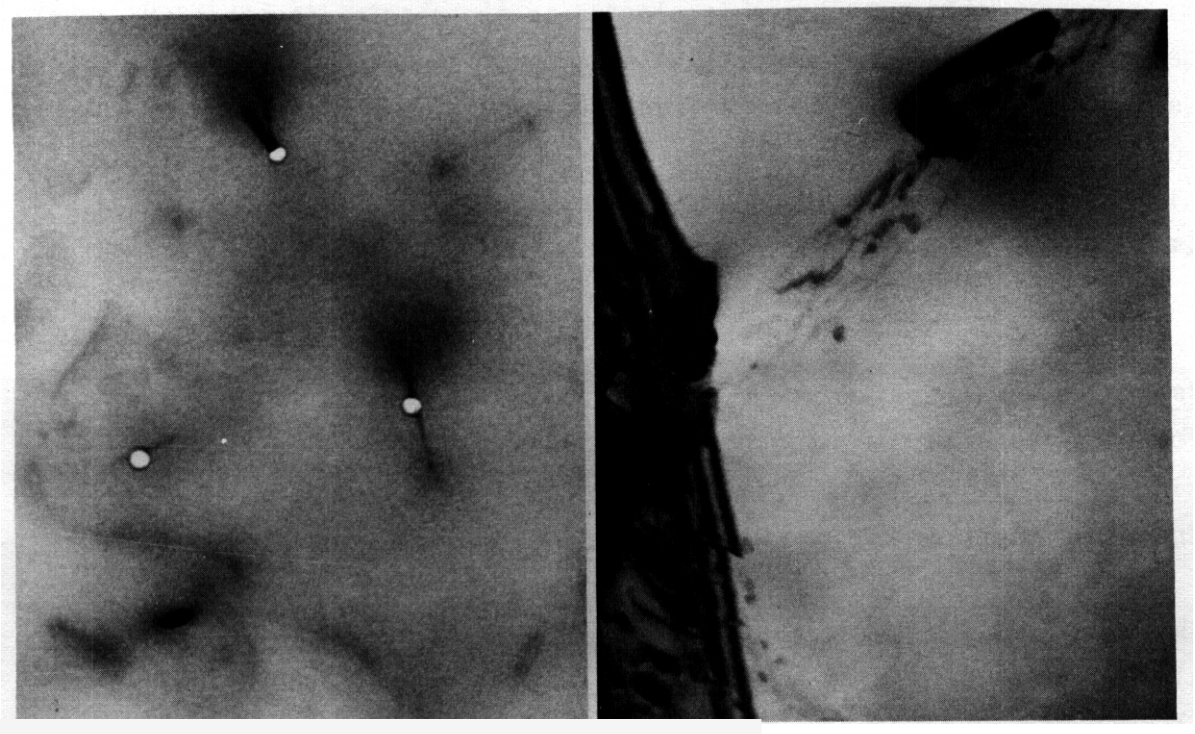

FIGURE 4. Effect of (a) Solution Annealing and (b) Cold-Working 20% on Void Formation in AISI 316 Stainless Steel Irradiated in EBR-II at 560°C to 4.5 dpa.

5.4 Examination of Specimens with Preimplanted Helium

Two other specimens irradiated at 550°C exhibited no resolvable voids although density change measurements showed swelling comparable to that of the uninjected specimens discussed in the previous section. These specimens were (1) annealed plus 30 appm He and (2) annealed plus 30 appm He followed by aging at 750°C for one hour. It appeared that preinjection either completely suppressed the swelling or distributed it into such small cavities that they were unresolvable.

The density change measurements, however, suggest that the apparent suppression of swelling by heliun preinjection may be misleading. In other words, the cavity density may have been increased sufficiently by preinjection that the voids produced were smaller than the resolution limit (~3.0 nm) of the normal imaging techniques used in the electron microscope. This conclusion is clouded by the possibility that the small density decrease observed in these specimens may have risen from elemental segregation and not from unresolved cavities. In order to examine this possibility, it was decided to extend the resolution limit to smaller sizes by using careful through-focus series of potential cavities under kinematic conditions.

To differentiate between small voids and artifacts, the cavities were imaged in both the under- and over-focused conditions. In the under-focused condition the outer boundary of the cavity appears as a black ring surrounding a light area, while in the over-focused condition the inner region is darker than background and surrounded by a white ring.

In order to define the limit of resolution in the JEOLCO 100X, a preimplanted (30 appm) specimen irradiated at 550°C for ~4 dpa was aged out of reactor for one-quarter hour at 900°C. As shown in Figures 5 and 6 this led to detectable cavities where none were observed prior to irradiation. The mean diameter is 3 nm and their density is about 5×10^{15} cm^{-3}.

This concentration is similar to that found in irradiated specimens which were not preinjected with heliun, although the sizes are smaller by factors of 3 to 4. No cavities were detectable at <1.5 nm diameter.

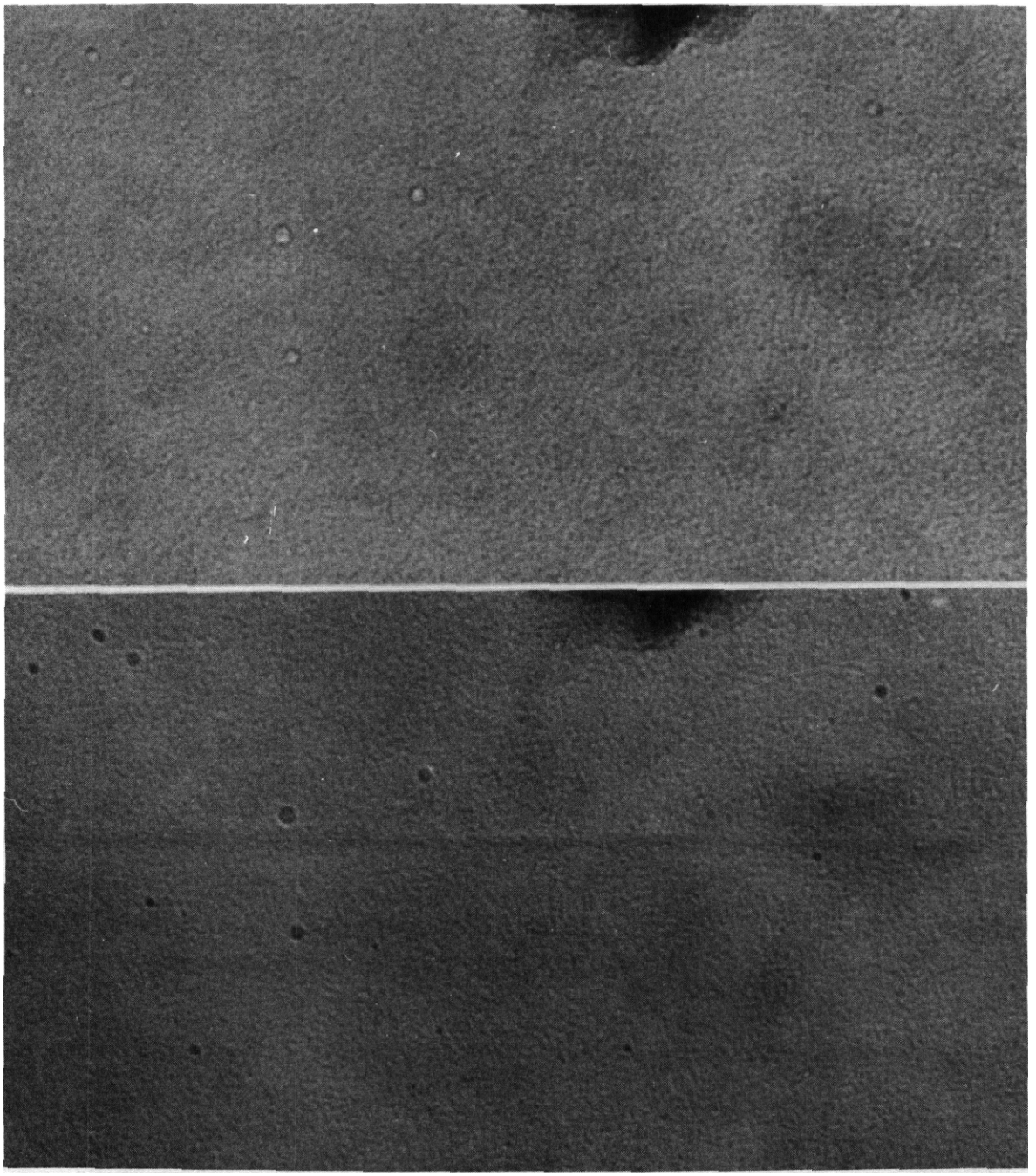

FIGURE 5. Under-Focused (Top) and Over-Focused (Bottom) Images of Cavities in Fe-17Cr-16.7Ni-2.5Mo + 30 appm Helium Irradiated in ORR at 550°C for 4 dpa and then Aged One-Quarter Hour at 900°C.

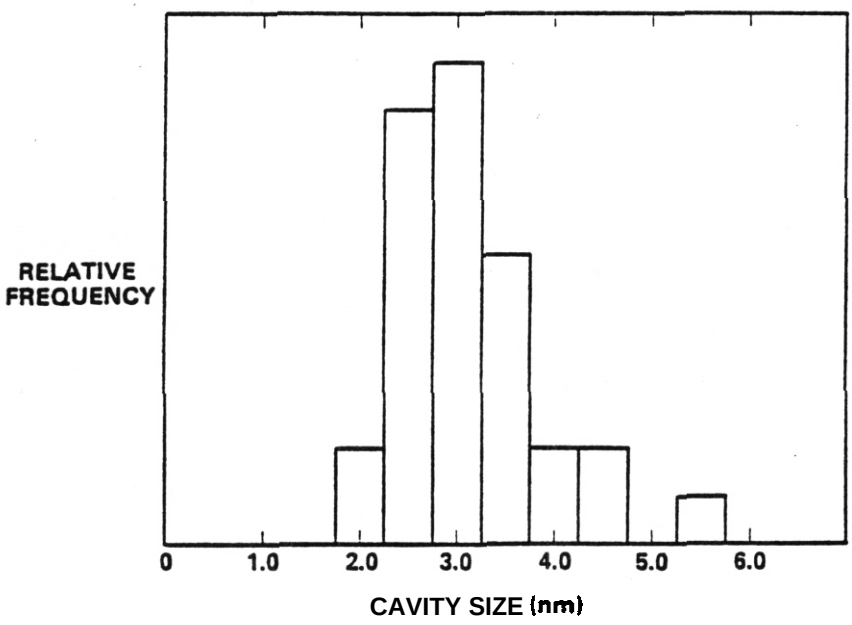

FIGURE 6. Distribution of Visible Cavities Observed in Specimen Described in Figure 5.

Re-examination of another identical specimen aged one-quarter hour at 700°C yielded a low density ($\lesssim 10^{14}$ cm^{-3}) of images, some of which were cavities, and some of which did not behave as cavities. The latter were probably artifacts on the foil surfaces.

An irradiated specimen preimplanted with helium without aging was examined using a careful and extensive through-focus series. This study led to no images which could be attributed to cavities. If indeed cavities exist in this specimen they must possess diameters of $\lesssim 1.5$ nm. Positron annihilation studies are now in progress to detect cavities smaller than this limit.

5.5 Discussion

Examination of the P-7 alloy in this experiment has shown that cold working of this "pure" 316 alloy has no influence on suppressing or encouraging void formation. In AISI 316 containing solutes, however, cold work has a pronounced effect on swelling as shown in Figures 7 and 8. In these and other studies it is clear that the effect of cold work is to extend

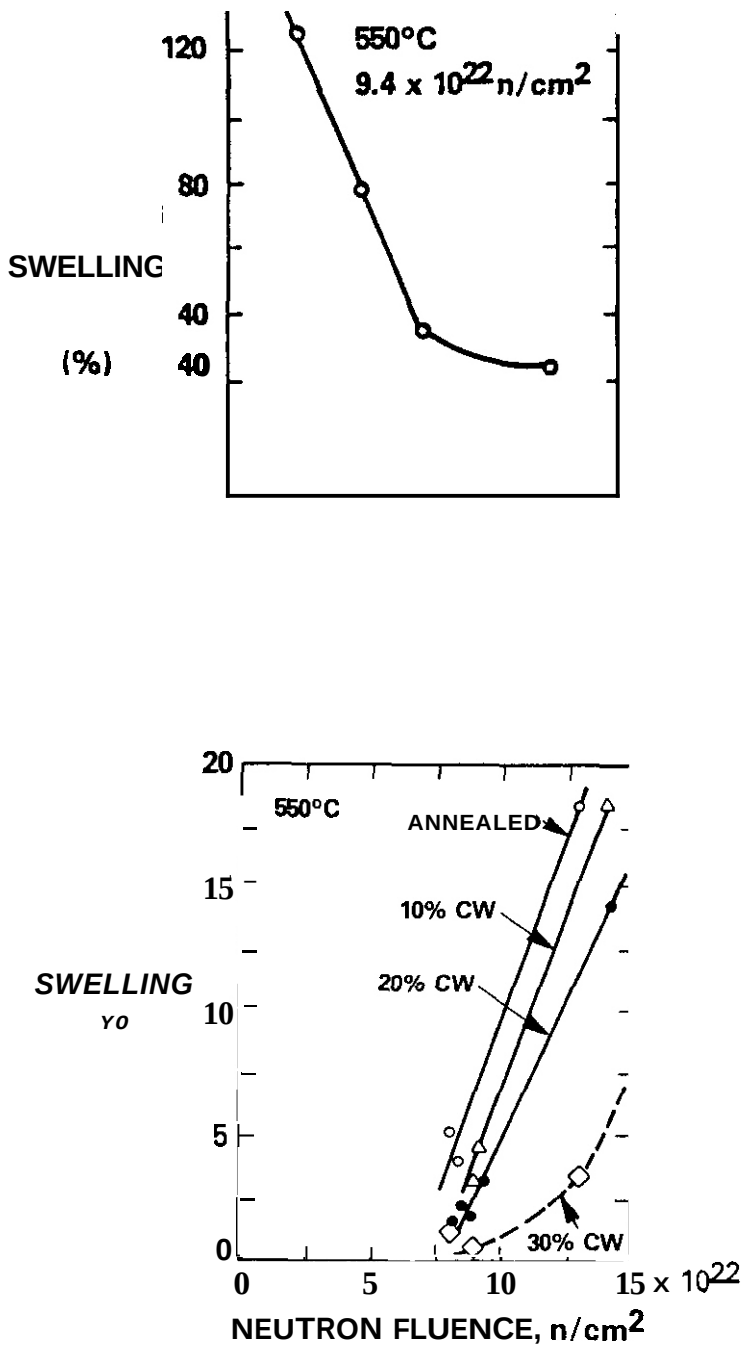

FIGURE 8. Dependence of Neutron-Induced Swelling on Cold Work Level in AISI 316 at 550°C as Reported by Appleby, et al.(23)

Another test of the proposed relative and interactive roles of dislocations and solutes lies in the examination of pure metals. Neutron irradiation data are rather sparse, but cold working of Al, Mg, Cu and Ni leads either to small increases in swelling or no change, Table II.[24] Vanadium seems to be an exception, however, in that cold work reduces swelling.

TABLE II

EFFECT OF COLD WORK ON SWELLING OF PURE METALS

	Impurity content, appm	Temperature, °C	ΔV/V,%		
			Annealed	Slightly cold worked	As rolled
Al•	60	55	0.064		0.35
Mg†	1	55	0.46	0.46	0.46
	100	55	0.16	0.18	0.20
Cu*	100	250	0.17	0.31	0.14
Ni*	500	335	0.5	0.65	1.0
V*	5000	435	0.25	0.08	<0.01

*∿5 x 10^{20} neutrons/cm^2 (E > 0.1 MeV)
†∿1.5 x 10^{20} neutrons/cm^2 (E > 0.1 MeV)

At low doses the void density induced by charged particles is higher in cold worked Cu[25] and Al[26] than in the annealed metal, although there appears to be some dislocation density beyond which the void density and swelling decrease again.[26] Leffers and Singh used charged particle irradiation to study the effect of cold work on swelling and concluded that the subsequent reduction in swelling with cold work is related to recrystallization induced by the energy stored in the dislocations. The recrystallization is assisted by the proximity of free surfaces, especially in charged particle irradiations.[27] In general, the effects of cold work on swelling in ion or electron-irradiated specimens has yielded rather ambiguous results and probably reflects the difficulty in establishing

or maintaining high near-surface dislocation densities.[29]

The apparent suppression of void swelling in this experiment by preinjection of heliun may be an illusion. The density change data imply the possibility that the additional nucleation sites provided by the preinjected heliun may have provided sufficient new voids to cause the small amount of swelling to fall below the void size resolution limit. The definitive answer awaits further studies in progress. At higher displacement levels, there are quite convincing data reported in the literature to show that preinjected helium can either suppress or accelerate[30,31] the onset of swelling.

5.6 Conclusions

Examination of specimens of the P-7 alloy irradiated in ORR shows that the pre-irradiation dislocation density has no significant effect on cavity formation when interstitial solutes like silicon and carbon are absent. These results support the prediction based on a microchemical model that the void formation in "pure" 316 or other alloys that do not develop precipitate phases will be insensitive to cold working.

6.0 References

1. H. R. Brager, F. A. Garner, E. R. Gilbert, J. E. Flinn and W. G. Wolfer, in Radiation Effects in Breeder Reactor Structural Materials, M. L. Bleiberg and J. W. Bennett, Eds., the Metallurgical Society of the American Institute of Mining, Metallurgical and Petroleum Engineers, 1977, pp. 727-755.

2. F. A. Garner, "The Microchemical Evolution of Irradiated Stainless Steels," in Phase Stability During Irradiation, Symposiun Proceedings, the Metallurgical Society of AIME, Pittsburgh, PA, Oct. 5-9, 1980, pp. 165-189.

3. H. R. Brager and F. A. Garner, "Radiation-Induced Evolution of the Austenite Matrix in Silicon-Modified AISI 316 Alloys," ibid., pp. 219-235.

4. W. J. S. Yang, H. R. Brager and F. A. Garner, "Radiation-Induced Phase Development in AISI 316," ibid., pp. 257-269.

5. E. H. Lee, P. J. Maziasz and A. F. Rowcliffe, "The Structure and Composition of Phases Occurring in Austenitic Stainless Steels in Thermal and Irradiation Environments," ibid., pp. 191-218.

6. H. R. Brager and F. A. Garner, J. Nucl. Mat., 73 (1978, pp. 9-19.

7. H. R. Brager and F. A. Garner, "Dependence of Void Formation on Phase Stability in Neutron-Irradiated Type 316 Stainless Steel," Effects of Radiation on Structural Materials, ASTM STP 683, J. A. Sprague and D. Kramer, Eds., ASTM (1979). pp. 207-232.

8. H. R. Brager and F. A. Garner, "Microchemical Evolution of Neutron-Irradiated 316 Stainless Steel," Effects of Radiation on Materials, ASTM STP 725, D. Kramer, H. R. Brager and J. S. Perrin, Eds., ASTM (1981), pp. 470-483.

9. H. R. Brager and F. A. Garner, J. Nucl. Mat., 103/104 (1981), pp. 993-997.

10. H. R. Brager and F. A. Garner, "Influence of Neutron Spectra on the Radiation-Induced Evolution of AISI 316," Proceedings of International Conference on Neutron Radiation Effects, Argonne National Laboratory, U.S., Nov. 9-12, 1981 (J. Nucl. Mat., in press).

11. F. A. Garner and D. L. Porter,, "History Dependence and Consequences of the Microchemical Evolution of AISI 316," Effects of Radiation on Materials: Eleventh Conference, ASTM STP 782, H. R. Brager and and J. S. Perrin, Eds., American Society for Testing and Materials, 1982.

12. W. G. Wolfer, F. A. Garner and L. E. Thomas, "Radiation-Induced Segregation and the Compositional Dependence of Swelling in Fe-Ni-Cr Alloys," Effects of Radiation on Materials: Eleventh Conference, ASTM STP 782, H. R. Brager and J. S. Perrin, Eds., American Society for Testing and Materials, 1982.

13. H. R. Brager and F. A. Garner, "Stability of Radiation-Induced γ' Phase in 316 Stainless Steel," accepted for publication in J. Nucl. Mat.

14. F. A. Garner and W. G. Wolfer, J. Nucl. Mat., 102 (1981), pp. 143-150.

15. J. Weitman, N. Daverhog and S. Farvolden, Trans. Amer. Nucl. Soc. 13 (1970), p. 557.

16. A. A. Bauer and M. Kangilaski, J. Nucl. Mat., 42 (1972), pp. 91-95.

17. G. R. Odette, R. W. Powell and F. V. Nolfi, "DAFS Experiment in the ORR MFE-2 Test," Damage Analysis and Fundamental Studies Quarterly Progress Report DOE/ET-0065/5, May 1979, p. 5.

18. L. Greenwood, "Fission Reactor Dosimetry," Damage Analysis and Fundamental Studies Quarterly Progress Report DOE/ER-0046/6, Aug. 1981, p. 17.

19. W. G. Johnston, T. Lauritzen, J. H. Rosolowski and A. M. Turkalo, "The Effect of Metallurgical Variables on Void Swelling," General Electric Report 76CRD010, Jan. 1976; also J. M. Leitnaker, E. E. Bloom and J. O. Stiegler, J. Nucl. Mat., 49 (1973). pp. 57-66.

20. K. Farrell and N. H. Packan, J. Nucl. Mat., 85 and 86 (1979), pp. 683-687.

21. N. H. Packan and K. Farrell, ibid., pp. 677-681.

22. K. Uematsu, T. Kodama, U. Ishida, K. Suzuki and M. Koyama, "Swelling Behavior of Cold Worked Type 316 Stainless Steel," reference 1, pp. 571-589

23 W. K. Appleby, E. E. Bloom, J. E. Flinn and F. A. Garner, "Swelling in Neutron-Irradiated 300 Series Stainless Steels," reference 1, pp. 509-527.

24. Y. Adda, "Report of the CEA Program on Investigations of Radiation-Induced Cavities in Metals: Presentations of Some Results," Proc. Symposium on Radiation-Induced Voids in Metals, AEC Symposium Series 26, June 9-11, 1971, Albany, NY, pp. 31-83.

25. M. Labbe and J. P. Poirier, J. Nucl. Mat., 46 (1973), pp. 86-98.

26. A. Risbet and V. Levy, J. Nucl. Mat., 46 (1973), pp. 341-352.

27. T. Leffers and B. N. Singh, "The Effect of Cold Work on Void Formation and Growth in Copper During High Voltage Electron Microscopy Irradiation," Proc. International Conference on Irradiation Behavior of Metallic Materials for Fast Reactor Components, Ajaccio, Corsica, June 4-8, 1979, pp. 235-240.

28. L. K. Mansur, Nucl. Tech., 40 (1978), pp. 5-34.

29. F. A. Garner and W. G. Wolfer. "A Model for the Evolution of Network Dislocation Density in Irradiated Metals," Effects of Radiation on Materials: Eleventh Conference, ASTM STP 782, H. R. Brager and J. S. Perrin, Eds., American Society for Testing and Materials, 1982.

30. S. C. Agarwal, G. Ayrault, D. I. Potter, A. Taylor and F. V. Nolfi, J. Nucl. Mat., 85 and 86 (1979), pp. 653-657.

31. K. Farrell, Experimental Observations of Effects of Inert Gas on Cavity Formation During Irradiation, Oak Ridge National Laboratory Report ORNL/TM-7193, April 1980.

7.0 Future Work

Positron annihilation studies are in progress.

8.0 Publications

This report will be published in Effects of Radiation on Materials: Eleventh Conference, ASTM STP 782, H. R. Brager and J. S. Perrin, Eds., American Society for Testing and Materials, 1982.

THE EFFECT OF HELIUM ON SWELLING IN STAINLESS STEEL: INFLUENCE OF CAVITY DENSITY AND MORPHOLOGY - R. E. Stoller and G. R. Odette (University of California, Santa Barbara)

1.0 Objective

The purpose of this work is to develop physically based models of the microstructural evolution of stainless steels under irradiation and to use these models to develop better understanding of the processes which give rise to cavity swelling in this material.

2.0 Summary

One effect of increasing the helium/dpa ratio (He/dpa) in irradiations of 316 stainless steel is an increased cavity density. This effect is observed in both HFIR (~ 70 appm He/dpa) and dual ion (variable He/dpa) irradiations when compared with EBR-II irradiations (– 0.35 appm He/dpa) The cavity density appears to scale as $(He/dpa)^p$, where $0<p<1$. A second observation is that the relative fraction of cavity swelling which is a result of precipitate associated voids appears to be lower in some HFIR irradiated materials relative to the EBR-II irradiations. A rate theory model has been developed to consider these He/dpa ratio effects. The model was calibrated using data from EBR-II irradiations of 20% cold worked 316 stainless steel. The parametric dependence of cavity swelling on the value of p and the He/dpa ratio has been examined for values of the He/dpa ratio between the EBR-II and HFIR values. The fusion He/dpa ratio falls in this range (~ 10 appm/dpa).

The results indicate that beyond a critical value of p there is a bifurcation in the cavity evolution path from microstructures dominated by precipitate-associated voids to matrix bubble dominant. Reduced swelling is observed as a result of the bifurcation. However, the model also predicts peak swelling near the fusion He/dpa ratio suggesting that the use

of fission reactor swelling data may lead to non-conservative estimates of swelling for fusion.

3.0 Program

Title: Damage Analysis and Fundamental Studies for Fusion Reactor Materials Oevelopment

Principal Investigators: G. R. Odette and G. E. Lucas

Affiliation: University of California, Santa Barbara

4.0 Relevant OAFS Program Plan Task/Subtask

Subtask C Correlation Methodology

5.0 Accomplishments and Status

5.1 Introduction

The fundamental concepts presented here are an extension of earlier work which focused on the influence of cavity sink density, as mediated by helium, on swelling [1-3]. In this paper we attempt to explore the implications of a recent experimental observation that widely varying levels of the helium generation rate can apparently lead to qualitatively different cavity microstructures [4-5]

That work involved a comparison of a single heat of 20% cold-worked 316 type stainless steel irradiated under roughly similar conditions in both fast (Experimental Breeder Reactor-11, EBR-II) and mixed-spectrum (High Flux Isotope Reactor, HFIR) reactors, which produce low and high helium to displacement-per-atom (He/dpa) ratios respectively. While the effect of the varying helium level on gross cavity swelling in the range of data overlap is not large, and is the subject of some controversy, a clear

qualititive difference in the character of the cavity microstructure is observed. Namely, the alloys irradiated in HFIR, at high helium generation rates, are dominated by a high density of relatively small matrix cavities; while the irradiations in EBR-II, which produces much less helium, resulted in a lower density of large cavities, generally found to be attached to precipitate particles (precipitate-associated). A comparison of these microstructures is shown in Figure 1. Helium inventory estimates and modeling studies suggest that the HFIR cavities are near equilibrium gas bubbles at temperatures greater than 500° C.[3,6,7], while the precipitate associated cavities observed in the EBR-II irradiated specimens are voids. None of the possible factors which might confound quantitative comparitive

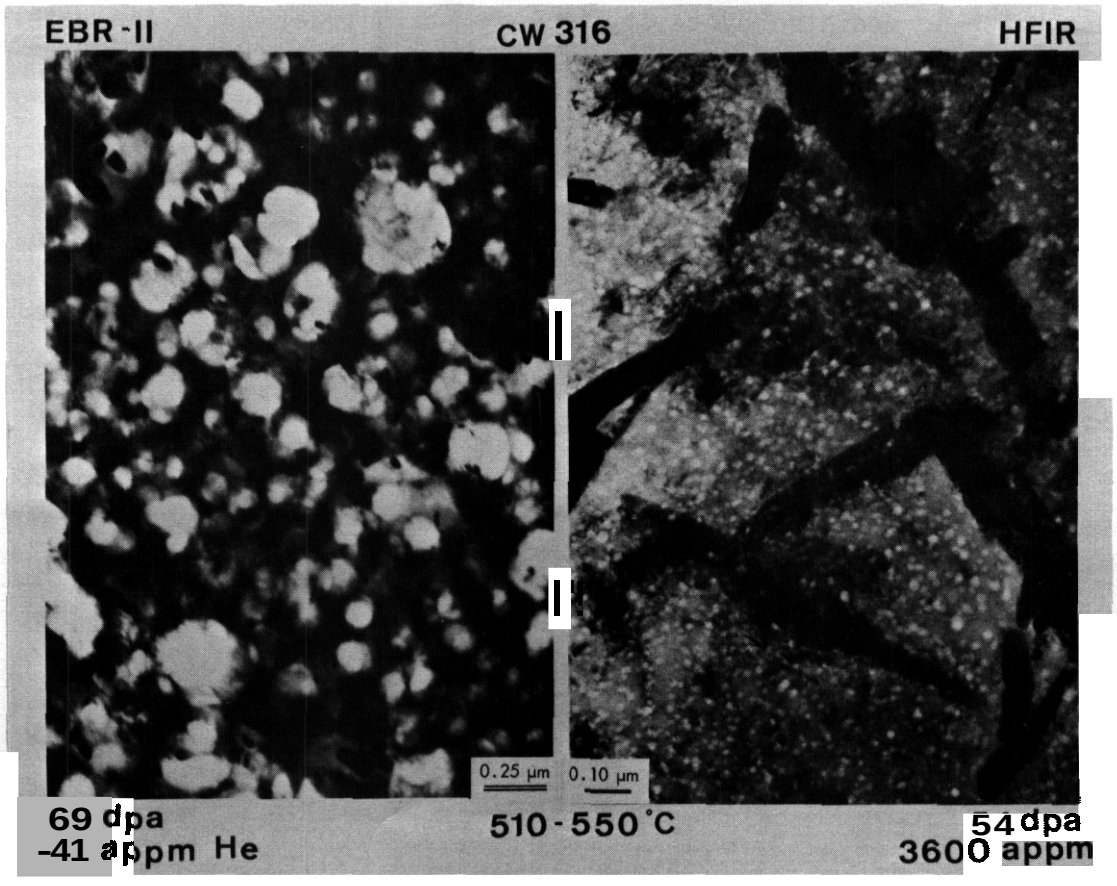

FIGURE 1. Influence of Helium/dpa ratio on cavity density and morphology EBR-II vs. HFIR (photo courtesy P.J. Mazaisz, ORNL).

interpretation of these results appear to explain these stark qualitative differences.

The same heat of steel irradiated in HFIR in the solution annealed condition, which had somewhat lower cavity densities (~ a factor of 5) than the cold-worked alloy, contained both matrix and large precipitate-associated cavities, [4]. These results are compared in Figure 2. One possible interpretation of the solution-annealed versus cold-worked results is that high cavity densities, beyond a critical number, may reduce or even suppress completely the formation of precipitate-associated voids which generally comprise the majority of cavity volume. We term the switch from precipitate-associated void to matrix bubble dominated cavity microstructures, mediated by cavity density, a bifurcation in the path of evolution.

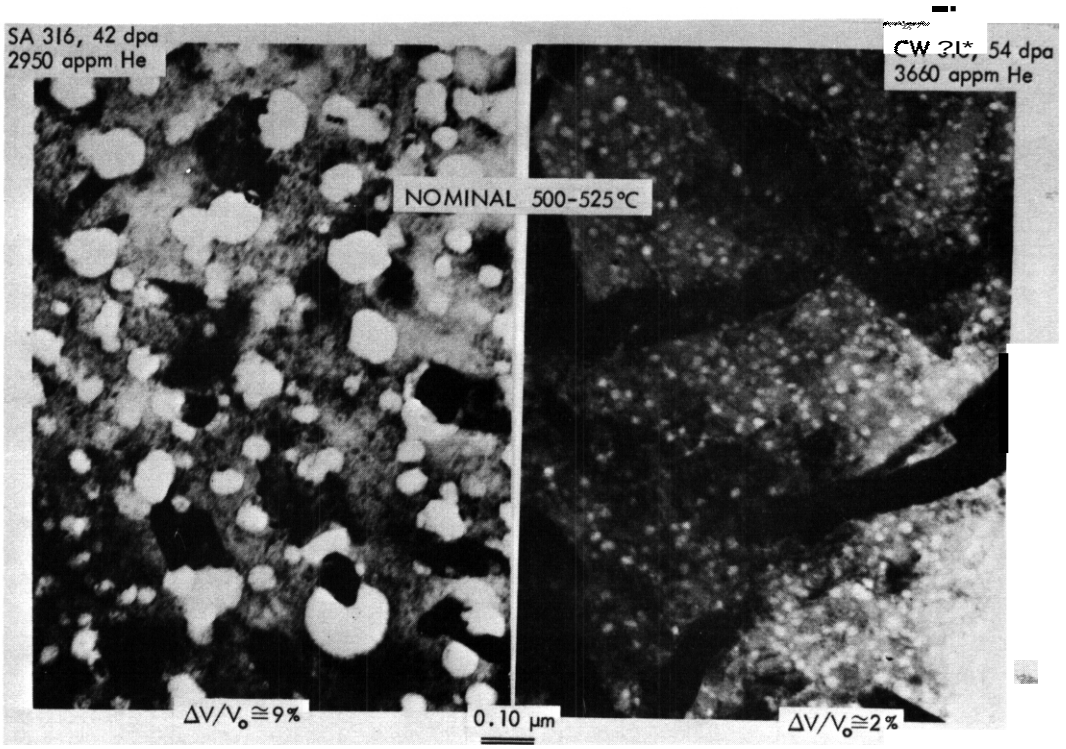

FIGURE 2. Influence of prior heat treatment in HFIR on cavity density and morphology (photo courtesy P.J. Mazaisz, ORNL).

Qualitative considerations suggest that such behavior is strongly influenced by the helium generation rate. Larger numbers of helium atoms per cavity promote bubble-to-void conversion, but at higher cavity densities, resulting from increased gas production, helium must also partition to more sites and the effective vacancy supersaturation (or net vacancy fluxes at cavity sinks) is reduced, supressing bubble-to-void conversions. Hence, the anticipated effect on swelling of increasing helium may not be a constant, monotonic trend. Theoretical considerations suggest that increasing helium would first increase void nucleation and swelling up to a peak, followed by a decline due to suppression of void (versus bubble) formation; the swelling would pass through a minimum when all the cavities are bubbles and increase thereafter with increasing helium. The broad trends observed in both helium preinjection followed by charged particle or neutron irradiation and dual-ion charged particle studies support these concepts [4]. An example of such non-monotonic swelling behavior is shown in Figure 3.

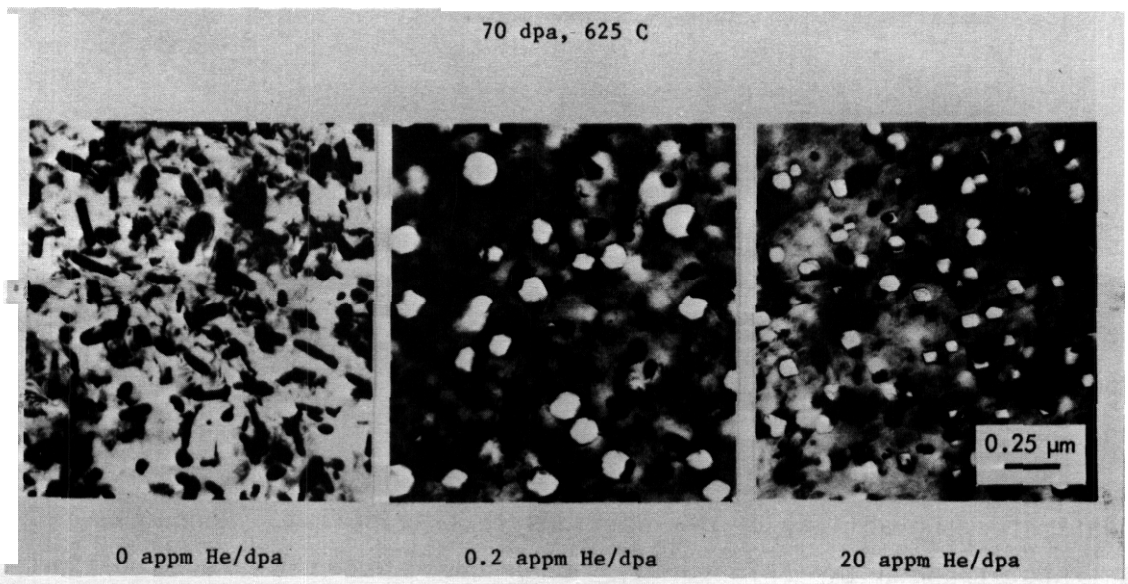

FIGURE 3. Influence of helium/dpa ratio on cavity density and void swelling in dual-ion irradiation of Ti-modified 316 (photo courtesy E. Kenik, ORNL). Observed swelling is 3.5% at 0.2 appm He/dpa and 1.8% at 20 appm He/dpa.

In order to test these qualitative ideas more rigorously a quantitiative model is required. As is generally the case when attempting to analyze complex phenomena, the available microstructural models are incomplete (i.e. do not cover all relevant mechanisms), contain significant approximations for computational expediency and require parameters (both material and irradiation) that are not known precisely. As a consequence, even if the model predictions are consistent with the existing data base, extrapolation beyond the range of observation is uncertain and predictive results generally are not unique. Hence, such models should be viewed as tools to be used to develop better understanding.

5.2 Model Development

With that caveat, we endeavor to develop a physically based quantitative rate theory model which allows us to examine the concepts discussed above. A mathematical description is included in Appendix A. The important elements of the model are described below.

5.2.1 Helium Partitioning

Treatment of helium partitioning between various sinks and between the sinks and the lattice is based on a conservation equation incorporating total and relative sink strengths, helium diffusivity and helium generation rate. Helium sinks include sub-grain structure, bubbles and voids. Dislocations are assumed to be helium collectors for matrix bubbles. Recent work by Spitznagel, et al. [8] indicates that using the dislocation sink strength for vacancies in helium partitioning calculations overestimates the ability of dislocations to trap helium. Hence, we reduce this sink strength by a factor f_{He} when computing the amount of helium partitioned to matrix bubbles. For this work, f_{He} was taken as 0.5. Precipitates act as collectors for precipitate-assoicated voids and bubbles. Guided by very limited data [4] in the range of ~ 500-600°C we use a constant sink strength of $4.0 \times 10^{10} cm^{-2}$ for the precipitate helium collectors.

5.2.2 Point Defect Sinks, Bias Factors, and Defect Fluxes

Calculation of self-consistent defect sinks strengths and associated bias factors is very complicated in an evolving microstructure, even if potentially significant microchemical effects [9] are not considered, as pointed out by Liu and Nichols and others [10,11]. We have adopted a first order effective medium approach calculation suggested by several workers [12,13]; interstitial bias is assumed to be a constant material parameter assigned solely to dislocations. The sinks include subgrain structure, voids, bubbles, dislocations and transient vacancy clusters in the form of loops or microvoids formed by the "collapse" of displacement cascades. Precipitates are not included as point defect sinks for several reasons: there is not much data in the open literature to characterize the size, number density and morphology of precipitate microstructures; the creep rupture literature suggests that incoherent interphase boundaries may be inefficient point defect sinks (at least for vacancies) [14]; various precipitates would be expected to have different sink efficiencies and bias factors; these sink parameters might be time-dependent due to relaxation of misfit strains; and using standard parameters, better agreement with observations is obtained when these sinks are not included. We cannot estimate precisely the effect of these approximations used in treating sink strength and effective system bias; clearly, additional research is needed to develop and apply improved sink and bias models.

5.2.3 Bubble Nucleation, Growth and Conversion to Voids

The general scenario for bubble nucleation and growth has been given previously [1-3]; bubbles nucleate and grow in the matrix and at precipitate interfaces at rates controlled largely by the helium generation and partitioning rates. The total cavity density is based on experimentally observed trends [7,15,16], and may be expressed

$$N_c^t = 2.53 \times 10^{20} \exp(-0.023\,T(°C))\ cm^{-3}. \qquad (1)$$

The temperature dependence of N_c^t is shown in Figure 4. The precipitate associated cavities are taken as a constant fraction $f_p = 0.1$ of the total cavity density. In reality, this parameter may be a function of temperature and other variables; however, there is insufficent data to guide a more precise choice. The matrix bubbles are assumed to form early in irradiation in the form of small clusters (d-5 Å). Formation of precipitate-associated bubbles and initial partitioning of helium to them is assumed to take place at a temperature-dependent exposure parameter τ_p, representing the average precipitation incubation time.

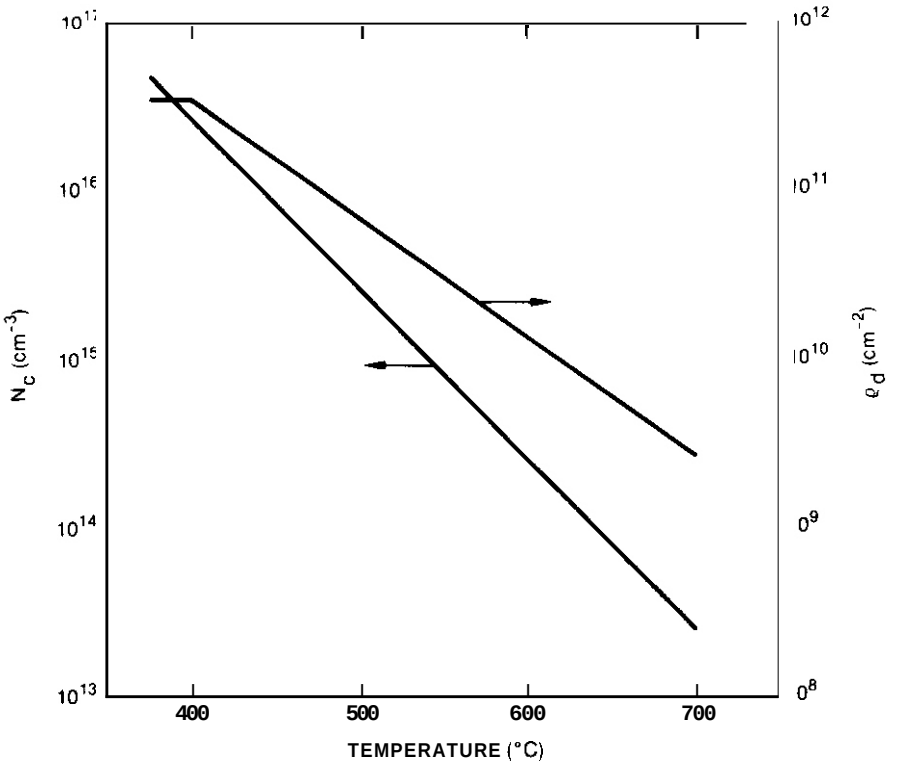

FIGURE 4. Temperature dependence of dislocation density (ρ_d) and cavity density (N_c) used in model.

There are several possible mechanisms by which precipitation of second phase particles could influence bubble-to-void conversions and swelling. A partial list includes:

a) Lattice composition changes influencing changes in sink biases and self-diffusion parameters (17, 18)

b) Non-equilibrium (transient) misfit strain effects where tensile strains would promote and compressive strains would supress void formation; and/or biased precipitate sinks where tensile strains would produce interstitial bias and compressive strains vacancy bias;

c) Point defect collector effects [19].

d) Non-spherical cavities and surface energy effects at precipitate interfaces.

While all of these can be modeled, we have chosen to concentrate on item (d), which has been extensively treated in the literature for stress induced creep cavity nucleation [20,21]. The effect of this mechanism can be represented by a single parameter β, which is a function of the relative surface energies of the cavity-matrix interface, γ, the precipitate-matrix interface, γ_{mp}, and the precipitate-cavity interface, γ_p [20] where

$$\beta = \cos^{-1}\left(\frac{\gamma_{mp} - \gamma_p}{\gamma}\right). \tag{2a}$$

The volume V and surface area A of the nonspherical cavity is given as

$$V = F_v \frac{4}{3}\pi r^3 \tag{2b}$$

and

$$A = F_s 4\pi r^2, \tag{2c}$$

where

$$F_v = \frac{1}{4}(2 - 3\cos\beta + \cos^3\beta), \tag{2d}$$

and

$$F_s = \frac{1}{2}(1 - \cos\beta). \tag{2e}$$

Hence for $y >> y_{mp} \gtrsim y_p$, $F_v = 0.3\text{-}0.5$; we use a value of 0.4 in this work; the corresponding value of F_s is 0.434. The result of a reduced volume for a given capillary radius is an expression for the critical number of helium atoms needed for bubble-to-void conversion of

$$n^*_{He} = f(S)\, F_v \left(\frac{\gamma}{kT}\right)^3 \left(\frac{1}{\ln S}\right)^2, \tag{3a}$$

where the effective vacancy supersaturation parameter, S, is defined as,

$$S = \frac{D_v C_v - D_i C_i}{D_v C_v^e} \tag{3b}$$

The function of $f(S)$ represents a non-ideal gas correction factor which approaches $1.62\times10^{-46}\,cm^6$ for an ideal gas (or low S) as discussed in Appendix C.

5.2.3 Other Irradiation and Material Parameters

The total dislocation density as shown in Figure 4 is expressed as a time independent function of temperature [15] as,

$$\rho_d = 1.99\times10^{14} \exp(-0.016T(°C))\ cm^{-2}. \tag{4}$$

No distinction is made between network dislocations and loops and the dislocation transient early in irradiation is ignored. The transient vacancy clusters can have either void and loop morphologies; we have examined both cases, but will present results only for microvoids here. We assume some fraction ξ of the initially created vacancies survive intra-cascade annealing, and that a fraction χ cluster as microvoids with a radius r_{mv}, we assume nominal values of $\xi = .4$ and $\chi = .8$ which are

consistent with computer simulation results [22] and use r_{mv} as an adjustable parameter. The displacement rate, G, was taken as 10^{-6} sec^{-1}.

The self-diffusion coefficient was taken using a standard activation energy of 2.9 eV and a pre-exponential of 0.8 $cm^2 sec^{-1}$ so as to be consistent with high-temperature data [12]. This activation energy is somewhat higher than measured in 304 stainless steel (~ 2.7 eV) [23] and lower than that found for some Fe-Ni-Si model alloys (– 3.2eV) [24]. Extrapolations to temperatures in the range of void swelling based on these alternate values lead to widely varying diffusivities. Since the model results are sensitive to these values it would be very useful to obtain a more accurate diffusion parameter in the temperature range of interest. Indeed, one might anticipate higher diffusion rates in alloys containing impurities or alloying elements such as Si and C (and He) due to impurity enhancement parameters ($D = D(C_i = 0) + b_i C_i$ where C_i is the impurity concentration - see Ref 18). This might explain in part the higher resistance to void formation of commercial alloys; or, as a corollary, one of the effects of microchemical evolution on swelling behavior.

Data on free surface energies of stainless steel alloys are very limited; some estimates based on zero creep measurements in 304 stainless steel suggest large and temperature dependent values in the range of 2500-3500 $ergs/cm^2$ [25]. However, when coupled with the estimates of the self-diffusion coefficient given above, these values are inconsistent with observed high temperature swelling in the context of postulated mechanisms and parameters. Hence, we reduce the magnitude of the zero creep estimate of γ by a factor of 2, in agreement with values used in almost all other theoretical studies of swelling (e.g. Ref. 11),

$$\gamma = 2025 - 0.875\ T\ (^{o}C)\ ergs/cm^2. \qquad (5)$$

Such reduced surface energies can be rationalized by the effect of solute segregation in alloys. The helium diffusivity was modeled based on a

divacancy mechanism assuming a binding energy of 0.5 eV as described in Appendix A. The model parameters are summarized in Appendix 8.

After fixing the reasonable (i.e. guided by observation or physical considerations) microstructure and material parameters described above, the major remaining adjustable parameter is the effective bias factor ε; other adjustable parameters are the precipitation time, τ_P and microvoid radius, r_{mv}. The bias factor has been assigned a wide range of values in the literature from ~ 0.02 to > 0.5 [12,26]. Its use to calibrate the model will be discussed below. However, it is important to emphasize that other combinations of adjustable parameters could have been chosen; and, indeed, we have studied a number of alternate cases. Use of the bias parameter provides both simplicity and clarity, and we have found that the qualitative trends revealed in our analysis are not seriously influenced by the choice of this expedient.

Clearly the model is approximate. The most serious assumptions include: the treatment of sinks and bias factors, both in terms of sink interaction effects and possible microchemical influences; use of constant diffusivity parameters independent of the evolving matrix composition; and the limited treatment of possible precipitate effects on void nucleation and growth. Nevertheless, we will show below that with reasonable microstructural and material parameters the model results are consistent with the broad trends in the breeder data base. Indeed, we believe a useful perspective is to view this form of rate theory as a semi-empirical algorithm to apply cumulative defect conservation (mass balance) requirements and to estimate the sensitivity of defect partitioning to various kinetic and sink structure parameters.

5.3 Model Calibration

We feel that the fast reactor data base for 20% cold-worked type 316 stainless steel is best suited for calibrating the model because of the

range of the temperatures and exposures covered and the practical interest in this general alloy condition. However, there is considerable heat-to-heat variation in the swelling of breeder steels (particularly in the incubation regime); hence, we have made use of a set of data for several heats of relatively swelling prone steels, usually known as first core steels [27,28]. Even this data, however, is not sufficient to develop a unique set of model parameters. For example, changes from the nominal void and dislocation microstructure parameters within the scatter of observed trends could be compensated for by slight changes in the activation energy for self-diffusion or surface energy. A number of similar examples could be mentioned. Hence, as noted above, we have chosen to concentrate on only three parameters: the bias factor ϵ, the precipitate nucleation time τ_p and the microvoid radius r_{mv}, the latter is only significant at temperatures $\lesssim$ 500°C.

The bias factor ϵ influences both the bubble-to-void conversion time, the pattern of precipitate-associated versus matrix bubble-to-void conversion pattern, and the post-incubation swelling rate, $\dot{S}$. The swelling rate parameter probably provides the best basis for fitting the model. Values of $\dot{S} \sim 0.5$-1%/dpa have been reported relatively insensitive to temperature in the range of 450-650°C [27,28]; this requires a choice of $\epsilon = 0.25$ which is in the range of values reported in the literature [12,26]

Coupled with the bias parameter, the precipitation time parameter has a significant influence in the swelling incubation time and can indirectly influence post-incubation swelling rates; the effect of τ_p on $\dot{S}$ is manifested in the number and order of bubble-to-void conversions for the matrix and precipitate-associated classes. Experimental observations show that τ_p is temperature-dependent. Assuming a linear model, $\tau_p \sim C\,(700-T)$ with $C = 0.16$, gives τ_p of 40 dpa at 450°C falling to ~ 0 at 700°C* which is

*Many complex processes occur at less than a few dpa (or $\sim$ 1000 hrs); hence, precipitation at times less than this is essentially at a negligible exposure with respect to the prediction of the model.

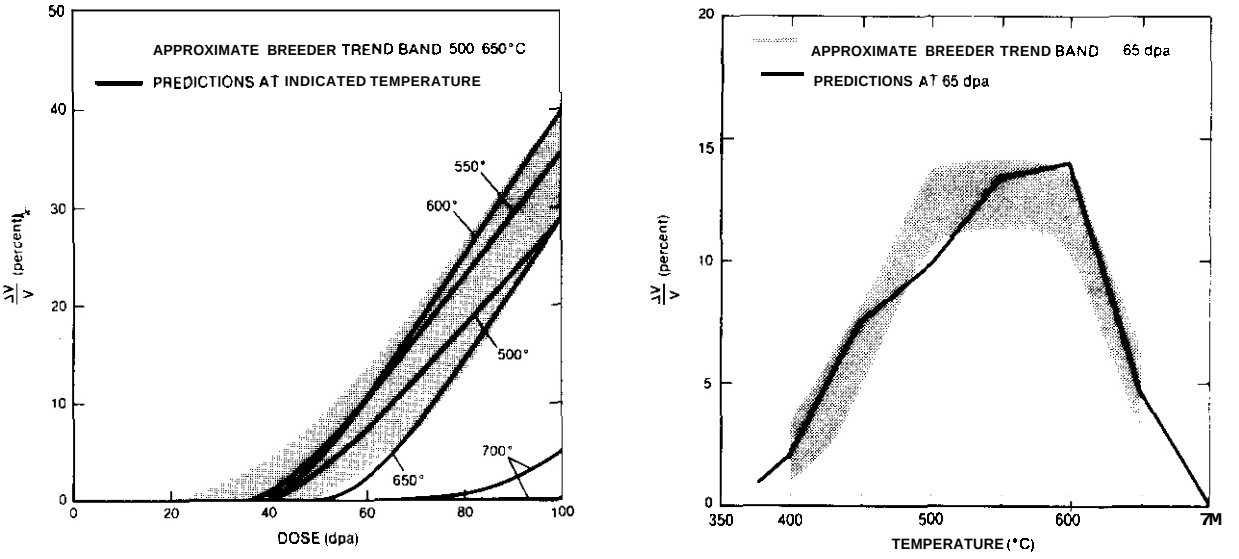

FIGURE 5. Comparison of predicted and observed fluence and temperature dependence of swelling for fast reactor conditions.

reasonably consistent with observation [4]; the resulting swelling as a function of exposure is shown in Figure 5a for the temperature range of 500-700°C. The trend band for swelling data in this temperature range is also shown as a grey-hatched region; reasonable agreement is observed.

Up to 700°C there is a single bubble-to-void conversion of precipitate-associated cavities. At 500°C the conversion takes place ~ 6 dpa greater than τ_P while at higher temperatures the post-precipitation dose to conversion is much longer, (increasing from ~10 dpa at 550°C to ~36 dpa at 650°C). Void swelling is not predicted at 700°C with the nominal parameters up to 100 dpa; however, by reducing the dislocation density at 700°C from 2.7×10^{9} to $\sim1.5\times10^{9}\,cm^{-2}$ (consistent with recrystallized steels) swelling is predicted as shown in the upper curve labeled 700".

At temperatures below ~500-550°C variations in the model parameters (e.g. cavity density, surface energy, etc.) can change the pattern of conversion. Matrix or precipitate-associated cavities may convert first and remain the only element of void population or double conversions may take place, again in various orders. However, at temperatures above 550°C (for the assumed material parameters representing commercial alloys) precipitation is a pre-requisite for void nucleation. In other words, at lower temperatures helium accumulation alone is sufficient for void formation while at higher temperatures <u>both</u> precipitation and helium accumulation are required.

At temperatures below ~ 450°C inclusion of transient vacancy clusters results in the reduced swelling observed experimentally. Using microvoid radii of 5.75Å, 6.25Å, and 7.5Å at T = 375, 400, and ≥ 450°C respectively, predicted swelling at 65 dpa is plotted as a function of temperature in Figure 5b. The trend band for the fast reactor data is also shown as a grey hatched region; again the agreement is reasonably good. The use of a variable microvoid radius reflects the fact that low temperature swelling data is taken from softer spectra, which would lead to lower cascade-cluster production efficiency. While this use of the variable microvoid radius is somewhat ad-hoc, it can be viewed as a surrogate for the other transient vacancy cluster parameters (ξ, χ and microvoid versus vacancy loop morphology). At 400 and 450°C the predicted swelling is due to the conversion and growth of the matrix cavities, while at 375°C both the matrix and precipitate-associated cavities have converted.

The agreement between the model predictions and observed trends in the breeder data base is encouraging. In particular, the model suggests that: void incubation times are strongly influenced by the precipitation of second phases, particularly above 500°C; steady-state swelling regimes are observed which are relatively insensitive to temperature above ~ 450; steady-state swelling rates are in the range of 0.5-1%/dpa; at lower temperatures (<450°C) swelling rates are reduced (in the model, primarily as a result of vacancy clusters); and at higher temperatures (>700°C)

significant swelling may occur (the model suggests that recovered dislocation microstructures are necessary for such swelling). The model also predicts the observed high degree of precipitate-void association, and demonstrates the close coupling between primary driving forces for void formation in complex alloys, namely, precipitation and helium accumulation.

5.4 Results of Parametric Study of Helium Generation Rates and Cavity Densities

The primary motivation for this work is to develop a better understanding of the potential effects of helium on microstructural evolution. It has been pointed out previously that while helium appears to have a number of subtle effects (e.g. on precipitate structure and composition), the most systematically observed trend is promotion of increased cavity density with increasing helium (4). Hence, we have focused on this effect and have examined the parametric effect of variations of the He/dpa ratio and cavity density using our calibrated model.

The correlation between cavity density and helium generation rates can be approximately represented as

$$N_c(\text{He/dpa}) \simeq N_c(\text{breeder}) \left[\frac{\text{He/dpa}}{\text{He/dpa (breeder)}}\right]^p , \qquad (6)$$

where p varies between 0 and 2, and is typically observed to be 0.5 to 1.0 (4). For convenience, we have carried out calculations for a range of He/dpa ratios between the values of EBR-II (fast reactor ~0.35 appm He/dpa) and HFIR (mixed spectrum reactor ~70 appm He/dpa). The He/dpa ratio for fusion falls in this range (~10 appm He/dpa).

Figure 6 shows the exposure dependence of the predictions for HFIR and fusion at the indicated temperatures for p = 0.2, 0.5 and 0.8. For purposes of comparison, the EBR-II curve at each temperature has also been

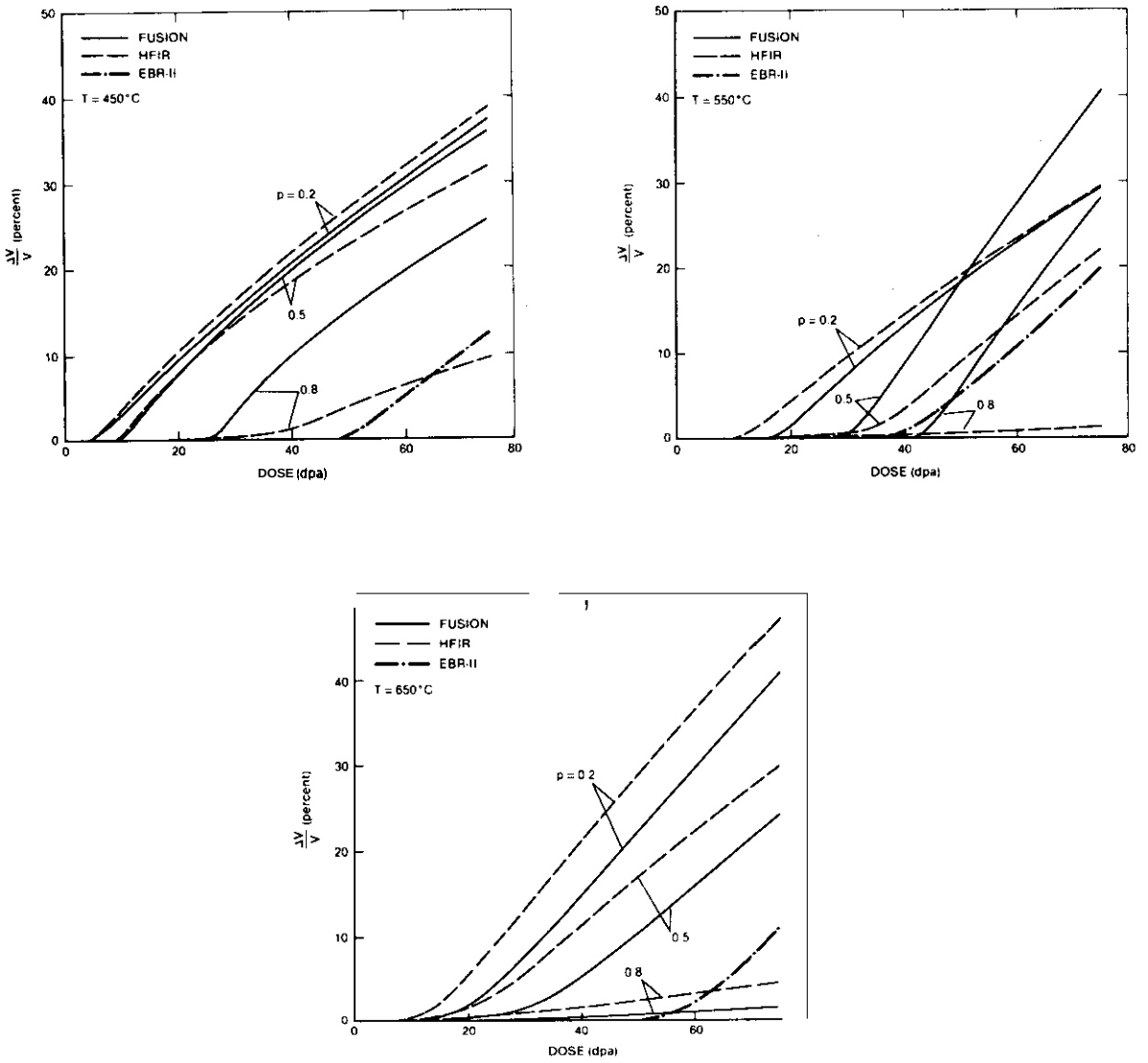

FIGURE 6. Comparison of predicted fluence dependence of swelling behavior for EBR-II, HFIR, and fusion at the indicated temperatures and values of p (see text).

plotted. Both incubation exposures, and in some cases swelling rates, vary as a function of He/dpa ratio and the cavity density scaling parameter p. For 450 and 650°C there appears to be a monotonic decrease in swelling as p increases in both environments, while at 550°C the swelling appears to peak for a value of p near 0.5 for fusion. This trend is more clearly observed in Figure 7 which shows a cross plot of swelling at 75 dpa for both fusion and HFIR helium/dpa ratios; the bubble-to-void conversion pattern is also indicated with m and p indicating the conversion of matrix or precipitate-associated cavities respectively. The swelling for an E8R-II He/dpa ratio is also shown. The quantitative behavior is dependent on both the temperature and absolute He/dpa ratio. However, a broad trend of enhanced swelling (relative to breeder conditions) is observed for p up to ~ 0.5-0.7 for HFIR, and p up to ~ 0.6-0.9 for fusion conditions. This derives from the effect of decreased incubation exposures and in some cases conversion of extra (matrix or precipitate) void classes leading to higher swelling rates. At very high cavity densities (or p values), however, swelling is diminished, primarily as a consequence of high cavity to dislocation sink strength ratios or bifurcation of the path of cavity evolution from precipitate-associated voids to matrix cavities. The tendency towards bifurcation is enhanced (at a given level of p) by high temperatures or He/dpa ratio - e.g. HFIR versus fusion conditions.

These results are qualitatively consistent with interpretations of reduced swelling and alteration of the temperature dependence of swelling indicating a minimum at ~ 550°C for HFIR relative to breeder conditions for one heat of breeder steel [4,29]. For the fusion He/dpa ratio swelling is generally enhanced relative to breeder conditions. In particular, incubation times are reduced; and swelling rates are approximately equal to, or in some cases, because of extra bubble-to-void conversions, exceed breeder rates except at high temperatures and large values of p.

Figure 8 shows the ratio of incubation times, τ (to 1% swelling) and quasi-steady-state swelling rates (at 75 dpa) for fusion relative to

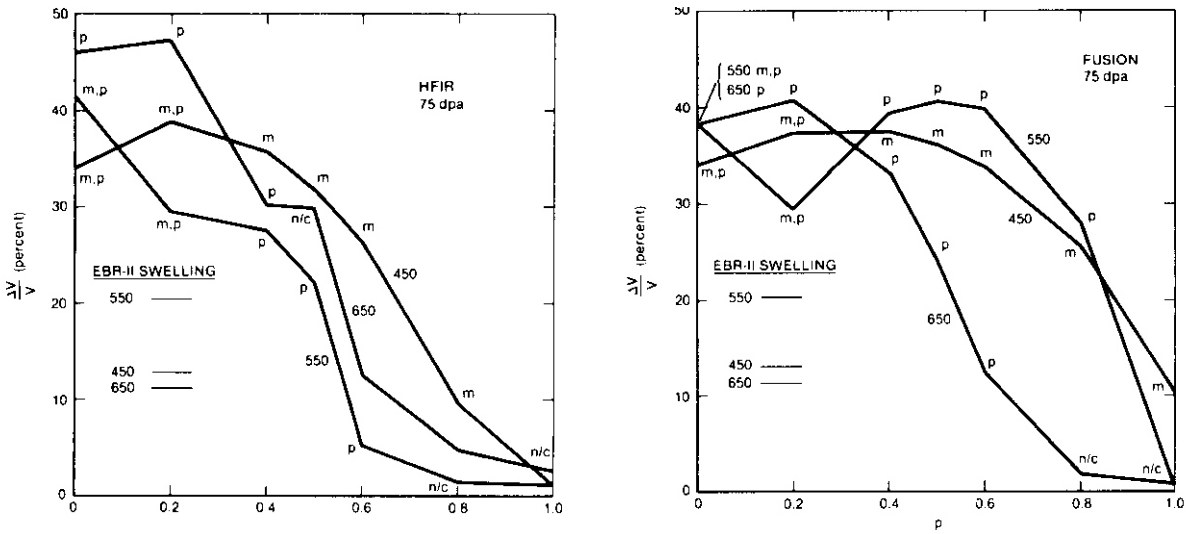

FIGURE 7. Predicted swelling at 75 dpa for HFIR and fusion as a function of p. The predicted swelling in EBR-II is also indicated. m and p denote bubble-to-void conversion of matrix and precipitate-associated cavities respectively: n/c denotes no conversions.

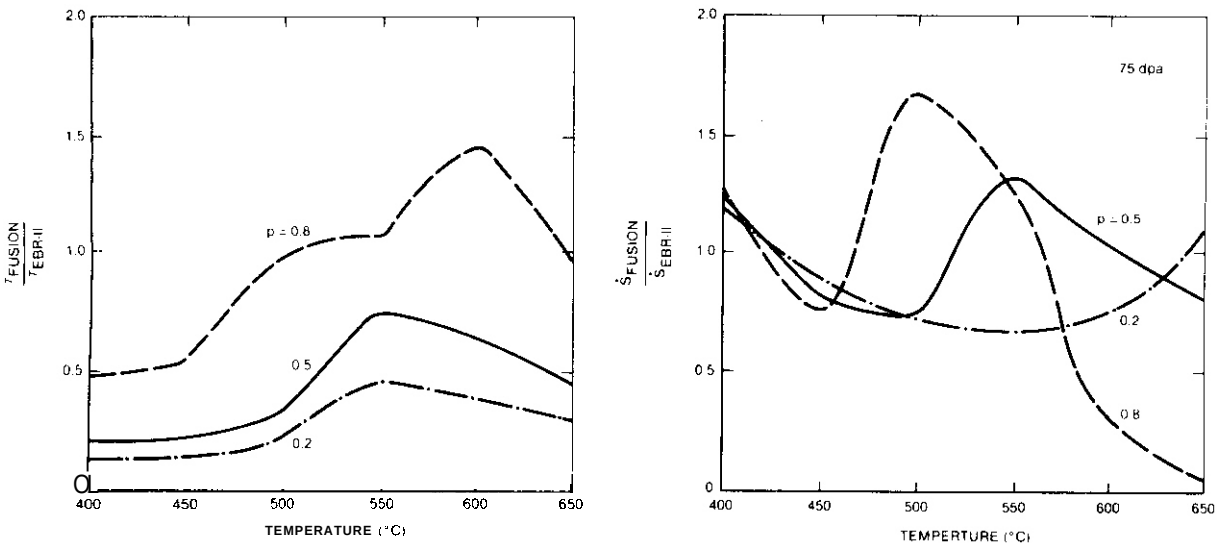

FIGURE 8. Predicted temperature dependence of incubation exposure (τ=dose to 1% swelling) and steady-state swelling rate ($\dot{S}$=swelling rate at 75 dpa) for fusion when normalized to EBR-II values.

breeder conditions for p = 0.2, 0.5 and 0.8. For p $\leq$ 0.5 the difference between fusion and breeder swelling is primarily due to the effect on the incubation time (except at 550°C); at p = 0.8 both swelling rates and incubation times are affected with the importance of these two contributions and the magnitude and sign of the effect varying with temperature. We believe that the predicted effects on the incubation exposure are less sensitive to the model assumptions and parameters than are the predicted effects on the swelling rate; hence, effects on the incubation time should be given more weight in assessing the implications of these results. Indeed, since the maximum tolerable swelling may be less than several percent, the incubation time is probably the swelling parameter of most practical significance.

The explicit dependence of swelling as a function of the He/dpa ratio is shown in Figure 9 where the swelling at 75 dpa has been plotted for p = 0.2, 0.5 and 0.8 at T = 450, 550 and 650°C. For purposes of comparison, the predicted swelling in EBR-II is also indicated. The results show non-monotonic behavior and indicate that a simple extrapolation or interpolation using fission reactor data from either EBR-II or HFIR, or both, may lead to significant errors in predicting swelling under fusion conditions. In fact, the predictions suggest that swelling may peak near the fusion He/dpa ratio except for high values of p and high temperatures.

It should again be emphasized that these specific results are sensitive to model assumptions and parameters; for example, the use of alloys with different swelling behavior than that used to calibrate the model would have led to somewhat different quantitative predictions [3,4]. However, the general trends observed are a consequence of the physical considerations discussed in the introduction and not the details of the model.

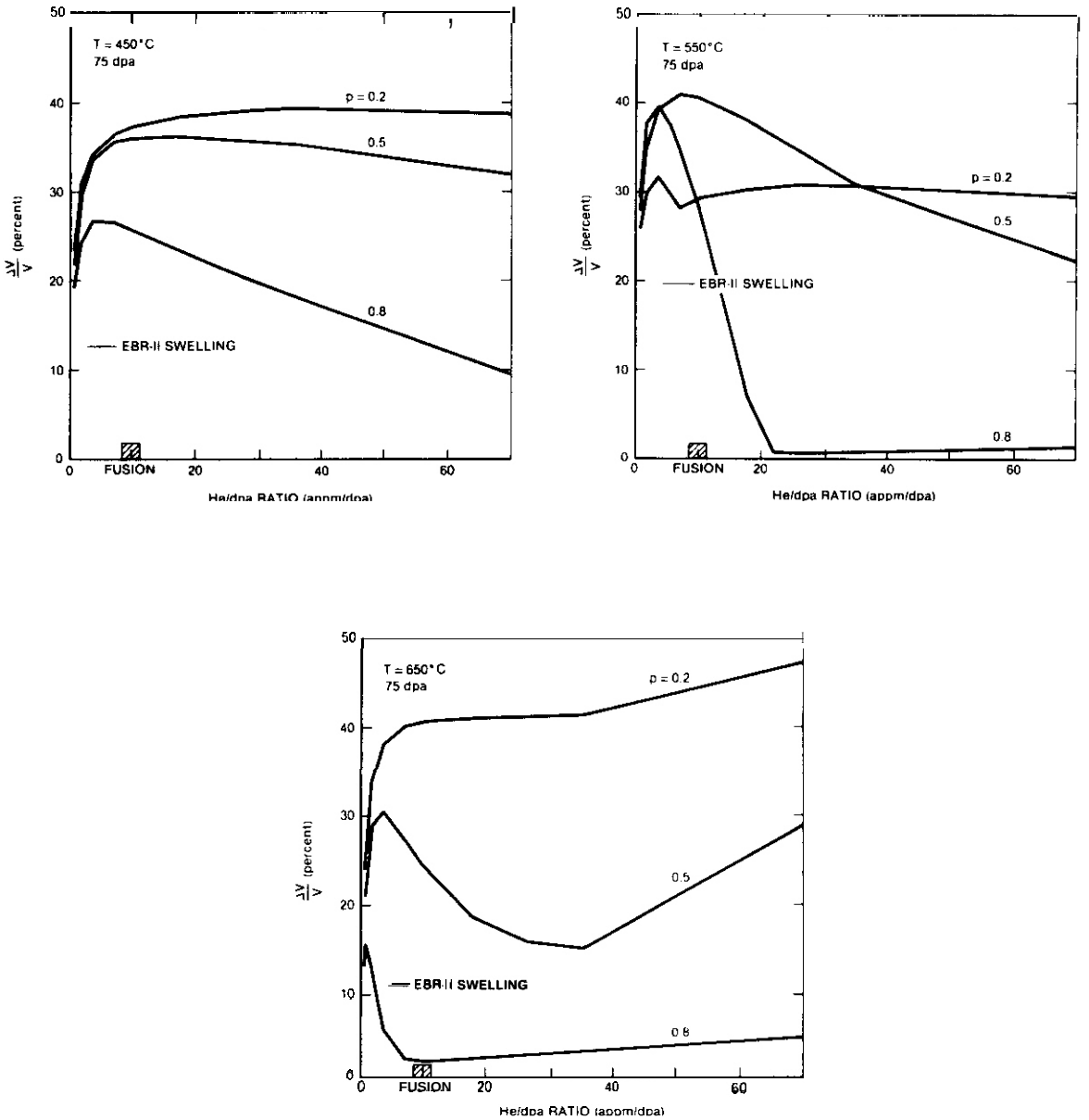

FIGURE 9. Predicted He/dpa ratio dependence of swelling at 75 dpa and at the indicated temperatures and values of **p**.

5.5 Discussion

Our model-based analysis suggests that the effect of increased helium on cavity swelling is complex, and a function of a number of parameters; quantitative behavior is governed by a balance between several competing and interactive mechanisms. Direct effects on swelling can be divided into categories which influence void nucleation and void growth.

For the nucleation category, higher levels of helium would reduce the exposure at bubble-to-void conversion at constant cavity density; however, increased helium also increases cavity densities, requiring available helium to partition to more sites. This, combined with the effect of higher cavity sink densities (both bubbles and voids) which reduce the effective vacancy supersaturations, tends to increase void-to-bubble conversion exposures. The net effect of these factors appears to reduce incubation exposures if increased helium results in moderate increases in cavity density, and longer incubation times at very high cavity densities. Hence, the cavity density scaling parameter p, $[N_c \alpha He/dpa^p]$ is critical. However, the influence of p also depends on the absolute helium generation rate.

The transition regime between incubation and rapid steady-state swelling also depends on cavity density: larger numbers of smaller voids result in enhanced vacancy emission; this tends to increase the transition time. However, the post-transition or steady-state swelling rates are relatively insensitive to emission related parameters. In this regime, point defect partitioning effects dominate, and the effect of void density is variable: if the void sink strength is much smaller than the dislocation sink strength, increased void density leads *to* higher swelling rates; if the void sink strength is much greater than the dislocation sink strength, further increases lower swelling. Increased bubble sink strength, which can result from increased helium, always reduces steady-state swelling rates. As noted in the introduction, the precipitate-associated voids are

a particularly important component of swelling under fast reactor conditions. If very high cavity densities suppress the formation of these voids, swelling is greatly reduced; we term this a bifurcation between a void (or mixed void and bubble) and bubble dominated microstructure.

These results suggest that use of either fast or mixed-spectrum reactor irradiation results to predict swelling in fusion environments may be highly misleading. For example, there is evidence that peak swelling may occur at He/dpa ratios characteristic of fusion spectra (see Figure 9); this is primarily associated with reduced incubation times.

Clearly, additional theoretical and experimental work needs to be done to determine the relative importance of the various direct and indirect effects of high helium generation rates [4,30]. For example, we have not considered a number of possible indirect effects of helium, such as perturbations of precipitate evolution. Spectral tailoring experiments in mixed-spectrum reactors, which achieve He/dpa ratios closer to fusion values, are most important. Additional experimental work and a careful examination of the existing data to more precisely determine the effect of the helium on cavity densities is also needed. Further, modeling should be done to better identify and quantify the numerous potential mechanisms which influence bubble nucleation and growth, bubble-to-void conversion and subsequent swelling rates.

6.0 References

1. Odette, G.R. and Frei, M.W., Proc. of First Topical Meeting On the Technology of Controlled Nuclear Fusion, CONF-740402, 1974 pp. 485-499.

2. Odette, G.R. and Langley, S.C., Radiation Effects and Tritium Technology for Fusion Reactors, CONF-750989, 1975 pp. I:395-I:416.

3. Stoller, R.E. and Odette, G.R., J. Nuc. Mat., Vol. 103-104, 1981, pp. 1361-1365.

4. Odette, G.R. Maziasz, P.J. and Spitznagel, J.A., ibid, pp. 1289-1303.

5. Maziasz, P.J. and Grossbeck, M.L., Ref. 3, pp. 987-991.

6. Glasgow, B.B., et al., Ref. 3, pp. 981-986.

7. Maziasz, P.J., Wiffen, F.W., and Bloom, E.E., Ref. 2, pp. I:259-I:288.

8. Spitznagel, J.A., et al., Ref. 3, pp. 1463-1467.

9. Garner, F.A., AIME Symposium on Phase Stability Under Irradiation, 1980 pp. 165-189.

10. Nichols, F.A. and Liu, Y.Y., Effects of Radiation on Materials: Tenth Conference, ASTM STP 725, 1981 pp. 145-165.

11. White, R.J., Fisher, S.B. and Heald, P.T., Phil. Mag., Vol. 34, No. 4, 1976 pp. 647-652.

12. Bullough, R. and Hayns, M.R., SM Archives, Noordhoof International Publishing, The Netherlands, Vol. 3, 1978 pp. 73-106.

13. Goselle, U., J. Nuc. Mat. Vol. 78, 1978 pp. 83-95

14. Beere W., J. Mat. Sci., Vol. 15, 1980 pp. 657-669.

15. Brammon, et. al., Radiation Effects in Breeder Reactor Structural Materials, 1977, pp. 479-507.

16. Brown, C., Butler, J.K. and Fulton, E.J., Int. Conf. Irradiation Behavior of Metallic Materials for Fast Reactor Core Components, 1979 pp. 129-136.

17. Wolfer, W.G. and Mansur, L.K., J. Nuc. Mat., Vol. 91, 1980 pp. 265-276.

18. Le Claire, A.D., J. Nuc. Mat., Vol. 69 & 70, 1978 pp. 70-96.

19. Mansur, L.K., ORNL/TM-7645, Oak Ridge National Laboratory, Oak Ridge, Tenn., 1981.

20. Raj, R. and Ashby, M.F., Acta. Met., Vol. 23, 1975 pp. 653-666.

21. Raj, R. Acta. Met., Vol. 26, 1978 pp. 995-1006.

22. Heinisch, H.L., DAFS Quarterly Progress Report, DOE/ER-0046/2, 1980 pp. 60-72.

23. Assassa, W., and Guialdenq, Met. Sci, Vol. 12, No. 3, 1978 pp. 123-128.

24. Rothman, S.J., Nowicki, L.J. and Murch, G.E., J. Physics. F: Metal Phys., Vol.10, 1980, pp. 383-398.

25. Murr, L.E., Wong, G.I. and Horylev, R.J., Acta. Met., Vol. 21, 1973 pp. 593-603.

26. Heald, P.T., Phil. Mag., Vol. 31, 1975, pp. 551-558.

27. Bates, J.F. and Korenko, M.K., Nuc. Tech., Vol. 48, 1980, pp. 303-314.

28. Yang, W.J.S. and Garner, F.A., Effects of Radiation on Materials: Eleventh Conference, ASTM STP 782, 1982, in press.

29. Maziasz, P.J. and Grossbeck, M.L., Alloy Development for Irradiation Performance (ADIP) Quarterly Progress Report, DOE/ER-0045/6, January-March 1981, pp. 28-56.

30. Odette, G.R., J. Nuc. Mat., Vol. 85 & 86, 1979, p. 533-545.

31. Brearley, I.R. and MacInnes, D.A., J. Nuc. Mat., Vol. 95, 1980 pp. 239-252.

32. Standard Mathematical Tables, 24th Edition, CRC Press, Cleveland, Ohio, 1973 pp. 82-83.

33. Melius, C.F., Wilson, W.D., and Bisson, C.L., Rad. Effects, Vol. 53, 1980 pp. 111-120.

34. Simons, R.L., Effects of Radiation on Structural Materials, ASTM STP 683, J.A. Sprague and D. Kramer, Eds., American Society for Testing and Materials, 1979, pp. 365-379.

7.0 Future Work

The cavity evolution model described above will be included in a more comprehensive treatment of microstructural evolution which includes the network dislocation and faulted dislocation loop components as well.

8.0 Publications

1. Stoller, R.E. and Odette, G.R., "The Effect of Helium on Swelling in Stainless Steel: Influence of Cavity Density and Morphology", Effects of Radiation on Materials: Eleventh Conference, ASTM STP 782, 1982, in press.

APPENDIX A MODEL CALCULATIONS

The point defect concentrations are obtained from equations (A1) and (A2) assuming quasi-steady-state:

$$\frac{dC_i}{dt} = \xi G - \alpha C_i C_v - D_i \sum_j S_j^i = 0 \qquad \text{(A1)}$$

$$(1-\chi) + D_v \sum_j S_j C_v^j - \alpha C_i C_v - D_v \sum_j S_j^v = \emptyset \qquad \text{(A2)}$$

where G is the damage rate (dpa/sec); ξ and χ have already been defined, S_j is the sink strength of the extended defects, and C_v^j is the vacancy concentration in equilibrium with the j-th sink. Specifically, we compute the sink strengths as follows:

$$S_{v,b}^{i,v} = 4\pi F_s r_{v,b} N_{v,b} (1+r_{v,b} S_t) \qquad \text{(A3)}$$

for voids and bubbles (but neglecting the sink strength correction term for microvoids since

$r_{mv} << 1/S_t$),

$$S_\rho^v = \frac{2n}{\ln(r_s/r_c)} \rho_d \qquad \text{(A4)}$$

$$S_\rho^i = \frac{2\pi}{\ln(r_s/r_c)} (1+\varepsilon)\rho_d \qquad \text{(A5)}$$

for the network dislocations;

$$S_g^{i,v} = \frac{6S_o}{D_g} \qquad \text{(A6)}$$

for the subgrain structure. The superscripts i and v denote interstitial and vacancy respectively; r_c is the dislocation core radius (taken as 4 times the Burgers vector); r_s is the dislocation half spacing, $(2\rho_d)^{-\frac{1}{2}}$, $(1+\varepsilon)$ is the interstitial/dislocation bias: and

$$S_o = (S_\rho^v + \sum_j 4\pi F_s r_j N_j)^{1/2} \quad \text{(A7)}$$

$$S_t = (S_o^2 + S_g^v)^{1/2} \quad \text{(A8)}$$

Vacancy emission from each of the sinks is obtained by computing the following equilibrium vacancy concentrations

$$C_v^{mv} = C_v^e \exp\left(\frac{2\gamma\Omega}{r_{mv} kT}\right) \quad \text{(A9)}$$

for microvoids;

$$C_v^c = C_v^e \exp\left[\frac{\Omega}{kT}\left(\frac{2\gamma}{r_c} - P\right)\right] \quad \text{(A10)}$$

for bubbles and voids;

$$C_v^g = C_v^\rho = C_v^e \quad \text{(A11)}$$

for network dislocations and the subgrains. The gas pressure, P is computed using an equation of state developed by Brearley and MacInnes [31] and C_v^e is thermal equilibrium vacancy concentration.

The number of microvoids is computed by first determining the lifetime, τ_{mv}, of a vacancy cluster with radius r_{mv};

$$\frac{\quad}{D_v C_v - D_i C_i - D_v C_v mv} \quad \text{(A12)}$$

and then integrating equation (A13);

$$\frac{dN_{mv}}{dt} = G_{mv} - N_{mn}\, \tau_{mv}^{-7} \quad \text{(A13)}$$

in which the cluster generation rate is given by;

$$G_{mv} = \frac{G\xi\chi}{\Omega n_v} \quad \text{(A14)}$$

The number of vacancies in the cluster is computed as;

$$n_v = \frac{4\pi r_{mv}^3}{3R} \tag{A15}$$

The equation describing the cavity growth rate is;

$$\frac{dr_c}{dt} = \frac{1}{r_c}(D_v C_v - D_i C_i - D_v C_v^c) \tag{A16}$$

A schematic plot of equation (A16) is shown in Figure A1 where r_b and r_v denote the stable bubble and void radii respectively. Prior to its converting to a void, the equilibrium bubble radius at any time can be found as a root of equation (A16) by setting the derivative to zero and substituting from equation (A10) for C_v^c. For the ideal gas case, the following equation is obtained:

$$r_c^3 - r_c^2 \left(\frac{2\gamma\Omega}{kT\ln S}\right) + \frac{3m_{He}\Omega}{4\pi F C_v \ln S} = 0 \tag{A17}$$

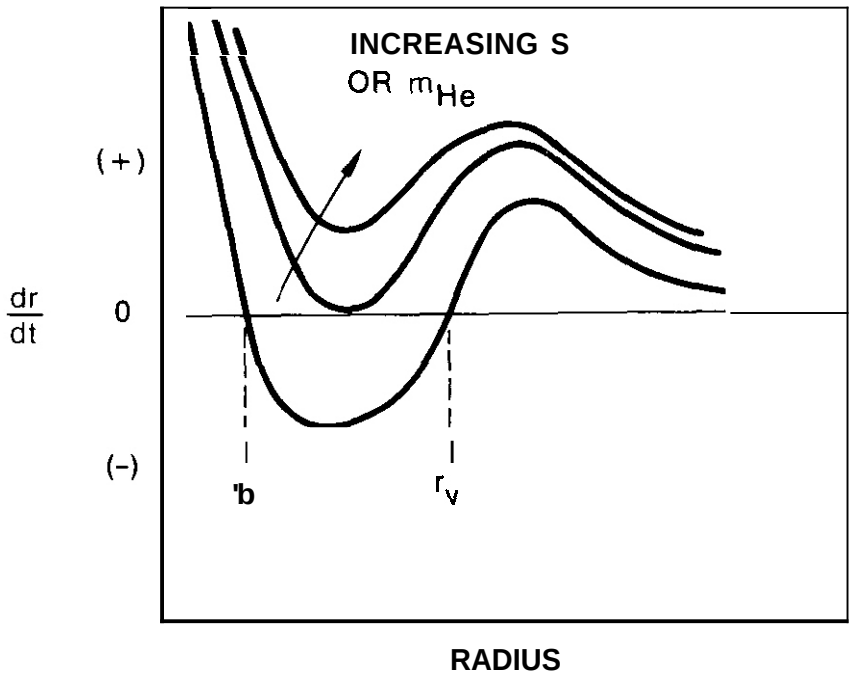

FIGURE A1. Sthematic plot of cavity growth rate as a function of the cavity radius.

where m_c and r_c denote the critical number and critical radius respectively. The critical number can be obtained by solving equation (A17) for the case in which there are two real and equal roots [32]; i.e. the stable bubble and void roots coincide (for this case the third root can be shown to be negative). The critical number (again for the ideal gas case) is:

$$m_c = \frac{128\pi}{81} \left(\frac{\gamma}{kT}\right)^3 \left(\frac{\Omega}{\ln S}\right)^2 F_v \qquad \text{(A18)}$$

An analytical result is not possible in the real gas case due to the fact that the real gas equivalent of equation (A17) is ninth order. In that case the bubble-to-void conversion criterion is similar but must be determined iteratively. An alternate analytical solution for the real gas case is discussed in Appendix C. After the cavity has converted, its radius is found by integrating equation (A16) directly.

As helium is continuously generated, the matrix helium concentration can be obtained as the solution of the following conservation equation;

$$\frac{dM_{He}}{dt} = G_{He} - D_{He} \sum_j S_j^{He} \qquad \text{(A19)}$$

Here the S_j^{He} are the sink strengths of the network dislocations, matrix cavities, subgrains and precipitates. For times greater than $\sim 10^5$ sec. the solution of equation (A19) reduces to the steady state solution.

$$M_{He} = \frac{G_{He}}{D_{He} \sum_j S_j} \qquad \text{(A20)}$$

The helium diffusivity (D_{He}) is computed assuming radiation enhanced diffusion of a divacancy-helium atom complex[34] with a binding energy of 0.5 eV.

$$D_{He} = S \exp\left[-\frac{(E_v^m + E_v^f - E_B)}{kT}\right] \qquad \text{(A21)}$$

The helium partitioning scheme has been described above and the amount of helium allocated during a small time step At is;

$$\Delta He_{mb} = 4\pi r_{mb} D_{He} \frac{(S_{mb} + S_{\rho} f_{He})}{S_{mb}} M_{He} \Delta t \qquad (A22)$$

for matrix bubbles,

$$\Delta He_{mv} = 4\pi r_{mv} D_{He} M_{He} \Delta t \qquad (A23)$$

for matrix voids and

$$\Delta He_{pc} = 4\pi r_{p} N_{p} D_{He} M_{He} \Delta t \qquad (A24)$$

for precipitate-associated cavities when the time is greater than τ_p.

APPENDIX B MODEL PARAMETERS

Material Parameters

Vacancy formation energy, E_v^f	1.5 eV
Vacancy migration energy, E_v^m	1.4 eV
Interstitial migration energy, E_i^m	0.5 eV
Helium-divacancy binding energy, E_B^{He}	0.5 eV
Vacancy diffusivity pre-exponential, D_v^o	0.8 cm^2/sec
Interstitial diffusivity pre-exponential, D_i^o	0.08 cm^2/sec
Recombination parameter, α	$1x10^{16}$ D_i sec^{-1}
Dislocation-interstitial bias, ε	0.25
Surface free energy, γ	2025-0.875T(°C) ergs/cm^2
Total dislocation density, ρ_d	$1.99x10^{14}$ exp(-0.016 T(°C))cm^{-2}
Total cavity density, N_c^t	$2.53x10^{20}$ exp(-0.023 T(°C))cm^{-3}
Precipitate-associated cavity fraction, f_p	0.1
Precipitate sink strength, S_P	$4.0x10^{10}$ cm^{-2}
Precipitate nucleation time, τ_P	0.16 (700-T (°C)) dpa
Cavity volume factor, F_v (β)	ppt-associated; 0.4 (82.3°) matrix; 1.0 (180')
(Corresponding surface area factor, F_s (β)	0.434 (82.3°); 1.0 (180°)

Irradiation Parameters

Damage Rate, G	10^{-6} dpa/sec
Cascade efficiency, ξ	0.4
Fraction of vacancies clustered in microvoids, χ	0.8
Microvoid radius, r_{mv}	5.75Å; T = 375°C
	6.25Å; T = 400°C
	7.50Å; T ≥ 450°C
He/dpa ratio, G_{He}	0.35 appm/dpa (EBR-II)
	10 appm/dpa (fusion)
	~ 70 appm/dpa (HFIR) (34)

APPENDIX C ANALYTICAL SOLUTION WITH REAL GAS EOUATION OF STATE

As discussed in Appendix A, the use of a real gas equation of state requires an iterative solution of equation (A16) in order to compute the bubble radius prior to bubble-to-void conversion. In addition, it is not possible to compute the real gas critical number analytically. Hence the use of the real gas equation of state(31) significantly complicates the computational procedure used in obtaining the results discussed above. We have developed an approximate analytical solution which may be used in order to simplify such calculations without a significant loss of accuracy.

The solution requires two "master" curves as shown in Figure C1 and C2 which were obtained by reducing exact results over a broad range of temperatures (T), surface energies (γ) and cavity volume factors (F_v) using appropriate lumped parameters. For simplicity, polynomial fits of the master curves were obtained using a least-square procedure. The use of a tenth order polynomial yielded excellent agreement with the reduced data and coefficients of the master curves are given in Table C1. The shape of the curves suggest that a simpler non-linear fit may also be possible.

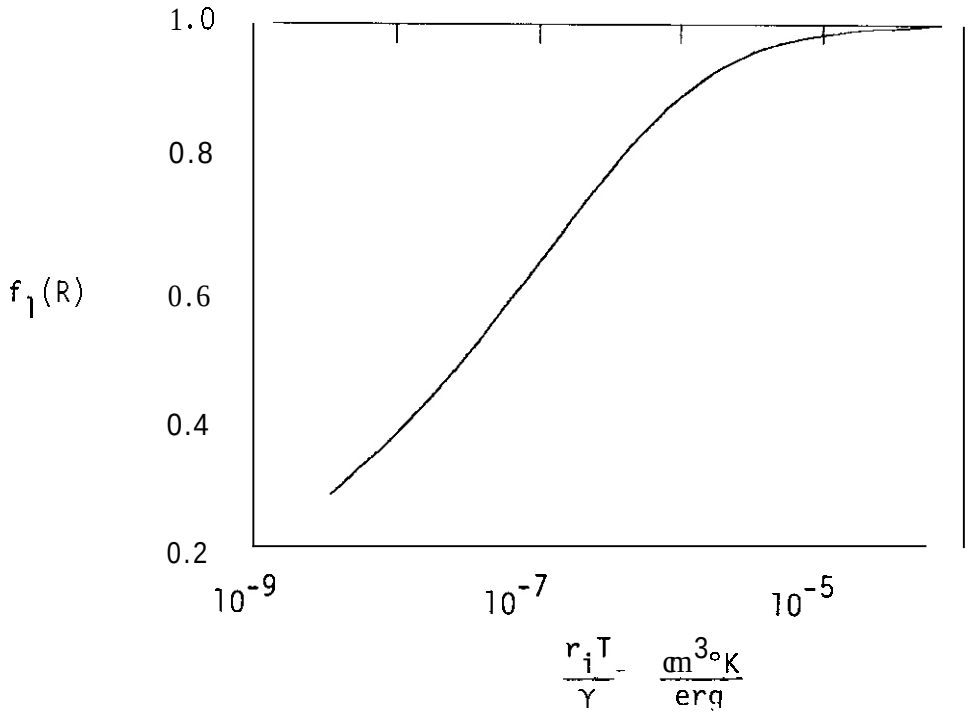

FIGURE C1. Master curve **used** to obtain real gas bubble radius.

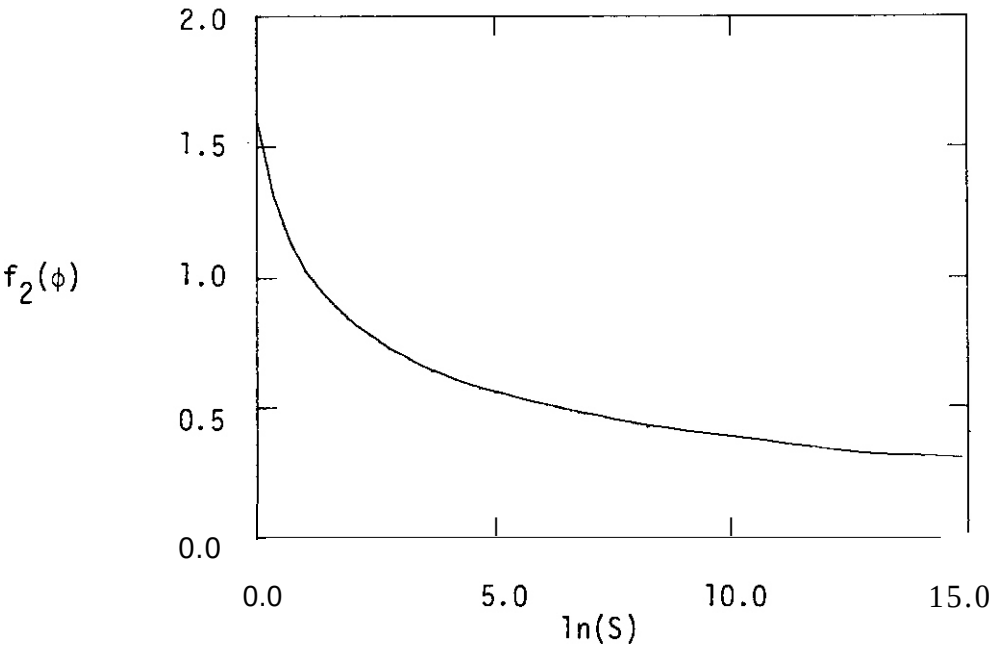

FIGURE C2. Master curve used *to* obtain real gas critical number.

The first master curve permits one to compute the real gas radius (r_r) as a function of T, γ and the ideal gas radius (r_i). After defining the following parameter:

$$R = \frac{r_i(\text{cm})\ T\ (^{o}K)}{\gamma\ (\text{ergs/cm}^2)}\ X10^9\ , \tag{C1}$$

the ratio of r_i/r_r is given simply as,

$$f_1(R) = \frac{r_i}{r} = a_o + a_1R + a_2R^2 \ldots + a_{10}R^{10}. \tag{C2}$$

One obtains r_i as a solution of equation (A17) and r_r is directly computed

$$r_r = \frac{r_i}{f_1(R)} \tag{C3}$$

The error in r_r is $\lesssim$ 1%, increasing near the critical number.

The use of the second master curve permits the direct calculation of the real gas critical number using an expression (see equation (3a)) analogous to equation (A18). In this case the non-ideal properties of the gas are expressed as a function of the effective vacancy supersaturation, *S*,

$$\phi = \ell n\ (S). \tag{C4}$$

The real gas critical number may then be computer using $f_2(\phi)$ where

$$f_2(\phi) = b_o + b_1\ \phi + b_2\ \phi^2 \ldots + b_{10}\phi 10 \tag{C5}$$

and the critical number (n^*_{He}) is

$$n^*_{He} = f_2(\phi)\ F_v\ (\frac{\gamma}{kT})^3\ (\frac{1}{\phi})^2 x10^{-46}. \tag{C6}$$

The error in the critical number thus computed is quite small, <1%.

The use of these approximations was tested in the computational procedure described above. Prior to bubble-to-void conversion, the bubble radii were computed using equation (C3). The bubble-to-void conversion criterion was that the accumulated helium in a cavity exceed the critical number computed

using equation (C6). Table C2 compares the dose at bubble-to-void conversion, τ_{conv}, and the swelling at 100 dpa at the indicated temperatures computed using the analytical approximation with the results obtained using the iterative solution. The agreement is very good and we note that the results encompass a broad parameter range; T=450-700, S=1.01-19.3, γ=1402-1631 and F_v=0.4-1.0.

TABLE C1

POLYNOMIAL COEFFICIENTS FOR MASTER CURVES

i	a_i	b_i
0	2.014733×10^{-1}	1.607500
1	5.236620×10^{-2}	-1.050792
2	2.099011×10^{-2}	7.369905×10^{-1}
3	-1.208723×10^{-2}	-3.465587×10^{-1}
4	6.763545×10^{-3}	1.029474×10^{-1}
5	-2.343054×10^{-3}	-1.956408×10^{-2}
6	5.284246×10^{-4}	2.406067×10^{-3}
7	-7.749721×10^{-5}	-1.902285×10^{-4}
8	6.939713×10^{-6}	9.319578×10^{-6}
9	-3.400417×10^{-7}	-2.571950×10^{-7}
10	6.954455×10^{-9}	3.054073×10^{-9}

TABLE C2

COMPARISON OF ITERATIVE AND ANALYTICAL SOLUTIONS

T(°C)	τ_{conv}(dpa)		Swelling (% at 100dpa)	
	Iterative	Analytical	Iterative	Analytical
450	45.89	47.05	24.41	24.59
500	38.46	38.51	28.77	28.78
550	34.63	34.60	35.45	35.64
600	35.31	35.10	39.53	40.08
650	44.43	43.33	28.79	30.16
700	N/A	N/A	0.18	0.19

MICROSTRUCTURAL/MICROCHEMICAL EVOLUTION OF AISI 316 IRRADIATED AT TEMPERATURES IN THE RANGE 650-750°C

H. R. Brager, W. J. S. Yang and F. A. Garner (Hanford Engineering Development Laboratory)

1.0 Objective

The object of this effort is to determine the relative contributions of helium and the radiation-induced microchemical evolution to void swelling in AISI 316 at high temperatures.' This segment concentrates on the evolution at low helium/dpa ratio.

2.0 Summary

In the comparison of HFIR and EBR-II swelling data for AISI 316 it is important to recognize that the reported HFIR temperatures are believed to be underestimated by 75-125°C. In order to have data from EBR-II irradiations comparable to those available from HFIR, two specimens were examined which were irradiated to 700-720°C. The swelling is comparable to that observed at 650°C and below, but the void densities are lower. Total swelling does not appear to be as sensitive to void density or helium content as previously expected.

While the swelling is heterogeneous on a grain-to-grain level, voids always appear first in grains which have nickel levels below 12-13 wt.%. The matrix content of nickel declines to ~9% as the swelling increases to substantial levels. This value of 9% has been observed at other lower temperatures. Nickel and silicon segregate not only to precipitates but also to the surface of voids.

3.0 Program

Title: Irradiation Effects Analysis (AKJ)
Principal Investigator: D. G. Doran
Affiliation: Hanford Engineering Development Laboratory

4.0 Relevant DAFS Program Task/Subtask

II.C.2 Effects of He on Microstructure
II.C.17 Microstructural Characterization

5.0 Accomplishments and Status

5.1 Introduction

The need to develop a predictive equation for void swelling in fusion devices has recently led to a comparison of the microstructures that develop in a single heat of AISI 316 (designated DO-heat) when irradiated in either the HFIR or EBR-II reactors.[1-2] While the examination of this steel in two reactor environment; is nominally directed toward the determination of the role of helium on void swelling, the analysis is complicated by the additional influence of differences in solid transmutants.[3-4] There is also a substantial difference in the displacement generation process[5] and very large uncertainties in the irradiation temperatures, particularly in the specimens irradiated in HFIR.

It appears that the nominal temperatures quoted in the original paper[6] describing swelling of AISI 316 in HFIR are low by 75-125°C.[7] When comparisons are made with EBR-II data it is therefore important that specimens be compared at comparable temperatures. This requires that data on swelling in EBR-II be available to temperatures in excess of 700°C.

Although the swelling-oriented subassemblies of the U.S. Breeder Program did not probe the temperature regime above 650°C, pressurized tubes used to study irradiation creep were irradiated at temperatures as high as 720°C. (Above this temperature the thermal creep rate is too high to warrant the service of AISI 316 in a breeder reactor.) Two nominally unstressed specimens irradiated at temperatures above 700°C have been examined by electron microscopy and energy dispersive x-ray analysis. Both specimens were irradiated for several EBR-II irradiation cycles in

the YY06 experiment and then completed irradiation in the AA-II experiment. The first irradiation was a controlled-flow temperature-monitored experiment while the latter is an uninstrumented heat-pipe experiment.

The first specimen was extracted from a tube designated K65, fabricated from a tubing lot of 20%CW steel designated CN-13. This heat is known to swell relatively early compared to the DO-heat, but is otherwise expected to exhibit comparable post-transient swelling behavior. The K65 specimen was irradiated to 7.5 x 10^{22} n/cm^2 at a nominal temperature of 700°C. The actual temperature varied from 667 to 710°C with about half of the total fluence accumulated at 710°C. Diameter and density change measurements showed that a volumetric increase of 2.5% had occurred. It is known that some fraction of this volume change is due to volume changes arising from formation of intermetallic phases.[8] As shown in Figure 1, there is several percent of void swelling in this specimen. This figure also shows that the swelling $\gtrsim$700°C is comparable to that observed in another experiment on this and three related heats at 650°C.

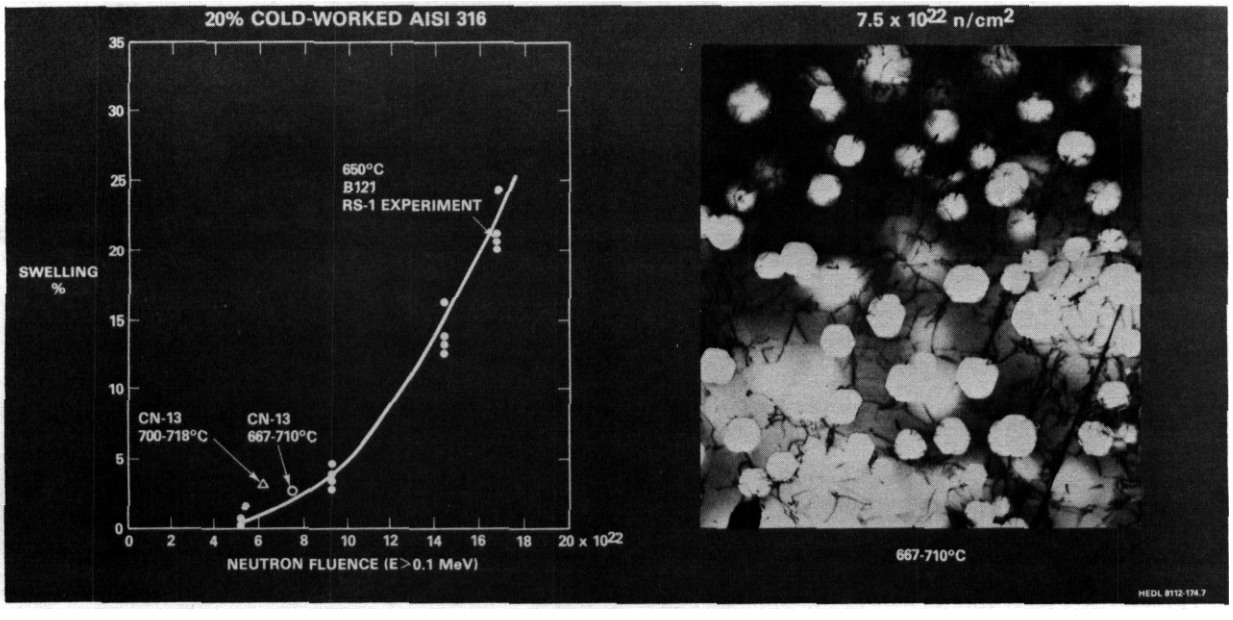

FIGURE 1 High Temperature Swelling of 20%CW AISI 316 Stainless Steel Specimens Showing Comparison Between CN-13 Creep Tube Data with Data at 650°C for CN-13 and Three Closely Related Heats.

The second specimen was derived from another CN-13 tube designated KE6. This specimen reached 1.2×10^{22} n/cm^2 (E >0.1 MeV) at 718°C, continued to 2.3×10^{22} at 700°C and finally reached 6.2% at 710°C. The volume change of this specimen was measured to be 2.8%. A large fraction of the volume change in this specimen may be due to the formation of large intermetallic precipitates, one of which is also shown in Figure 2.

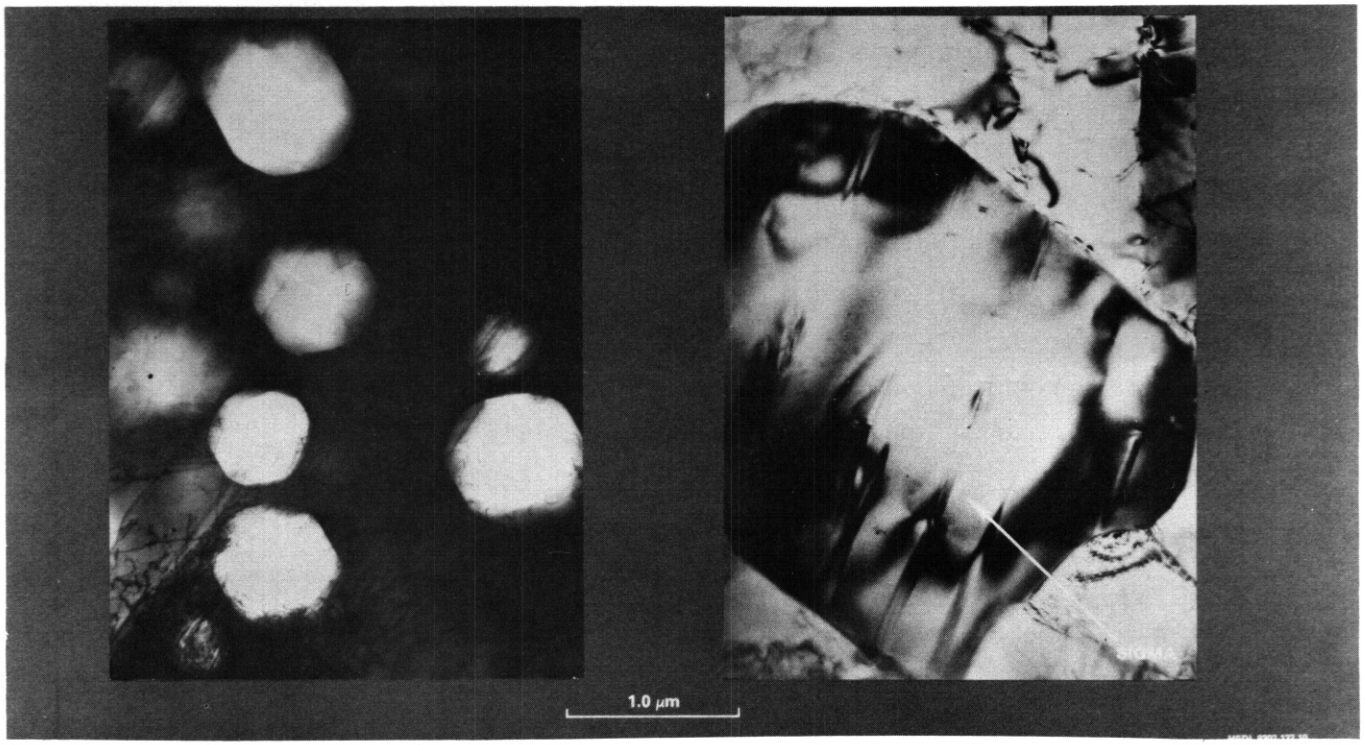

FIGURE 2. High Temperature Swelling of CN-13 Creep Tube KE6 at 700-718°C and 6.2×10^{22} n/cm^2 (E >0.1 MeV). The swelling is very nonuniform at the voids at low densities ($\sim 10^{13}$ cm^{-3}). Some areas contain large intermetallic precipitates.

5.2 X-ray Analysis of Specimen K65 (667-710°C)

Void formation was found to be relatively homogeneous within any one grain but to be rather heterogeneous from grain-to-grain. Grain boundaries frequently separated heavily-voided grains from totally unvoided grains. The possible relationship of such behavior to the details of the local microchemical environment was investigated using three different types of measurements.

First, entire grains were scanned with the electron beam. Each grain chosen for examination had a relatively uniform void array and was adjacent to other grains with widely differing swelling levels. These areas inevitably contained some precipitates but the level of precipitation was rather low compared to that which evolves at lower temperatures. As shown in Table 1 those areas which contained voids had lower nickel levels than observed in non-voided regions. In this comparison the voided regions also had higher molybdenum levels.

TABLE 1

COMPOSITION DETERMINED BY BROAD BEAM SCAN IN SPECIMEN K65

	weight %				
Voids?	Si	Cr	Fe	Ni	Mo
Yes	0.6	17	66	12.8	1.8
Yes	0.7	23	61	9.5	3.4
Yes	0.5	22	63	10.3	3.0
Yes	0.6	16	67	13.6	1.6
No	0.4	16	66	15.6	1.2
No	0.5	16	66	15.3	1.1

The second type of measurement used a smaller electron probe diameter of 10 nm and the matrix concentrations were randomly sampled in an area previously scanned by a broader beam. This measurement determined the average matrix composition away from both void and precipitate boundaries. As shown in Table 2 and Figure 3, the mean matrix nickel level of voided regions was found to be 9.8 wt.%, while that of an adjacent unvoided region was 13.4%. There were no other significant differences in elemental composition found between the two regions selected for analysis. (A comparison of the results of the two measurement techniques is shown in Figure 4.)

TABLE 2

MATRIX SPOT ANALYSIS OF COMPOSITION IN SPECIMEN K65

	weight %				
Voids?	Si	Cr	Fe	Ni	Mo
Yes	0.7	19	69	9.3	0.6
Yes	0.7	18	68	10.0	1.2
Yes	0.7	19	68	10.0	1.2
Yes	0.7	19	69	8.6	1.4
Yes	0.7	19	68	9.8	1.3
Yes	0.6	19	68	9.2	1.7
Yes	0.7	19	69	9.3	1.3
Yes	0.7	19	67	11.1	1.1
Yes	0.6	19	68	9.9	1.0
Yes	0.6	20	67	9.9	1.4
Yes	0.6	19	69	9.5	0.9
				average 9.7% compared to 9.5% by broad beam analysis	
Yes	0.4	19	70	9.3	0.8
Yes	0.5	20	68	9.8	1.1
Yes	0.4	19	67	11.7	1.0
Yes	0.3	19	68	10.7	1.0
Yes	0.4	19	69	10.0	1.2
				average 10.3% compared to 10.3% by broad beam analysis	
Yes	0.3	19	68	9.5	1.8
Yes	0.4	19	68	10.3	1.9
Yes	0.3	20	69	8.5	2.0
				average 9.4% compared to 13.6% by broad beam analysis	
No	0.7	18	69	9.5	1.1
No	0.6	15	66	15.9	1.1
No	0.5	17	69	11.2	1.2
No	0.4	17	66	14.3	1.5
No	0.7	18	68	10.2	1.6
No	0.4	15	66	16.1	1.1
No	0.3	16	67	14.5	1.2
No	0.4	16	66	15.5	1.2
No	0.3	17	67	12.7	1.4
No	0.2	18	68	11.9	1.2
No	0.3	17	67	14.0	1.2
No	0.5	16	67	14.6	0.8
Averages	0.4	17	67	13.4	1.2

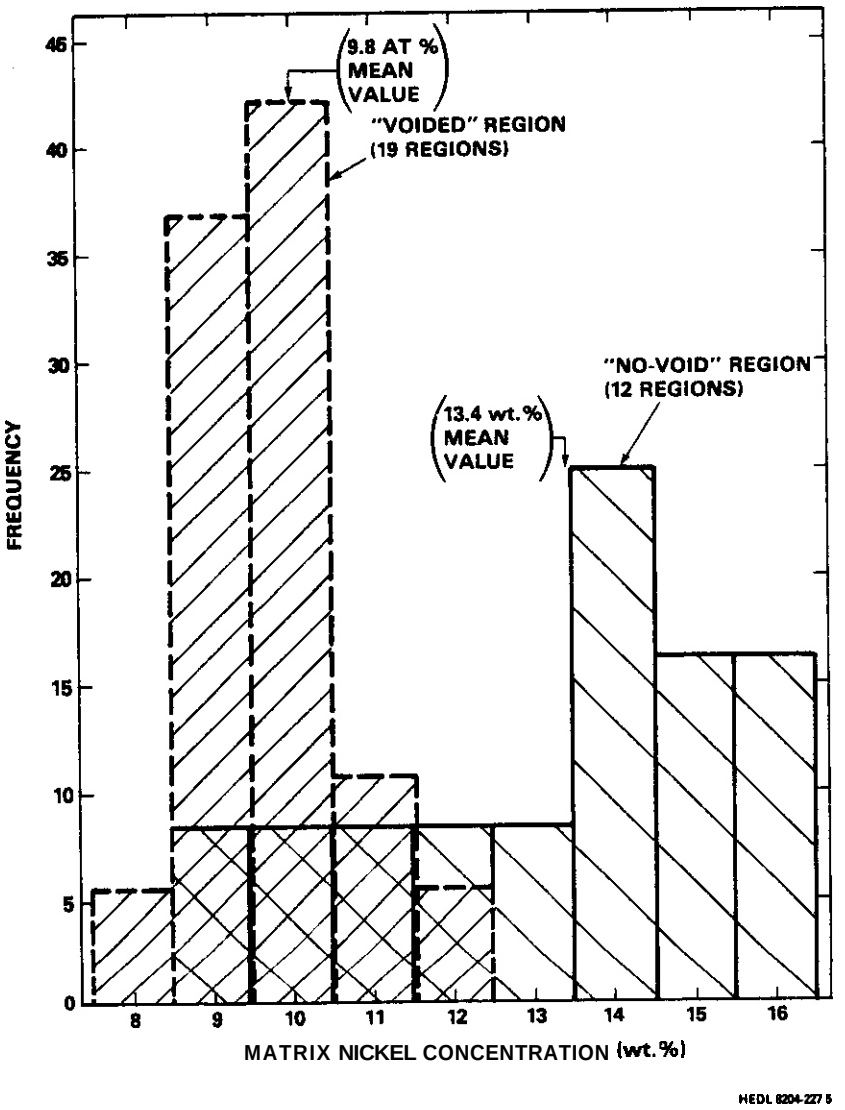

FIGURE 3. Local Matrix Composition of Nickel in Two Adjacent Grains of Specimen K65 of 20% Cold-Worked AISI 316 Irradiated at 667-710°C and 7.5 x 10^{22} n/cm^2 (E >0.1 MeV). Note that voided regions have lower nickel content than non-voided regions.

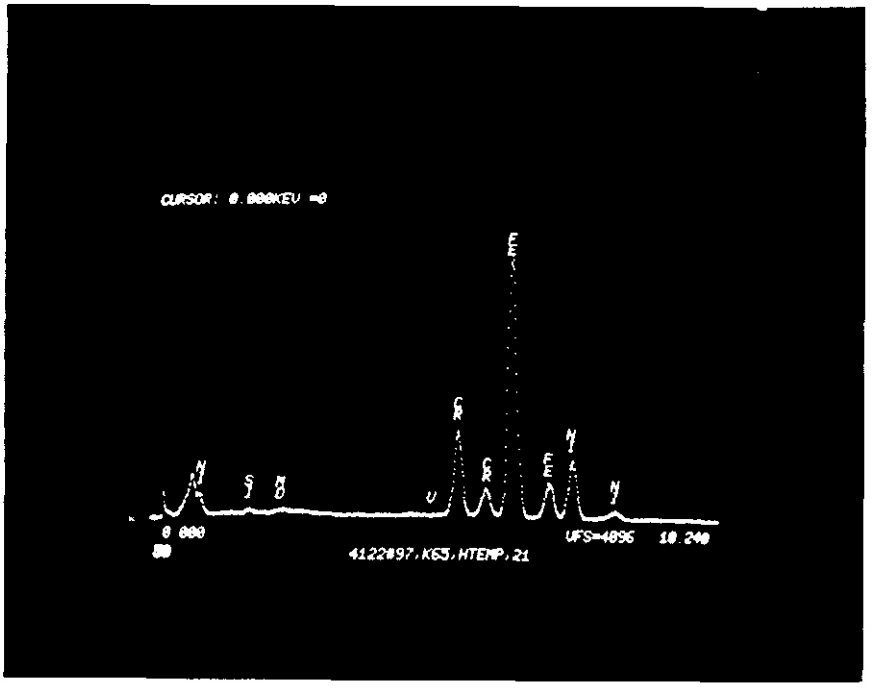

(a)

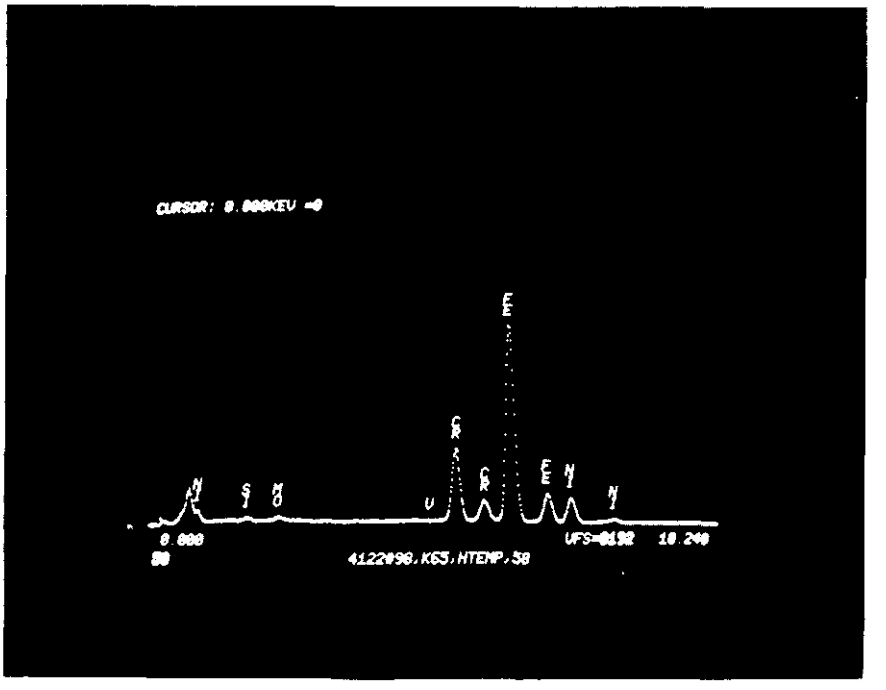

(b)

FIGURE **4.** Typical EDX Spectra of Specimen K65. Spectrum (a) is a between-void spot-analysis and (b) is a broad matrix scan of a no-void region. There is 9.2% nickel in the former and 15.6% nickel in the latter. Note the absence of a vanadium peak, in contrast to that found in **AISI** 316 irradiated in HFIR.(2,4,15)

Note in Table 2 that in two of the three voided areas studied the mean matrix composition corresponds very well to the value obtained by scanning the entire region, which includes both voids and occasional precipitates. This implies that the large grain-to-grain variations in nickel content observed in scanning measurements are not the result of voids and precipitates within the grain being the major reservoir for the segregated nickel. Nickel does segregate to void surfaces and into the few precipitates formed at this temperature, however. This is shown by the third type of measurement employed in this study.

The use of line-of-sight composition-averaged measurements usually yields an underestimate of the concentration of a segregated species. When a concentration gradient exists, a traverse of measurements along that gradient can yield information on the direction of flow of various elements. Figures 5-8 show the results of typical traverses across three types of microstructural boundaries. Figure 5 is a typical profile across a void boundary and shows that substantial segregation of nickel and also silicon has occurred to the void surface. When traversing a grain boundary between voided and non-voided grains (Figure 6) an abrupt change in nickel level can also be observed. At some grain boundary positions (Figure 7) it appears that the grain boundary also segregates nickel but not silicon. This behavior has been previously observed in this alloy.[9]

The line-of-sight averaging technique is somewhat more difficult to apply to precipitate/matrix boundaries. Any compositional gradient across the boundary is obscured somewhat as the beam averages both precipitate and matrix composition and also by the beam's tendency to spread as the electrons are scattered in the foil. If a thickness gradient exists in the precipitate or if the boundary is inclined with respect to the beam there will be additional smearing of the profile.

There are however in Figure 8 gradients in elemental composition which extend well beyond the distances involved in the above problems. The presence of these gradients indicates that the microchemical evolution

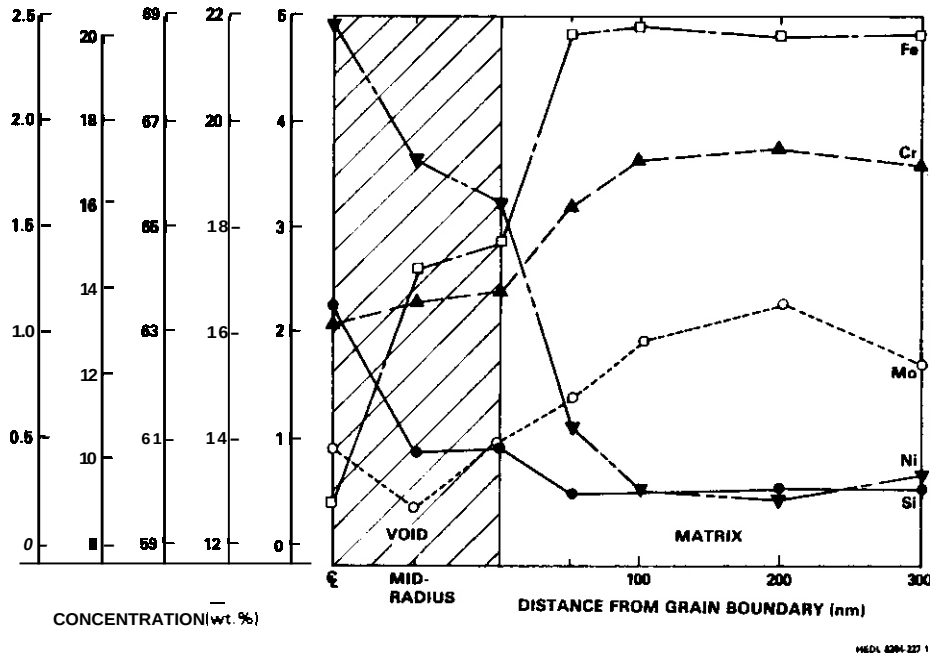

FIGURE 5. Line-of-Sight Composition Profile Along a Traverse Across a Void in Specimen K65.

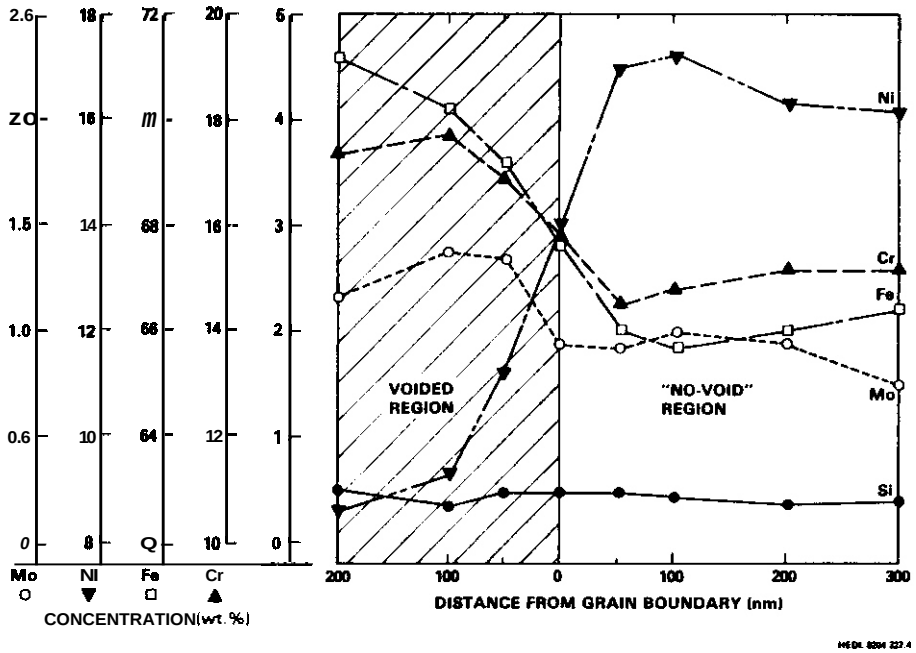

FIGURE 6. Line-of-Sight Composition Profile Along a Traverse Across a Grain Boundary Separating Voided and No-Void Regions in Specimen K65.

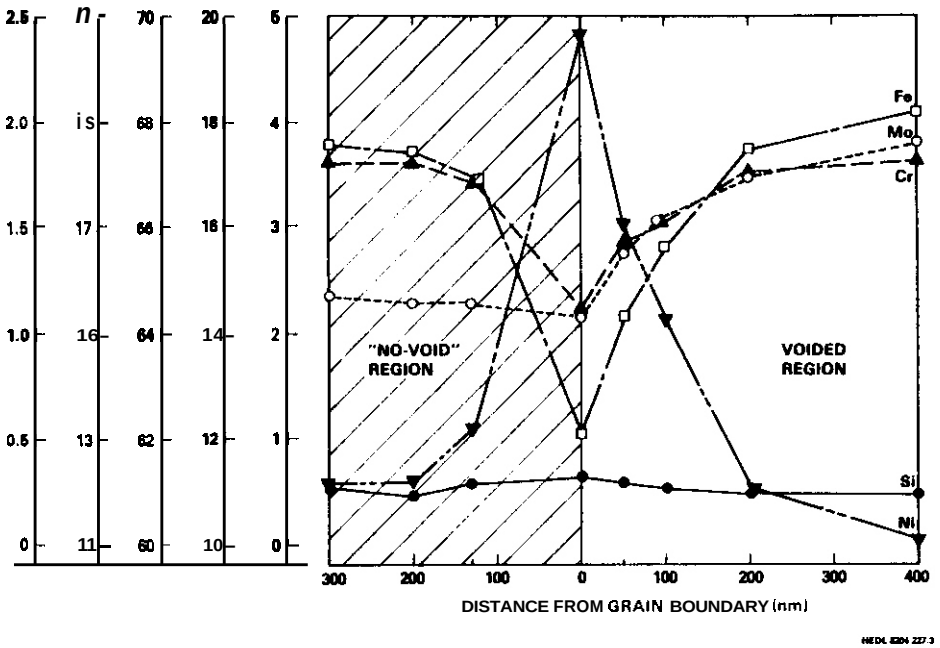

FIGURE 7. Line-of-Sight Composition Profile Along a Traverse Across a Grain Boundary Showing Evidence of Nickel Segregation.

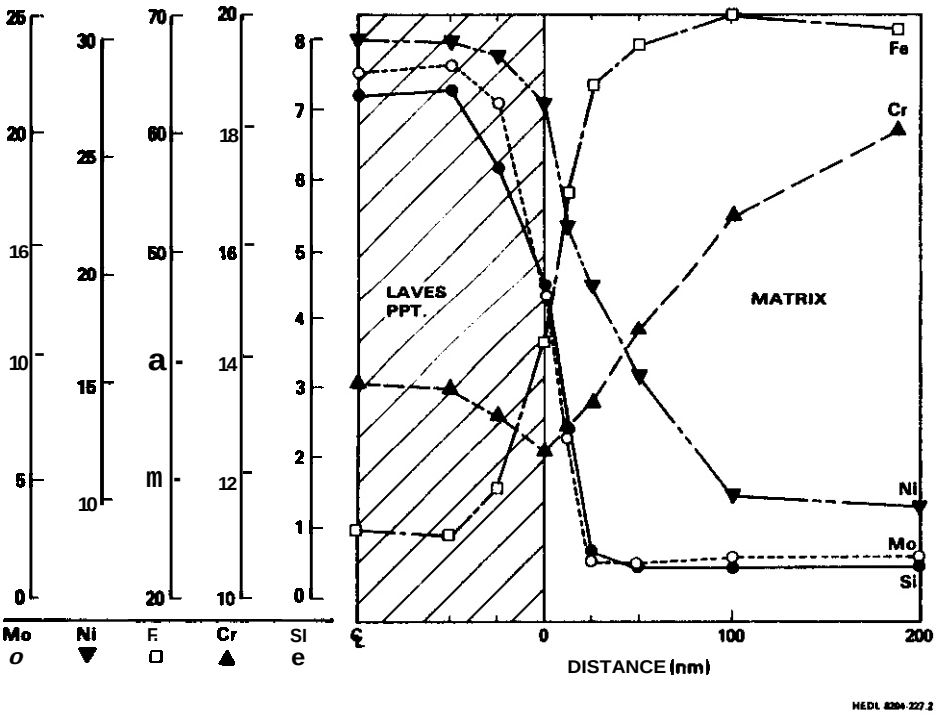

FIGURE 8. Line-of-Sight Composition Profile Across Precipitate/Matrix Interface in Specimen K65. The precipitate has been identified as Laves.

of the matrix is still in progress. Note that the nickel and silicon levels of this precipitate (identified as Laves) are quite high, indicating that precipitation plays a role in the removal of nickel from the matrix.

5.3 X-ray Analysis of Specimen KE6 (700-718°C)

The voids in this specimen are in general much larger than those observed in K65 and are even more non-uniformly distributed. Once again the swelling was observed to be relatively uniform within any given grain, however. The substantial heterogeneity of swelling did not allow an estimate of the relative contribution of voids and phase-related density changes to the measured volume change of 2.3%.

Table 3 shows that in unvoided grains the analysis of the matrix composition at discrete locations (spot-matrix) and of large portions of a grain (scanned-matrix) measurements agree, showing a relatively high nickel content of 15-16%. In an adjacent voided grain the nickel content was lower at 13%. The silicon level was also lower.

EOX measurements of the nickel content showed line-of-sight enrichments at void surfaces approaching 21%, as shown in Table 4.

5.4 Discussion

It has previously been shown that the average nickel content of the alloy matrix can be used as an index of the degree of completion of the microchemical evolution.(") In this study the use of this index has again been confirmed. When the swelling process is just starting to accelerate to measurable levels, those regions which fall below 12-13% nickel first exhibit swelling. The possibility exists however that the variation in nickel contents (12-16%) on a grain-to-grain level represents more the natural heterogeneity of the steel than the results of the radiation-induced nickel segregation process. (The CN-13 heat of steel contains an average nickel content of 13.7%.) This possibility will be investigated shortly.

TABLE 3

EOX ANALYSIS OF SPECIMEN KE6

Voids	weight %				
	Si	Cr	Fe	Ni	Mo
			MATRIX SCAN ANALYSIS		
No	0.4	17	66	14	2.0
No	0.3	16	63	18	1.7
No	0.6	17	65	15	0.8
No	0.5	18	68	12	0.8
No	0.7	15	62	19	1.0
No	0.8	16	62	19	0.7
No	0.8	16	63	18	0.6
No	0.8	17	65	16	0.8
No	0.7	16	66	15	0.7
No	0.7	16	66	15	0.8
Averages	0.6	16	65	16	1.0
			MATRIX SPOT ANALYSIS		
No	0.7	17	66	14	1.2
No	0.5	17	65	15	0.9
No	0.7	17	64	14	2.0
No	0.7	16	64	16	1.3
No	0.6	16	65	16	1.0
No	0.3	17	66	14	0.8
Averages	0.6	17	65	15	1.2
			MATRIX SCAN ANALYSIS		
Yes	0.3	18	67	13	1.0
Ye5	0.3	18	67	12	1.3
Yes	0.4	17	66	13	1.1
Yes	0.3	18	67	13	1.4
Ye5	0.2	18	67	13	0.9
Ye5	0.3	18	66	13	1.4
Yes	0.3	19	67	12	1.0
Yes	0.2	19	67	12	1.0
Averages	0.3	18	67	13	1.1

TABLE 4

EDX ANALYSIS OF VOIDS IN SPECIMEN KE6

	Si	Cr	Fe	Ni	Mo
Void A centerline	0.4	17	65	15	1.1
Void A mid-radius	0.4	17	65	16	1.0
Void B centerline	0.8	17	59	21	0.8
Void B mid-radius	0.7	20	56	21	0.9
Void C centerline	0.2	16	63	20	0.7
Void C mid-radius	0.3	16	63	19	0.6
Averages	0.5	17	62	19	0.9

The reduction of the matrix nickel level to ~9% by the time substantial swelling has occurred is typical of that observed in other studies[10-12] when the silicon level is ~0.5 wt.%. This value appears to be relatively independent of temperature. For higher silicon levels the nickel content of the matrix falls even lower.[13]

While the matrix nickel content has been chosen as a convenient index, a more appropriate index of the extent of the evolution might be the average silicon content. Silicon has an even greater effect on void nucleation than does the nickel content,[14] but the silicon level is much smaller and therefore harder than the nickel to quantitatively measure.

The most significant result of this study lies in the observation that not only does swelling occur in AISI 316 at temperatures above 700°C, but that the swelling does not decline with temperature in this range as previously anticipated. It had previously been thought that swelling would not occur at 650-700°C in EBR-II due to its low helium/dpa ratio. It appears that the total swelling does not depend very strongly on the helium level at any temperature investigated to date, although the void density is sensitive to the helium content.[1,2]

5.5 Conclusions

In the comparison of HFIR and EBR-II swelling data for AISI 316 it is important to recognize that the reported HFIR temperatures have been underestimated by 75-125°C. In order to provide comparable specimens from EBR-II irradiations, two specimens have been examined which were irradiated to temperatures in the range 700-720°C. Swelling at these temperatures is comparable to that observed at 650°C and below, but the void densities are lower. Total swelling does not appear to be as sensitive to void density or helium content as previously expected.

While the swelling is heterogeneous on a grain-to-grain level, voids always appear first in grains which have nickel levels below 12-13 wt.%. The matrix content of nickel declines to ~9% as the swelling increases to substantial levels. This value of 9% has been observed at other lower temperatures. Nickel and silicon segregate not only to precipitates but also to the surface of voids.

6.0 References

1. H. R. Brager and F. A. Garner, "Comparison of the Swelling and the Microstructural/Microchemical Evolution of AISI 316 Irradiated in EBR-II and HFIR," DAFS Quarterly Progress Report, DOE/ER-0046/6, August 1981, p. 162, also Proc. Second Topical Meeting on Fusion Reactor Materials, Seattle, WA, August 9-12, 1981 (J. Nucl. Mat., 104 (1981) p. 993).

2. H. R. Brager and F. A. Garner, "Influence of Neutron Spectra on the Radiation-Induced Evolution of 316," Proc. International Conference on Neutron Irradiation Effects, Argonne National Laboratory, November 9-12, 1981 (to be published in J. Nucl. Mat.).

3. J. F. Bates, F. A. Garner and F. M. Mann, "The Effect of Solid Transmutation Products on Swelling in 316 Stainless Steel," ibid.

4. F. A. Garner, F. M. Mann and H. R. Brager, "Measurement and Calculation of Solid Transmutants Formed in AISI 316," DAFS Quarterly Progress Report, DOE/ER-0046/7, November 1981, p. 198.

5. L. R. Greenwood and R. K. Smither, "Neutron Dosimetry Measurements for the HFIR-CTR3 Irradiation," also F. A. Garner and F. M. Mann, "The Impact of the $Ni^{59}(n,\alpha)^{56}Fe$ Reaction on Damage Calculations for HFIR," DAFS Quarterly Progress Report, DOE/ER-0046/9, April 1982.

6. P. J. Maziasz, F. W. Wiffen and E. E. Bloom, "Swelling and Microstructural Changes in Type 316 Stainless Steel Irradiated Under Simulated CTR Conditions," Oak Ridge National Laboratory Report ORNL/TM-5396, also pp. 259-288 in Radiation Effects and Tritium Technology for Fusion Reactors, CONF-750989, Volume 1, March 1976.

7. G. R. Odette, P. J. Maziasz and J. A. Spitznagel, "Fission-Fusion Correlations for Swelling and Microstructure in Stainless Steels: Effect of the Helium to Displacement Damage Per Atom Ratio," in Reference 2.

8. F. A. Garner, "Extrapolation of Stress-Affected Swelling Models into Compressive and Cyclic Stress States," DAFS Quarterly Progress Report, DOE/ER-0046/5, May 1981, p. 198.

9. H. R. Brager and F. A. Garner, "Analysis of the Radiation-Induced Microchemical Evolution in 300 Series Stainless Steels," DAFS Quarterly Progress Report, DOE/ER-0046/1, May 1980, p. 157.

10. F. A. Garner, "The Microchemical Evolution of Irradiated Stainless Steels," in Phase Stability During Irradiation, J. R. Holland, D. I. Potter and L. K. Mansur (Eds.), AIME 1980, p. 165.

11. H. R. Brager and F. A. Garner, J. Nucl. Mat., 73 (1978) p. 9.

12. H. R. Brager and F. A. Garner, "Microchemical Evolution of Neutron-Irradiated Stainless Steel," Effects of Radiation on Materials: Tenth Conference, ASTM STP 725, D. Kramer and J. S. Perrin (Eds.), American Society for Testing and Materials, 1981, pp. 470-483.

13. H. R. Brager and F. A. Garner, "Radiation-Induced Evolution of the Austenitic Matrix in Silicon Modified AISI 316 Alloys," in Reference 10, p. 219.

14. F. A. Garner and W. G. Wolfer, J. Nucl. Mat., 102 (1981) pp. 143-150.

15. H. R. Brager and F. A. Garner, "Microchemical Examination of Annealed AISI 316 (DO-heat) Irradiated in HFIR," DOE/ER-0046/9, April 1981, p. 160.

LITHIUM DOPING OF 316 STAINLESS STEEL TO SIMULATE IRRADIATION DAMAGE IN A FUSION REACTOR ENVIRONMENT

J. Megusar, O. K. Harling and N. J. Grant (Massachusetts Institute of Technology)

1.0 Objective

The objective of this study was to develop a lithium doping technique to simulate simultaneous helium production and displacement damage in bulk specimens of non-nickel bearing material such as ferritic steels when irradiated in a fission reactor.

2.0 Summary

Lithium doped austenitic stainless steel was prepared by using rapid solidification processing and a powder metallurgy salt decomposition technique. Neutron autoradiography verified a uniform distribution of lithium in the alloy. Although the same approach can be used to dope material uniformly with a stable boron compound, it should be an advantage to use lithium doping because this dopant produces only helium and hydrogen which are also produced by the CTR environment.

3.0 Program

Title: Alloy Development for Irradiation Performance in Fusion 'Reactors
Principal Investigators: O. K. Harling and N. J. Grant
Affiliation: Massachusetts Institute of Technology

4.0 Relevant DAFS Program Plan Task/Subtask

Some of the tasks/subtasks relevant to the experimental simulation of fusion reactor irradiation effects are:
Task II.A.4 Gas Generation Rates

Task 11.C.2 Effects of Helium on Microstructure
Task 11.C.8 Effects of Helium and Displacement on Fracture

5.0 Accomplishments and Status

5.1 Introduction

In fusion reactors the helium producing nuclear reactions become much more important with increasing energy and because of this, the relatively low energy fission sources cannot properly simulate the higher helium production rates expected in fusion reactors. In terms of helium production, nickel offers a compromise for fission systems; for example, the 8 to 20% Ni in austenitic stainless steels produces helium through a double thermal neutron capture process. Although certain experimental difficulties arise in this technique, the method is currently the best for those materials that contain a significant amount of nickel. For ferritic steels or for refractory/reactive materials, other methods must be developed since additions of nickel will probably significantly alter the structures and properties of commercial base metals or alloys.

To simulate simultaneous helium production and displacement damage in bulk specimens of non-nickel bearing materials, helium producing elements can be added. The materials with high thermal neutron cross section for helium production are ^{10}B and ^{6}Li. Provided that a material can be uniformly doped with enough ^{10}B or ^{6}Li so that the total amount burned up would be relatively small, simultaneous helium production and displacement damage can be investigated with fast reactors. The reason for excess boron is that helium production during the experiment should be nearly linear.

In previous work[1] an austenitic stainless steel was doped with 1000 appm 92% enriched ^{10}B and 5000 appm natural boron; these boron concentrations produce about 3 appm He/dpa in the core of EBR-II. Rapid solidification techniques have been used to prepare these alloys. The maximum solubility of

boron in a typical austenitic 18 Cr - 10 to 14%Ni stainless steel is about 500 appm at 1100-1150°C[2]; consequently 100% of the boron cannot be retained in solid solution with conventional processing. Cooling rates of the order of 10^6°C/sec, which are achieved by twin roller solidification, permit large solid state supersaturation and thereby make possible preparation of uniformly doped austenitic stainless steel at 1000 and 5000 appm boron.[1]

It has been shown that boron will segregate to the grain boundaries, even at overall levels as low as 10 appm, during high temperature exposure.[3] For the boron doping to produce a uniform helium dispersion at concentrations and temperatures of interest, the boron is fixed as a fine ZrB_2 precipitate by doping the austenitic stainless steel with stoichiometric amounts of boron and zirconium for ZrB_2 formation and by choosing appropriate heat treatment conditions.[1,4] Irradiation experiments of this material are presently in progress and initial estimates of the boron kinetics suggest that ZrB_2 should be stable during long term irradiation at 450° and 550°C.[5]

Solubility of lithium in ferritic steels and in austenitic and ferritic stainless steels is negligibly small; at 600°C solubility of lithium in iron is 11 ppm.[6] Therefore lithium cannot be retained in solid solution by using conventional ingot technology in amounts of several 1000 appm to simulate the first wall fusion reactor environment, i.e., to simulate simultaneous helium production and displacement damage. Lithium can, however, be introduced into a ferritic steel, for example, as a stable compound and as a uniform dispersion by using rapid solidification PM processing and advanced powder metallurgy techniques. For this purpose, material to be doped with lithium is rapidly solidified by ultrasonic gas atomization to produce fine spherical powders. The powders can be used directly if fine enough or can be attrited to finer sizes, for example, as fine flakes. A stable lithium compound is then introduced by using any one of several solid state powder metallurgy techniques such as powder blending, mechanical alloying or salt decomposition, etc. In the powder blending technique, fine powders which should be ideally near-micron size are mechanically blended with fine powders of the

stable compound, for example, pure or alloyed lithium oxide, to obtain a uniform distribution of lithium in the alloy. This technique has been used successfully in preparing several dispersion stabilized alloys such as alumina dispersion stabilized copper alloys[7] and a 316 stainless steel - Y_2O_3 alloy.[8] In the salt decomposition technique, which has been used in preparing thoria dispersion stabilized nickel,[9] for example, metal powders are ball-milled with a thorium nitrate liquid solution; the thorium nitrate is subsequently decomposed by heating under vacuum, resulting in a uniform dispersion of fine thoria particles in the nickel matrix. Both the mechanical blending and salt decomposition techniques should be equally applicable in preparing lithium doped alloys, with lithium present as a stable compound. This report describes the preparation of lithium doped austenitic stainless steel by using a salt decomposition technique and characterizes the lithium distribution in terms of neutron autoradiography. Lithium doping could be used as an alternative method to boron doping to simulate simultaneous helium production and displacement damage in bulk specimens of non-nickel bearing materials such as ferritic steels.

5.2 Experimental Procedures

An ultra low C+N stainless steel was provided by Allegheny Ludlum Company of the following chemical composition (in wt%): 16.36 Ni, 16.67 Cr, 2.26 Mo, 1.25 Mn, 0.51 Si, 0.0027 C, 0.003 N, 0.0027 S, bal Fe. The alloy was remelted and modified by the addition of 1 percent aluminum. This alloy was rapidly solidified to produce fine powders by means of high velocity jets of nitrogen and argon. The estimated cooling rate was 10^4°C/sec. Powders finer than 53 μm were comminuted in an attrition mill using stainless steel balls; 200 gram lots of powders were attrited under isopropyl alcohol for 48 hrs at approximately 170 RPM. The alcohol slurry of near micron thick flakes was decanted and vacuum dried.

The stainless steel flakes were mixed with $LiAlH_4$ powder in the amount corresponding to 1000 ppm of lithium. Ether was added while stirring the

powder mixture in order to dissolve the $LiAlH_4$ and to wet the stainless steel flakes uniformly with the $LiAlH_4$ solution. Stirring was continued until the ether evaporated. The stainless steel flakes were heated for 1 to 3 hrs at 150°C under vacuum to decompose $LiAlH_4$ and to remove hydrogen.

Stainless steel flakes doped with lithium were then consolidated by using a dynamic powder (shock wave) compaction technique of the Institute Cerac, Ecublens, Switzerland. A two-stage high speed gun was used; the compaction was effected by the shock wave[10] which is produced by impact of the projectile on the powder at a speed of 1200 m/sec. The diameter of the compacted disc was 5 cm and the height was 1 cm. The dynamically compacted alloy was heated to 1000°C and rolled to 40% R.A.

The amount of lithium in the consolidated alloy was obtained by flame emission spectroscopy and the distribution of lithium was determined by neutron autoradiography.

5.3 Experimental Results

Figure 1 shows the morphology of a -53 μm powder fraction of rapidly solidified alloy. The powder particles are spherical; previous work[11] showed the dendrite arm spacing is typically 1-3 μm, indicating a cooling rate of approximately 10^4°C/sec.

These powders were attrited for 48 hrs under isopropyl alcohol and the resultant flake morphology is shown in Figure 2. An average flake thickness is 0.5 μm. Attrition has been considered an important step in preparing lithium doped material in order to obtain an average lithium interparticle spacing finer than several microns, i.e., less than the range of the helium ions produced in the $^6Li(n,\alpha)^3T$ reaction.

Commercially available $LiAlH_4$ powders were rather coarse and SEM examination showed that the average particle diameter exceeded 100 μm. By adding ether

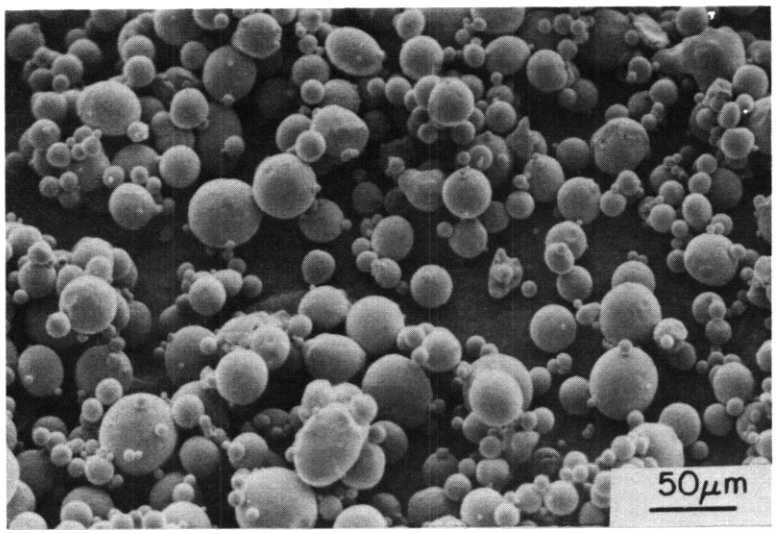

FIGURE 1. STEM Micrograph Showing the Morphology of Rapidly Solidified Powders of 316 Stainless Steel Alloyed with 1% Al. **Size** Fraction below 53 μm.

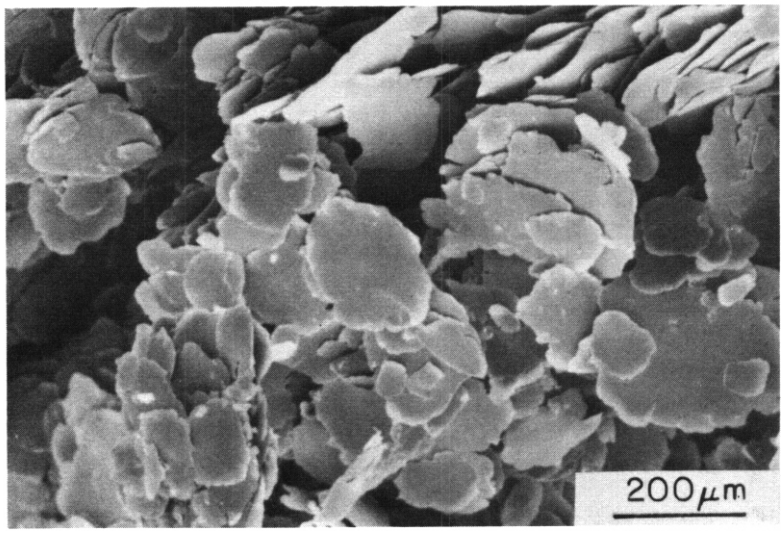

FIGURE 2. SEM Micrograph Showing the Morphology of Attrited Flakes. The 48 hr Attrition Resulted in Uniform (0.5-pm) Flake Thickness.

while stirring the stainless steel and $LiAlH_4$ powder mixture, $LiAlH_4$ first dissolved in the ether and then reprecipitated on the stainless steel flake surfaces as fine $LiAlH_4$ particles. The solubility of $LiAlH_4$ in ether is approximately 30 gm per 100 cc.[12] An attempt has been made to determine the size and distribution of the $LiAlH_4$ particles on the flake surfaces by Scanning Auger Microscopy; however, the interpretation of results was not straightforward due to the fact that the stainless steel matrix was alloyed with aluminum. Instead, small (1 gm) samples of flaked material were selected randomly and analyzed for lithium content. Very consistent values were obtained suggesting a uniform distribution of lithium on the flaked material.

The stainless steel flakes were heated for 1 to 3 hrs at 150°C under vacuum to decompose the $LiAlH_4$. These conditions were chosen based on the data available in the literature.[12] Mass spectroscopy analysis showed that hydrogen has been almost completely removed during this heat treatment; the residual hydrogen was below 5 ppm (the sensitivity limit for hydrogen analysis was 0.1 parts per million).

Consolidation of stainless steel flakes was performed by a dynamic powder compaction (shock wave compaction) technique. During the passage of the shock wave the pressure rises extremely rapidly, remains at this high value for some time and later falls as the pressure release occurs. Calculations showed[10] the following relation between the shock speed, particle velocity and the internal energy imparted to the material: steel powder of approximately 50% loose density compacted to shock pressure of 5 GPa gives a shock velocity of 1600 m/sec, a particle velocity of 800 m/sec and an internal energy change of 3×10^5 J/kg. This energy change corresponds to a temperature rise of 600°K and if the energy is considered to be deposited predominately at the powder particle surface, values for energy density and power density of 2×10^4 J/m^2 and $\sim 2 \times 10^{11}$ W/m^2 respectively are deduced. These values correspond to those of the upper end of the laser glazing process.

Microstructural examination showed that the as-compacted material was not fully dense. This was ascribed to the unfavorable geometry of the stainless

steel flakes, with the length to thickness ratio exceeding 100 (see Figure 2). Dynamic compaction, under identical conditions, of spherical powders or flakes with the length to thickness ratio less than 30 to 1 has normally resulted in density values greater than 99%.[10] Consequently, samples of dynamically compacted material were put in a container made of low carbon steel, evacuated and hot rolled (starting temperature was 1000°C) to 40% R.A. (10% reduction on each of 4 passes.) During the hot rolling operation the lithium doped stainless steel and the low carbon steel welded together; the low carbon steel was later removed by grinding.

The lithium content in the consolidated material, as determined by flame emission spectroscopy, was 985 wppm. This is the same amount within a few percent of that measured in lithium doped stainless steel prior to consolidation. Consequently, neither surface melting of the stainless steel flakes during dynamic compaction nor the subsequent exposure to 1000°C during hot rolling had an effect on the lithium content. This confirmed that the lithium was present as a stable oxide compound. in the future, therefore, it will not be necessary to use dynamic powder compaction for lithium doping, hot extrusion will suffice.

Specimens of lithium doped stainless steel were covered with plastic (C.N.) film and were irradiated in the 2PH2 facility in MITR-II. The thermal exposure was 10 sec at a flux of 6×10^{11} n/cm^2 sec. The film was developed for 10 min in 50% KOH at 50°C to enlarge the size of the damage tracks produced by alpha particles. A detailed procedure of film preparation and etching is described elsewhere.[13] The film was next coated with a thin layer of gold and examined by SEM. It has been found that the several 100 Å thick layers of gold which are normally used to prepare specimens for SEM observation was too thin to protect plastic film from deterioration under the electron beam. The thickness of the gold layer had to be doubled. This permitted an examination of the damage tracks in the SEM over an extended period of time. The results are shown in Figures 3 and 4. Figure 4 shows the distribution of damage tracks in a stainless steel sample doped with 1000 ppm lithium.

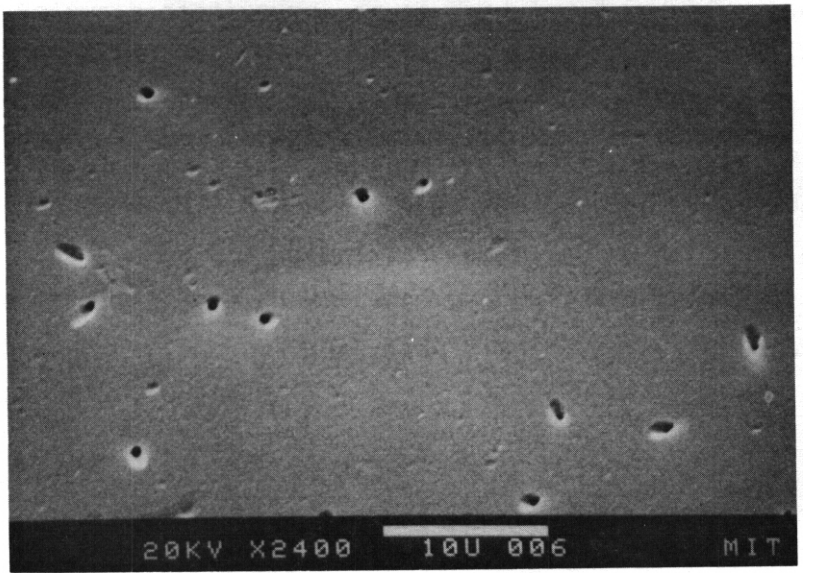

FIGURE 3. Neutron Autoradiograph of 316-Type Stainless Steel Without Lithium Addition. The Fluence is 6 x 10^{12} n/cm^2.

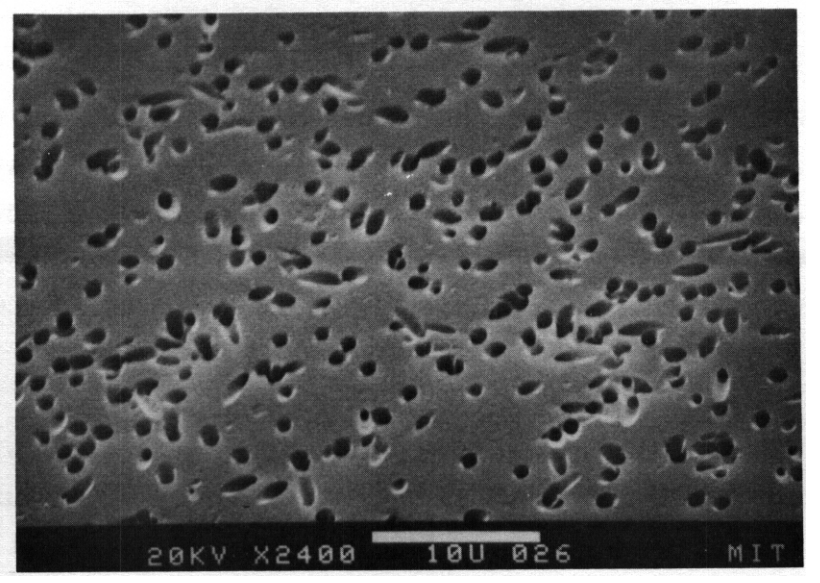

FIGURE 4. Neutron Autoradiograph of 316-Type Stainless Steel Doped with 1000-wppm Lithium. The Fluence is 6 x 10^{12} n/cm^2.

Damage tracks were enlarged by etching to an approximate diameter of 0.7-0.9 μm. The average spacing between the damage tracks, which reflects directly the lithium distribution in the stainless steel, is in the order of a few microns. Track density, as obtained from Figure 4, is 1.8 x 10^7 tracks/cm^2. Figure 3 is a neutron autoradiograph of a reference sample of stainless steel, without the lithium addition. Damage tracks may originate either from residual elements in the stainless steel or may possibly be due to contamination during neutron autoradiography. The track density in Figure 3 is low and approximately 0.9 x 10^6 tracks/cm^2.

5.4 Oiscussion

It has been shown in this study that by using rapid solidificaiton processing to produce fine powders and subsequently by powder metallurgy solid state techniques to disperse lithium uniformly in some form into the alloy as a stable lithium compound, useful lithium containing alloys are possible. As shown in the neutron autoradiograph in Figure 4, lithium interparticle spacing is of the order of several microns; this should assure uniform helium distribution in bulk specimens of non-nickel bearing materials when irradiated in fast fission reactors. The advantage of using powder metallurgy techniques is that the dopant (lithium in this case) can be introduced as a stable compound, such as an oxide. Similar powder metallurgy approaches may be used to dope alloys with a fine dispersion of a stable boron compound and thus reduce the problem of possible boron segregation to the grain boundaries with subsequent problems of coarsening and embrittlement as discussed in the introductory part of this report.

A salt decomposition technique was used to dope stainless steel with lithium. The ^6Li content in the $LiAlH_4$ compound was analyzed by neutron autoradiography. The observed transmission was 0.6125 ± 0.005. It is slightly lower than the expected transmission (0.6771) for natural lithium; the difference may be due to an error in density measurement. $LiAlH_4$ powders have been decomposed before neutron autoradiography in order to avoid the interference of

hydrogen in determining ^6Li content. These results indicate that lithium in a $LiAlH_4$ compound is present as natural lithium containing approximately 7.5% of ^6Li; consequently, the stainless steel was doped with approximately 75 ppm of ^6Li. As discussed in the introductory part of this report, mechanical blending with fine particles of a stable lithium compound as well as the salt decomposition technique should produce a uniform dispersion of Li dopant in the material. Lithium oxides are among the most stable lithium compounds; their particle size should be ideally of the order of 100 Å when incorporated as a dopant in the alloy by mechanical blending.

There may be a certain advantage in using lithium doping as compared to boron doping to generate simultaneous helium and displacement damage. This was based on the observation[14] that enhancement of swelling at 400°C was due to both lithium and helium atoms deposited in halos surrounding M_3B_2 precipitates. Consequently, the interpretation of the helium effect on swelling may be easier when lithium is used as a dopant instead of boron. Furthermore, the other reaction product of the $^6Li(n,\alpha)$ reaction is ^3H, which will, of course, also be present in a fusion reactor environment.

Both lithium and boron doping techniques appear to be promising in simulating simultaneous helium production and displacement damage in non-nickel bearing materials such as ferritic steels. The powder metallurgy approach, as described in this report, appears to be particularly attractive in developing lithium or boron doped ferritic steels which may be either oxide or carbide dispersion stabilized in order to improve the high temperature structural or mechanical stability. Established procedures to prepare dispersion stabilized materials[8] include the following steps: a) rapid solidification of a master alloy to prepare fine powders, with size fraction smaller than about 50 μm (see Figure 1); b) attrition of powders to produce near-micron size flakes (see Figure 2); c) ball milling of the flakes with oxide/carbide particles (several 100 Å in size) in amounts of several volume percent to obtain a uniform dispersion of a second phase. Lithium or boron doping, as discussed in this report, can then be simply integrated in this production scheme.

5.5 Conclusions

Lithium and boron doping techniques are possibilities for simulating simultaneous helium production and displacement damage in bulk specimens of non-nickel bearing materials such as ferritic steels when irradiated in fast fission reactors.

The rapid solidification processing and powder metallurgy salt decomposition technique has been used to prepare lithium doped austenitic stainless steel. Neutron autoradiography verified a uniform distribution of lithium in the alloy.

Although the same approach can be used to dope material uniformly with a stable boron compound, thus reducing the problem of grain boundary segregation and coarsening, it should be an advantage to use lithium doping because this dopant produces only helium and hydrogen which are also produced by the CTR environment.

6.0 References

1. G. W. Dansfield, "The Influence of Boron on Fusion Reactor Materials During Helium Embrittlement Simulation," MIT M.S. Thesis, Feb. 1980.

2. H. J. Goldschmidt, "Effect of Boron Additions to Austenitic Stainless Steels: Part II, Solubility of Boron in 18% Cr, 15% Ni Austenitic Steel," Journal of the Iron and Steel Institute, 209, 910 (1971).

3. D. R. Harries, A. C. Roberts, G. T. Rogers, J. D. H. Hughes and M. A. P. Dewey, "Role of Boron in the High-Temperature Irradiation Embrittlement of Austenitic Steel," Proceedings of the Symposium on Radiation Damage in Reactor Materials, Vienna, IAEA (1969), p. 357.

4. N. Kanani, L. Arnberg and O. K. Harling, "Pre-Irradiation Spatial Distribution and Stability of Boride Particles in Rapidly Solidified Boron Doped Stainless Steels," J. Nucl. Mater., 103 & 104, 1115 (1981).

5. H. Frost, J. Megusar and K. C. Russell, "Initial Estimates of the Kinetics and Distribution of Boron in Stainless Steel," in "Boron Doping of Stainless Steel by Rapid Quenching," DAFS Quarterly Progress Report, DOE/ET-0065/6, July 1979, p. 140.

6. F. A. Shunk, Constitution of Binary Alloys, Second Supplement, 1969, p. 332.

7. K. M. Zwilsky and N. J. Grant, "Dispersion Strengthening in the Copper-Alumina System," Trans. Met. Soc. AIME, 221, 371 (1961).

8. A. I. Ibrahim, J. Meausar and N. J. Grant, "Mechanical Properties and Structure of Y_2O_3 Dispersion Stabilized, Rapidly Solidified 316 Type Stainless Steel," to be published in the Fifteenth ADIP Progress Report for Period Oct. 1981-Mar. 1982.

9. J. J. Rasmussen and N. J. Grant. "Thoria Dispersion Strenathened Nickel and Nickel-Molybdenum Alloys Produced by Selective Reduction," Powder Met., Vol. 8, No. 15, 95 (1965).

10. D. G. Morris, "Dynamic Compaction of Metallic Glasses and Microcrystalline Materials," in Rapid Solidification Processing, Principles and Technologies, Proc. Int. Conf., 2nd, Clairton's Publishing Div., 1980, p. 372.

11 J. Megusar, L. Arnberg, J. B. Vander Sande and N. J. Grant, "Microstructure of Rapidly Solidified Al_2O_3 Dispersion Strengthened Type 316 Stainless Steel," J. Nucl. Mater., 103 & 104, 1109 (1981).

12. Handbook of Physics and Chemistry, 58th Ed., 1977-78, CRC Press, p. 8-125.

13. A. Fadaai, "Determination of 3-D Boron Distribution," MIT M.S. Thesis, June 1978.

14. D. S. Gelles and F. A. Garner, "An Experimental Method to Determine the Role of Helium in Neutron-Induced Microstructural Evolution," J. Nucl. Mater., 85 & 86, 689 (1979).

DISTRIBUTION

UC-20 (108)

UC-20c (76)

DOE-HQ/Office of Breeder Technology Projects
NE-53
Washington, DC 20545

PB Hemmig, Asst Director, Reactor Physics Tech

DOE-HQ/Office of Fusion Energy (2)
Washington, DC 20545

JF Clark, ER-70
JF Decker, ER-54, G-256

DOE-RL/Office of Asst Manager for Projects & Facilities Management (2)
FMIT Project Office

GM Chenevert, Project Manager

DOE-RL/Office of Asst Manager for Advanced Reactor Programs
Breeder Technology Division

KR Absher, Chief, Technology Development Branch

Argonne National Laboratory (5)
9700 South Cass Avenue
Argonne, IL 60439

LR Greenwood
BA Loomis
A. Taylor
H. Wiedersich
RE Nygren

Battelle Memorial Institute (3)
Pacific Northwest Laboratory
P.O. Box 999
Richland, WA 99352

JL Brimhall
DA Oingee
TD Chikalla

Brookhaven National Laboratory
Associated Universities
Upton, Long Island, NY 11973

Chairman, Nuclear Energy Dept

Columbia University
Plasma Physics Laboratory
New York, NY 10027

RA Gross

General Atomic Company (2)
P.O. Box 81608
San Diego, CA 92138

GR Hopkins
JR Gilleland

INESCO
11011 Torreyana Rd
San Diego, CA 92121

RD Stevenson

Lawrence Livermore Laboratory (3)
P.O. Box 808
Livermore, CA 94550

WL Barmore
MW Guinan, L-396
CM Logan

Los Alamos National Laboratory (4)
P.O. Box 1663
Los Alamos, NM 87544

DJ Dudziak
J. Fowler, E-546
CR Emigh
G. Hurley, E-546

Massachusetts Institute of Technology (5)
77 Massachusetts Avenue
Cambridge, MA 02139

L. Lidsky
I-W Chen, 13-5118
NJ Grant, 8-305
DB Montgomery, NW21
JB Vander Sande, 13-5025

DISTRIBUTION (Cont'd)

Massachusetts Institute of Technology
Nuclear Reactor Laboratory
138 Albany St
Cambridge, MA 02139

OK Harling, NW12-204

McDonnell-Douglas Astronautics Co.
P.O. Box 516
St. Louis, MO 63166

D. Kummer

Mound Laboratory
P.O. Box 32
Miamisburg, OH 45342

Manager, Tech Appl & Dev

National Bureau of Standards
Gaithersburg, MD 20760

JA Grundl

Naval Research Laboratory (3)
Washington, DC 20375

I. Manning, Code 6672
JA Sprague, Code 6395
LE Steele, Code 6390

North Carolina State University
Department of Nuclear Engineering
Raleigh, NC 26707

JR Beeler, Jr.

Oak Ridge National Laboratory (12)
P.O. Box X
Oak Ridge, TN 37830

Director, Bldg 9201-2
K. Farrell FG Perey
ML Grossbeck J. Sheffield
PJ Maziasz JO Stiegler
LK Mansur C. Weisbin
NH Packan RV Wiffen
M. Roberts, Bldg 9204-1

Princeton University (2)
Plasma Physics Laboratory
Forrestal Campus
P.O. Box 451
Princeton, NJ 08544

K. Wakefield
H Furth

Rockwell International
8900 DeSoto Ave
Canoga Park, CA 91304

D. Kramer

Sandia Laboratories (2)
P.O. Box 5800
Albuquerque, NM 87185

FL Vook, Org 5100

Sandia Laboratories
Livermore, CA 94550

WD Wilson

Science Applications, Inc.
200 Prospect
LaJolla, CA 92037

Dr. H. Gurol

University of California (2)
Los Angeles, CA 90024

RW Conn
NM Ghoniem

University of Michigan
Nuclear Engineering
Ann Arbor, MI 48109

T. Kammash

University of Missouri
Mechanical & Aerospace Engineering
1006 Engineering Bldg
Columbia, MO 65211

M. Jolles

DISTRIBUTION (Cont'd)

University of Missouri
Dept of Nuclear Engineering
Rolla, MO 65401

A. Kumar

University of Virginia
Dept of Materials Science
Charlottesville, VA 22901

WA Jesser

University of Wisconsin
1500 W. Johnson Drive
Madison, WI 53706

WG Wolfer

Westinghouse
Advanced Reactors Division
P.O. Box 158
Madison, PA 15663

A. Boltax

Westinghouse
Research and Development Center (2)
1310 Beulah Road
Pittsburgh, PA 15235

S. Wood
JA Spitznagel

Commission for the European Communities
200, rue de la Loi
B-1049 Brussels, Belgium

J. Darvas

Energieonderzoek Centrum Nederland
Westerdionweg 3
NL-1755 ZG Petten, The Netherlands

B. Van Der Schaaf

EURATOM
Joint Research Center Ispra
Materials Science Division
I-21020 Ispra, Varese, Italy

P. Schiller

Hahn-Meitner Institute fur Kernforschung
Glienickerstrasse 100
D-1000 Berlin,
Federal Republic of Germany

H. Wollenberger

Hokkaido University
Faculty of Engineering
Sapporo 060, Japan

T. Takeyama

Japan Atomic Energy Research Institute (2)
Physical Metallurgy Laboratory
Tokai Research Establishment
Tokai-mura, Naka-gun, Ibaraki-ken, Japan

S. Iwata, Physics
K. Shiraishi, Nuclear Fuel Research

Kernforschungsanlage Jülich GmbH
Postfach 1913
D-517 Julich,
Federal Republic of Germany

H. Ullmaier

Kernforschungsanlage Karlsruhe
Institut für Reaktorbauelemente
Postfach 3640
D-7500 Karlsruhe 1,
Federal Republic of Germany

K. Ehrlich

DISTRIBUTION (Cont'd)

Kyushu University
Research Institute for Applied Mechanics
6-10-1 Hakozaki, Higashi-ku,
Fukuoka 812, Japan

K. Kitajima

National Research Council
Montreal Road
Ottawa, Canada

EV Kornelson

National Research Institute for Metals
Nuclear Materials Division
1-2-1 Sengen, Sakura-mura,
Niihari-gun, Ibaraki 305, Japan

N. Kishimoto

Netherlands Energy Research Foundation
Materials Department
P.O. Box 1
NL-1755 ZG Petten, The Netherlands

W. Van Witzenburg

Osaka University
Dept of Nuclear Engineering
2-1, Yamada-oka, Suita,
Osaka 565, Japan

K. Sumita

Science University of Tokyo
Engineering Dept
Kagurazaka, Shinjuku-ku,
Tokyo 162, Japan

RR Hasiguti

Studiecentrum voor Kernenergie
Centre d'Étude de 1'Energie Nucleaire
Boeretang 200
B-2400 Mol, Belgium

J. Nihoul

Swiss Federal Institute
for Reactor Research
- 303 Wuerenlingen, Switzerland

WV Green

Tokyo Institute of Technology
- , 2-Chome, O-Okayama
Meguro-ku, Tokyo, Japan

K. Kawamura

United Kingdom Atomic Energy Authority
Atomic Energy Research Establishment
Metallurgy Division
Building 388
Oxfordshire, OX11 ORA, UK

DR Harries

University of Tokyo (3)
Bunkyo-ku,
Tokyo 113, Japan

Naohira Igata, Met & Mater Science
Shiri Ishino, Nuclear Eng
Taijiro Uchida

DISTRIBUTION (Cont'd)

HEOL (36)

SD Adkin	W/A-58	EK Opperman	W/A-58
HR Brager	W/A-64	NF Panayotou	W/A-65
WL Bunch	W/B-47	EF Parker	W/E-17
LL Carter	W/B-47	RW Powell	W/A-64
DG Doran (5)	W/A-57	RJ Puigh	W/A-58
EA Evans	W/C-23	FH Ruddy	W/C-39
FA Garner	W/A-57	FA Schmittroth	W/A-4
DS Gelles	W/A-64	WF Sheely	W/C-62
R. Gold	W/C-39	RL Simons	W/A-57
HL Heinisch	W/A-57	AL Trego	W/E-15
DL Johnson	W/A-4	GL Wire	W/A-58
GD Johnson	W/A-65	HH Yoshikawa	W/C-44
NE Kenny	W/C-115	Central Files (3)	W/C-110
FM Mann	W/A-4	Publ Services	W/C-115
WN McElroy	W/C-39	Doc Clearance	W/C-123